Technische Universität München
TUM School of Engineering and Design

Aerodynamic Design and Performance Analysis of a Morphing Wing Racing Sailplane

Dipl.-Ing. Univ. Johannes Achleitner

Vollständiger Abdruck der von der TUM School of Engineering and Design der Technischen Universität München zur Erlangung eines

Doktors der Ingenieurwissenschaften (Dr.-Ing.)

genehmigten Dissertation.

Vorsitz: Prof. Dr.-Ing. Klaus Drechsler

Prüfende der Dissertation:

1. Prof. Dr.-Ing. Mirko Hornung
2. Prof. Dr.-Ing. Rolf Radespiel

Die Dissertation wurde am 13.11.2024 bei der Technischen Universität München eingereicht und durch die TUM School of Engineering and Design am 20.06.2025 angenommen.

ABSTRACT

A key design goal for racing sailplanes is improving the glide ratio over a wide speed range. This work proposes a wing with a morphing forward section and a conventional trailing edge flap to achieve this. This study focuses on the aerodynamic design of the wing using a decomposed approach, with airfoils and wing planform designed separately through novel numerical optimization methods using fast potential flow solvers.

A new geometry parameterization method is introduced for airfoil design, enabling consistent description in both morphed and undeformed states. The optimized wing airfoils exhibit extended laminar low drag regions, achieving up to 20% higher lift coefficients and comparable drag coefficients to conventional airfoils with trailing edge flaps. This allows for a reduction in wing area and an increase in maximum wing loading by the same percentage, without raising the minimum speed.

An efficient numerical optimization method is introduced for the wing planform and winglet design. This includes a new geometry parameterization method, that allows to describe a wide variety of wing and winglet planform shapes with a low number of design variables.

The performance of a sailplane, which combines the newly designed morphing wing with the fuselage and tailplane of an existing 18 meter class flapped racing sailplane is evaluated. A new performance metric, based on real competition flights, condenses aircraft performance into a single scalar value. The morphing wing sailplane demonstrates a 3.4% performance increased compared to an existing 18 meter class flapped aircraft. Further improvements could be achieved by redesigning the rest of the aircraft, particularly through reducing the tail surface area.

KURZFASSUNG

Das Ziel des Entwurfs von Hochleistungssegelflugzeugen ist die Verbesserung der Gleitleistung über einen weiten Geschwindigkeitsbereich. Zu diesem Zweck wird in dieser Arbeit ein Flügel mit einer formvariablen Flügelvorderkante in Kombination mit einer konventionellen Hinterkantenklappe vorgeschlagen. Der Schwerpunkt der Arbeit liegt auf dem aerodynamischen Entwurf des Flügels in einem separierten Entwurfsansatz. Dabei werden die Flügelprofile und der Grundriss des Tragflügels inklusive Wingletgeometrie getrennt entworfen. Beide Entwurfsaufgaben werden mithilfe neuartiger numerischer Optimierungsverfahren und schneller potentialtheoretischer Strömungslöser durchgeführt.

Für den Profilentwurf wird eine neuartige Geometrieparametrisierungsmethode vorgestellt, die es ermöglicht, die Geometrie des Flügelprofils in deformiertem und unverformtem Zustand konsistent zu beschreiben. Damit wurde eine Reihe von Flügelprofilen optimiert. Diese verfügen im Vergleich zu Profilen mit Wölbklappen um 20% höhere Auftriebsbeiwerte innerhalb der Laminardelle bei ähnlichen Widerstandsbeiwerten. Dies erlaubt eine Verkleinerung der Flügelfläche und eine Erhöhung der maximalen Flächenbelastung um den gleichen Prozentsatz, ohne die Mindestgeschwindigkeit zu erhöhen.

Für den Entwurf der Flügelgrundriss- und Wingletgeometrie wird eine effiziente numerische Optimierungsmethode eingeführt. Dazu gehört eine weitere neue Geometrieparametrisierungsmethode, die es ermöglicht, eine große Vielfalt an Flügel- und Wingletformen mit einer geringen Anzahl von Designvariablen zu beschreiben.

Die Kombination des neu gestalteten, formvariablen Flügels mit Rumpf und Leitwerk eines bestehenden 18-Meter-Klasse-Hochleistungssegelflugzeugs wird analysiert. Dazu wird eine neue Leistungsmetrik basierend auf realen Wettbewerbsflügen entwickelt, die die Flugzeugleistung mit einem einzigen skalaren Wert beschreibt. Das Morphing-Wing-Segelflugzeug zeigt eine um $3,4\%$ höhere Leistung im Vergleich zu bisherigen Flugzeugen der 18-Meter-Klasse. Weitere Verbesserungen sind durch einen Neuentwurf des gesamten Flugzeugs, insbesondere durch eine Reduktion der Leitwerksflächen möglich.

ACKNOWLEDGMENTS

Diese Arbeit widme ich all den Menschen, die mich auf meinem Weg begleitet haben.

Meinen Eltern Ilse und Günter Achleitner danke für ihre bedingungslose Unterstützung. Sie haben mir mein Studium und schon in jungen Jahren das Segelfliegen ermöglicht.

Mein Dank gilt auch Heinz Gattermeier, der mir die Liebe zum Segelflug nähergebracht hat. Ohne ihn hätte ich diesen Weg nicht eingeschlagen. Der gesamten Akaflieg München danke ich für die wunderbare Gemeinschaft, die ich während meiner Studienjahre erleben durfte. Die Akaflieg ist eine einzigartige Institution, die sich mit Leidenschaft dem Segelflugsport widmet, neben dem Studium großartige Flugzeuge entwirft und baut und aus vielen tollen Menschen besteht. Besonders möchte ich Philip Theilmann und Philipp Strobach danken. Sie waren wertvolle Mitstreiter im Projekt und darüber hinaus großartige Freunde.

Meinem Bürokollegen und Freund Fabian Sturm danke ich für die vielen wertvollen Diskussionen über das Projekt und darüber hinaus sowie für die zahlreichen gemeinsamen Fahrradtouren.

Meinem Freund und Bürokollegen Dr. Matthias Weinzierl danke ich für die vielen spannenden und interessanten Diskussionen. Matthias war mir immer ein Vorbild und ein großer Freund. Ein großer Dank gebührt auch Dr. Erich Wehrle, als eines meiner großen Vorbilder als Wissenschaftler.

Einen wesentlichen Beitrag zu dieser Arbeit hat Kai Rohde-Brandenburger geleistet. Trotz großer räumlicher Distanz verbindet uns eine starke Freundschaft. Kai hat mir die Grundlagen der aerodynamischen numerischen Formoptimierung beigebracht und in zahlreichen gemeinsamen Arbeitstreffen wesentlich zum Gelingen dieses Projekts beigetragen.

Mein Dank gilt auch Loek M.M. Boermans für die zahlreichen Tipps und Tricks im Flugzeugentwurf und die Bereitstellung des Quellcodes von *XFOILSUC*. Zudem gebührt Ulrich Deck, ehemaliger Mitarbeiter der Firma Schleicher und nunmehriger Leiter des Laminarwindkanals Stuttgart, großer Dank für sein Engagement im Projekt und dafür, dass ich durch seine Erfahrungen aus der Windkanalpraxis so viel über den Profilentwurf lernen durfte.

Der Firma Schleicher gilt mein großer Dank für die unschätzbare Unterstützung in den *Mü 31*-Zeiten und dafür, dass sie sich dieses gewagten Projekts angenommen haben. Insbesondere danke ich Joschka Schmeisl und Paul Anklam.

Meinem Doktorvater Prof. Dr.-Ing. Mirko Hornung danke ich dafür, dass er den Lehrstuhl für Leichtbau so souverän durch die nicht ganz einfache Zeit der kommissarischen Leitung geführt und uns stets den Rücken freigehalten hat, sodass wir uns auf die Forschung konzentrieren konnten. Seine wertvollen Hinweise und Diskussionen haben wesentlich zur Qualität dieser Arbeit beigetragen.

Prof. Dr.-Ing. Horst Baier möchte ich herzlich danken für die Chance, die er mir mit der Anstellung als wissenschaftlicher Mitarbeiter geboten hat. Den Werkstattmitarbeitern Manfred Bauer, Josip Stokić, Bernhard Lerch und Ludwig Krämer gilt besonderer Dank für die tatkräftige Unterstützung im Projekt.

Ebenso danke ich Prof. Dr.-Ing. Rolf Radespiel für die Übernahme der Zweitprüferschaft meiner Dissertation.

Zu guter Letzt danke ich von Herzen meiner lieben Frau Eva, die mir stets treu zur Seite steht und mich immer wieder motiviert hat, diese Dissertation zum Abschluss zu bringen.

CONTENTS

LIST OF FIGURES

LIST OF TABLES

ACRONYMS

AFT Amplification Factor Transport equation transition model

CAD Computer Aided Design

CAS Calibrated Air Speed

CFD Computational Fluid Dynamics

CFRP Carbon Fiber Reinforced Polymer

CNC Computer Numerical Control

CST Class function Shape function Transformation methodology

DES Detached Eddy Simulation

DLM Doublet Lattice Method

DLR	Deutsches Zentrum für Luft- und Raumfahrt, German aerospace center
EASA	European Union Aviation Safety Agency
FAI	Fédération Aéronautique Internationale
FEM	Finite Element Method
FRP	Fiber Reinforced Polymer
GFRP	Glass Fiber Reinforced Polymer
GPS	Global Positioning System
IBL	Integral Boundary Layer method
ICAO	International Civil Aviation Organization
Idaflieg	Interessensgemeinschaft Deutscher Akademischer FLIEGergruppen, umbrella organization of German academic flying groups
IGC	International Gliding Commission
IMU	Inertial Measurement Unit
ISA	International Standard Atmosphere
LES	Large Eddy Simulation
MTOM	Maximum Take Off Mass
MMA	Method of Moving Asymptotes
PA	PolyAmide
PET	PolyEthylene Terephthalate
PP	PolyPropylene
RANS	Reynolds Averaged Navier Stokes
SIMP	Solid Isotropic Material with Penalization
SLS	Selective Laser Sintering
SST	Shear Stress Transport turbulence model
SVD	Singular Value Decomposition
SUMT	Sequential Unconstrained Minimization Technique
VLM	Vortex Lattice Method

NOMENCLATURE

α	Angle of attack
α_{NMS}	Nelder–Mead simplex method reflection coefficient
$\alpha_{\max}$	Angle of attack at maximum lift coefficient
$\bar{c}$	Wing chord length
$\beta = \beta_r = \omega$	Tollmien-Schlichting wave frequency
β_{NMS}	Nelder–Mead simplex method contraction coefficient

$\boldsymbol{\sigma}_{\mathrm{NMS}}$	Vector of initial simplex size factors for each design variable
$\Delta\tilde{N}$	Increase of amplification factor due to step
Δc	Change of camber
Δt	Change of thickness
δ_F	Flap deflection angle
δ_{NMS}	Nelder–Mead simplex method shrinkage (massive contraction) coefficient
$\delta_{f,0}$	Flap deflection angle, where top side contour is continuous
Γ	Circulation of a vortex line
γ	Circulation of a vortex sheet
γ_{NMS}	Nelder–Mead simplex method expansion coefficient
$\hat{\alpha} = \hat{\alpha}_r + i\hat{\alpha}_i$	Complex Tollmien-Schlichting wave number
$c_{\hat{TS}}$	Tollmien-Schlichting wave propagation speed
$\hat{x}$	Scaled x coordinates
κ	Wing dihedral angle
Λ	Wing aspect ratio
$\mathbf{c_3}$	Blunt trailing edge summand vector
$\mathbf{c_4}$	Design flap summand vector
$\mathbf{M}$	CST coefficient matrix
$\mathbf{R}$	Rotation matrix
$\mathbf{r}_{\mathrm{SUB}}$	SUBPLEX step size vector
$\mathbf{x}$	Position vector
$\mathbf{x}_r$	Flap rotation point
$\mathbf{x}_{\mathrm{LE}}$	Leading edge point
$\mathbf{x}_{\mathrm{TE}}$	Trailing edge point
$\mathbf{x}_f$	Rotated trailing edge point
ω	SUBPLEX step reduction/expansion coefficient
$\mathbf{\Phi}$	Amplitude of the perturbation stream function
ϕ	Wing sweep angle
ϕ_b	Bank angle
ψ_{SUB}	Simplex size reduction tolerance in SUBPLEX algorithm

ρ	Density of air
ρ_{ISA}	Density of air at sea level according to the International Standard Atmosphere
θ	Camber line slope
$\tilde{x}$	Deformed x coordinates
A	Wing area
a	Amplitude of Tollmien-Schlichting wave
a_0	Initial amplitude of Tollmien-Schlichting wave
a_1, a_2, a_3	Wing planform parameterization basis functions
A_{comp}	Wing area of the comparison sailplane
B	Bernstein polynomial
b	span width
C	Class function
c	Airfoil camber
c_1, c_2	Residual drag Reynolds correction coefficients
C_d	2D section drag coefficient
c_d	Airfoil drag coefficient
C_L	Overall aircraft lift coefficient
C_l	2D section lift coefficient
c_l	Airfoil lift coefficient
C_{Di}	Induced drag coefficient
C_{Dp}	Wing profile drag coefficient
C_D	Overall aircraft drag coefficient
c_{tol}	Contraint violation tolerance
D	Drag force
D_F	Fuselage drag
D_i	Induced drag force
d_i	Airfoil geometry design variable
D_p	Profile drag force
D_{inter}	Interference drag
D_{Pa}	Parasitic drag

D_{res}	Residual drag
E	glide ratio
e_1	Superellipse wing planform parameterization basis function
f	Objective function
f_p	Penaltized objective function
f_t	Statistical distribution of flown lift coefficient over competition flights
$f_{d,p}$	Profile drag correction factor
g	Gravitational acceleration of earth
g_j	Inequality constraint function
h_k	Equality constraint function
k	Induced drag factor
$K_{i,n}$	Binomial coefficient
L	Lift force
m_{flight}	Aircraft flight mass
m_{MTOM}	Maximum take off mass
Ma	Mach number
n	Number of design variables
$N_1 \cdots N_4$	CST coefficients
n_z	Normal acceleration in z direction
n_{SUB}	Number of SUBPLEX subspaces
$n_{s,i}$	index of SUBPLEX subspace
n_{SE}	Superellipse exponent
q	Parabolic wing planform parameterization basis function
R	Residual
r_0	Inequality constraint penalty factor
Re	Reynolds number
S	Shape function
s	Arc length coordinate of the wing (spanwise)
s_b	Arc length of the half-wing
t	Thickness distribution

Tu	Freestream turbulence level
U_∞	Air speed
W	Aircraft weight force
w_s	Sink speed
w_{op}	Optimization weighing factor for operation point *op*
x, y, z	Local, cartesian-basis coordinate
x_e	End of morphing region
x_m, y_m	Airfoil coordinates in morphed configuration
x_o, y_o	Airfoil coordinates in undeformed configuration
x_s	Start of morphing region
$\bar{()}$	Scaled coordinates in morphing section
$\square_{\text{comp}}$	Index referencing comparison sailplane (*ASG 29*)
$\square_{\text{new}}$	Index referencing morphing wing sailplane

The nomenclature is defined as the following: vectors and matrices are in bold. Vectors are lower case and matrices are upper case. In the case of scalars lower and upper case has no further meaning other than distinction.

1 INTRODUCTION

The common objective for both pilots and design engineers of racing sailplanes is the increase of the average cross-country speed in soaring competition tasks, which normally range over a few hundred kilometers. The use of thermals is the dominant source of lift for cross-country soaring, although in some parts of the world ridge lift and mountain waves are used as energy source. For covering such distances, sailplanes normally gain altitude by circling in thermals with low speed and dash in between those thermals with high speed.

The pilot optimizes the cross-country speed primarily by choosing the flight path. During climbing in thermals, the pilot tries to adjust the center of the circle inside the thermal to maximize the climb rate. Simultaneously, the bank angle, sideslip angle and speed must be controlled. In inter-thermal flight, the pilot tries to optimize both the time it takes to fly to the next thermal as well as the altitude loss. Again, choosing the right flight path is key, i.e. search for rising air whilst flying with minimum detour. The higher the flight speed, the lower the time spent to the next thermal, but also the higher the sink rate. Therefore, also the choice of the flight speed in inter-thermal dash is an optimization problem, as the MacCready [72] theory shows.

For the sailplane design engineer, the objective of increasing the cross country speed can be achieved by minimizing the sink rate both in thermal circling flight and in inter-thermal dash. In history, the development of sailplane performance was pushed forward by new technological developments, like the introduction of Glass Fiber Reinforced Polymer (GFRP) and Carbon Fiber Reinforced Polymer (CFRP) or the development of new and better laminar airfoils. Fig. 1.1 shows the historical evolution of the best glide ratio of various sailplanes. The different line colors represent the corresponding technologies used. The lower lines of the same color show the best glide ratio for 15 meter class sailplanes, the upper lines show open class sailplanes without span limitations. However, this graph is of qualitative nature, but is backed with data of some concrete sailplanes, which mark a milestone for pushing forward the development of sailplane performance. When new technologies emerge, they allow an improvement in performance compared to existing technology, although the technology is not well understood at first. Over time, more knowledge is gained of the technology, and the performance increases further on. At some point, it becomes hard to increase performance further with the existing technologies. Only small incremental improvements are possible. Until the next technology emerges. For example, this was the case with the advent of GFRP as the main construction material. Better knowledge of the material made thinner airfoils and/or larger wing span possible, which was not utilized at first when the technology was introduced. Also RANS based CFD with transition prediction had not been applied in sailplane design at the time fig. 1.1 was created, but lead to a further increase in sailplane performance in the last ten years. However, the next technological advancement is sought in sailplane design.

In this thesis, a new concept for a sailplane wing equipped with a morphing forward section is introduced. A brief overview of the concept is given in section 1.1 and a more detailed introduction is given in chapter 2. The concept could lead to a significant performance gain. The aerodynamic design objective and the requirements are discussed in chapter 3. The aerodynamic design is done utilizing wide use of numeric optimization in a decomposed design approach. The airfoils and the wing planform are designed separately. The design of the new morphing airfoils is shown in chapter 4. A new optimization method for the wing planform including winglets is presented in

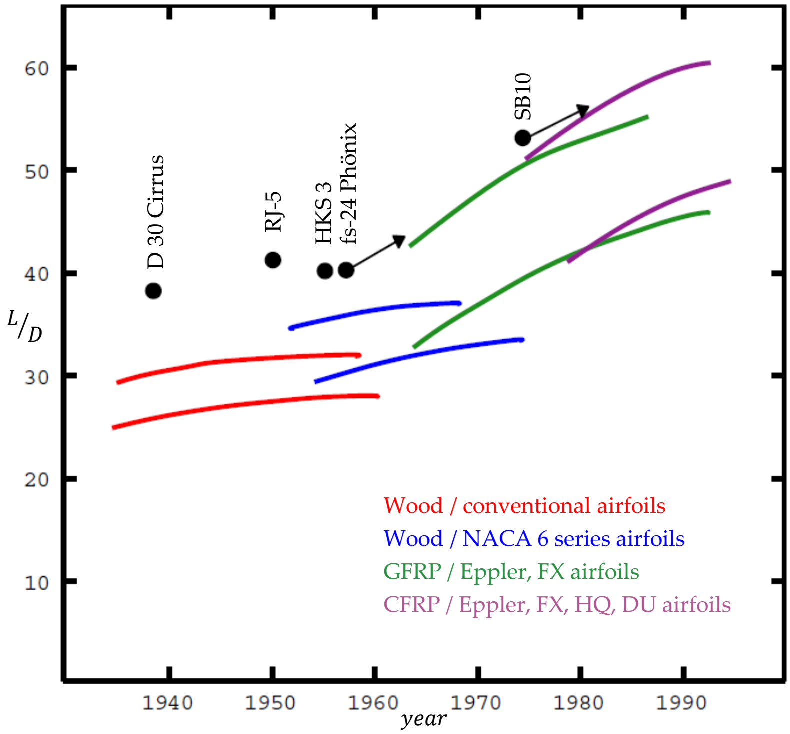

Figure 1.1: Evolution of best glide ratio of sailplanes, from [111]

chapter 5. The potential performance gain of the morphing wing sailplane in comparison to the current technological state of the art is analyzed with an extrapolation method based on measured performance data. This is shown in chapter 6. Finally, conclusions are drawn and an outlook on potential improvements of the morphing concept and the methods used in this work is given in chapter 7.

This work has the following goals:

- To shed light on the question if it is possible to improve sailplane performance with a wing with a morphing forward section.
- To introduce the structural concept for a wing with a morphing forward section.
- To develop the best suited design and analysis methods for the prediction of the aerodynamic performance of a morphing sailplane wing.
- To develop a method for fast and accurate numerical optimization of morphing forward section airfoils
- To develop a method for fast and accurate numerical optimization for wing planform design including winglets
- To quantify the performance difference between the morphing wing and a conventional sailplane with a trailing edge flap with a precise and coherent metric. The metric should represent a typical sailplane competition environment.

1.1 A MORPHING DROOP-NOSE CONCEPT FOR SAILPLANES

This section introduces the structural concept that forms the foundation of this work. Although the primary focus is not on developing a structural concept for a morphing wing sailplane, the design has significant implications for the aerodynamic configuration of the wing, and vice versa. For example, the compliant mechanisms within the structure enable specific deformations in the morphing section. However, they come with certain limitations that must be considered in both airfoil and wing planform design. The reduction in wing area leads to a decreased height of the main spar, presenting structural challenges that necessitate constraints on the minimum airfoil thickness during design. The airfoil optimization methodology introduced in chapter 4 is specifically adapted to create airfoils compatible with the structural concept described here. Consequently, this section provides a brief overview of the structural concept for the morphing forward section, with a more detailed discussion available in chapter 2.

An overview of the structural concept of the morphing wing sailplane is shown in fig. 1.2. It is introduced by the author [3] and Sturm [116]. The morphing forward section, shown in yellow, spans the entire wing. Furthermore, the wing comprises of the primary load carrying structure and a conventional trailing edge flap, shown in blue. The morphing wing shell is a Fiber Reinforced Polymer (FRP) laminate with high stiffness anisotropy. It is stiffer in spanwise direction and more flexible in direction of flight. The morphing wing shell is discussed in detail in section 2.2. On the upper wing surface it is bonded to the wing shell of the primary structure, whereas on the lower wing surface the morphing shell slides on a recessed sliding surface in front of the main spar. This sliding joint is covered with a hydraulically smooth 0.2 mm thick biaxially oriented polyethylene terephthalate (boPET, trade name Mylar) foil seal, ensuring laminar flow across the joint.

The sliding joint allows the leading edge region, the front 5% of the chord, to perform a pure rigid body motion during morphing actuation. This is in contrast to other morphing leading edge concepts, like the concepts of the Composite Structures and Adaptive Systems research group of the German Aerospace Center (DLR) (see Kintscher et al. [59], Radestock et al [95], Sinapius et al [112] and Vasista et al [123]), where the morphing section is attached to the primary structure on both upper and lower side. During morphing actuation, this attachment method requires the wing shell to unbend at the current leading edge radius. Simultaneously, a new leading edge radius is formed through significant bending at another location. This kinematic requirement, inherent in designs with clamped upper and lower morphing shells, induces high bending stresses within the wing shell and leads to deviations from the desired aerodynamic contour. However, a drawback of the concept of this work is that the torque box cross section is reduced to the area behind the main spar. Additionally, the elastic axis is positioned significantly behind the aerodynamic center, potentially leading to higher torsional stresses and deformations.

The morphing shell is deformed by compliant mechanism ribs. Each rib consists of six mechanisms stacked in spanwise direction. All individual mechanisms share the same input point and drive different output points on the shell. Their geometry is synthesized using nonlinear topology optimization. The objective of the mechanisms is to actuate the shell with an as-precise-as-possible output precision, so that the target morphed airfoil shape is met with minimal deviation. The ribs are located in a regular spanwise pattern, with a distance of approximately 0.5 m. A torsional drive actuates all compliant mechanisms on a common axis. A detailed discussion of the design of the compliant mechanisms, material selection and manufacturing is given in section 2.1. The morphing droop leading edge and the trailing edge flap are actuated together. The aileron movement is superimposed with the flap deflection.

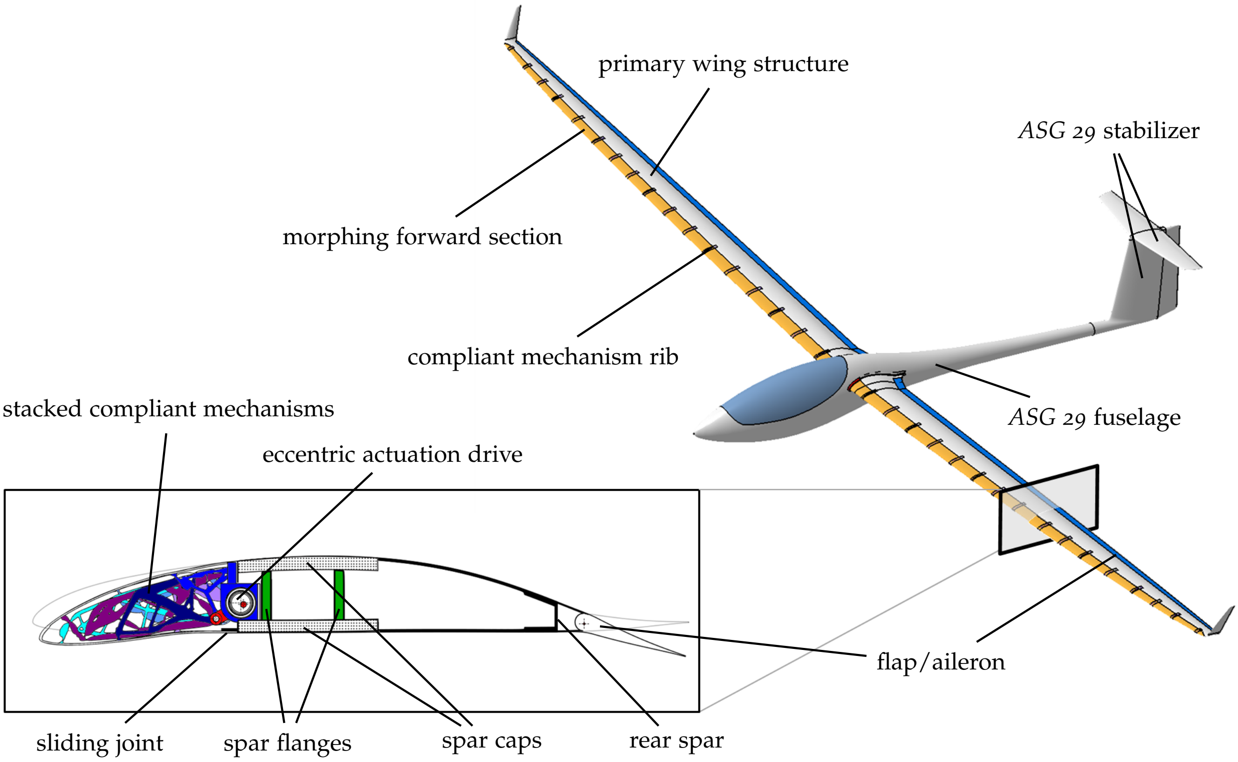

Figure 1.2: Morphing wing sailplane structural concept, from [3]

1.2 REFERENCE SAILPLANE: ASG 29

In this work, the *ASG 29* 18 meter class sailplane, manufactured by the *Alexander Schleicher Segelflugzeugbau GmbH* is used as the reference for performance analysis. A three side view of the sailplane is shown in fig. 1.3. Although newer designs exist in the 18-meter class, the *ASG 29*'s performance is comparable to the latest designs. For instance, Stefan Langer won the 2023 World Sailplane Grand Prix in Pavullo, Italy, flying an *ASG 29*, competing successfully against newer models. The morphing wing sailplane concept comprises of the fuselage and tailplane of the *ASG 29*, as shown in fig. 1.2.

Comprehensive design and performance data of the sailplane is made available by the manufacturing company and various other sources for this work, which makes it possible to perform detailed analysis and comparison. The data is given in appendix A.2. The design and wind tunnel measurements of the main wing airfoil *DU89-134-14* is published by Boermans and van Garrel [16]. In-flight performance measurements according to the method of Paetzold [86] is available. This enables to conduct precise performance estimation of the morphing wing sailplane and performance comparison to the current state-of-the-art sailplane *ASG 29* as presented in chapter 6.

1.3 POTENTIAL PERFORMANCE IMPROVEMENT OF A MORPHING WING SAILPLANE

In the design of a racing sailplane, optimizing to minimize the sink rate across a wide range of airspeeds is critical. Therefore, the contributions of various drag components to the total sailplane drag and thus the sink rate has to be analyzed. In this dissertation, the focus lies on the wing design. Hence, in this section, the influence of the wing profile and the induced drag is analyzed.

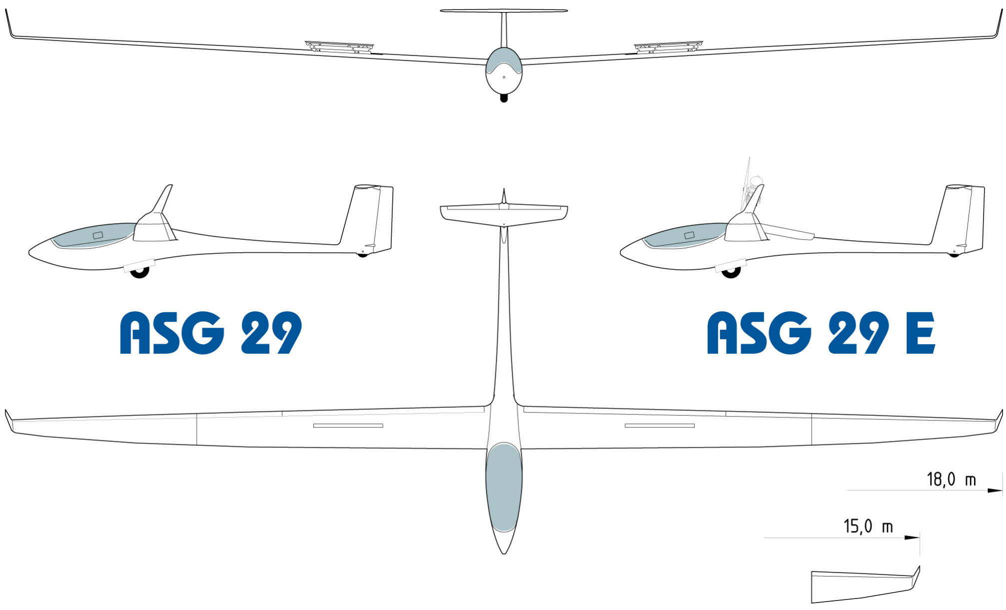

Figure 1.3: Three side view of the *ASG 29* sailplane, from Alexander Schleicher website

A parametric variation shows how an increase in the aircraft's maximum lift coefficient, $c_{l,\max}$, influences the sizing of the wing area. In further consequence, this influences the profile and induced drag of the wing and ultimately the overall aircraft performance.

The total drag of the sailplane is the sum of the induced drag D_i, the wing profile drag D_p and residual drag D_{res}. The residual drag consists of all other drag components. These are tailplane, fuselage, interference and parasitic drag. An analysis of the drag breakdown of the *ASW-27* sailplane is given by Boermans [14] and shown in fig. 1.4. It has to be mentioned, that the sink speed is proportional to the total drag D of the sailplane. Boermans shows the contribution of the drag components of the aircraft to total drag over airspeed. The induced drag is predominant at low airspeeds and decreasing with higher airspeed. The wing profile drag is low at low speed. At higher speeds, the wing profile drag becomes the main drag contributor. As a sailplane flies at low speed during climb, and high speed during inter-thermal glide, wing design is a trade off between profile and induced drag.

Now the influence of morphing concepts on the drag if an aircraft is discussed. Morphing concepts can either aim on reducing the profile drag coefficient or on increasing the maximum lift coefficient or a combination of both. However, also an increase in the maximum lift coefficient can lead to a decrease in total wing drag as will be shown. Therefore, the influence of the maximum lift coefficient of the wing on aircraft drag is discussed. The lift force L is calculated as:

$$L = \frac{1}{2}\rho U_\infty^2 C_L A \approx W = m_{\text{flight}} g n_z, \tag{1.1}$$

with A being the wing area, U_∞ the air speed, ρ the air density, m_{flight} the current flight mass and C_L being the overall aircraft lift coefficient. For sailplanes, which are characterized by a high glide ratio E, the small angle approximation can be effectively applied. Under this approximation, the lift force L is approximately equal to the weight W of the sailplane. In steady, unaccelerated flight, the normal acceleration is $n_z = 1$. As outlined in detail in Section 3.2.1, certification standards for sailplanes require a minimum speed of $90\ \mathrm{km/h}$ or lower at MTOM. Therefore, the wing must

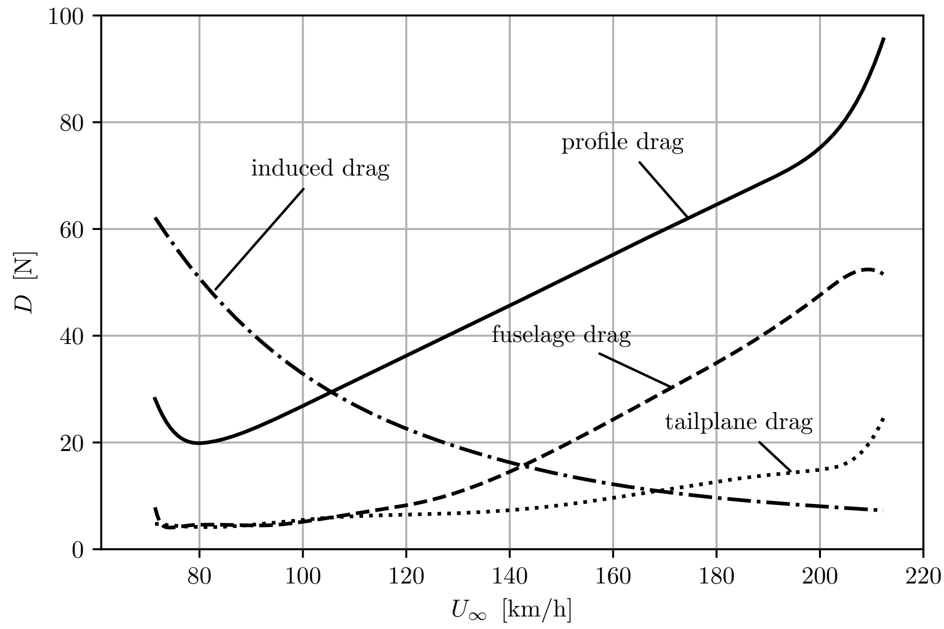

Figure 1.4: Drag components of *ASW 27* sailplane, data from reference [14]

generate sufficient lift at this speed to support the sailplane's maximum weight. This requirement necessitates a minimum value for the product of $c_{l,\max}$ and A, where A represents the wing area. This can be achieved by using airfoils with a higher maximum lift coefficient $c_{l,\max}$, typically associated with higher drag coefficients, or by increasing the wing area A while using airfoils with a lower $c_{l,\max}$ and correspondingly lower drag coefficients c_d. However, determining which design minimizes total drag is complex. To assess this, the drag force D must be calculated using the aircraft's overall drag coefficient C_D:

$$D = \frac{1}{2}\rho U_\infty^2 C_D A. \tag{1.2}$$

The induced drag coefficient is calculated as:

$$C_{Di} = k\frac{C_L^2}{\pi\Lambda}, \tag{1.3}$$

with the wing aspect ratio $\Lambda = \frac{b^2}{A}$ and the induced drag factor k, that mainly depends on the wing planform shape and the twist distribution. It is 1 for planar wings with elliptic circulation distribution. By re-arranging eq. 1.1 and plugging it into eq. 1.3, the induced drag results:

$$D_i = \frac{1}{2}\rho U_\infty^2 C_{Di} A = \frac{2k}{\pi\rho U_\infty^2}\left(\frac{G}{b}\right)^2. \tag{1.4}$$

Interestingly, assuming constant lift, the induced drag is independent of the wing aspect ratio. The driving factor is the span loading $\frac{G}{b}$ and the induced drag is proportional to $\frac{1}{U_\infty^2}$, as the steady decrease in induced drag in fig. 1.4 indicates. The induced drag can be reduced significantly by minimizing the weight or maximizing the span. Minimizing the weight decreases the wing loading and deteriorates high speed performance, hence this is not done for sailplane wing designs. The strategy of maximizing the span can be observed for the development of open class gliders in history. However, most of the racing sailplane classes are span-limited by competition rules. Furthermore, the contest rules limit the maximum weight of the sailplanes, as shown in section 3.2.1. Therefore, the span loading is fixed for span-limited sailplanes. Ultimately, if the induced drag coefficient k is unchanged, the induced drag D_i is constant at equal airspeed. Hence, analyzing the impact of the airfoil $c_{l,\text{max}}$ on the wing drag, which is the sum of the profile drag and the induced drag

$$D_{\text{wing}} = D_i + D_p, \tag{1.5}$$

a closer look on profile drag must be taken. The wing profile drag is calculated as:

$$D_p = \frac{1}{2}\rho U_\infty^2 C_{Dp} A, \tag{1.6}$$

with the product of the wing area and the profile drag coefficient for the whole wing C_{Dp} being calculated from the two-dimensional section drag coefficients C_d:

$$C_{Dp}A = \int C_d(s)\bar{c}(s)ds, \tag{1.7}$$

where s is the arc-length coordinate of the wing in the y-z plane and $c(s)$ is the wing chord length. If the two-dimensional flow assumption holds, the section drag coefficient C_d is equal to the airfoil drag coefficient c_d. The validity of the two-dimensional flow assumption for high aspect ratio sailplane wings is discussed in section 1.4. The wing profile drag depends linearly on the wing area A, because the chord length scales with the wing area. Therefore decreasing the wing area also decreases profile drag in a first order approximation. However, the profile drag coefficient increases with decreasing chord length c because of Reynolds effects. The Reynolds number is defined as:

$$Re = \frac{U_\infty \bar{c}}{\nu}. \tag{1.8}$$

Decreasing the wing area and hence the chord length decreases the Reynolds number at equal airspeed. As long as the proportional increase in profile drag coefficient is lower than the decrease in chord length in eq. 1.6, the profile drag of the wing decreases with decreasing wing area. As the induced drag is independent of the Reynolds number in good approximation, the total drag of the wing would decrease.

To analyze the impact of decreasing the wing area, the increase in profile drag coefficient with decreasing chord length and thus Reynolds number must be analyzed. Fig. 1.5 left shows the measured polars of the main wing airfoil of the *ASW 27* and of the *ASG 29* sailplane, the *DU89-134-14* at different chord Reynolds numbers and at 0° flap deflection. Withing the operational lift coefficient range for this flap setting $0.3 \geq c_l \geq 0.8$, the profile drag coefficient c_d increases with decreasing Reynolds number at a fixed lift coefficient. A comparison of the profile drag coefficient in dependence of the Reynolds number at a fixed lift coefficient $c_l = 0.5$ is shown for the *DU89-134-14* and the *DU92-131-14* in fig. 1.5 right in a double-logarithmic plot. At high Reynolds numbers, the drag dependence on Re is small, whereas at low Reynolds number, the profile drag coefficient increases drastically with decreasing Re. The point, where the profile drag increases over-proportionally is identified, where the $c_d(Re)$ graph gets steeper than the inverse proportional function $c_d(Re) \propto \frac{1}{Re}$. In a double-logarithmic plot, the inverse proportional relation becomes a straight line. The point, where profile drag increases over-proportionally is identified, where the proportional function is tangent to the $c_d(Re)$ function. For the *DU89-134-14* airfoil, this is the case for $Re < 4.5 \times 10^5$. However, if the Reynolds number is accounted for in airfoil design, the wing chord can be decreased further. This is shown by the $c_d(Re)$ curve of the *DU92-131-14* airfoil, which is designed for a smaller operational Re range than the *DU89-134-14*. The *DU92-131-14* has smaller drag coefficients at $c_l = 0.5$ than the *DU89-134-14* for $Re < 1.4 \times 10^6$. The point, where a chord reduction becomes uneconomical for the *DU92-131-14* reduces to $Re = 3.3 \times 10^5$. This corresponds to a chord length of approximately $180\ \mathrm{mm}$ at sea level and an airspeed of $100\ \mathrm{km/h}$. This shows, that as long as the airfoils are specifically designed for the operational Reynolds number range, the chord length can be reduced significantly before the profile drag increases over-proportionally. A further re-design of the airfoil to an even lower design Re-range would shift the cross-over point to an even lower Reynolds number.

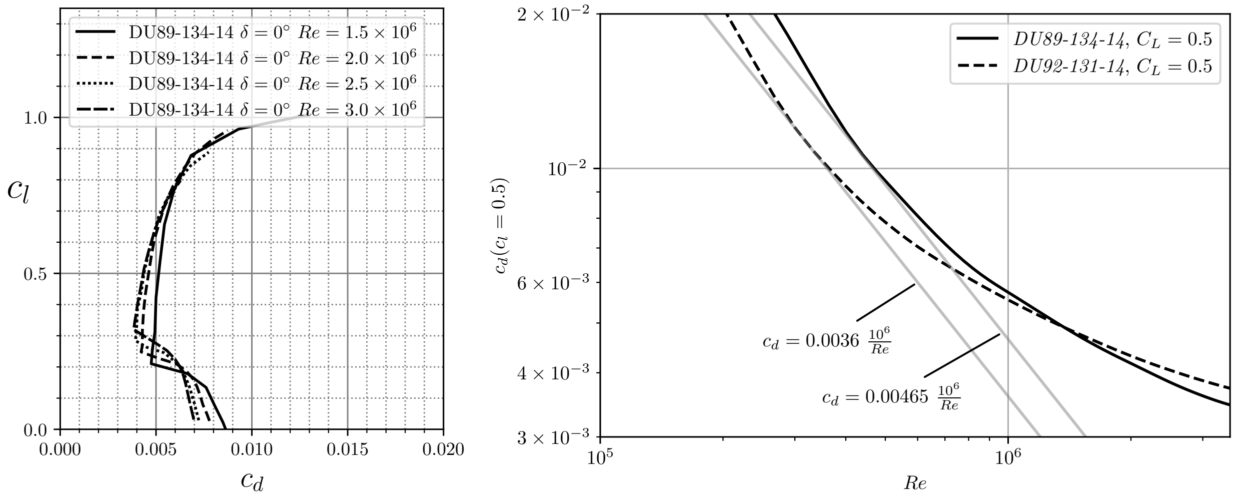

Figure 1.5: Measured polars of the *DU89-134-14* airfoil (left), calculated dependence of the profile drag coefficient of the *DU89-134-14* and the *DU92-131-14* airfoil at $C_L = 0.5$ (right)

For the wing design of sailplanes it can be concluded, that the profile drag can be reduced when the wing area is decreased, as long as Reynolds effects do not overcompensate the direct impact of the profile drag reduction due to chord reduction. Stall speed requirements in the certification specification and the $c_{l,\mathrm{max}}$ of the airfoil impose a lower limit on the wing area. As shown in section 3, the certification specifications require a minimum stall speed of $90\ \mathrm{km/h}$ at MTOM. Hence, the wing area is determined by the maximum lift coefficient of the aircraft $c_{l,\mathrm{max}}$,

$$L = \frac{\rho}{2} U_{\mathrm{stall}}^2 A c_{l,\mathrm{max}} \approx m_{\mathrm{MTOM}}\ g. \tag{1.9}$$

Thus, if an airfoil with a higher maximum lift coefficient is available with the same or only slightly higher profile drag coefficient c_d, the absolute profile drag would decrease and overall aircraft performance would improve. One possibility for increasing the maximum lift coefficient would be a morphing leading edge wing.

In fig. 1.6, the contours of the *DU89-120-14* airfoil with a camber changing flap deflected to $20°$ is shown. The *DU89-120-14* is obtained from the *DU89-134-14* by a uniform reduction of the airfoil thickness from 13.4% to 12%. Furthermore, a profile derived from the *DU89-120-14* with a morphing leading edge is shown. This profile is based on early unpublished work by the author and analyzed by Wiessmeier [128] and further on by Weinzierl, the author and Baier [126]. The morphing leading edge extends the forward 40% of the chord. The morphed contour is derived from the baseline contour by increasing the camber of the forward section with a constant factor.

The thickness is unchanged. The polars show, that the maximum lift coefficient is increased from $c_{l,\max} = 1.6$ for the airfoil with a camber changing flap only to $c_{l,\max} = 1.85$ for the airfoil with a camber changing flap and a morphing leading edge. Based on the *ASW-27* sailplane, Wiessmeier calculates an increase of the best glide ratio of 3 for the sailplane with this airfoil and a significant gain in high speed performance. However, this comes with a significant increase in c_d in morphed configuration. Boundary-layer separation at the upper surface flap region of the morphing airfoil leads to almost doubling the profile drag coefficient at the upper corner of the useful lift range compared to the flapped airfoil. The separation could also reduce aileron effectiveness. Hence new dedicated morphing airfoils are designed in this work, which should have low profile drag both in the undeformed and the morphed configuration. Then, significant performance gains in combination with good handling characteristics could be possible with a morphing wing sailplane.

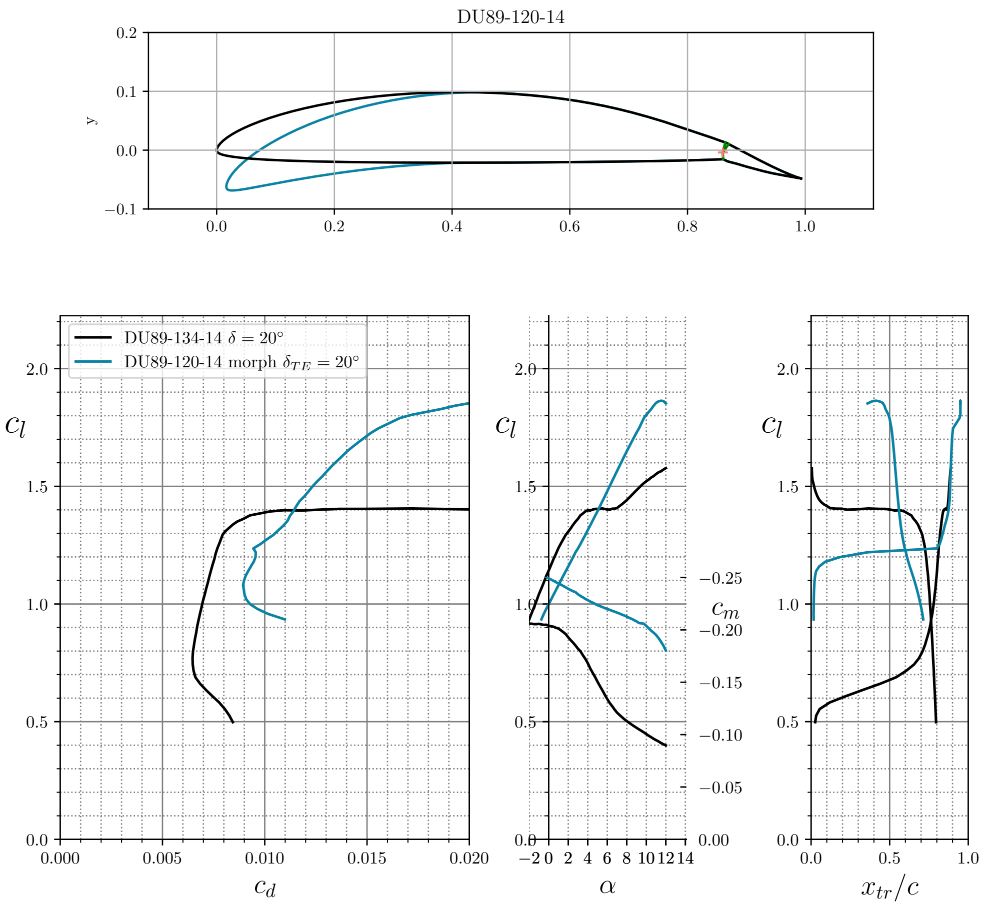

Figure 1.6: Airfoil contours (top) and polars (bottom) of the *DU89-120-14* airfoil with 20° flap deflection, compared to airfoil with morphing forward section and trailing edge flap from [128] (blue) at $Re = 10^6$

1.4 DESIGN AND ANALYSIS METHODS

The aerodynamic design of the morphing wing in this work is done by wide use of aerodynamic shape optimization. A decomposed design philosophy is used, where the airfoils and the wing planform shape including the winglet are optimized separately. For each, a novel aerodynamic shape optimization approach is developed. The airfoil design methodology is discussed in chapter 4 and wing planform including winglet design is introduced in chapter 5. Here, a brief introduction in numerical optimization is given. Furthermore, the used decomposed design philosophy requires the validity of the two-dimensional flow assumption on the bulk part of the wing.

According to Baier et al. [11], a general optimization problem can be formulated mathematically as:

$$
\begin{array}{llll}
\min_{\mathbf{d}} & f(\mathbf{d}) & & \text{(objective function)} \\
\text{subject to:} & g_j(\mathbf{d}) \leq 0 & j = 0, \ldots, l & \text{(inequality constraints)} \\
 & h_j(\mathbf{d}) = 0 & j = 0, \ldots, m & \text{(equality constraints)} \\
 & d_i^l \leq d_i \leq d_i^u & i = 0, \ldots, n & \text{(bounds)} \\
\text{where:} & \mathbf{d} = [d_0, d_1, \ldots, d_n]^\intercal & \mathbf{d} \in \mathbb{R}^n & \text{(design variables)}
\end{array}
\tag{1.10}
$$

For solving this typically nonlinear optimization problem, most methods use an iterative procedure, shown in the flow chart of fig. 1.7. A starting set of design variables $\mathbf{d}^{(0)}$ is updated, until a minimum of the objective function f is found, requiring that the inequality constraints g_j, the equality constraints h_k and the bounds of the design variables d_i^l and d_i^u are not violated. A geometry is calculated from design variables $\mathbf{d}$ by a geometry parameterization algorithm. In aerodynamic design optimization, the geometry is usually a discretization of the aircraft surface or a discretization of the flow volume with the aircraft surface contour as a boundary.

The objective function value f is calculated from a set of response values. In the context of aerodynamic shape optimization, these responses typically include aerodynamic coefficients such as the drag coefficient C_D, the lift coefficient C_L, and the moment coefficient C_M. These coefficients are computed by a flow solver based on the geometry defined by the design variables. Similarly, the constraint functions g_j and h_k are evaluated from the response values, which may also consist of aerodynamic derivatives. In addition to aerodynamic constraints, geometric constraints are frequently imposed, such as thickness, internal volume, or minimal leading-edge radii requirements, which are directly computed from the parameterized geometry.

An optimization algorithm updates the design variables with the aim to reduce the objective function value and to meet the constraints. Some optimization algorithms require the sensitivities, i.e. the derivatives of the objective and constraint function values w.r.t. the design variables. These can be calculated for instance via a finite difference, complex step approach or analytically via an adjoint multiplier approach, which is much more computationally efficient. The optimization iteration is repeated until a stopping criterion is fulfilled. This can be a minimum required change in the design variables or objective function and simultaneous fulfillment of the constraints.

Aerodynamic shape optimization approaches can be categorized by the type of the aerodynamic flow solver used. RANS-CFD methods and panel method approaches of various kinds are both widely used. RANS-CFD based aerodynamic shape optimization methods made significant progress over the last decade. Today it is even possible to perform optimization of full transport aircraft configurations [74][47]. However, this comes also with large computational effort. Large computer clusters are required to perform the optimization in reasonable time. For the precise prediction of the drag of sailplanes, laminar-turbulent transition prediction is very important. In RANS-CFD based numerical shape optimization methods, approaches exist [48], but these are still in an early stage. Currently, the usage is limited to two-dimensional airfoil optimization.

On the other hand, panel methods offer rapid calculation, but they are more limited in the physics they can capture. They are limited to either pure subsonic or pure supersonic problems.

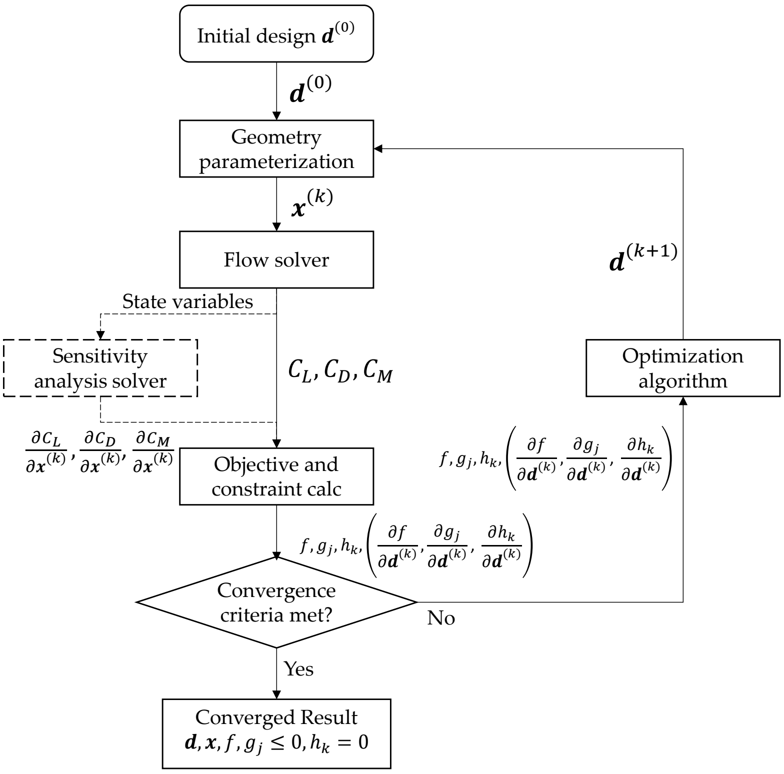

Figure 1.7: General aerodynamic optimization flow chart

Transonic flow problems cannot be calculated. three-dimensional panel codes can only capture the induced drag of aircraft configurations. Vortex Lattice Method (VLM) codes are further limited to calculate the induced drag of lifting surfaces only. two-dimensional panel Integral Boundary Layer method (IBL) codes like *XFOIL* [30], *Profil07* [36] or *RFOIL* [136] are able to consider transitional viscous flows, but are limited to two-dimensional isolated airfoils. Recently, three-dimensional IBL codes have been developed by Drela [32] and further developed by Zhang [132]. These codes promise fast and efficient calculation for full three-dimensional aircraft configurations considering viscous effects including transitional flows. However, these codes are not published yet and have not been demonstrated to be used in an numerical optimization environment.

In this work, an aerodynamic shape optimization approach for the design of the morphing wing sailplane is used, which relies on fast and accurate panel methods. For this, a decomposed design strategy is used, in that the airfoils and the wing planform shape are optimized separately and consecutively. First, the airfoils used on the wing are optimized using modified variants of *XFOIL*. The airfoil shape optimization is shown in chapter 4. Second, the wing planform including winglet is optimized using the multi-lifting line method *Lifting_Line* [52], which is a higher-order VLM approach. Viscous drag is considered by profile drag interpolation from pre-calculated lookup tables, generated with the modified variant of *XFOIL*. The wing planform optimization method is introduced in chapter 5. Performing aerodynamic shape optimization of the morphing wing with this decomposed design strategy has proven to be computationally very efficient.

However, the approach requires, that the profile drag calculated in the lookup-tables for the wing planform optimization closely corresponds to the real viscous drag of the wing. This is only valid, if the flow on the wing sections is nearly two-dimensional. A full aircraft RANS CFD analysis of the *Schempp Hirth Ventus-3* sailplane using the research code *Overflow* has been done by Maughmer et al. [79] and repeated with the proprietary *StarCCM+* software by Axten [10], both utilizing the recent Amplification Factor Transport equation transition model (AFT) transition model developed by Coder [25]. The skin friction coefficient and the streamlines at $C_L = 1.2$ of the latter study are shown in fig. 1.8. Axten concludes, that the streamlines are nearly parallel almost everywhere on the wing, supporting the two-dimensional flow assumption. Only close to the fuselage and on the winglet root, significant deviations and three-dimensional flow effects exist. Also a performance analysis comparison of the CFD results to potential flow methods similar to those used in this work reveals, that the results lie close together. This legitimates the decomposed design philosophy. Nevertheless, a detailed design using transitional CFD of three-dimensional flow areas like the wing-fuselage junction and the winglet root would be beneficial in later design stages. But this is not the focus of this work.

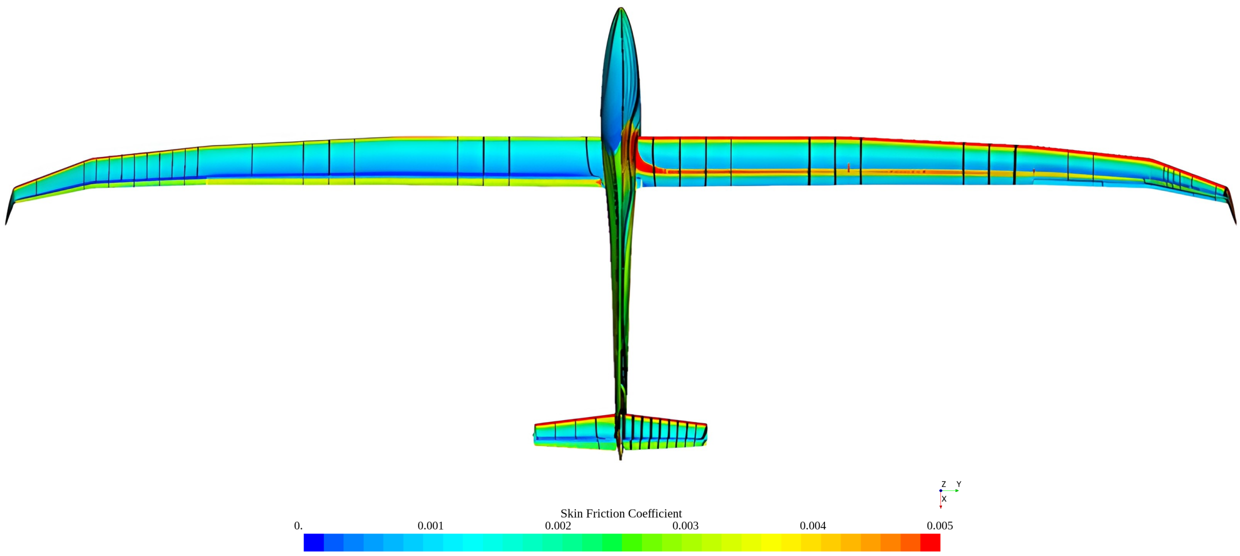

Figure 1.8: Transitional RANS CFD analysis of the Ventus 3, top (right) and bottom (left) view at $C_L = 1.2$, from [10]

Comparisons of theoretical methods for predicting airfoil aerodynamic characteristics has been done by Maughmer and Coder [78], later by Coder and Maughmer [24] and by Morgado et al. [81]. In the first paper, the results of the integral boundary-layer codes *Profil07* by Eppler [36] and *XFOIL 6.96* for six airfoils are compared to low turbulence wind tunnel results and results obtained by the RANS CFD code *OVERFLOW 2.1ae* with the *Spalart-Allmaras* turbulence model, assuming fully turbulent flow. It is shown, that the prediction of aerodynamic coefficients of the integral boundary-layer codes is significantly more precise than of the fully turbulent RANS CFD methods. In a more recent study by Coder and Maughmer [24], the prediction results for six different airfoils of the Langtry-Menter $\gamma - Re_\theta$ transition model coupled with the Shear Stress Transport turbulence model (SST), implemented in *OVERFLOW 2.2e* are shown. These results are again compared with wind tunnel results and *Profil07* and *XFOIL 6.96* results. The transitional CFD method showed significant improvements compared to fully turbulent results, with errors being in the same order of magnitude as of the integral boundary-layer methods. However, the integral boundary-layer methods still provide better results, especially in predicting the corners of the laminar low-drag region and are particularly more precise in predicting drag close to the upper corner of the laminar low-drag region. In most cases, *XFOIL 6.96* showed better results than *Profil07*. Further improvements for RANS CFD have been reported by the new AFT transition model by Coder [25], which is based on the envelope e^N method by Drela [34]. With this model, drag values and the corners of the laminar low-drag region are calculated with similar precision as *XFOIL*. However, *XFOIL* calculations are orders of magnitude faster than RANS CFD. Therefore, integral boundary layer methods are still better suited for numerical optimization of isolated airfoils in the pure subsonic regime.

However, there is still some potential for improvement of integral boundary layer methods. In *XFOIL*, transition is predicted with the envelope e^N method, as discussed in section 4.4.2.2. As shown by Dini [27], this method is only valid in constant shape factor boundary-layers. Hence, if pressure gradients exist, as is the case for most airfoil boundary-layer flows, a systematic error is made in predicting the transition location and thus drag. Therefore, a full lookup-table based e^N method has been developed by van Ingen [135], which is discussed in section 4.4.2.3. The method is implemented in a variant of *XFOIL* by Bongers [17]. The new variant is designated as *XFOILSUC*. As shown in section 4.4.2.4, this significantly improves the precision of drag prediction compared to *XFOIL* in most cases.

As already shown in section 1.3, the prediction of the maximum lift coefficient of an airfoil is crucial for a precise prediction of the performance of a wing. *XFOIL* significantly overpredicts maximum lift in most cases [78][24][81][25]. Van Rooij [136] suggests some improvements for the prediction of $c_{l,\max}$. These improvements are discussed in section 4.4.2.5 and implemented in *XFOIL 6.99* and in *XFOILSUC* in this work. The modified variants are denominated *XFOIL-mod* and *XFOILSUC-mod*. In section 4.4.2.5 it is shown, that significant improvements for predicting maximum lift of airfoils are achieved with these modifications.

Summarized, it can be stated, that to date potential flow solvers with integral boundary-layer calculation are of similar precision for predicting the profile drag, but orders of magnitudes faster than RANS CFD solvers. Together with a fast and precise potential flow solver for the prediction of the induced drag like LIFTING_LINE, the total wing drag can be predicted accurately and fast, if the two-dimensional flow assumption is valid in the vast part of the wing. As this is the case for a high aspect ratio sailplane wing, these are the methods of choice for wing design optimization in this work.

2 STRUCTURAL CONCEPT OF THE MORPHING WING

The key structural components of the morphing wing sailplane are introduced in this chapter. The actuation system of the morphing leading edge, consisting of a mechanical drive system and the compliant mechanisms is shown in section 2.1.

A morphing wing shell is designed, which allows for the deformation of the wing shell with low actuation forces, but also requiring stiffness for ensuring precision between the compliant mechanisms. It must withstand morphing actuation forces, wing bending deformation and aerodynamic loads and must not buckle. This is introduced in section 2.2.

The primary structure consists of a main spar that takes the wing bending loads and a torsional box, which takes wing torsional loads. The cross sectional area of the torque box of the morphing wing is reduced compared to conventional sailplane wings. Furthermore the elastic axis is well behind the center of lift. Both facts create challenges for strength and undesired wing twist. The design of the primary structure as well as an aeroelastic tailoring approach to minimize detrimental wing twist is discussed in section 2.3.

As the wing area is reduced compared to conventional sailplanes, there are some challenges to address with respect to the available space for the actuator mechanisms, the control system and the water ballast system. In addition, the water ballast tank in front of the spar has to be sealed, because it is integrated in the morphing section. The important aspects of this topics are discussed in section 2.4.

Although the definition, design, and sizing of the structural concept are not the primary focus of this dissertation, they have significant implications for the aerodynamic design, and vice versa. For instance, while compliant mechanisms facilitate certain deformations of the wing, they also impose limitations, such as constraints on maximum deformation and stress levels. To address these challenges, a gap is introduced in the lower surface, which must be meticulously sealed to avoid adversely affecting aerodynamic performance. Moreover, the sliding joint along this gap necessitates a specific motion of the morphing forward section, which must be carefully accounted for in the parameterization of the airfoil geometry.

A reduction in wing area leads to a decrease in the height of the main wing spar, thereby exacerbating structural challenges. Consequently, the airfoil thickness must be constrained during optimization, depending on its spanwise position. These intricate interactions between the selection, design, optimization, and sizing of the wing's primary structural components, and the aerodynamic design of the outer mold line and target morphed contour, underscore the necessity of a comprehensive introduction to the structural concept. This is presented in this chapter.

2.1 COMPLIANT MECHANISM DESIGN

The main objective for an actuator mechanism is to precisely deform a morphing wing shell from an undeformed initial shape to a deformed, i.e. morphed shape. In both the initial state and the deformed state it should be stiff, so that external loads, e.g aerodynamic loads or wing bending loads do not change the desired shape much. This is, because such a deformation would deviate the shape of the wing profile and would probably deteriorate the aerodynamic performance of the wing. Also backlash has the same effect and should be minimal. Furthermore, the actuation should be done with low forces. So the mechanism should store as little elastic energy for actuation as required and should have low friction losses. One obvious requirement is that the mechanisms must be designed so that failure is either improbable (fail-safe design) or does not lead to catastrophic failures (safe-life design). Furthermore, the complexity should be put into the design, not in manufacturing.

Compliant mechanisms have some characteristics that make them well suited for this intended use. Complex planar mechanisms can be integrated into a single rib and manufactured using 3D printing or Computer Numerical Control (CNC) cutting technologies. The compliant mechanism ribs integrate the function of precise deformation steering of the morphing wing shell into one single part. The assembling can be done by conventional bonding techniques. So both the manufacturing and assembly complexity does not increase much compared to a conventional wing with camber changing flaps. Furthermore, compliant mechanisms offer the advantage of being frictionless and free of play.

However, there are also several challenges arising with compliant mechanisms. First, the design of such mechanisms can be highly complex, in particular if it is done manually by a human designer. Therefore, numerical optimization and in particular topology optimization offers the opportunity that this complex process is done by a computer and design time is cut down to a minimum. The mechanisms undergo large deformations, therefore a nonlinear finite element analysis must be performed in the topology optimization routine. The stresses in the elastic hinges can be high, which could lead to failure and fatigue. Therefore, stress constraints must be incorporated into the topology optimization method to prevent highly stressed hinges. Furthermore, compliant mechanisms store elastic energy during deformation, which increases actuation forces compared to conventional mechanisms.

To achieve good aerodynamic performance, a morphing leading edge sailplane requires to have multiple different airfoils on the wing at different spanwise stations. This in turn hinders the use of scaled versions of one single design of a compliant mechanism actuation rib. Hence a large number of individual compliant mechanisms must be designed. Therefore, an automated method for designing the mechanisms help to save huge design effort. Continuum-based topology optimization offers wide design freedom and more than thirty years of knowledge result in a wide literature base. However, limited efforts have been taken so far on the design of compliant path-generating mechanisms with large deformations and stress constraints.

2.1.1 *First designs with commercial topology optimization software*

The first designs of compliant mechanisms for this project were made by Salehar [103] under the advisement of the author with the proprietary topology optimization software *OptiStruct*, see fig. 2.1. An eccentric torsion shaft actuates the compliant mechanism via a pull-rod. The compliant mechanism deforms to a high lift shape with increased camber. The approach was able to demonstrate the principal feasibility of a compliant mechanism for morphing wing design. However, the software used is not tailored for compliant mechanism design. Convergence to a discrete design without a significant amount of intermediate density elements ("black and white design") could be achieved with linear, but not with non-linear Finite Element Method (FEM). The use of linear FEM for a mechanism which undergoes large deformations lead to kinks in the airfoil contour in morphed configuration. Furthermore, also stress constraints could not be employed without getting large regions of intermediate density elements. The omission to use stress restrictions lead to designs with overstressed hinges. In the 3D printed demonstrator mechanism (fig. 2.1) the hinge regions developed cracks within few actuation cycles.

Figure 2.1: Compliant Mechanism, optimized with *Altair Optistruct* by Salehar [103]

2.1.2 *Compliant mechanism design with nonlinear topology optimization*

To achieve accurate compliant mechanism designs, without over-stressed hinges, a continuum-based topology optimization software has been developed. The software is originally written by Reinisch [97] under the advisement of the author and has been extended by Reinisch [98] [99], Grosse [46], all under the author's guidance and by the author himself [4].

In the continuum-based topology optimization, the design domain is discretized with membrane (2D) or solid (3D) elements. The density of each element is a design variable. The topology is defined by the density of the elements. It should be either zero or one. Zero density corresponds to a void region without material and hence zero stiffness. A density of one indicates, that there is material and hence full bulk material stiffness. Zero density elements are also designated white or void elements, whereas elements with a density of one are often designated as solid or black elements.

Finding such a topology via numerical optimization is a combinatoric integer programming problem, which becomes tremendously large and expensive to evaluate even with small problem sizes (i.e. number of elements). To overcome this, Bendsøe [12] developed the Solid Isotropic Material with Penalization (SIMP) approach. In this, intermediate material densities between 0 (void) and 1 (solid) are allowed. The elements Youngs modulus is coupled to the density with a cubic interpolation law. Therefore, intermediate density elements have a reduced modulus compared to a direct, linear coupling of the modulus to the density. This penalizes intermediate densities. Sigmund [110] showed, that this leads to black and white topologies.

The software uses the path generating objective function introduced by Pedersen [87]. In this, the objective function is the sum squared deviation of the output points from target points. Target points could be arranged in a path. Each target point corresponds to a different input displacement. The objective function allows to find topologies with the least deviation to the desired output path. Pedersen also shows, that it is necessary to incorporate load cases with two counter loads acting perpendicular and opposed to the direction of the output path at the output port in addition to an unloaded loadcase. Otherwise, the resulting mechanism would contain gray regions and would not be stiff.

A nonlinear FEM solver has been implemented in *Matlab* for the topology optimization software in the work of Reinisch [97]. Green-Lagrange strains are used, which consider geometric nonlinearity. Second Piola-Kirchhoff stresses are coupled to Green-Lagrange strains using the linear St. Venant-Kirchhoff material law. The Newton-Raphson method is used for iterative calculation of the solution. The results of the underlying FEM solver are verified by the proprietary FEM solver *ABAQUS implicit*.

2.1.2.1 *Volume and stress constraints*

A volume inequality constraint is used, which specifies the maximum allowable volume fraction of material in the design domain.

For constraining the stresses of the compliant mechanisms, the p-norm stress aggregation method by De Leon [66] is implemented in the topology optimization solver. This prevents overstressed hinges in the optimized designs. The combination of nonlinear compliant mechanism synthesis with p-norm stress constraints is first shown by Reinisch [97], with the extension to path generating compliant mechanisms in successive work of the same author [98].

2.1.2.2 *Filter and projection methods*

For avoiding nonphysical checker board patterns and mesh dependence in the final designs, the Helmholtz type diffusion partial differential equation filter by Lazarov and Sigmund [65] is implemented. However, the filter methods also introduce gray boundaries between solid and void areas as a side effect. To achieve black and white designs, the Heavyside projection scheme published by Xu et al. [131] is used. However, Wang et al. [124] showed, that using this projection approach causes the minimum length scale on the material region getting lost. For imposing a minimum length scale with the projection approach and to add robustness w.r.t. geometrical deviations, the three stage projection approach introduced by Schevenels [105] is implemented in the topology optimization code. Three different designs are obtained by three different Heaviside projection thresholds, designated the eroded, the intermediate and the dilate design. The eroded design has the narrowest material structures, whereas the dilate design has the thickest. A FEM solution is calculated on each of the designs. The objective function of the three designs are summed in one objective function. This approach leads to designs, which are robust w.r.t. geometrical variations, not only regarding the objective function, but also more importantly regarding the stresses. Also a minimum length scale is imposed. The computational cost is increased threefold, because three FEM solutions and sensitivity analyses have to be calculated in each topology optimization iteration instead of one.

2.1.2.3 *Adjoint sensitivity analysis*

The sensitivities of the objective function and constraints w.r.t. the design variables are calculated analytically using the adjoint sensitivity analysis method, enabling efficient topology optimization for even large problems with millions of elements [1]. With the objective and constraint function values and the sensitivity information, a gradient based optimization algorithm calculates new design variable values. The procedure starts again with the finite element solution of the updated design and so forth, until convergence is achieved to an optimal design.

2.1.2.4 *Optimization Algorithm*

For solving the topology optimization problem, an efficient and stable optimization algorithm is required. Here, the Method of Moving Asymptotes (MMA) approach by Svanberg [118] is used, in which a sequence of simpler convex approximations of the original problem are solved under the use of sensitivity information. The confidence interval for each design variable is adopted based on the solution of the last two iterations. The MMA has proven itself to be versatile and well suited for large scale topology optimization problems [13], even up to a billion design variables [1].

2.1.2.5 *Topology optimization results*

The design approach for the compliant mechanism system for the morphing leading edge is to stack six distinct mechanisms into one rib. Each mechanism is attached to a common belt, which is bonded to the morphing wing shell, deforming it as precisely as possible. It is assumed, that a series of parallel compliant mechanisms deforms more precise and with less deformation work and stresses than a single mechanism, which has to actuate the whole wing shell at once, because the single mechanism is more distorted than a series of parallel mechanisms.

PolyAmide (PA) 11 material is used in a Selective Laser Sintering (SLS)-process to manufacture the compliant mechanisms. PA 11 features high strength with moderate stiffness, which makes them well suited for that application. Furthermore, is has a low moisture soak, which enables to use the morphing leading edge region as a water tank and submerge the mechanisms in water. Detailed considerations on material selection is presented in the paper of the author [4].

The design space for topology optimization of one of the sub-mechanisms is shown in fig. 2.2. It is intended for a section with a wing chord length of $550\ \mathrm{mm}$, corresponding to the spanwise position of $y \approx 3400\ \mathrm{mm}$. The actuation point is shown in green, with the input displacement direction shown as a green arrow. In some regions, material must be placed and may not be removed by the optimization algorithm, e.g. around the actuation point or near the output point. These are designated *non-design solid* regions and are colored black in fig. 2.2. The design space, where the optimization algorithm may change the material density is colored gray in fig. 2.2. The input displacement is $4\ \mathrm{mm}$ in local x-direction. The thickness of the sub-mechanism is $7\ \mathrm{mm}$. Only one single counter load case is considered in addition to the unloaded load case, with the counter loads being derived from the pressure distribution at design maneuvering speed as specified in *CS22.335*, with density of air at sea level. The geometry for the compliant mechanism design space is derived from the overall aircraft CAD model generated in *CATIA V5*. Mesh generation is done with *Abaqus CAE*.

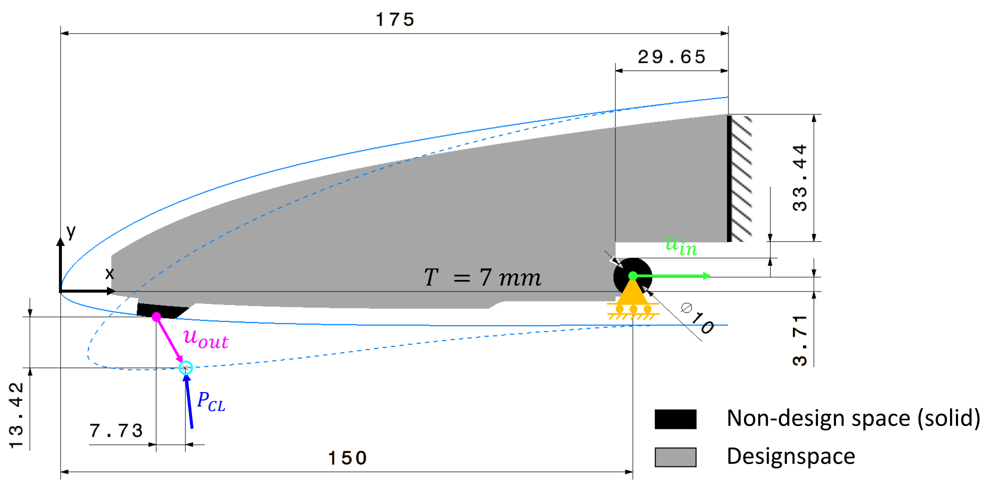

Figure 2.2: Compliant mechanism design space (gray), non-design solid area (black), with input point (green), output point (red), counter loads, target output displacement (purple arrow), target output point (light blue circle), counter load (dark blue)

The problem has 114781 four node fully integrated quadrilateral linear elements with an average element size of $0.5\ \mathrm{mm}$ and 231648 degrees of freedom. The results are calculated on an *Intel Xeon E3-1280 v6* CPU running at 3.9 GHz with four logical cores and with 64 GB RAM. The optimization is terminated, when the maximum change of all physical densities is below the specified tolerance of 0.02. The calculation required 238 iterations and hence $3 \cdot 238 = 714$ nonlinear

FEM solutions and $2 \cdot 3 \cdot 238 = 1428$ adjoint sensitivity analysis solutions until convergence is achieved, requiring 7 hours and 45 minutes computation time.

The density distribution of the topology optimization result is shown in fig. 2.3. It is shown with three different Heavyside projection threshold levels, which are used for FEM calculation in the geometrically robust design method. The erode design has the least structural width, whereas the dilate design has the largest structural width. The range of the structural width between the erode and the dilate design can be viewed as allowable manufacturing uncertainty. A truss-like design is obtained with a clearly visible minimum length scale. No one-node connected hinges are present. Instead, the hinges have finite length and finite thickness due to the incorporation of stress constraints. The stresses of all three projection levels are shown in fig. 2.5. The allowable von Mises stress limit is 30 MPa. It can be seen, that the stress in the compliant hinges is just below the stress limit. Between the hinges, thicker regions are inserted for increased stiffness. The stresses are maintained within limits at all three projection levels.

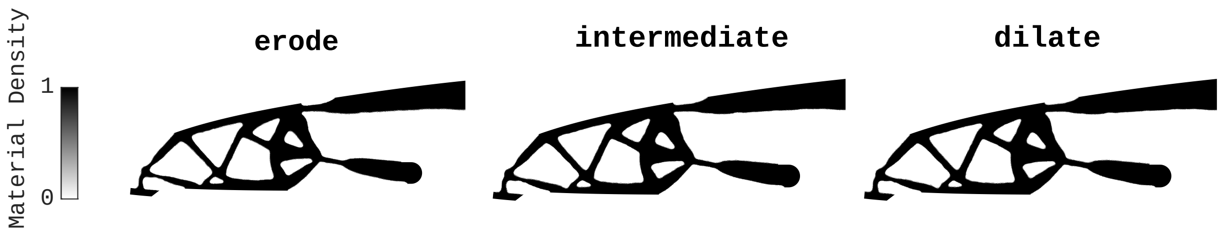

Figure 2.3: Density distribution of the compliant mechanism at three different projection levels

The displacement figure at the intermediate projection level without and with counter load is shown in fig. 2.4. The target deformation point is shown as a light blue circle. It can be seen, that the target point is matched fairly close. The output point shows a little overshoot compared to the target point in the case without a counter load, with a deviation of ≤ 0.34 mm at all projection levels. In the case with full counter-load, the target point is not fully reached, the absolute value of deviation is ≤ 1.04 mm for all projection levels. However, as the full counter-load is calculated at the maneuvering load factor, it is expected that the overshoot in the non-counter-load case and the undercut in the case with the full counter-load somehow compensate at normal flight conditions. The target point is then expected to be matched very closely.

After topology optimization, the results are stored as *stl*-files and smoothed with a Laplacian filter using the open source software *Meshlab*. A *step* file of the smoothed result is generated with the open source software *FreeCAD* and subsequently imported in *CATIA*, where all sub-mechanisms are assembled to the stacked compliant mechanism rib and equipped with the mechanical torsion drive system. Manufacturing is done on a *SLS Formiga P110* machine made by the company *EOS GmbH*. A demonstrator of the compliant mechanism rib with six sub-mechanisms, with the common belt and the torsional drive system is shown in fig. 2.6 in undeformed (left) and deformed (right) shape.

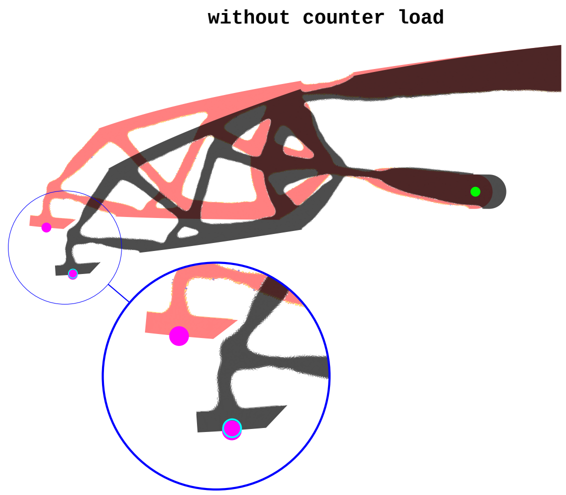

Figure 2.4: Displacement figure without (left) and with (right) counter load at intermediate projection level with undeformed configuration in background (red), target deformation point (light blue circle)

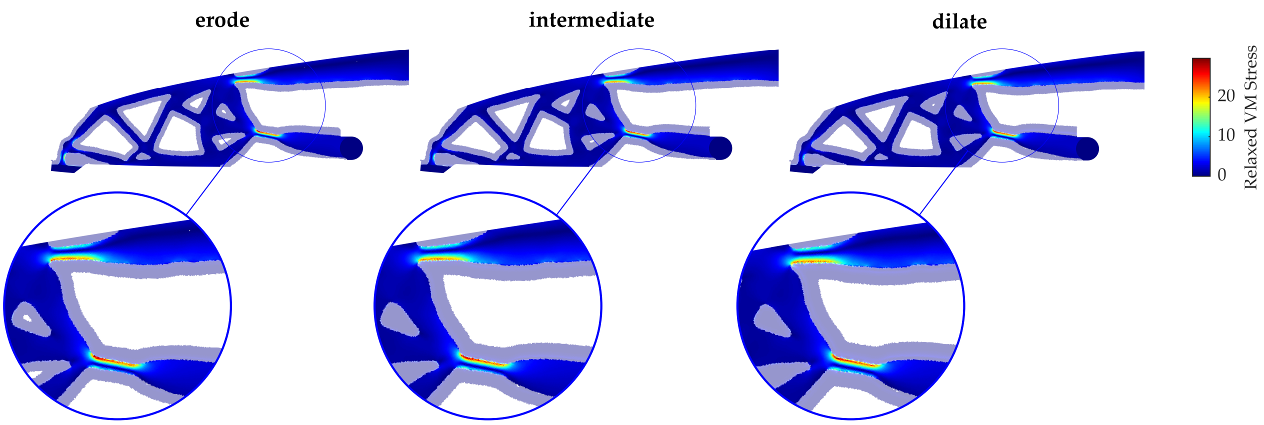

Figure 2.5: Stress distribution of the compliant mechanism at three different projection levels at the load case with counter load

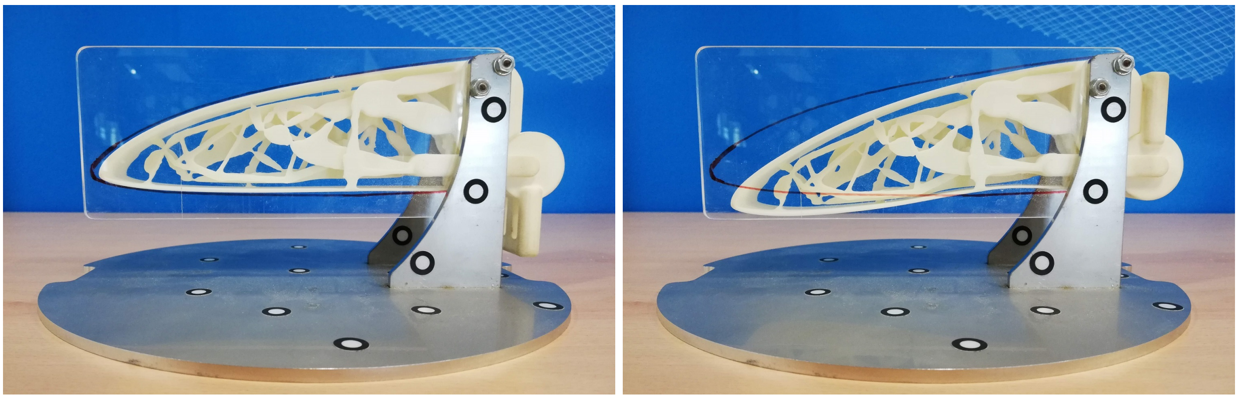

Figure 2.6: Stacked compliant mechanism rib demonstrator in undeformed (left) and deformed (right) configuration

2.2 MORPHING WING SHELL

The main function of the wing shell of a conventional sailplane is the transfer of wing torsion loads caused by aerodynamic forces. The morphing shell has some different requirements. The shell must withstand the morphing and aerodynamic loads. Under these loads, it must be free of fatigue with sufficient margins of safety. Also, it must be free of buckling up to the limit load.

The best possible aerodynamic performance of the wing can only be achieved, when the target shape both in undeformed and morphed condition is maintained precisely. This requires moderate bending stiffness in direction of flight, so that the shell is stiff enough between the compliant mechanism actuation points. It also requires high spanwise bending stiffness to transfer deflection between ribs, allowing for increased spacing and reduced rib count.

Airfoil performance is extremely sensitive to premature transition, thus the morphing wing shell must have a smooth surface with low waviness. Also the gap on the lower surface must be covered smoothly, e.g. with a *Mylar* tape seal which must be smoothly integrated in the contour with an indentation step designated for that purpose. Also the trailing edge *Mylar* thickness must be small enough, so that the boundary-layer remains laminar without transition. This is analyzed in section 4.8.

Another key requirement is low actuation force for morphing. This not only reduces the work needed for morphing, but also reduces loads on the compliant mechanisms and the actuation system, making them more lightweight and less suspect for failure, but also increases precision, as the mechanisms and control system stiffness is finite.

Also some practical requirements for a flawless day to day operation of a competition sailplane exist. It must be robust to withstand rigging loads, ground handling loads (sailplane on ground are mostly pushed on the leading edge) and for storage in trailers, where the de-rigged wings normally lie nose-down on an approx. $30\ \mathrm{cm}$ long mold covered with carpet.

Last, but not least, simple manufacturing is required to ensure competitive production effort and cost. Repair of possible damages should also be easy. It would be good, if repairs could be performed with standard methods and without special tools. Also, the structural weight and thus the areal weight of the wing shell should be acceptably low.

2.2.1 *Flexible wing shell concepts*

Three different structural concepts for the morphing wing shell are introduced by Sturm et al. [116] and shown in fig. 2.7. On the left, a classical monolithic fiber reinforced plastic layup is shown. The main fraction of fiber material is unidirectional carbon fiber, with fiber orientation in spanwise direction. The unidirectional layers have a high bending anisotropy per se, resulting in high bending stiffness in spanwise direction and low bending stiffness in direction of flight and thus low actuation forces. A GFRP woven fabric outer layer oriented in $\pm 45°$ direction serves as a crack arrestor. A woven fabric PolyPropylene (PP) fiber, also oriented in $\pm 45°$ direction serves as core layer. The PP fiber has low density and low stiffness compared to other fiber materials, but high impact resistance, making it well suited as core layer.

In the second concept, the PP core layer is substituted by a classical foam sandwich material like Polyvinylchloride or Polymethacrylimid of low thickness ($1 - 2\ \mathrm{mm}$). The foam core material density is considerably less than with a fabric core layer, resulting in a weight saving potential for this variant. Also the bending anisotropy could be higher, due to the negligible stiffness of the foam material compared to PP. Manufacturing of the first two variants could be done by classical

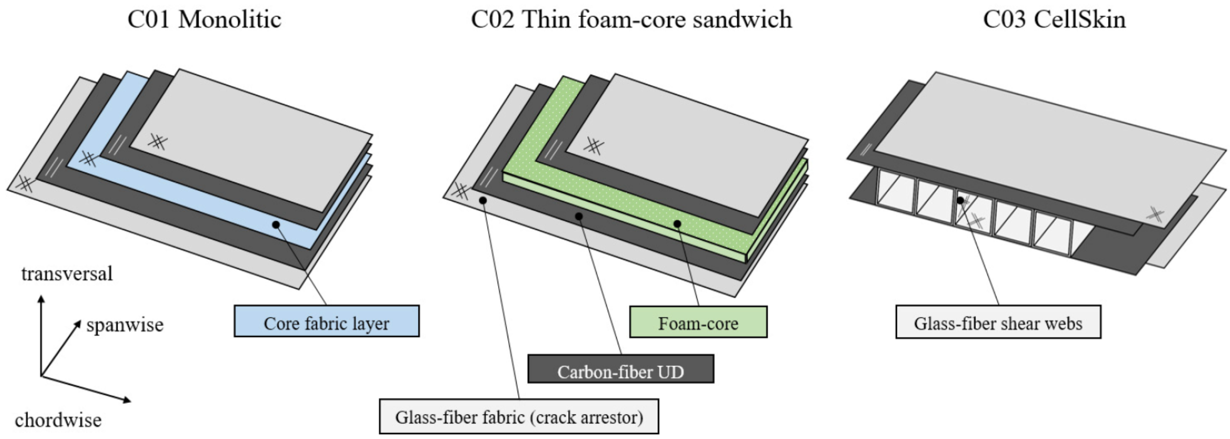

Figure 2.7: Three different structural morphing wing shell concepts, as shown by Sturm et al. [116]. Monolithic (left), foam core sandwich (center) and CellSkin (right)

wet layup, optionally assisted by vacuum pressing, or with resin infusion or prepreg processes. The specimen tested by Sturm were made as a wet layup with vacuum pressing.

The third variant is a new design with a core made of thin, spanwise oriented GFRP shear webs of woven fabric and a CFRP outer shell, designated as CellSkin. The shear webs are transversely shear compliant due to tilting of the shear webs relative to the outer layers. The shear webs fiber orientation of $\pm 45°$ makes the concept shear stiff in spanwise direction and thus gives high overall stiffness against bending deformation in this direction. The deformation behavior of the CellSkin is shown in fig. 2.8. The CellSkin manufacturing process is shown by Jocham [55]. The top and bottom layers are manufactured in a wet-layup process in the same mold. The core layup is a square wave cross section manufactured in a special mold. Finally, the top layup, the core layup and the bottom layer are co-bonded together.

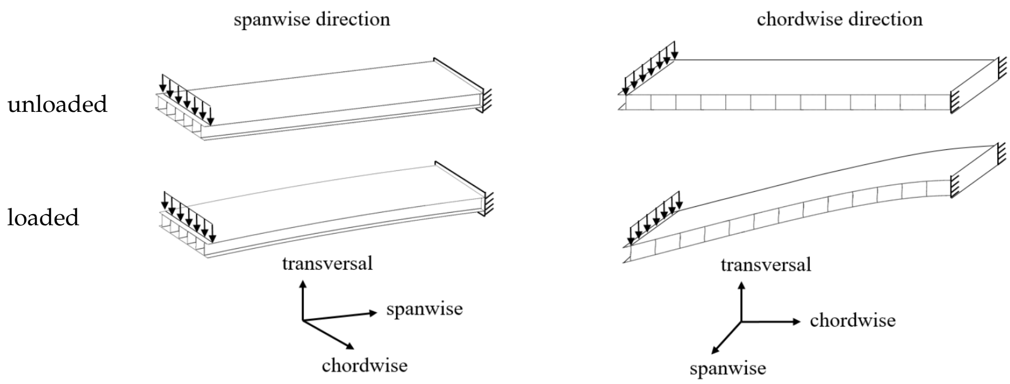

Figure 2.8: In-plane shear compliant deformation principle of the CellSkin, from Sturm et al. [116]

2.2.2 *Test results and concept selection*

Sturm et al. [116], along with the author, present the results of FEM calculations and an extensive experimental campaign, comparing the monolithic shell concept, the sandwich and two variants of the CellSkin, each fabricated using different manufacturing techniques. The CellSkin has shown the least areal weight, followed by the foam core sandwich and the monolithic concept. The CellSkin is also superior in terms of high spanwise stiffness and low stiffness in direction of flight shown by four point bending tests, resulting in low work for morphing according to simulations. The monolithic and the foam core sandwich variant show comparable bending stiffness ratios. Indentation tests are performed to proof the robustness of the skin material concept w.r.t. handling loads. The results indicate, that the monolithic and foam core sandwich are more than acceptably robust to usual handling loads, but the CellSkin variants have inferior performance. The manufacturing time for the CellSkin specimen is three to six times higher than for the monolithic and foam core concepts. Furthermore, the CellSkin concepts show slight waviness when deformed, caused by the moments due to the shear-compliant rotation of the shear webs. Also the CellSkin is remarkably thicker than the other variants, limiting available space, which can become particularly problematic close to the wing tip. Together with still unsolved problems like a simple manufacturing process for spanwise tapered CellSkin sections and a proven repair concept, it was decided to not further pursue the CellSkin concept. Finally the monolithic variant was selected because of utterly simple manufacturing and repair, superior robustness to handling loads and still acceptable low morphing actuation work.

2.3 PRIMARY STRUCTURE

2.3.1 *Conceptual design*

The primary structure of the morphing wing sailplane is based on a conventional sailplane structural design and shown in fig. 2.9. The load-bearing wing box is composed of a main spar, a wing shell, and a rear spar, as illustrated in fig. 1.2. The main spar features a double I-beam configuration. It consists of two spar caps made from unidirectional high-strength CFRP aligned in the spanwise direction and a shear web constructed from a woven $\pm 45°$ CFRP layup. Each component is specifically designed to handle distinct load components. The wing shell is responsible for transferring torsional loads, requiring sufficient strength to withstand torsional stresses and adequate stiffness to minimize wing twist. Excessive twist can lead to deviations in the spanwise lift distribution from the optimal, thereby increasing induced drag. Additionally, twist negatively affects profile drag, causing premature dropping out of the laminar low-drag region, particularly in the high-speed range. A low torsional eigenfrequency may render the wing susceptible to flutter, necessitating a certain level of torsional stiffness. The spar caps primarily bear the wing's bending moment, with the fuselage mass being the most significant contributor to this moment. In comparison to conventional flapped sailplanes, the increase in fuselage mass due to the actuator drive is minimal, resulting in only a negligible increase in bending moments. The morphing wing concept demands for a reduction in wing area, which subsequently decreases the available height for the spar caps, imposing structural challenges for these. Morphing airfoil optimization yields designs with reduced thickness relative to conventional flapped airfoils, as demonstrated in Chapter 4. Wing bending loads are particularly high close to the wing root. Therefore, a constraint must be imposed for the airfoil thickness of the inner wing and root airfoils. The shear webs take the shear flux from shear forces and torsional moments. The shear flux is transferred from the spar caps to the web via the bonding surface on the inner spar cap surfaces, which can be critical at high shear regions like the spar interconnection. The rear spar closes the torsional cell and thus is designed with a woven $\pm 45°$ CFRP shear layup. Last, but not least, the primary structure has also to offer enough space for the control system and secondary systems as airbrakes.

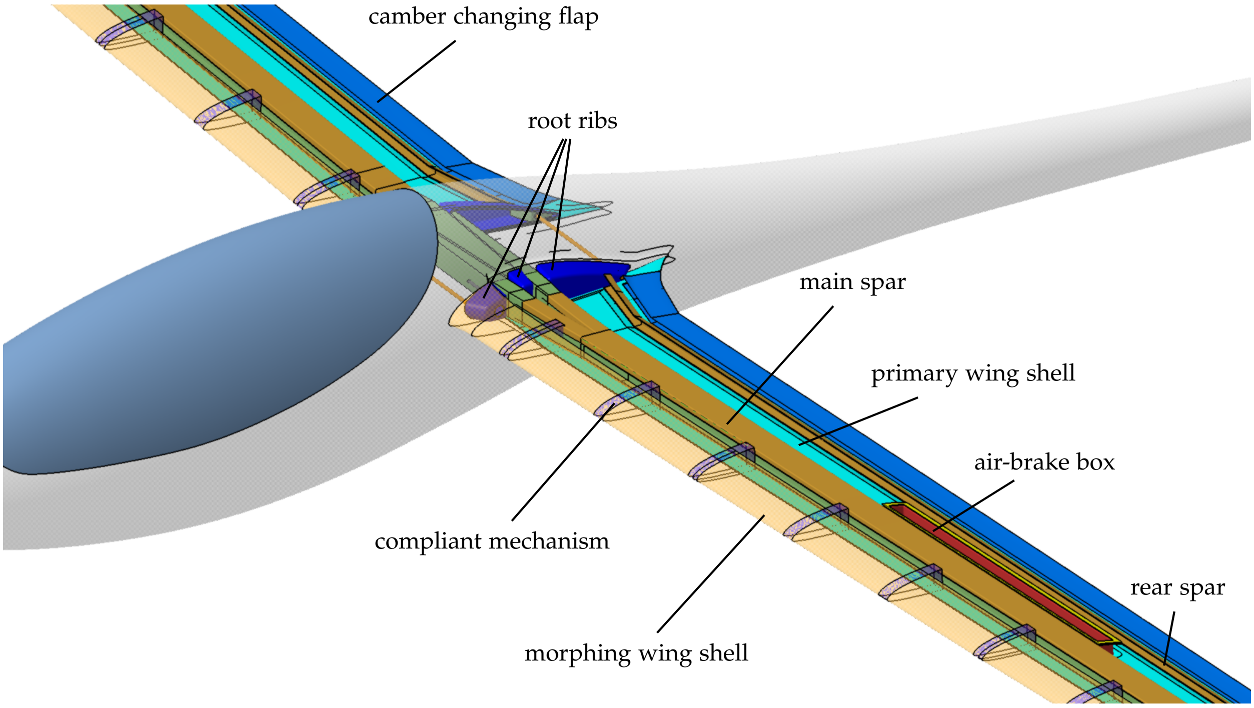

Figure 2.9: illustration of morphing wing sailplane with the primary structure of the wing. Top shell not displayed

2.3.2 *Reduced cross section torque box*

A specific challenge associated with the morphing wing sailplane is the reduction in the torque box cross-sectional area, as discussed by Wiessmeier [128] and depicted in fig. 2.10. The left side of the figure illustrates a conventional sailplane structural design, where the cross-sectional area available for transferring torsional loads extends from the leading edge to the rear spar. In contrast, for the morphing wing sailplane, not only is the torsional cross-sectional area reduced, but the center of shear also shifts rearward compared to the conventional configuration, thereby further increasing torsional loads. To achieve torsional stiffness comparable to the conventional design, either an increase in the number of layers or the use of high modulus carbon fibers is required. These fibers were first employed in the *Akaflieg Braunschweig SB-13* tailless sailplane and have increasingly been incorporated into the design of modern sailplanes in recent years. Notably, they were used in the Concordia project [15] and have also been integrated into production sailplanes [50]. Additionally, static aeroelastic tailoring could be employed to counteract torsional twist by appropriately adjusting the fiber orientations.

2.3.3 *Structural design and aeroelastic tailoring*

The structural design is done in coupled iteration loops with the aerodynamic design. A first preliminary aerodynamic design was the baseline for an analytic structural loads analysis with a simple lifting line method and an analytic sizing of the main structural components. Implications from the calculations also set requirements for the successive airfoil design iterations and the wing planform design. Finally, a higher fidelity analysis and sizing was done using a FEM shell model of the wing by Illenberger [54] calculated with *Nastran*. A 2.4 m. long test spar of the inner

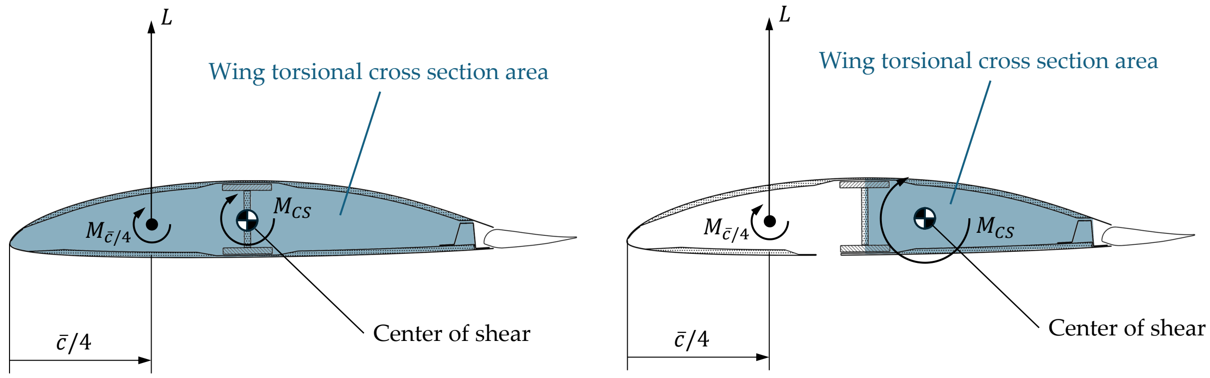

Figure 2.10: Wing torsional cross sections of a conventional sailplane structural design (left) and the morphing wing sailplane structural concept (right)

wing section has been fabricated by the project partner *Alexander Schleicher GmbH* and has been tested in a structural test rig.

An aeroelastic analysis of the morphing wing sailplane was conducted by Illenberger [54] to examine the bending and torsional deformations of the wing resulting from aerodynamic loads, as well as their subsequent impact on spanwise lift distribution and induced drag. In this study, a Doublet Lattice Method (DLM) model is coupled with a FEM model using *Nastran SOL144*. The elastic wing twist distribution is calculated for the most critical load cases, along with the influence of this aeroelastic effects on the lift distribution. The resulting cross-sectional load distributions were then compared with those obtained from a rigid wing analysis and the analytical results from the preliminary design phase obtained by a Multhopp lifting line method. The local spanwise lift distribution for the pull-up load case in the morphed configuration is shown in Fig. 2.11. The study demonstrates that the preliminary design results with the Multhopp method, which accounted for elastic wing deformation, closely align with the DLM results. Additionally, it can be seen that aeroelastic effects significantly influence the lift distribution. This leads to increased bending moments due to higher lift on the outer wing section.

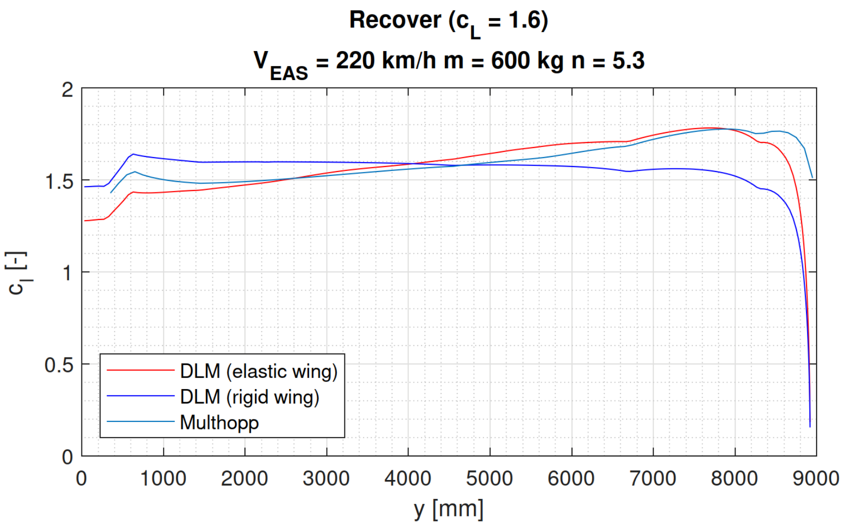

Figure 2.11: Local spanwise lift distribution of recover load case in morphed configuration, from [54]

From a performance perspective, the two most crucial load cases are determined. The first corresponds to cruise flight condition in undeformed configuration at $C_L = 0.3$, corresponding to an airspeed of $220\ km/h$ at MTOM. The second is a circling flight condition in morphed configuration at a bank angle of $40°$, corresponding to a load factor of 1.3, $C_L = 1.5$ resulting in $110\ km/h$ airspeed fully ballasted to MTOM. From an aerodynamic performance perspective, as little as possible wing twist is demanded, because the wing is designed to have optimal lift distribution when remaining untwisted. From a handling qualities perspective, especially at low speed flight, it is beneficial, if the wing tip has a slight negative twist, so that the first stall effects occur at the inner wing section and thus the ailerons remain effective without a tendency for wing drop. Illenberger shows in the results presented in fig. 2.12, that aeroelastic tailoring can shift the twist distribution in an advantageous direction. He also shows, that aeroelastic tailoring could decrease maximum structural loads of the wing.

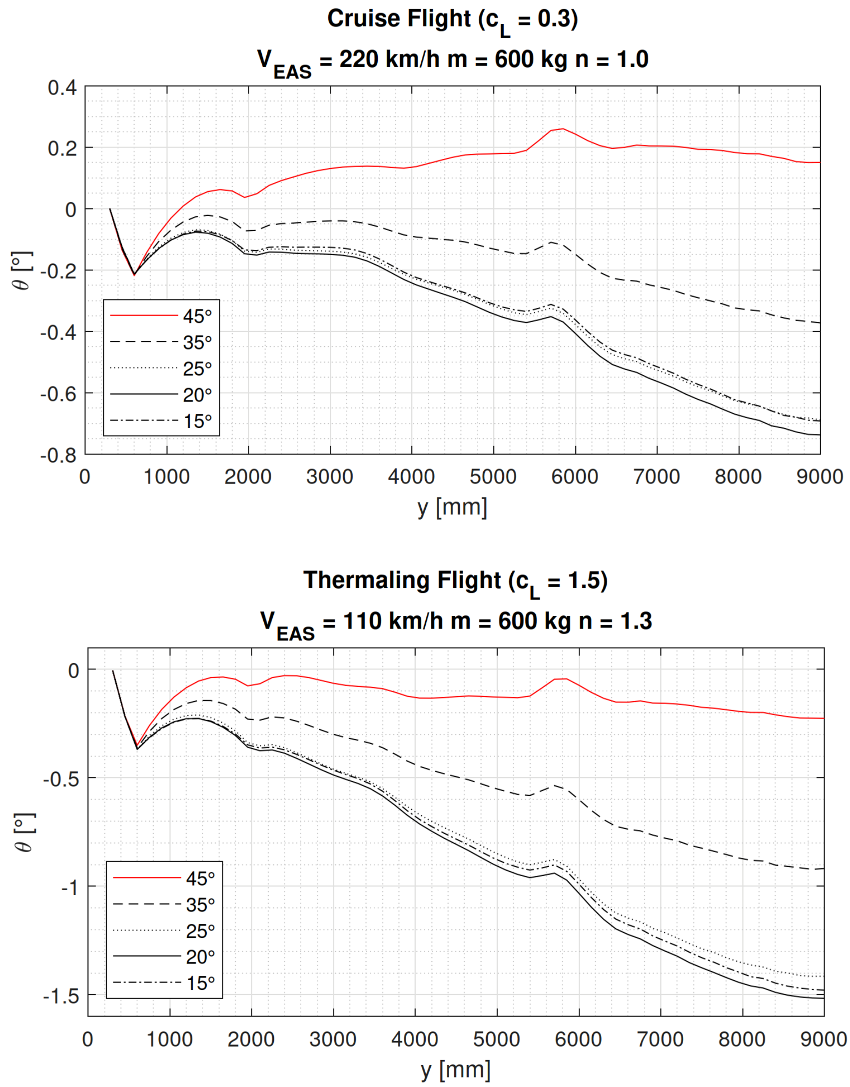

Figure 2.12: Effect of ply angle variation in the wing shell for high speed flight in undeformed configuration (left) and thermalling flight in morphed configuration (right), from [54]

It has to be mentioned, that the results of Illenberger are not based on the latest aerodynamic design iteration as presented as the results of this thesis. Thus the static and aeroelastic calculations have to be repeated with the latest design.

2.4 SYSTEMS INTEGRATION

Besides structural questions there are challenges regarding integration of systems into the morphing wing, due to the reduction of airfoil thickness. This causes a considerable decrease in available space for the systems. A sailplane with trailing edge flaps has control systems for flap and aileron actuation, which could be reduced to one common system, when flaperons are used. A further subsystem is the air brake system. Schempp-Hirth type air brakes, which are common for modern racing sailplanes, are intended to be used. The water ballast system, which allows to increase the gross weight of the sailplane to MTOM also provides challenges due to limited available volume for the tanks and sealing. If an increase of the maximum lift coefficient of 25% can be achieved as postulated in section 1.3, the average profile thickness will be reduced by the same fraction, provided the relative airfoil thickness remains the same.

2.4.1 *Control system*

A control system of a sailplane has to transfer the control inputs from the stick, the rudder pedals, the flap lever and the air brake lever in the cockpit to the respective control surfaces. In conventional sailplanes, cables are used for rudder actuation. For all other control systems, push- and pull-rods as well as torsional drive mechanical control systems are typically used, as they offer higher stiffness, less play and friction compared to cables. Connections have to be considered for attaching the fuselage side control systems to the removable wing and horizontal tail and for inner/outer wing connection if the wing tips are removable and equipped with control surfaces. In almost all modern sailplanes, all control connections are automatically joined when mounting the removable parts, mostly by *Hänle* hookups for push-rods (cf. Selinger [109]) or torsion drive connectors.

However, the limited available space due to the trend to reduce wetted area for less aerodynamic drag on sailplanes already poses challenges on the design of the mechanical control system. For a morphing wing sailplane, the space is further restricted inside the wing. Inside the fuselage, the elevator and rudder control system could remain as on current sailplanes, without notable interference with the aileron, flap and air brake control systems. Hence, only the influence of the morphing system on the control system of the wing is discussed here.

For the mechanical control system, a preliminary design study was done by the project partner *Alexander Schleicher Flugzeugbau GmbH*. It could be shown, that the available space inside the wing is sufficient for the control system of the flaps, ailerons and air brakes. *Schleicher* sailplanes traditionally have ailerons and camber changing flaps separated. The flap movement is superimposed fully on the ailerons, whereas one third of the aileron movement is superimposed on the inboard flap. The advantage in comparison to a flaperon is reduced induced drag during circling. Additionally, there exists a flap setting dedicated for landing. The flaps deflect to high positive angles of approx. 45°, but the ailerons have a deflection of 10°. This increases induced and profile drag for the approach and landing in combination with a gentle stall behavior. The disadvantage in comparison to a flaperon system is increased complexity and weight, because a mechanism is required, which mixes aileron and flap movement. For the *ASG 29*, this mechanism is located inside the wing. Further details on the flap/aileron mixing system on *Schleicher* aircraft are given in Selinger [109]. In the morphing wing sailplane, the design study revealed, that there is not sufficient space for the mixing mechanism inside the wing. A new mixing mechanism was designed, which is located in the center fuselage. Albeit the available space is very limited, the study showed, that it is possible to design a system, which fits in the limited fuselage space.

A further challenge is the flap thickness, or flap cross section area. Airfoils with thinner flaps have improved performance [16]. On the other hand, a minimum flap thickness is required for several purposes. First, a flap must be stiff in torsion. Otherwise, the lift distribution is negatively influenced or even flutter could occur. For thin shells like a wing flap, the torsional stiffness depends on the material in-plane shear stiffness and on the cross section area. Furthermore, the flap must provide space in front of the hinge line for mass balance due to flutter reasons. Some designs suffered from too thin flaps, like the *Akaflieg Braunschweig SB 14*, requiring for a redesign of the airfoil with increased flap thickness (cf. [5] p.232). However, modern high-modulus carbon fibers allow thinner flaps as was possible in earlier times. Nevertheless, the considerations regarding the torsional stiffness and space required for mass balance of the flaps influence the airfoil design of the wing. This is accounted for by a minimum thickness distribution constraint imposed at the flap region in the airfoil optimization method, as showed in section 4.2.

The control system for the actuation of the morphing leading edge consists of a torsional shaft, which actuates the compliant mechanism via an eccentric drive and a pullrod. The torsion shaft must be placed in a straight line inside the wing, or as straight segments coupled with Kardan gears. However the preliminary design study mentioned above shows, that the torsion drive control hookup at the wing fuselage joint collides with the main shear pins of the wing. Furthermore, it revealed that it is difficult to downsize the torsional drive for the tiny dimensions of the available space in the outer wing stations. This requires alternative solutions. Currently, a much simpler pull rod solution is under investigation, which directly actuates the morphing wing shell. Hence, the compliant mechanisms solely act as passive contour shaping devices. It is expected, that this reduces loads on the morphing wing shell.

2.4.2 *Water ballast system*

The water ballast system allows the pilot to select optimal wing loading based on current weather conditions. Thus, it must provide enough volume to ballast the sailplane from minimum take off mass to maximum take of mass. Mass estimations from structural design based on *ASG 29* weights show, that the minimum take off mass of the morphing wing sailplane with a sustainer engine will be around 430 kg, hence requiring for 170 kg of water ballast to be placed inside the wing.

The water ballast normally is placed in front of the main spar, because this space is not needed for control systems. However, for the morphing wing sailplane, the morphing system is located in this region. This requires extensive sealing of the ballast tanks and an actuation and compliant mechanism system to partially work in wet conditions. A flexible lid is intended to seal the gap on the lower wing shell in front of the main spar, which allows free movement of the morphing shell relative to the fixed part of the wing. Furthermore, the available water ballast volume is proportional to the square of the wing area. Water ballast capacity calculations show, that only 117 l water ballast can be loaded in the morphing section. Therefore, a partial usage of the primary wing structure section as ballast tank is required. This in turn requires a separation of the control system and the water tank, as already shown on the *Concordia* sailplane.

For deteriorating weather conditions and for landing, the water ballast needs to be dumped. Hence, valves that can be operated by the pilot need to be installed at the lowest point of each tank.

3 AERODYNAMIC DESIGN OBJECTIVE AND CONSTRAINTS

The primary design goal of a racing sailplane is to maximize average speed in soaring competitions. These tasks typically span 100 to 1000 km, with one or more turn points, starting and finishing at the competition aerodrome. The sailplane gains altitude via circling in thermals at low speed of around 100 km/h and dashes to the next thermal with high speed, ranging typically between 130 km/h and 220 km/h depending on the thermal strength. In inter-thermal flight, the pilot tries to find lift in straight flight. Thereby, the glide is stretched as far as possible, so that the loss of altitude is as small as possible and the probability of finding a strong lift for the next circling flight segment is maximized. An ideal sailplane has minimum sink rates at low speed and high glide ratios at high speed. In section 3.1, the qualitative goal of maximizing the average cross-country speed is converted to a quantifiable scalar metric, that is usable for comparison of sailplane performance.

Apart from the design objective, also a set of legal and other requirements has to be fulfilled to finally get a certified and competition ready production sailplane. In Europe, the *CS-22* [37], issued by the European Union Aviation Safety Agency (EASA) have to be fulfilled to obtain a type certification for a sailplane. In section 3.2, the most important paragraphs of the *CS-22*, which regulate and limit the aerodynamic design of a morphing wing sailplane are introduced.

National and international soaring competitions are governed by the International Gliding Commission (IGC), a subsidiary of the Fédération Aéronautique Internationale (FAI). The IGC introduced sailplane competition classes in order to ensure fairness in competition, but also to establish a stable environment for the sailplane manufacturing companies and for competition participants. Competition classes are discussed in appendix A.1. The FAI sporting code defines rules for competitions and in consequence poses requirements on sailplane design. These are also discussed in section 3.2.

3.1 DESIGN OBJECTIVE FOR A RACING SAILPLANE: MAXIMIZING THE CROSS-COUNTRY SPEED

Today's gliding competitions have the goal to complete a series of racing tasks with as high average speed as possible. Therefore, not only a skilled pilot is required, gaining the maximum amount of climb rate from thermal lift and flying with maximum efficiency and minimum detour. Also a well performing racing sailplane is necessary with minimum sink rate during thermal climb and inter-thermal dash. The climb in thermals is conducted at or close to the speed of minimum sink rate, which is below the speed of the best glide ratio and slightly higher than the stall speed. Reasonable speeds for inter-thermal flights are higher than the speed at the best glide ratio. In this section, fundamental figures of merit for the performance of a sailplane are introduced. First, the glide ratio polar of the aircraft is shown in section 3.1.1. Second, the mean sink rate is developed in section 3.1.2. This is a scalar performance metric, which gives the sink rate of a sailplane over an average competition flight.

3.1.1 *Aircraft polars*

The classical performance metric for a sailplanes is the glide ratio polar. Here, the glide ratio E of a sailplane is shown as a function of the equivalent airspeed u_{EAS}, which is the airspeed at sea level. The glide ratio polar of the *ASG 29* sailplane at MTOM is shown in fig. 3.1. The polar is measured the DLR with the comparison flight method of [86], which is discussed in section 6.1 and extrapolated from the flight mass of the test flight to MTOM with the method shown in chapter 6. The figure consists of six individual polars, shown in black. Each individual polar corresponds to a specific flap setting. The composite hull polar, shown in blue, represents the best achievable glide ratio for each airspeed. The *ASG 29* sailplane reaches a best glide ratio $E_{\max} = 50.6$, a minimum speed of $U_{\min} = 86.2\mathrm{km/h}$

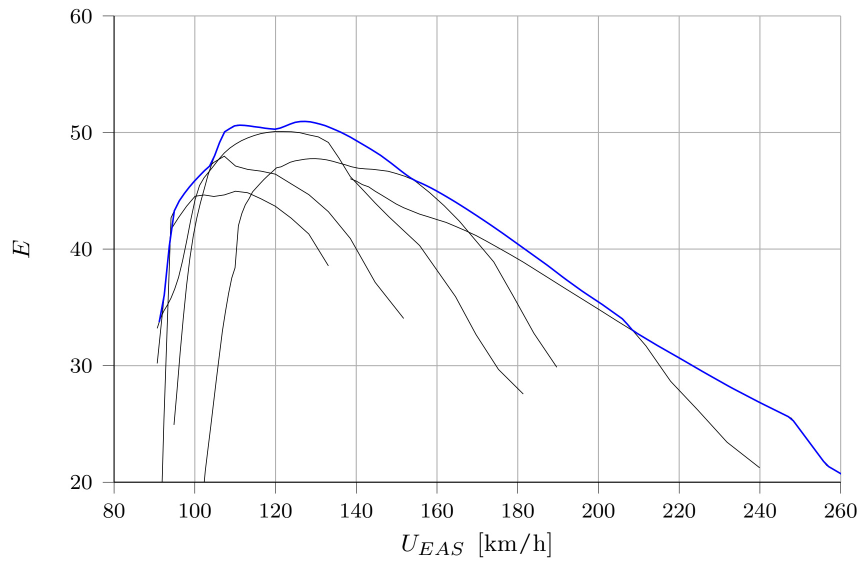

Figure 3.1: Measured glide ratio polars for flap settings 1 to 6 of the ASG 29 sailplane at MTOM, measured by the DLR with the method of Pätzold [86]. Individual flap polars black, composite envelope polar blue

3.1.2 *Average sink rate*

When comparing two distinctive sailplanes via their glide ratio polars, it is difficult to say, which one is better. One be a better "climber", i.e. has a better glide ratio at low flight speed and the other one could a better "glider" with a higher glide ratios at high speed. Therefore, a scalar performance metric could be better interpreted than a polar. In this section, the average sink speed is derived. This condenses a polar curve and a statistical distribution of flown lift coefficients to a scalar performance metric.

Maughmer et al. [79] studied the statistical frequency distribution of lift coefficients observed in high-level gliding competitions. Their analysis is based on post-processed Global Positioning System (GPS) logger data. This extensive dataset, comprised of multiple competition flights by top-tier pilots, includes information on lateral and longitudinal positions from GPS data, as well as altitude and airspeed data derived from static and total pressure measurements. All flights were conducted in the double-seater class using Schempp-Hirth Arcus sailplanes, which served as the reference aircraft for these frequency distribution analyses. The reference aircraft data is denoted by the index $\square_{\mathrm{R}}$. The take off mass is known for each flight. The data is logged at one-second intervals. The lift coefficient for each data point is computed using eq. 1.1. Lift coefficient intervals are defined and the frequency of each interval's occurrence is counted. The resulting frequency distribution is normalized, so that:

$$\int f_t(C_{L,\mathrm{R}})\,\mathrm{d}C_{L,\mathrm{R}} = 1. \tag{3.1}$$

The relative frequency of these coefficients is shown in fig. 3.2. The bars represent the frequency f_t for each interval of lift coefficients. Red bars indicate straight flight, yellow bars represent circling flight phases, and green bars show the combined frequency of both phases. Additionally, the airfoil c_l-c_d polars of the main wing airfoil, *WW07K130*, from the *Arcus* sailplane are shown alongside the frequency distributions. Maughmer highlights the strong alignment between the *Arcus* airfoil polar and the statistical distribution of flown lift coefficients.

It is generally assumed that experienced competition pilots tend to fly near the optimal lift coefficients of their sailplane, adapting to prevailing weather conditions. However, newly designed sailplanes may feature different optimal lift coefficient ranges, which could influence a pilot's choice of lift coefficient during flight. As a result, it is not possible to predict in advance how innovative design elements, such as a morphing airfoil, might affect the range of lift coefficients pilots would choose to fly at. Therefore, the lift coefficient frequency distribution shown in fig. 3.2 would likely differ if flown with a sailplane equipped with a morphing wing.

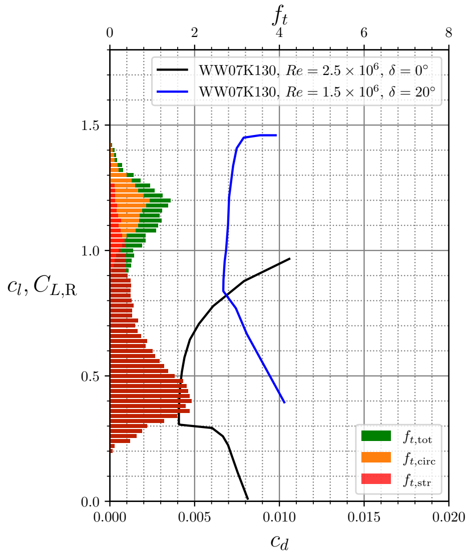

Figure 3.2: Frequency distribution f_t of flown $C_{L,\mathrm{R}}$ of the reference aircraft *Schempp-Hirth Arcus* and *WW07K130* (*Arcus* main wing) airfoil c_l-c_d polars for flap settings $\delta = 0°$ and $\delta = 20°$. Data from [79].

Maughmer et al. [79] also calculated the bank angle from the flight logger data and derived a frequency distribution of flown bank angles from the competition flight data set. This is shown in fig. 3.3. There, only the circling flight segments are considered. Most frequently flown bank angles are between $\phi_b = 35°$ and $40°$.

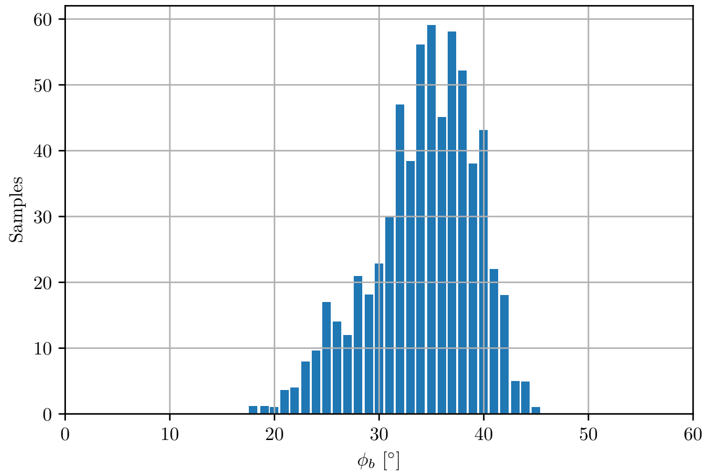

Figure 3.3: Frequency distribution of flown bank angle ϕ_b. Data from reference [79]

A frequency distribution of flown lift coefficients $f_t(C_L)$ and an aircraft polar can be condensed to an average sink rate. First, the current sink rate w_s is calculated from the aircraft lift coefficient C_L and drag coefficient C_D:

$$w_s = \sqrt{\frac{2mgn_z}{\rho A}\frac{C_D}{C_L^{3/2}}}, \tag{3.2}$$

where ρ is the density of air, m is the aircraft mass, n_z is the normal acceleration. The term $\frac{C_D}{C_L^{3/2}}$ is the climb index. Next, the mean sink rate of a reference sailplane is calculated. For the calculation of the mean sink rate, some simplifications and assumptions are made. A theoretical flight consists of a straight flight segment and a circling flight segment. In the straight flight segment, it is assumed, that the flown lift coefficients correspond to a statistical frequency distribution $f_{t,\text{str}}(C_L)$. Furthermore, the assumption is made that the aircraft flies unaccelerated. Thus, the normal acceleration in straight flight is $n_{z,\text{str}} = 1$. In the circling flight segment, the flown lift coefficients are assumed to correspond to the frequency distribution $f_{t,\text{circ}}(C_L)$. A constant bank angle ϕ_b is assumed, resulting in a constant normal acceleration $n_{z,\text{circ}} = \frac{1}{\cos\phi_b}$. It has to be noted, that the simplification is made, that the aircraft drag coefficient depends solely on the lift coefficient, thus $C_D = f(C_L) = C_D(C_L)$. And the density of air ρ is assumed to be constant. Finally the mean sink rate of the reference sailplane can be calculated:

$$\overline{w}_{s,\text{R}} = \sqrt{\frac{2m_\text{R}g}{\rho A_\text{R}}} \int \left[f_{t,\text{str}}(C_{L,\text{R}})\sqrt{n_{z,\text{str}}} + f_{t,\text{circ}}(C_{L,\text{R}})\sqrt{n_{z,\text{circ}}}\right] \frac{C_{D,\text{R}}(C_{L,\text{R}})}{{C_{L,\text{R}}}^{3/2}}\, \mathrm{d}C_{L,\text{R}}. \tag{3.3}$$

As mentioned above, the frequency distributions for straight flight $f_{t,\text{str}}$ and circling flight $f_{t,\text{circ}}$ are taken from Maughmer et al. [79] as shown in fig. 3.2. The bank angle for circling flight is also obtained from measurements done by Maughmer et al. [79]. It is the modal value of the bank angle distribution shown in fig. 3.3, which is $\phi_b = 37°$, resulting in $n_{z,\text{circ}} = 1.252$. The density of air is taken to be constant with $\rho = 1.006\ \text{kg}/\text{m}^3$, corresponding to an altitude of $2\ \text{km}$.

Now the mean sink rate of a new sailplane with index $\square_\text{N}$, is calculated. The new sailplane has a different drag polar $C_{D,\text{N}}(C_{L,\text{N}})$ and wing loading $\frac{m_\text{N}}{A_\text{N}}$ than the reference sailplane. In eq. 3.3, the square root of the wing loading $\frac{m}{A}$ influences the mean sink rate. Therefore, if the new sailplane has a higher maximum wing loading and the flown lift coefficients remain unchanged, the mean sink rate increases. And so does the airspeed. Therefore, the mean sink rate is not suited as a good figure of merit, when assuming the same flown lift coefficient. To account for this, flying at equal airspeed is assumed. As most modern competition sailplanes are designed to a stall speed of $90\ \mathrm{km/h}$, the thermalling speeds of the most modern sailplanes are similar. Thus, in the thermalling flight segment, the assumption of equal airspeed is realistic. However, a pilot flying with a higher wing loading would normally perform the inter-thermal dash at a higher speed. Evaluating the mean sink rate at equal airspeed allows for an analysis of which sailplane would achieve a higher finishing altitude after completing the same competition task at the same speed. A higher finishing altitude can be converted to higher speed and thus, the sailplane with higher finishing altitude is better. The ratio of the wing loadings is defined as:

$$K_{\mathrm{NR}} = \frac{\frac{m_{\mathrm{N}}}{A_{\mathrm{N}}}}{\frac{m_{\mathrm{R}}}{A_{\mathrm{R}}}}. \tag{3.4}$$

For equal airspeed, the lift coefficient of the new sailplane is higher than the lift coefficient of the reference sailplane by the factor of the wing loadings:

$$C_{L,\mathrm{N}} = K_{\mathrm{NR}} C_{L,\mathrm{R}}. \tag{3.5}$$

The sink rate of the new sailplane can be expressed by the lift coefficient of the reference sailplane by plugging eq. 3.4 and eq. 3.5 into eq. 3.2:

$$w_{s,\mathrm{N}} = \sqrt{\frac{2 m_{\mathrm{R}} g n_z}{\rho A_{\mathrm{R}}}} \frac{C_{D,\mathrm{N}}(K_{\mathrm{NR}} C_{L,\mathrm{R}})}{K_{\mathrm{NR}} C_{L,\mathrm{R}}^{3/2}}, \tag{3.6}$$

Finally, the mean sink rate of the new sailplane, flying at the same airspeed as the reference sailplane is calculated as:

$$\overline{w}_{s,\mathrm{N}} = \sqrt{\frac{2 m_{\mathrm{R}} g}{\rho A_{\mathrm{R}}}} \int \left[f_{t,\mathrm{str}}(C_{L,\mathrm{R}}) \sqrt{n_{z,\mathrm{str}}} + f_{t,\mathrm{circ}}(C_{L,\mathrm{R}}) \sqrt{n_{z,\mathrm{circ}}} \right] \frac{C_{D,\mathrm{N}}\left(K_{\mathrm{NR}} C_{L,\mathrm{R}}\right)}{K_{\mathrm{NR}} C_{L,\mathrm{R}}^{3/2}} \, \mathrm{d}C_{L,\mathrm{R}}. \tag{3.7}$$

The most frequently selected take off mass by pilots in competitions is MTOM. Therefore, all comparisons are done at the maximum wing loading. For calculation of the mean sink rate of a sailplane, it's aircraft envelope polar $C_{D,\mathrm{N}}\left(C_{L,\mathrm{N}}\right)$ is required. In this work, the polars for all flap settings of a sailplane are calculated with the performance estimation method as described in chapter 6. From the individual flap polars, the envelope polar is calculated, which determines the flap setting with the lowest drag at a certain lift coefficient. Finally, the envelope polar is interpolated and evaluated at the lift coefficients $K_{\mathrm{NR}} C_{L,\mathrm{R}}$ according to the lift coefficient frequency distribution from Maughmer et al. Finally, for the evaluation of the integral in eq. 3.7, a simple trapezoidal rule is used.

In fig. 3.4, the $C_{L,\mathrm{R}}$-$(C_{D,\mathrm{N}})$ polar, the climb index polar $\frac{C_{D,\mathrm{N}}}{C_{L,\mathrm{R}}^{3/2}}$ and the weighted climb index polar $(f_{t,\mathrm{str}} + \sqrt{n_{z,\mathrm{circ}}} f_{t,\mathrm{circ}}) \frac{C_{D,\mathrm{N}}}{K_{\mathrm{NR}} C_{L,\mathrm{R}}^{3/2}}$ of the *ASG 29* sailplane are shown. The latter is the integrand in eq. 3.7. Thus, integrating the area between the vertical axis and the curve of the right graph in fig. 3.4 and multiplying with the constant $\sqrt{\frac{2 m_{\mathrm{R}} g}{\rho A_{\mathrm{R}}}}$ gives the mean sink rate for the sailplane. The maximum wing loading of the *ASG 29* is $57.1\ \mathrm{kg/m^2}$, the maximum wing loading of the *Arcus* is $54.5\ \mathrm{kg/m^2}$. Thus $K_{\mathrm{NR}} = \frac{57.1}{54.5}$. The *ASG 29* sailplane achieves a mean sink rate of $1.019\ \mathrm{m/s}$.

The mean sink rate is the key performance index for racing sailplanes, because it directly determines the time which needs to be spent thermalling and hence the average speed over the racecourse. Weighing the climb index polar of different sailplanes with the frequency distribution as done in fig. 3.4 and comparing the area under the curve, i.e. the mean sink rate, gives one single scalar performance index for different sailplanes. This makes sailplane performance directly comparable in an average competition environment.

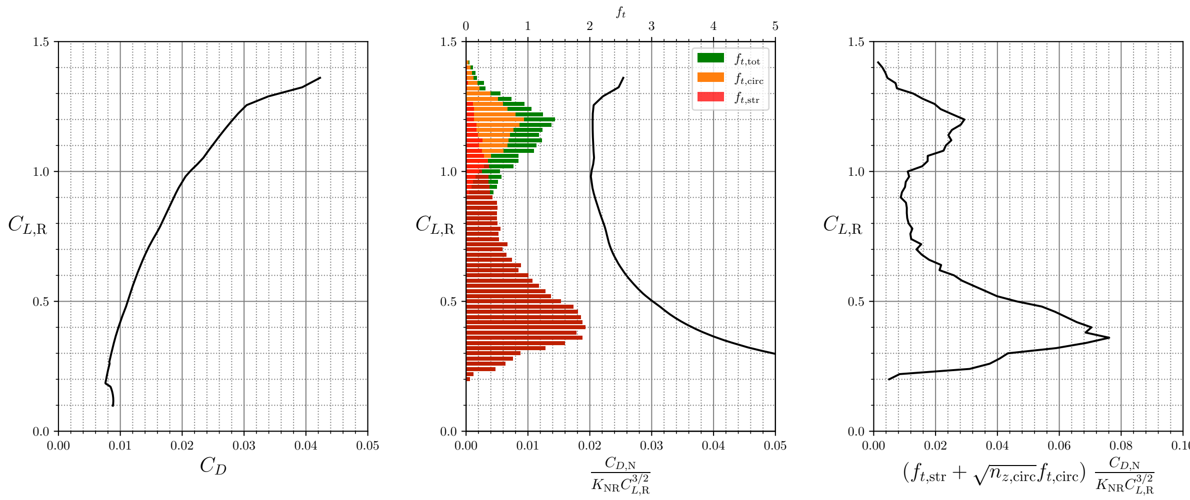

Figure 3.4: C_L - C_D polar (left,) climb index polar $\frac{C_D}{C_L^{3/2}}$ (center) and the weighted climb index polar $\left(f_{t,\mathrm{str}} + \sqrt{n_{z,\mathrm{circ}}} f_{t,\mathrm{circ}}\right) \frac{C_D}{C_L^{3/2}}$ (right) of the *ASG-29* sailplane

3.2 SAILPLANE DESIGN LIMITATIONS AND REQUIREMENTS

For the design of a sailplane, some limiting factors also have to be considered. First, the legal requirements defined in the *CS-22* must be met by the design for successful type certification of the aircraft. Several paragraphs therein affect the aerodynamic design. Furthermore, rules for gliding competitions are established by the world air sports association FAI, which organizes sailplane championships. The rules have the goal to ensure the fairness of competition between the pilots and the sailplane manufacturers and to limit costs. Sailplanes are grouped into competition classes. Criteria for class distinction are the span of the sailplane, the allowance of camber changing flaps and for the double-seater class, a two place cockpit is mandatory. Currently, six sailplane competition classes exist: The standard class, a 13.5 meter class, a 15 meter class, an 18 meter class, a 20 meter double-seater class and an open class. The class definitions and exemplary production sailplanes are further discussed in the appendix A.1. The design of the sailplane introduced in this thesis is targeted for the 18 m class, where a span of not more than $18\ m$ is allowed combined with camber changing flaps.

The requirements for type certification of new sailplanes in the European Union are specified by the EASA in the *Certification Specifications for Sailplanes and Powered Sailplanes CS-22* [37]. The document consists of nine subparts, of which subpart B is crucial for aerodynamic design. In this section, the paragraphs of the *CS-22* influencing the aerodynamic design of a sailplane are shown and the influences are explained.

3.2.1 *Requirements affecting maximum lift of the wing*

In this subsection, the paragraphs of the *CS-22* affecting the minimum required maximum lift of the wing are shown and the influences on the design are explained.

One important paragraph influencing the aerodynamic design is *CS 22.49*. In this requirement, the stalling speed is specified with landing gear extended, wing flaps in landing position and the center of gravity in the most unfavorable position. The stalling speed must not exceed $90\ \mathrm{km/h}$ at

MTOM and 80 km/h with water tanks empty. Thomas [119] shows, that earlier sailplane designs before the 2000s let more or less big margins to the requirement specified in *CS 22.49*. The stalling speeds are lower than required, wing areas larger than necessary and maximum wing loadings lower than possible. However, it has become clear in the last years, that a low sink rate at high speed is key to win gliding competitions. Hence the last generation designs in the 18 meter class all strive for a take off mass as high as possible and the stall speeds are just below the requirements specified in *CS 22.49*. However, the Annex A to the FAI sporting code section 3 [39] limits the MTOM to 600 kg. Therefore, the sailplane in this work is targeted for 600 kg MTOM.

The relationship between the required stalling speed and the product of maximum overall aircraft lift coefficient $c_{l,\max}$ and wing area A is derived from eq. 1.1:

$$c_{l,\max}\, A = \frac{2 m_{\text{flight}}\, g}{\rho_{\text{ISA}}\, U_{CAS}^2}. \tag{3.8}$$

Eq. 3.8 requires a minimum $c_{l,\max}\, A$ for a given maximum take-off mass m_{MTOM} and a required minimum calibrated stall speed U_{CAS}. The Calibrated Air Speed (CAS) is obtained by using the sea level air density according to the International Standard Atmosphere (ISA), being $\rho_{\text{ISA}} = 1.225\ \text{kg}/\text{m}^3$. The required stall speed U_{CAS} is defined by *CS 22.49*. Airfoils designed to achieve a higher maximum section lift coefficient ($c_{l,\max}$) generally exhibit higher drag coefficients c_d at low lift coefficients. This remains true even when a morphing wing forward section is used. Consequently, a trade-off must be considered between two types of airfoils: those with higher $c_{l,\max}$ and c_d, which require less wing area, and those with lower $c_{l,\max}$ and c_d, which necessitate a larger wing area. Preliminary studies [128] indicated, that maximum section lift coefficients of $c_{l,\max} = 1.825$ could be achieved with a morphing wing airfoil with decent low lift performance. The maximum section lift coefficient $c_{l,\max}$ must be a bit higher than the overall aircraft maximum lift to account for loss of lift due to fuselage interference and potential tailplane downforce. Deck [26] measured differences of below 3% between the aircraft lift coefficient C_L and the section lift coefficient c_l . According to the results of eq. 3.8, a maximum wing loading of $\frac{m_{\text{MTOM}}}{A} = 69\ \text{kg}/\text{m}^2$ would result in an required overall aircraft maximum lift coefficient of $c_{l,\max} = 1.77$, which gives some reserve to the maximum section lift coefficient. A maximum wing loading of $\frac{m_{\text{MTOM}}}{A} = 69\ \text{kg}/\text{m}^2$ is more than 10% higher than the highest value achieved for todays production sailplanes, promising very good high speed performance. The maximum take off mass without water ballast, including pilot, sustainer engine system and fuel must be below $m_{\text{TOM}} = 475$ kg to fulfill *CS 22.49(b)(1)* with a $c_{l,\max} = 1.77$.

The requirement given in *CS 22.49(b)(3)* demands a maximum stall speed at MTOM of 95 km/h with air brakes fully extended in landing configuration, which is an increase of 5 km/h compared to the requirement in clean configuration set in *CS 22.49(b)(2)*. For common three stage Schempp-Hirth type airbrakes properly sized to fulfill the requirement for air brake effectiveness defined in *CS 22.73* and *CS22.75*, a 5 km/h increase in stall speed is a common value. For example, the *JS3* flight manual [71] reports a stall speed increase of about 5 km/h for all flap settings. However, the estimation of the increase in stall speed due to extension of air brakes requires extensive CFD analysis or wind tunnel test which is unfeasible for a preliminary sailplane design. Therefore this value remains somewhat uncertain. In this work, it is assumed, that the 5 km/h tolerance is sufficient for the design.

3.2.2 *Requirements on handling qualities affecting preliminary aerodynamic design*

In this subsection, the requirements on handling qualities, which affect the preliminary aerodynamic design of the wing, are discussed. The design should result in an aircraft with benign handling behavior for the pilot. Therefore not only the regulatory design requirements for the handling behavior of the aircraft must be considered, but also requirements, which are not covered by the regulations. These will be also discussed in this subsection.

One design requirement directly affects the wing planform design and airfoil distribution. *CS 22.201* (wings level stall) requires, that the aircraft remains controllable by normal use of the controls until the stall occurs without control reversal, i.e. rolling to the opposite direction relative to the aileron deflection. *CS 22.203* states, that it must be possible to regain normal level flight without encountering uncontrollable rolling or spinning tendencies when the sailplane is stalled in a coordinated $45°$ banked turn. For the aerodynamic design of the wing, both paragraphs effectively require, that the flow on the outer wing remains attached at higher angles of attack than on the inner wing. This gives some reserves, so that small sideslip angles, aileron deflections and asymmetric gusts will not cause an asymmetric loss of lift on one wing. In consequence, this would lead to excessive wing drop. This further requires, that the wing either has to be designed with twist (angle of incidence lower at the wing tip than that at the root section), or with an over-elliptical planform (between elliptic and rectangular), or with outer-wing and wingtip airfoils featuring a more gentle stall behavior than the inner wing airfoils. However, both wing twist and over-elliptic planform cause increased induced or profile drag at least at certain lift coefficients. Therefore specifically designed airfoils with emphasis given on a gentle stall behavior are used for the outer wing and wing tip regions. The wing remains untwisted for minimum induced drag at all lift coefficients.

Furthermore, there are requirements affecting the aerodynamic design, as the minimum roll rate, specified in *CS 22.147*. The time for reversing the direction of a turn with a $45°$ bank angle in the opposite direction must not be longer than $b/3$ seconds at $1.4\ v_{S,1}$. $v_{S,1}$ is the stall speed in clean configuration. For most modern sailplanes, this paragraph is easy to fulfill. However, most pilots demand higher rolling speeds for easy maneuvering of the sailplane, especially for the centering of thermals.

There are further requirements affecting the horizontal and vertical stabilizer sizing, as *CS 22.175*, *CS 22.581* and *CS 22.583*. However, stabilizer sizing will not be coped in this thesis, as the empennage will be taken in unmodified form from the *ASG 29* sailplane for reference.

4 TWO-DIMENSIONAL AIRFOIL DESIGN OPTIMIZATION

In this chapter, the design of the airfoils for the morphing leading edge wing is shown. Five different airfoils are designed for different spanwise positions on the wing, specifically tailored to their requirements. The requirements are discussed in section 4.1. A novel numerical optimization method is developed, that makes it possible to design airfoils making use of the morphing leading edge concept introduced in section 1.1.

The mathematical problem formulation is discussed in section 4.2. For numerical optimization, the airfoil contour has to be calculated from design variables. The parameterization of the airfoil geometry including the morphing of the forward section using a modified variant of the CST method is shown in section 4.3. For drag calculation of the airfoil designs in each iteration, two modified variants of *XFOIL* are used. *XFOIL* is an integral boundary-layer solver, developed by Drela [29]. The modified variants are designated *XFOIL-mod* and *XFOILSUC-mod*. The modifications aim to improve maximum lift prediction and transition location prediction, which are both crucial for a precise optimization. The solver and the modifications are introduced in section 4.4. The used optimization algorithm – *SUBPLEX* by Rowan [102] – is introduced in section 4.5. The optimization results of the main wing airfoil are shown in section 4.6. The results of the root, inner wing and the tip airfoils are briefly discussed in section 4.7. Premature laminar-turbulent transition on the gap seal between the morphing forward section and the main wing could lead to significantly increased drag, offsetting all possible advantage of the morphing wing concept. The risk for this to occur is analyzed in section 4.8.

4.1 AIRFOIL DESIGN REQUIREMENTS AND OBJECTIVE

In total, five airfoils shall be designed for the main wing up to the winglet root, all specifically designed for their respective operational Reynolds number range and other requirements. The airfoils are shown in fig. 4.1 and denominated:

- Root airfoil
- Inner wing airfoil
- Main wing airfoil
- Outer wing airfoil
- Tip airfoil

The initial planform design is shown in fig. 4.1 bottom. Also the planned positioning of the airfoils and their chord lengths, that are used for Reynolds number calculation are shown. For comparison, the *ASG 29* planform and spanwise airfoil distribution is shown in fig. 4.1 bottom. The comparison shows the smaller wing area of the morphing wing sailplane. Both wings have a straight flap hinge line without the need for splitting the flap at each trapezoidal kink for free motion of rotation. The morphing sailplane wing has a slightly increased forward sweep of the flap hinge line compared to the *ASG 29* to obtain an identical location of the aerodynamic center. The *ASG 29* airfoils are designed for a camber changing flap of 14% of the chord length.

The morphing sailplane wing's higher aspect ratio leads to increased roll damping. To improve aileron effectiveness, the flap and aileron lengths were increased to 16% for the inner and main wing airfoil. The lower Reynolds number of the outer wing airfoils leads to increased viscous decambering, particularly at high lift coefficients, compared to the higher Reynolds number inner wing airfoils.. If uncorrected, this would lead to a sub-optimal spanwise circulation distribution and hence increased induced drag at high lift coefficients. In morphed configuration, the camber of the outer wing and tip airfoils is enhanced by extending the trailing edge flap length. This counteracts the effect. The increase is linear, starting from 16% of the chord length at the last main wing section at $y = 3258$ mm and ending with 17% of the chord length at $y = 8888$ mm.

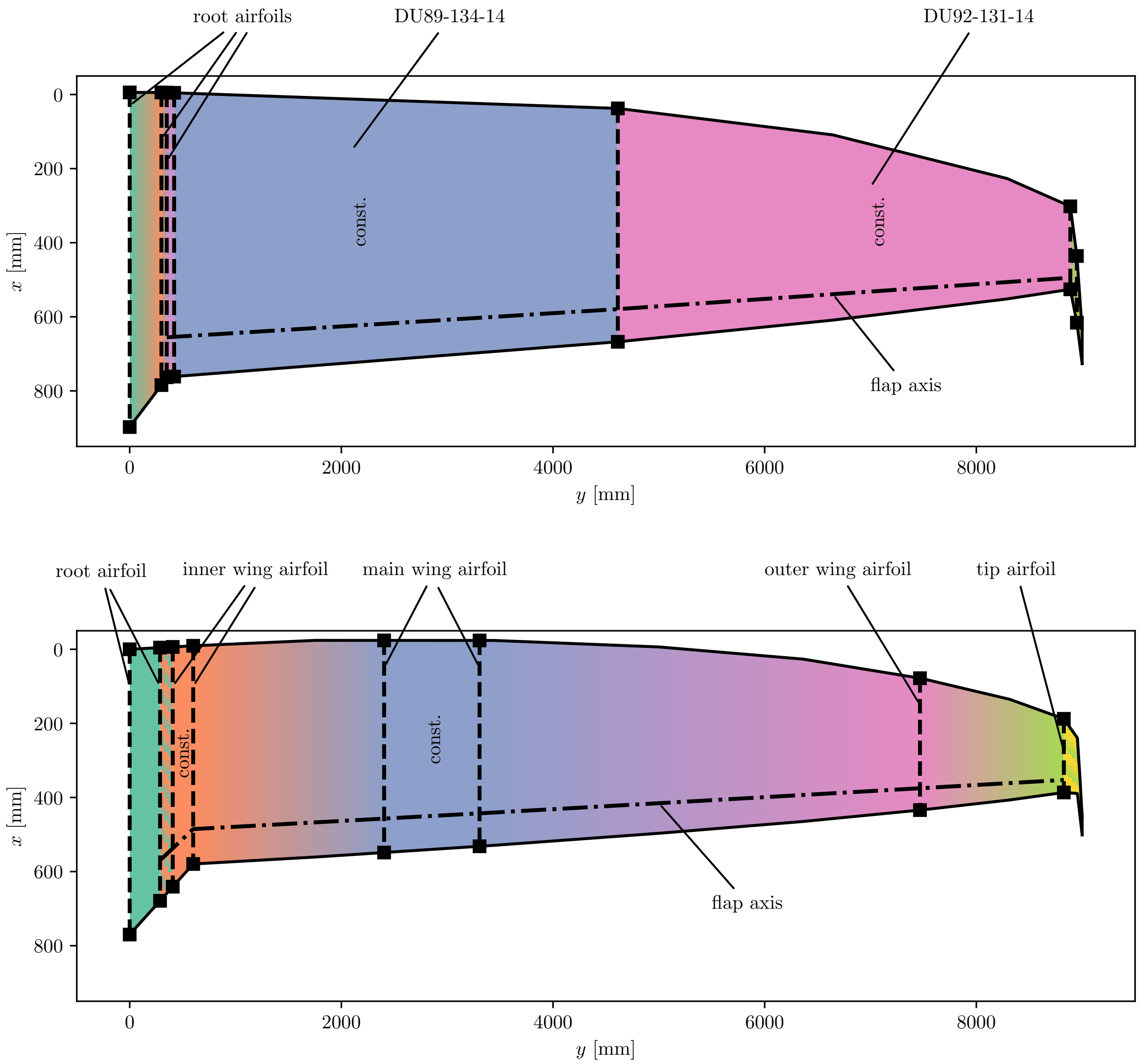

Figure 4.1: Planform and airfoil distribution of *ASG 29* sailplane (top), Initial planform design and planned distribution of airfoils for morphing wing sailplane (bottom)

The requirements for the airfoil design are broken down from the aircraft design requirements. As shown in section 3.2.1, the aircraft must have a stall speed not greater than 90 km/h at MTOM.

Based on the results of a preliminary design morphing airfoil of Wiessmeier [128], which are shown in fig. 1.6, it is expected that an increase of at least 25% of the maximum lift coefficient is possible. Hence, the wing area can be reduced by 25%, maintaining equal or lower stall and circling speed in thermals. The Reynolds number range, for which the morphing airfoils are optimized, are calculated assuming that the sailplane is ballasted to MTOM. A bank angle of $45°$ is assumed for circling flight, leading to a normal acceleration of $n_Z = \sqrt{2} \approx 1.41$.

In summary, the requirements for the main wing airfoil design are:

- Laminar low drag region in undeformed configuration at lift coefficients between $c_l = 0.3$ and 0.9, corresponding Re range calculated in straight flight, $n_z = 1$.
- Laminar low-drag region in morphed condition between $c_l = 1.3$ and $c_l = 1.725$. Corresponding Re range calculated at bank angle of $45°$.
- Maximum lift coefficient of at least $c_l = 1.825$ at $30°$ flap deflection.
- Insensitive to leading edge contamination (insects or rain).
- The leading edge must not encounter any geometry change during morphing actuation except rigid body motion. It must remain on the same upper shell curve length position.
- Good aileron effectiveness, even close to upper corner of laminar low-drag region without major separation at the upper surface.
- Gradual stalling characteristics.
- Free of leading edge stall at all feasible angles of attack with ample reserve.
- Minimum airfoil thickness of about 12.5%.
- Trailing edge angle of $7°$ or more.

The main wing airfoil is the first to be designed. The design conditions for all airfoils are given in table 4.1. A minimum thickness requirement of 12.5% is set for the main wing airfoil. The start designs for the other airfoils are derived from the inner wing airfoil optimization results.

The inner wing airfoil has the same design conditions as the main wing airfoil, except the Reynolds number range is adopted to the larger chord length. And for a sufficient main spar strength reserve, the minimum thickness must be increased to $\approx 14.5\%$.

The root airfoil has the same design conditions as the inner wing airfoil, except Reynolds number adoption. Additionally, the upper surface must be designed to account for the turbulent inflow due to the fuselage boundary-layer, which makes it more prone to separation. Some tries have been made to design a suitable root airfoil with numerical optimization accounting for the turbulent inflow, but the resulting airfoils were geometrically incompatible. Therefore, the root airfoil is designed as a derivative of the inner wing airfoil. The pressure distribution is adopted for turbulent inflow using inverse design.

The outer wing airfoil has a lower Reynolds number range due to the smaller chord length. The main wing airfoil is used as start design. For good handling characteristics, it is essential that the inner wing stalls first. Hence the outer wing airfoil requires some lift reserve compared to the inner and main wing airfoils. Thus, the upper design lift coefficient is raised from $c_l = 1.725$ to $c_l = 1.735$.

The same holds for the tip airfoil. However, the minimum thickness limits could be relieved a bit for the tip airfoil, because the wing bending loads decrease drastically further outward.

Table 4.1: Design conditions for airfoils of morphing wing

Airfoil	y [mm]	$\bar{c}$ [mm]	$Re(C_L = 0.3)$	$Re(C_L = 1.725)$	$C_{L,upper,req}$	x_r [%]	$t_{\min,tot}$ [%]
Root	287	683	2.66×10^6	1.32×10^6	1.725	84	14.75
Inner	600	589	2.25×10^6	1.11×10^6	1.725	84	14.75
Main	3300	533	2.08×10^6	1.03×10^6	1.725	84	12.5
Outer	7480	340	1.48×10^6	7.32×10^5	1.735	83.26	12.5
Tip	8920	220	8.57×10^5	4.23×10^5	1.735	83	12

4.2 MATHEMATICAL PROBLEM FORMULATION

This airfoil shape optimization minimizes an objective function f by identifying the optimal set of design variables $\mathbf{d} = \left\{d_0, d_1, \ldots, d_i, \ldots, d_n\right\}$ with $\mathbf{d} \in \mathbb{R}^n$. Each individual design variable d_i has an upper bound d_i^u and a lower bound d_i^l. Inequality constraints $g_j \leq 0$ must be satisfied to obtain a valid design.

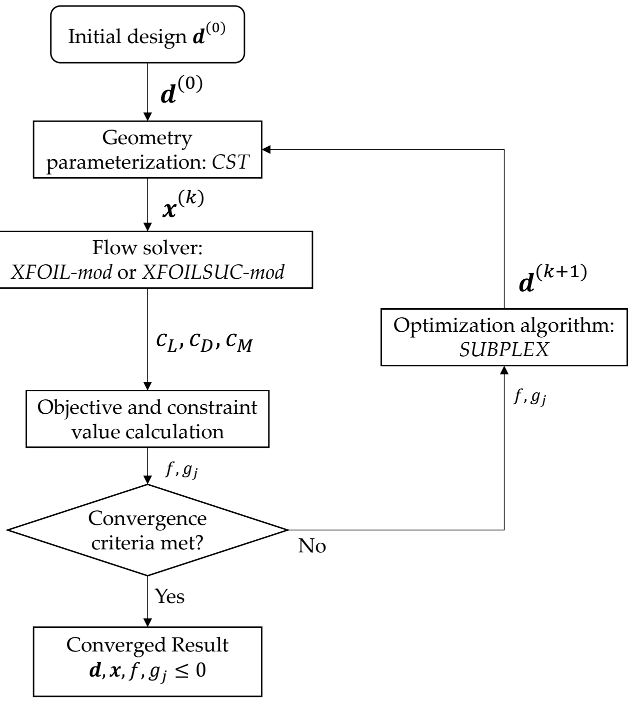

Figure 4.2: Aerodynamic optimization flow chart

Fig. 4.2 shows the iterative optimization procedure. The CST parameterization algorithm, described in section 4.3 converts the design variables $\mathbf{d}$ to airfoil coordinates $\mathbf{x}$. A flow solver, in this work *XFOILSUC-mod* and for some operation points alternatively *XFOIL-mod*, calculates the drag coefficients $c_{d,op}$ for each operation point op. An operation point corresponds to one particular lift coefficient and one particular morphing/flap configuration. The solvers are described in section 4.4. The objective function is calculated from the drag coefficients. As long as the termination criterion is not met, the design variables are updated for the next iteration $k + 1$ by the *SUBPLEX* optimization algorithm, described in section 4.5.

The numerical airfoil optimization problem in this work is given as:

$$
\begin{array}{lll}
\min_{\mathbf{d}} & f(\mathbf{d}) = \sum_{op} w_{op}\, c_{d,op}(c_{l,op}, \mathbf{d}) & \\
\text{subject to:} & g_0(\mathbf{d}) = 1 - \max\left(\frac{t(x,\mathbf{d})}{t_{\min}(x)}\right) \le 0 & \text{where } t(x) = y_u(x) - y_l(x) \\
& g_1(\mathbf{d}) = 1 - \frac{\max(t(x,\mathbf{d}))}{t_{\min,\mathrm{tot}}} \le 0 & \\
& g_2(\mathbf{d}) = 1 - \frac{y_u(x=0.0125,\mathbf{d})}{y_{0.0125,\min}} \le 0 & \\
& d_i^l \le d_i \le d_i^u & i = 0,\dots,n \\
\text{where:} & \mathbf{d} = [d_0, d_1, \dots, d_n]^\intercal & \mathbf{d} \in \mathbb{R}^n
\end{array}
\tag{4.1}
$$

The objective function f is a sum of the weighted drag coefficients $c_{d,op}$, with weights w_{op} over all operation points op. Three inequality constraints $g_j \le 0$ are employed: The first constraint g_0 specifies a minimum allowable thickness distribution $t_{\min}(x)$. For that purpose, a polygonal line is used. The coordinates of the polygon vertices used for all airfoil optimizations in this work are shown in table 4.2. The thickness distribution is constrained in the rear region behind $x = 0.8$ to ensure the minimum trailing edge angle of 7° and a minimum flap thickness. This is required for sufficient torsional stiffness of the flap and for space for mass balance for flutter suppression. The second constraint, g_1, sets a lower bound for the overall thickness of the airfoil, as specified in table 4.1. The third constraint g_2 ensures, that the upper surface contour of the airfoil at $x = 0.0125$ is at $y_{0.0125,\min} = 0.018$ or higher. This ensures, that a critical leading edge stall condition yielding in bad handling characteristics doesn't occur. In section 4.4.3.1 it is discussed, why this constraint is required and why *XFOIL-mod* and *XFOILSUC-mod* are not able to detect the leading edge stall phenomenon.

Table 4.2: Vertices for the polygon $t_{\min}(x)$ of the local minimum thickness constraint

x	$t_{\min}(x)$
0.8	0.035
0.85	0.025
0.9	0.015
0.95	0.006
0.999	0

The *SUBPLEX* algorithm allows for bounded unconstrained optimization only. Constraints can not be considered directly. Therefore, a penalization approach is used, where the objective f function is increased by a penalty term if constraints are violated, giving the penalized objective function f_p. The penalization approach used here is the Sequential Unconstrained Minimization Technique (SUMT) by Fiacco and McCormick [40]. The inequality constraints g_j are accounted by smooth barrier functions, which penalize the original objective function f:

$$f_p = f + \left(\sum_j r_0 \frac{-1}{g_j + c_{tol}}\right) \sum_{op} w_{op}. \tag{4.2}$$

For r_0, a small number should be used, so that the barrier functions rise rapidly, when approaching the inequality constraint. In contrast to the acSUMT, a tolerance c_{tol} for the constraints is used, so that the constraints can be slightly violated. With this, a moderately small number for r_0 can be used. This avoids ill-conditioning of the optimization problem. The factor $\sum_{op} w_{op}$ acts as normalization, when using a different number of operating points or different weights. When having a low number of operation points, the original objective function f is low compared to a higher number of operation points, as can be seen in eq. 4.1. Therefore, the penalty term would be overemphasized compared to the original objective function. The multiplication of the normalization term leads to a uniform increase in both the original objective function f and the penalty term in case of an increasing number of operation points or changing weights. Then it is not needed to adopt r_0 for each change of optimization points or weights. Unless otherwise stated, $r_0 = 5 \times 10^{-6}$ and $c_{tol} = 5.485 \times 10^{-2}$ are used in this work.

The termination criterion for the optimization is discussed in section 4.5.2.

4.3 AIRFOIL GEOMETRY PARAMETERIZATION

In this work, numerical airfoil optimization is done as part of the overall aircraft design optimization in the decomposed optimization strategy. The shape of the airfoil is altered in an iterative manner to obtain the best possible airfoil, i.e. the airfoil with minimal drag at certain lift coefficients.

For a fast and efficient optimization, a geometric parameterization of the airfoil contour is needed, which allows to describe a wide variety of possible airfoil shapes with a high level of detail. This should be done with a minimal number of design variables.

Masters et al. [76] have shown, that the CST airfoil geometry parameterization method proposed by Kulfan and Bussoletti [63] is very efficient compared to other methods. The airfoil contour is parameterized directly, which facilitates changing only the forward section of the airfoil by morphing. Therefore, the CST method is used in this work for geometry parameterization.

Typically, airfoils with camber-changing flaps have a single flap setting where both the upper and lower surfaces are smooth and free of kinks. However, there is a class of airfoils with two distinct flap settings. This concept was first introduced by Boermans and van Garrel [16] with the *DU89-134-14* airfoil, used as the main wing airfoil of the *ASG 29* sailplane. The *DU89-134-14* airfoil, featuring these two unique flap settings, is illustrated in fig. 4.3.

The first of these settings is the neutral setting, where the lower surface contour is continuous in slope and curvature, while the upper surface exhibits a concave kink. This setting is optimized for high-speed flight. Boermans and van Garrel demonstrated that this configuration allows for extended laminar flow runs on the lower surface, maintaining laminar flow up to the flap. Proper sealing of the flap gap with a plastic foil is required, and an artificial turbulator is used to induce transition in the middle of the flap.

The second setting involves a positive flap deflection angle, resulting in a continuous slope and curvature on the upper surface, while the lower surface shows a concave kink. This setting is suited for low-speed flight. The continuous contour on the upper surface prevents suction peaks and sharp pressure recovery, avoiding premature flow separation and enabling higher lift coefficients within the laminar low-drag region. In this study, this type of airfoil is referred to as *kinked flapped airfoils*.

However, the CST method is not capable of parameterization of airfoils with this features. Therefore, it has to be modified. Furthermore, the CST method has to be extended to be capable to parameterize the shape change of the morphing forward section. Both extensions are described in this section.

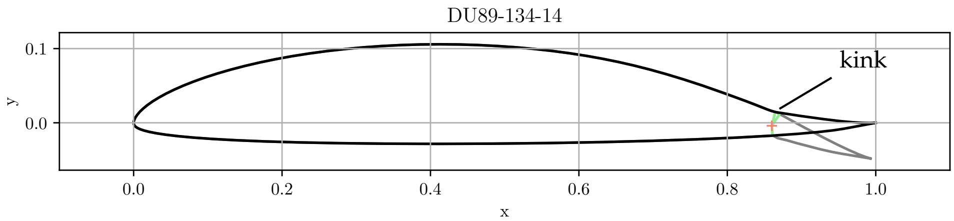

Figure 4.3: *DU89-134-14* airfoil in neutral (black) and positive (gray) flap setting with intentional concave kink

4.3.1 *The class function shape function transformation method*

In this approach, the geometry of the upper and lower contour of an airfoil is analytically parameterized as the product of a fixed class function and a modifiable shape function. The shape function is a linear combination of Bernstein polynomials, where the design variables act as coefficients for scaling the individual Bernstein polynomials [63]. The CST method has the following advantages: The slope of the leading edge is always infinite with an appropriate choice of the class function. Therefore a round leading edge is ensured. Similarly, the trailing edge angle is always finite. Furthermore, each design variable has a global influence on the airfoil geometry, which indicates that the solution space is less multi-modal compared to local perturbation parameterization approaches.

Masters [76] analyzes the performance of different shape parameterization methods for a range of design variables with regards to geometry precision and convergence to the aerodynamic properties compared to over 2000 validation airfoils. Masters concluded, that the CST method reached high precision with a given number of design variables compared to other parameterization methods. Only the method using the Singular Value Decomposition (SVD) (see Toal et al [121]) showed better results, but the performance strongly depends on the set of training airfoils for identifying the eigen-airfoils. Furthermore, it is difficult to ensure geometrical compatibility of the morphing leading edge and the rigid main structural section of a morphing leading edge airfoil. Also it is not clear how to parameterize *kinked flapped airfoil* type with SVD. Therefore, the CST method, that explicitly parameterize the airfoil geometry is used in this work.

However, there are also some disadvantages of the CST method. First, using the original formulation of CST, the parameterization of a *kinked flapped airfoil* requires a high number of design variables for its upper side contour. This is, because both the class function and the shape function are smooth, whereas a *kinked flapped airfoil* has a discontinuous upper contour slope in the baseline flap setting.

In contrast to the need for a high number of design variables, Ceze et al [20] show that the condition number of the CST parameterization matrix becomes exponentially high with increasing number of design variables. This leads to a non-unique geometry parameterization in case of a high number of design variables. In further consequence, this probably leads to a multi-modal objective function with many local minima. The optimization algorithm can then be easily trapped in an non-optimal local minimum. Ceze et al. point out, that this is due to the non-orthogonality of the Bernstein polynomials. Stanko [114] used the orthogonal Legendre polynomials and Karman [57] used Chebyshev polynomials to improve the conditioning of the parameterization matrix. In this work, Bernstein polynomials with nine design variables for the upper and lower side contour are used. In section 4.6 it is shown, that this is a good compromise between fidelity and good conditioning.

4.3.2 *Extensions to the CST method for a kinked flapped airfoil*

For a precise parameterization of *kinked flapped airfoils* with a low number of design variables an extension to the CST method is introduced. The parameterization of the airfoil upper surface contour is given by:

$$y_{u,d}(x) = C(x)\ S(x) + N_3\ x^2 + N_4\ x^2 \quad , \quad 0 \leq x \leq 1. \tag{4.3}$$

And the lower surface contour:

$$y_l(x) = C(x)\ S(x) - N_3\ x^2, \tag{4.4}$$

where $C(x)$ is the class function and $S(x)$ is the shape function. The class function for an airfoil shape with an infinite leading edge slope and a finite trailing edge angle is given as:

$$C(x) = x^{N_1}\ (x-1)^{N_2} \quad \text{, where} \quad N_1 = 0.5 \quad , \quad N_2 = 1. \tag{4.5}$$

The shape function is a sum of Bernstein Polynomials:

$$S(x) = \sum_{i=0}^{n} S_i(x) = \sum_{i=0}^{n} d_i\ B_i(x) \tag{4.6}$$

with:

$$B_i(x) = K_{i,n}\ x^i (1-x)^{n-i} \tag{4.7}$$

$$K_{i,n} = \begin{pmatrix} n \\ i \end{pmatrix} = \frac{n!}{i!(n-i)!}, \tag{4.8}$$

with the design variables d_i as scaling coefficients, which determine the airfoil shape. All Bernstein polynomials, except the first, are zero at the leading edge $x = 0$. Similarly, all except the last are zero at the trailing edge $x = 1$. Hence, the first and last parameters directly control the leading edge radius and the trailing edge angle, respectively. The factor $N_3 > 0$ in equations 4.3 and 4.4 gives a blunt trailing edge, with a trailing edge thickness $t_{\mathrm{TE}} = 2N_3$. In contrast, Kulfan and Bussoletti use a linear approach to handle a blunt trailing edge. But for thick trailing edges an unsteadiness in the curvature would arise on the leading edge. Therefore, the quadratic approach introduced here without unsteadiness is used. The *kinked flapped airfoil* is represented by the fourth term in eq. 4.3. A quadratic function is added to the upper side contour. N_4 is chosen, so that the upper side contour crosses the trailing edge point, when the flap is deflected with the design flap deflection angle $\delta_{f,0}$. At this flap deflection angle the upper side contour is continuous in slope and curvature. The calculation of the parameter N_4 is given in equations 4.9 and 4.11. First the trailing edge point $\mathbf{x}_{\mathrm{TE}}$ is rotated around the flap hinge point $\mathbf{x}_r$ with the design flap deflection angle $\delta_{f,0}$ (eq. 4.9):

$$\mathbf{x}_f = \mathbf{R}(\delta_{f,0})\ (\mathbf{x}_{\mathrm{TE}} - \mathbf{x}_r) + \mathbf{x}_r, \tag{4.9}$$

where

$$\mathbf{R}(\delta) = \begin{bmatrix} \cos\delta & \sin\delta \\ -\sin\delta & \cos\delta \end{bmatrix} \tag{4.10}$$

$$\mathbf{x}_{\mathrm{TE}} = [1, 0]^{\mathsf{T}}$$

$$\mathbf{x}_r = [x_r, y_r]^{\mathsf{T}}\ .$$

The upper side contour crosses the rotated trailing edge point $\mathbf{x}_f$ when N_4 is set to:

$$N_4 = \frac{y_f}{x_f^2}. \tag{4.11}$$

For obtaining the upper side contour of the airfoil at zero flap deflection, the parameterized contour given by eq. 4.12 first must be rotated back to zero degree flap deflection angle by $-\delta_{f,0}$ around the flap hinge point (eq. 4.12):

$$\mathbf{x}_{u,0} = \mathbf{R}(-\delta_{f,0})\ (\mathbf{x}_{u,d} - \mathbf{x}_r) + \mathbf{x}_r, \tag{4.12}$$

where

$$\mathbf{x}_{u,0} = \begin{Bmatrix} x_0(x) \\ y_{u,0}(x) \end{Bmatrix} \quad , \quad \mathbf{x}_{u,d} = \begin{Bmatrix} x \\ y_{u,d}(x) \end{Bmatrix}. \tag{4.13}$$

$\mathbf{x}_{u,0}$ then gives:

$$\mathbf{x}_{u,0} = \begin{Bmatrix} (x - x_r)\cos\delta_{f,0} - \big(C(x)\ S(x) + N_3\ x^2 + N_4\ x^2\big)\sin\delta_{f,0} + x_r \\ (x - x_r)\sin\delta_{f,0} + \big(C(x)\ S(x) + N_3\ x^2 + N_4\ x^2\big)\cos\delta_{f,0} + y_r \end{Bmatrix}, \tag{4.14}$$

where $\cos(-\delta) = \cos(\delta)$ and $\sin(-\delta) = -\sin(\delta)$ have been used. The crossing point between both contours can be found, where $y_{u,0} = y_{u,d}$. Therefore the x - location of the crossing point x_c has to be found, which can be obtained by solving eq. 4.15 with a root finding algorithm:

$$(x - x_r)\sin\delta_{f,0} + \Big(C(x)\ S(x) + N_3\ x^2 + N_4\ x^2\Big)\Big(\cos\delta_{f,0} - 1\Big) - x_r\cos\delta_{f,0} + y_r = 0. \tag{4.15}$$

The airfoil upper surface contour then is given as:

$$\mathbf{x}_u = \begin{cases} \mathbf{x}_{u,d} & \text{if} \quad 0 \leq x \leq x_c \\ \mathbf{x}_{u,0} & \text{if} \quad x_c < x \leq 1 \end{cases}. \tag{4.16}$$

This approach reduces to the standard CST method when $\delta_{f,0} = 0$, resulting in $N_4 = 0$. The procedure is visualized in fig. 4.4 for a ten parameter best-fit CST-representation of the DU89-134-14 airfoil. The class function (left) is the same for both the upper and the lower surface. The design variables are calculated for a best-fit of the contour. The airfoil upper side contour $\mathbf{x}_{u,d}$ at design flap setting is shown as a red line in the right plot. The de-rotated upper side contour $\mathbf{x}_{u,d}$ at zero degree flap setting contour given by eq. 4.12 is shown as a green line. The resulting airfoil contour defined by the distinction of cases in eq. 4.16 is defined by the non-transparent segments of both curves. The kink on the upper side contour can be clearly seen near the flap hinge axis $\mathbf{x}_r = \{0.86, -0.004\}^T$, shown as a green cross.
The parameterization of the airfoil y coordinates for m points, with $1 \leq i_{\text{LE}}$ being the indices of the upper side and $i_{\text{LE}} < m$ being the indices of the lower side points can alternatively be written as:

$$\mathbf{y} = \mathbf{M}\ \mathbf{d} + \mathbf{c}_3 + \mathbf{c}_4, \tag{4.17}$$

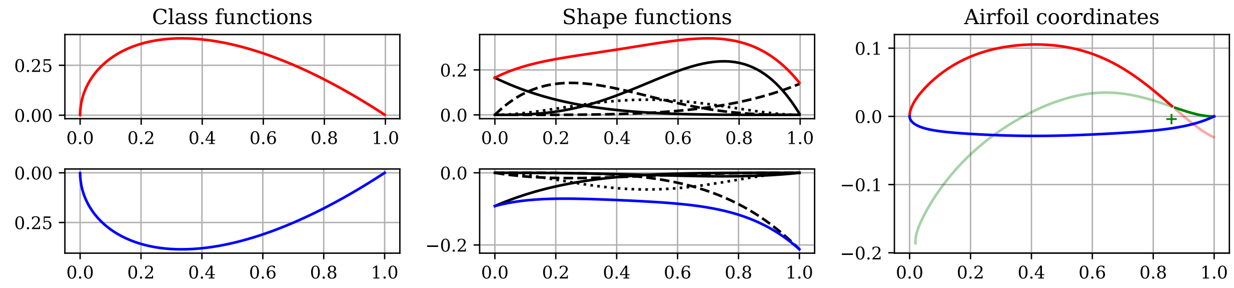

Figure 4.4: 10 parameter CST representation of DU89-134-14 airfoil with Boermans-Waibel type kink on the upper side. Class function (left), shape functions for upper and lower side (middle) and resulting airfoil shape (right)

where

$$\mathbf{M} = \begin{bmatrix} M_{00} & M_{01} & \cdots & M_{0n} \\ M_{10} & M_{11} & \cdots & M_{1n} \\ \vdots & & \ddots & \vdots \\ M_{m0} & M_{m1}(\overline{x}) & \cdots & M_{mn} \end{bmatrix}, \quad \mathbf{c}_3 = N_3 \begin{Bmatrix} x_0^2 \\ x_1^2 \\ \vdots \\ x_{\mathrm{LE}}^2 \\ -x_{LE+1}^2 \\ \vdots \\ -x_m{}^2 \end{Bmatrix}, \quad \mathbf{c}_4 = N_4 \begin{Bmatrix} x_0^2 \\ x_1^2 \\ \vdots \\ x_{\mathrm{LE}}^2 \\ 0 \\ \vdots \\ 0 \end{Bmatrix}, \tag{4.18}$$

and

$$M_{ij} = C(x_i) K_{j,n} x_i^j (1 - x_i)^{n-j}. \tag{4.19}$$

For finding the $n+1$ design variables d_i for $m+1$ given airfoil coordinates $\mathbf{x}_g$, the L^2-norm of the residual vector of the difference between the given airfoil coordinates y_g and the y-coordinates of the CST parameterization given in eq. 4.20 has to be minimized. It is noted that the upper side coordinates of the flap part of the given target airfoil y_g have to be rotated by the design flap angle $\delta_{f,0}$. Here, the singular value decomposition (SVD) is used for the minimization of the following expression:

$$\min_{\mathbf{d}} \|\mathbf{y}_g - \mathbf{y}\left(\mathbf{d}, \mathbf{x}\right)\|_2, \tag{4.20}$$

where

$$\mathbf{y}_g = \begin{Bmatrix} y_0(x_0) \\ y_1(x_1) \\ \vdots \\ y_m(x_m) \end{Bmatrix}. \tag{4.21}$$

Fig. 4.5 shows the log of the root mean square (RMS) error of CST representations of the DU89-134-14 airfoil over the number of CST parameters for the standard CST versus the *kinked flapped airfoil* approach. The CST representation of the airfoil with the *kinked flapped airfoil* methodology

($\delta_{f,0} = 12.5°$) shows approximately only half the error compared to the standard CST representation ($\delta_{f,0} = 0$) over the useful range of CST variables. Kulfan and Bussoletti [63] discuss the effect of geometric errors of airfoils on lift and drag for wind tunnel measurements. They conclude, that L/D converged to within $\approx 2\%$ error, if the deviation of the airfoil contour is less than 4×10^{-4} for the forward 20% of the chord length and 8×10^{-4} for the rearward 80%. For a RMS deviation of less than 4×10^{-4} at least 24 CST parameters are required with the standard CST representation, whereas only 14 CST parameters are needed with the *kinked flapped airfoil* methodology. Less parameters, i.e. design variables result in faster convergence rate and a reduced likelihood of ill-conditioning of the parameterization matrix and in consequence reduced chance of hitting non-optimal local minima. Therefore it is decided, that the *kinked flapped airfoil* methodology is used with 18 CST parameters for the baseline airfoil geometry parameterization in this work. This is a good compromise between fidelity and conditioning.

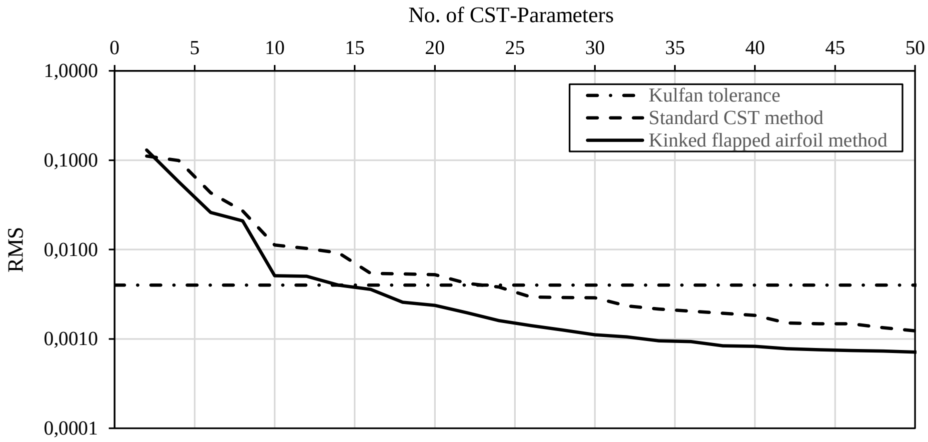

Figure 4.5: RMS error versus number of CST parameters for the approximation of the DU89-134-14 airfoil

4.3.3 *Extensions to the CST method for a morphing droopnose*

The parameterization of the morphing of the forward section is performed by adding a change to the camber line and the thickness distribution. The change in camber c and thickness t is parameterized using the CST method, but with different class functions. The camber line and the thickness distribution must be calculated from the baseline airfoil. It is desired that the leading edge region undergoes a rigid body motion only, and the leading edge must rotate with the camber line. Hence the thickness is defined to be normal to the camber line as in Abbott and von Doenhoff [2]:

$$x_u = x - t(x)\sin\theta \tag{4.22}$$
$$y_u = c(x) + t(x)\cos\theta \tag{4.23}$$
$$x_l = x + t(x)\sin\theta \tag{4.24}$$
$$y_l = c(x) - t(x)\cos\theta, \tag{4.25}$$

where:

$$\theta = \tan^{-1}\left(\frac{dc}{dx}\right). \tag{4.26}$$

In the classical approach, the thickness is the difference between the upper surface and the lower surface at a given x-coordinate and the camber line is halfway between the upper surface contour and the lower surface contour. Hence the thickness distribution and the camber line can be directly calculated from the airfoil coordinates. If the thickness distribution and the camber line are defined according to eqs. 4.23 – 4.26, the dependence of the camber line and the thickness distribution to the airfoil coordinates is nonlinear. Thus, calculating the camber line and thickness from the airfoil coordinates requires an iterative procedure. This is given in appendix B.

After the camber line and thickness distribution of the airfoil is calculated, morphing of the forward section can be performed by altering the camber line and thickness distribution. Here the CST approach is used for a perturbation function of the camber line and for a second one for the thickness distribution. First, the x-coordinates are scaled, because only a certain region of the airfoil should be deformed. The morphing region ends at x_e. As the leading edge should undergo a rigid body motion only, the camber line change has to be a straight tangent to the camber line change at x_s and the thickness distribution change has to be zero in the leading edge region reaching from $x = 0$ to $x = x_s$. The scaling of the x-coordinates is defined as:

$$\overline{x} = \frac{x_e - x}{x_e - x_s}. \tag{4.27}$$

For the camber line morphing, the following class function is used:

$$C_c = -2\overline{x}^3 + \overline{x}^4, \tag{4.28}$$

which has a constant slope at $\overline{x} = 0$ (i.e. beginning of the rigid airfoil region) and zero curvature at $\overline{x} = 1$ (i.e. beginning of rigid leading edge region). For the perturbation of the thickness distribution, a simple bell-shaped curve as the class function is used, thus enforcing the thickness change at the beginning and the end of the morphing region to be zero:

$$C_t = \overline{x}^2(\overline{x} - 1)^2. \tag{4.29}$$

As shape function the Bernstein polynomials according to eq. 4.6 are used, but as a function of the scaled x-coordinates $\overline{x}$. Again, the design variables d_i are used as coefficients for the shape functions. The morphed camber line is then given as:

$$c_m(\overline{x}) = c(\overline{x}) + \Delta c(\overline{x}), \tag{4.30}$$

with the change in camber:

$$\Delta c(\overline{x}) = \begin{cases} C_c(\overline{x})\ S_c(\overline{x}), & 0 \leq \overline{x} \leq 1, \\ \left.\frac{\mathrm{d}\Delta c(\overline{x})}{\mathrm{d}\overline{x}}\right|_{\overline{x}=1} (\overline{x} - 1) = \left[(-2-n)\ d_n + n\ d_{n-1}\right]\ (\overline{x} - 1), & \overline{x} > 1, \\ 0, & \text{otherwise}. \end{cases} \tag{4.31}$$

Note that the camber line change extends as a straight tangent for $\overline{x} > 1$. The morphed thickness distribution is given as:

$$t_m(\overline{x}) = t(\overline{x}) + \Delta t(\overline{x}), \tag{4.32}$$

with the change of thickness distribution:

$$\Delta t(\overline{x}) = C_t(\overline{x})\ S_t(\overline{x}). \tag{4.33}$$

After perturbation of the thickness distribution and the camber line, the airfoil has to be reassembled with the thickness distribution normal to the camber line according to equations 4.22 – 4.25, resulting in the morphed airfoil shape $y_{u,m}(x)$ and $y_{l,m}(x)$.

An overview of the procedure is shown in fig. 4.6, with $x_s = 0.05$ and $x_e = 0.4$. Here, three design variables with arbitrary values have been used for each altering the thickness distribution and the camber line. As mentioned in section 1.1, the leading edge of the airfoil should remain at the same curve length, starting at x_s at the upper surface. The camber line and the thickness distribution in y direction are altered, but the x coordinates are unchanged. Therefore, a geometrically linear mapping of the coordinates is obtained, which results in a change of the curve length. As a simple solution, the x coordinates between x_s and x_e are deformed using a cosine function, so that the curve length remains unchanged:

$$\tilde{x}(x) = \begin{cases} x + \Delta x_{\mathrm{LE}} & 0 \leq x \leq x_s \\ \frac{\Delta x_{\mathrm{LE}}}{2}\left(1 + \cos\left(\overline{x}\pi\right)\right) & x_s < x \leq x_e \\ x & x > x_e \end{cases} . \tag{4.34}$$

For determining Δx_{LE}, which is the displacement of the leading edge to the right, the morphed configuration of the airfoil is reassembled with variable Δx_{LE}. Then, a root search of the difference of the uncoiled length of the upper surface from x_e to the leading edge in morphed and in original configuration is performed:

$$\int_{t_{\mathrm{LE}}}^{t_e} \left(\frac{\partial x_m(\Delta x_{\mathrm{LE}})}{\partial t}\right)^2 + \left(\frac{\partial y_m(\Delta x_{\mathrm{LE}})}{\partial t}\right)^2 dt - \int_{t_{\mathrm{LE}}}^{t_e} \left(\frac{\partial x_o}{\partial t}\right)^2 + \left(\frac{\partial y_o}{\partial t}\right)^2 dt = 0. \tag{4.35}$$

A parametric spline representation for the coordinates of the airfoil in morphed and in undeformed configuration is used. For finding Δx_{LE} that solves eq. 4.35, a simple bisection algorithm is applied.

When parameterizing the forward section morphing, the number of design variables must be carefully selected. Preliminary studies indicate that using three design variables each for camber line modification and thickness distribution provides an optimal balance between the quality of optimization results, computational efficiency, and minimizing the risk of converging to local minima.

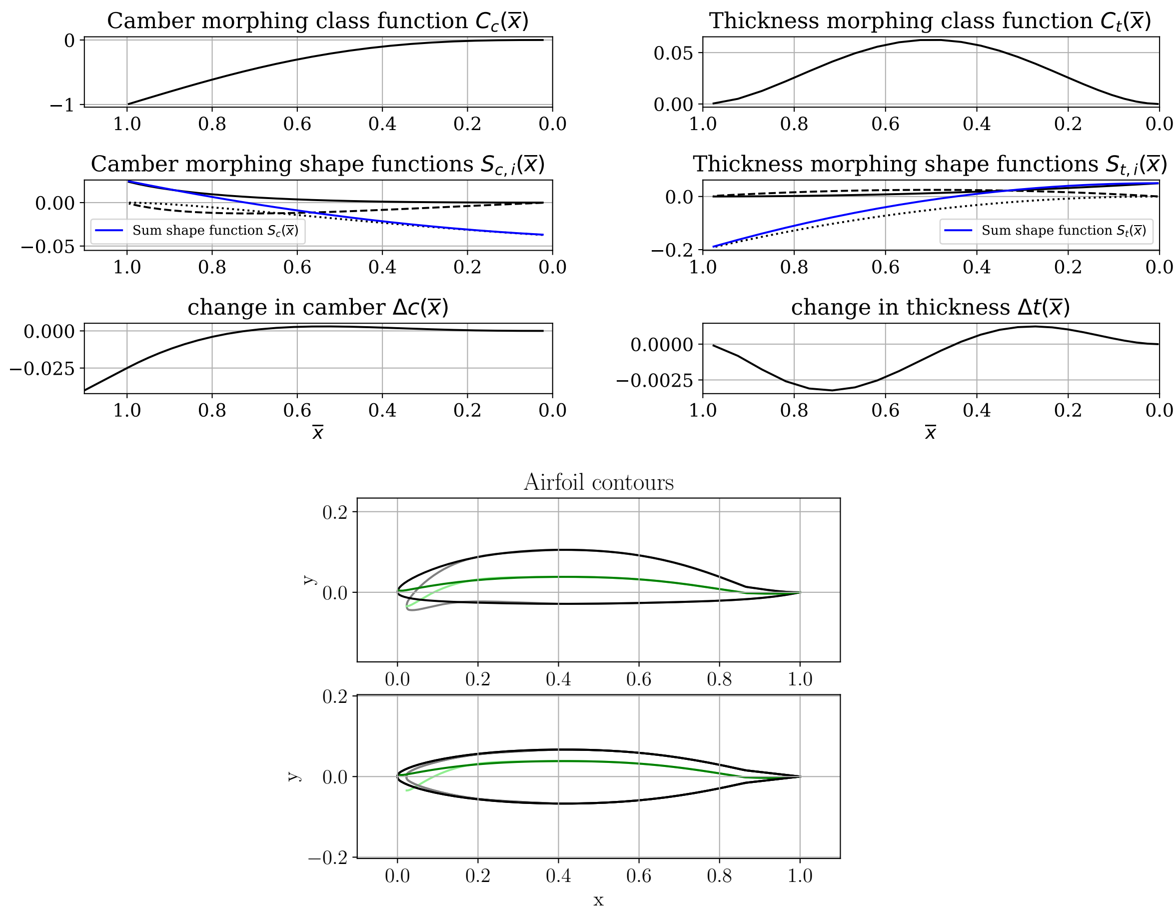

Figure 4.6: Class and shape functions for camber line (top left) and thickness distribution change (top right). Individual shape functions scaled by design variables d_i black, with sum shape functions blue and red. Resulting airfoil contour (bottom upper half) and camber line with thickness distribution (bottom lower half)

4.4 TWO-DIMENSIONAL FLOW SOLVERS – XFOIL-MOD AND XFOILSUC-MOD

In section 4.4.1, the two-dimensional flow solver *XFOIL* is introduced, which is the baseline for the two-dimensional flow solvers used in this work. *XFOILSUC*, a derivative of *XFOIL*, employs the *improved van Ingen full e^N database method* [134]. This transition prediction method shows improved precision compared to the simple *envelope method* used in *XFOIL*. Both transition prediction methods are introduced in section 4.4.2. Modifications on the turbulent closure relations can improve the prediction of the maximum lift. These modifications are shown in section 4.4.2.5 and are implemented both in *XFOIL* and *XFOILSUC* by the author for this work. The solvers are then designated as *XFOIL-mod* and *XFOILSUC-mod*. Finally, limitations of the solvers and possible mitigation strategies are discussed in section 4.4.3.

4.4.1 *Integral boundary layer solver XFOIL*

XFOIL is a widely recognized computational tool developed primarily for the analysis and design of subsonic isolated single element airfoils. Conceived by Professor Mark Drela [29] at the Massachusetts Institute of Technology, XFOIL has become a very important tool for aerodynamicists, aircraft designers, and researchers in the field of fluid dynamics.

XFOIL employs a linear-vorticity panel method for solving the inviscid outer flow outside of the boundary layer of the airfoil. A viscous solution incorporating the boundary layer development is obtained with an integral boundary layer formulation. For that, a two-equation lagged dissipation integral method is used, considering both laminar and turbulent boundary layers. Also laminar separation bubbles, which play a significant role in the prediction of lift and drag of low Reynolds number airfoils are considered. Laminar-turbulent transition is determined using a simplified e^N criterion, the envelope transition criterion, which is discussed into detail in section 4.4.2.2. The panel equations and the integral boundary layer equations are coupled via a constant strength source distribution on the surface panels and in the wake. They are solved simultaneously via an iterative Newton-Raphson method.

One of the standout features of XFOIL is its capability to design airfoil shapes directly and by inverse calculation from an inviscid pressure distribution. Users can modify existing airfoil geometries or create new ones from scratch, and then analyze their performance under various conditions. The software allows to calculate airfoil polars, which include lift, drag, and moment coefficients over a range of angles of attack.

The user-friendly interface, combined with its powerful analytical capabilities, has made XFOIL a preferred choice for both preliminary design evaluations and in-depth aerodynamic studies. Its open-source nature has further facilitated its widespread adoption and adaptation in various research and industrial applications.

4.4.2 *Laminar-turbulent transition modeling: e^N method*

As turbulent skin friction and transitional separation bubbles play the dominant role for the profile drag of low Reynolds number airfoils (c.f. Drela [31]), the precise and reliable prediction of the transition location is crucial for accurate drag calculation. Laminar-turbulent transition occurs caused by instability mechanisms in the boundary-layer. Morovkin et al. [82] showed that depending on the free-stream disturbance level five different instability mechanisms exist. The mechanism, which leads to transition at the lowest disturbance levels is the Tollmien-Schlichting type transition. The mechanism is illustrated in fig. 4.7. Free-stream disturbances (turbulence, sound) are transferred into initial disturbances in the boundary-layer, designated as Tollmien-Schlichting waves. This transfer process is called leading edge receptivity, it occurs on the leading edge close to the stagnation point [104]. Below a certain critical boundary-layer thickness, defined by the critical displacement thickness Reynolds number $Re_{\theta,o}$, this disturbances first decay exponentially. When the boundary-layer thickness exceeds the critical value at a certain downstream location, the disturbances are amplified exponentially from there on. This initial growth of the primary modes can be described with linear theory and is described in section 4.4.2.1. If a certain disturbance level is exceeded ($Tu > 1\%$ or $N_{\text{crit}} > 7$), nonlinear effects cause secondary growth of the disturbances. The dominant form of this nonlinear stadium are lambda-vortices. These vortices have the shape of the symbol Λ with the tip pointing downstream. The lambda vortices form hairpin vortices at their downstream tip, which break down to turbulent spots and subsequently fully turbulent flow. The processes from first nonlinear effects to full turbulence occur within short run length. Hence the laminar-turbulent transition location can be well determined in most low disturbance level cases using the linear stability theory.

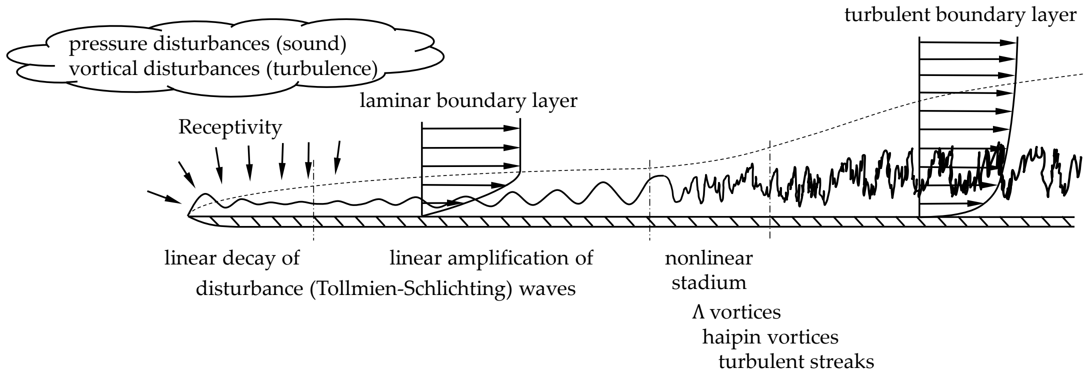

Figure 4.7: schematic illustration of the laminar-turbulent transition on a flat plate. Own figure based on [70]

In this section, the two different linear stability methods, which are used in this thesis for transition prediction are introduced. These are the *envelope method*, based on the theory of Gleyzes et al. [43] and implemented in *XFOIL* by Drela [29] and the *improved van Ingen method* [135], implemented in *XFOILSUC*. Both methods are fast database methods based on the linear stability theory, which itself has it's foundation in the Orr–Sommerfeld equation, introduced in section 4.4.2.1. The simplified *envelope method* is introduced in section 4.4.2.2. It has deficiencies in non self-similar flows (varying H), as also shown in that section. These problems are eliminated by the *improved van Ingen method*, as introduced in section 4.4.2.3. Both methods share one important empirical constant, the critical amplification factor N_{crit}. It accounts for the free-stream disturbance level of the incoming flow, which influences the transition location. Thus, a careful calibration is essential, which is presented in section 4.4.2.4.

However, the linear stability theory has it's limits. If the free-stream disturbance level is high, other transition mechanisms dominate according to Morovkin et al. [82]. At higher disturbance levels, nonlinear effects directly drive the transition process and it comes to earlier transition compared to lower disturbance environments. The linear regime thus is bypassed, the process is called *bypass transition*. On sailplanes in flight, the free-stream disturbance level is too low for this effect to occur, so considering only Tollmien-Schlichting type instability is sufficient.

But also surface discontinuities as wing junctions or gap seals contribute to the transition process. The morphing wing concept of this thesis as shown in fig. 1.2 employs a Mylar tape sealing within the laminar regime on the bottom surface of the wing on the end of the morphing section and a second one on the trailing edge flap gap. As this sealings should not have crucial detrimental effects on the laminar boundary-layer by causing premature transition, this has to be analyzed in detail. This is done in section 4.4.3.2.

4.4.2.1 *Orr–Sommerfeld equation and linear stability theory*

The Orr–Sommerfeld equation describes the growth of Tollmien-Schlichting type instabilities in laminar boundary-layers. These grow exponentially and subsequently lead to laminar-turbulent transition. The derivation is performed by plugging a harmonic perturbation ansatz into the incompressible x-momentum Navier-Stokes equation and subsequent linearization. The Orr–Sommerfeld equation reads as:

$$(\hat{u} - \hat{c}_{TS}) \left[\Phi'' - (\hat{\alpha}\theta)^2\Phi\right] - \hat{u}''\Phi = \frac{-i}{\hat{\alpha}\theta Re_\theta)} \left[\Phi'''' - 2(\hat{\alpha}\theta)^2\Phi'' + (\hat{\alpha}\theta)^4\Phi\right], \tag{4.36}$$

where a prime $'$ denotes a partial derivative $\frac{\partial}{\partial y}$ and a $\hat{\square}$ symbolizes non-dimensionalizing the quantity by multiplication with the factor $\frac{\theta}{u_e}$. θ is the boundary layer displacement thickness and $\hat{c}$ is the Tollmien-Schlichting wave propagation speed. The Orr–Sommerfeld equation is an Eigenvalue problem with the Eigenvalues α and β and the Eigenvector $u(y)$ and the perturbation amplitude $\Phi(y)$. It can be solved, if a base flow profile $u(y)$ is given. The actual value of Φ is irrelevant for solving the equation and is normalized to unity. In the approach used in *XFOIL-mod* and *XFOILSUC-mod*, the spatial version of the linear stability theory is used. In this, the wave number is complex $\hat{\alpha} = \hat{\alpha}_r + i\hat{\alpha}_i$ and the frequency is real $\hat{\beta} = \hat{\beta}_r = \omega$. The sign of $\hat{\alpha}_i$ determines, if the disturbance is stable ($\hat{\alpha}_i > 0$), neutrally stable ($\hat{\alpha}_i = 0$) or unstable ($\hat{\alpha}_i < 0$). Stability diagrams can be derived for known velocity profiles.

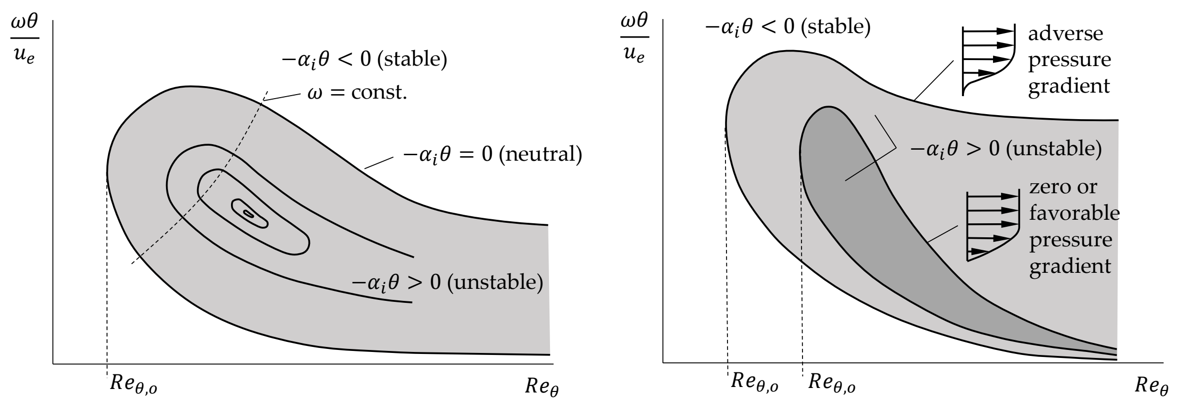

(a) Principle of the stability diagram

(b) Neutral curve for flows with & w/o inflection point

Figure 4.8: Stability diagrams

In fig. 4.8a, an exemplary stability diagram is shown. The horizontal axis is the momentum loss thickness Reynolds number:

$$Re_\theta = \frac{u_e\theta}{\nu}, \tag{4.37}$$

with the velocity at the edge of the boundary layer u_e and the momentum loss thickness of the boundary layer θ. The vertical axis is the non-dimensional frequency:

$$\hat{\omega} = \frac{\omega\theta}{u_e}. \tag{4.38}$$

The neutral curve is where the amplification α_i is zero. Inside the neutral curves, α_i is negative and hence amplification of the Tollmien-Schlichting waves occurs. Furthermore it can be seen that below a certain boundary-layer thickness no amplification is present. This is denoted as the critical Reynolds number $Re_{\theta,o}$. In the fig. 4.8b, the different characteristics of stability diagrams are shown, depending if the boundary-layer has an inflection point or not. This is the case if an adverse pressure gradient exists, i.e. $H = \frac{\delta^*}{\theta} > 2.59$, with the boundary layer displacement thickness δ^*. In this case, the neutral curve is open for high values of Re_θ, indicating amplification in a wide frequency range for thick boundary-layers. In case of accelerated flow, i.e. pressure decrease, the boundary-layer is mostly stable, except in a smaller frequency and thickness range. Furthermore, the critical boundary-layer thickness is higher than in the case of occurrence of an inflection point. Amplification curves for the Hartree velocity solutions of the Falkner-Skan laminar boundary-layer family for a wide range of shape factors are calculated by Arnal [9]. These are used in the *improved van Ingen method*.

Smith and Gamberoni [113] and independently van Ingen [133] derived an equation that governs the growth or decay of Tollmien-Schlichting waves based on local amplification ratios. The method is called the e^9 or e^N method. In this, the logarithmic amplification rates are integrated in streamwise direction, beginning at s_0, the streamwise location of the occurrence of the first instability ($Re_\theta > Re_{\theta,o}$):

$$\ln\left(\frac{a(s,\omega)}{a_0}\right) = \int_{s_0}^{s} -\alpha_i(\omega)\,\mathrm{d}s. \tag{4.39}$$

Because the initial amplitude a_0 is unknown, a strategy for solving the problem is to assume an arbitrary initial amplitude. Then, the N-factor, a measure for the amplification ratio can be defined:

$$N(\omega,s) = \ln\left(\frac{a(s,\omega)}{a_0}\right) = \int_{s_0}^{s} -\alpha_i(\omega,s)\,\mathrm{d}s. \tag{4.40}$$

It can be converted to a non-dimensional form:

$$N(\omega,\bar{s}) = \frac{U_\infty \bar{c}}{v} \cdot \int_{\bar{s}_0}^{\bar{s}} T(\omega,s)\hat{U}\,\mathrm{d}\bar{s}, \tag{4.41}$$

with:

$$T = \frac{-\alpha_i(\omega,s)\theta(s)}{Re_\theta(s)} \tag{4.42}$$

$$\hat{U} = \frac{u_e(s)}{U_\infty} \tag{4.43}$$

$$Re_\theta = \frac{u_e(s)\theta(s)}{\nu} \tag{4.44}$$

$$\mathrm{d}\bar{s} = \frac{1}{\bar{c}}\,\mathrm{d}s. \tag{4.45}$$

Neglecting secondary, nonlinear growth of instabilities and assuming instantaneous transition, a critical N-factor N_{crit} can be defined, which determines the transition location. The transition location is therefore defined, where the maximum of the N-factor of all frequencies equals the critical N-factor:

$$x_{tr} = \arg_{\bar{x}}\left(\max_{\omega}(N(\omega,\bar{s}(\bar{x}))) = N_{\text{crit}}\right). \tag{4.46}$$

Van Ingen suggested a critical N-factor of 9 for the onset of the turbulent regime. Thus, the method was initially called e^9 method. However, the choice of the critical N-factor, also denominated as N_{crit}, depends on the free-stream conditions and must be carefully calibrated. This is done in section 4.4.2.4.

4.4.2.2 *Envelope* e^N *method*

The envelope method does not calculate the amplification factor for all tracked frequencies ω, but approximates the envelope amplification factor, which is the maximum amplification factor of all frequencies at a given streamwise coordinate $\bar{x}$:

$$\tilde{N}(s) = \max_{\omega} \left(N(\omega, s) \right) . \tag{4.47}$$

The envelope method is developed by Drela and Giles [34] for the coupled Euler–integral boundary-layer code *ISES* and is based on work from Gleyzes et al. [43], who solve the spatial Orr–Sommerfeld equation for Falkner-Skan boundary-layers for a series of different frequencies. Drela and Giles have observed that the envelopes $\tilde{N}$ of the amplification curves for constant shape factors H as a function of Re_θ can be approximated well with straight lines (see fig. 4.9).

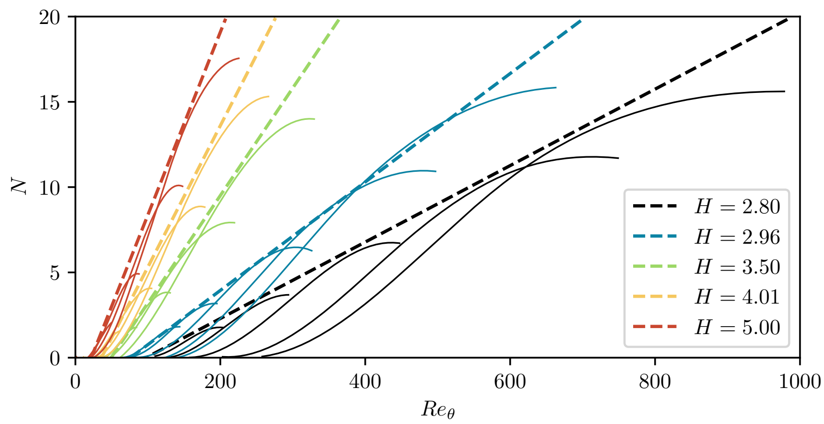

Figure 4.9: Amplification curves for constant H Falkner-Skan boundary-layers as a function of Re_θ. The solid lines show the individual amplification rates for constant shape factor H with different frequencies ω and the dashed lines show the constant envelope amplification rates $\tilde{N}$. Own figure based on [35]

Drela and Giles point out that the Re_θ parameterization is not well-suited for predicting the transition within laminar separation bubbles, because Re_θ is almost constant within these. This implies that almost no amplification exists within bubbles, which is clearly not the case. As a solution, they suggest to parameterize the growth rate f_{TS} of the envelope amplification curves with the streamwise coordinate s. This is possible, because the momentum thickness Reynolds number Re_θ grows monotonically with the streamwise coordinate $\bar{x}$ for self-similar (constant H) Falkner-Skan boundary-layers. The amplification of the envelope $\tilde{N}(s)$ is calculated as:

$$\begin{aligned} \log\frac{a}{a_0} &= (\tilde{N}(s)) \\ \tilde{N}(s) &= \int_0^s \frac{\mathrm{d}\tilde{N}}{\mathrm{d}s}\,\mathrm{d}s' \\ \text{where } \frac{\mathrm{d}\tilde{N}}{\mathrm{d}s} &= \begin{cases} 0, & Re_\theta < Re_{\theta_o}(H) \text{ (stable)} \\ \frac{1}{\theta}\, f_{\mathrm{TS}}(H), & Re_\theta > Re_{\theta_o}(H) \text{ (unstable)} \end{cases} \end{aligned} \quad . \tag{4.48}$$

The envelope growth rate, f_{TS}, and the critical Reynolds number, Re_{θ_o} in dependence of the shape factor H are shown in fig. 4.10. The envelope growth rate, f_{TS} is based on the constant envelope amplification rates of fig. 4.9. The spline functions for f_{TS} and Re_{θ_o} as shown in fig. 4.9 are given in ref. [17].

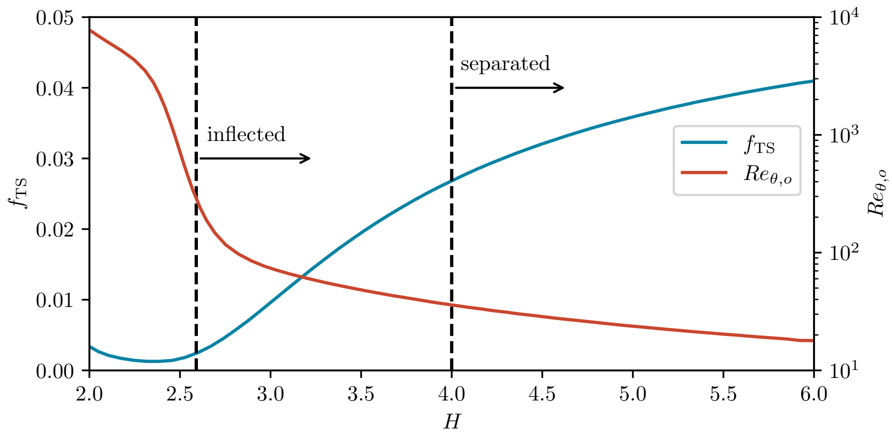

Figure 4.10: Envelope amplification ratio, f_{TS}, (top) and critical Reynolds number, $Re_{\theta,o}$. Own figure based on [33]

As shown by Dini [27], the linear envelope growth assumption only holds for constant H boundary-layers and hence the envelope method is only correct for these. Bongers [17] shows that substantial differences in the transition location exists between the envelope method and the full e^N method. The morphing airfoils optimized with the method presented in this work show a dump in the top side pressure distribution in undeformed configuration at the end of the morphing region at α values just below the upper corner of the laminar low-drag region. This means that the Tollmien-Schlichting waves are amplified in the first deceleration region, but then damped again, before the final amplification begins, which ultimately leads to transition. The damping followed after the initial amplification can not be predicted by the envelope method. This is, because the f_{TS} curve as shown in fig. 4.10 is strictly positive. In chapter 4.4.2.4, the envelope method and the improved van Ingen full e^N method are compared to transition locations obtained from wind tunnel measurements. It is shown that the full e^N method fits the measured transition curves more precisely within the laminar low-drag region. However, it can also be seen, that the lower corner of the laminar low-drag region is predicted more precisely with the envelope method. Therefore, the envelope method is also used in this work.

4.4.2.3 *Improved van Ingen full e^N database method*

The envelope method calculates only an approximate for the envelope amplification factor $\tilde{N}$ and hence neglects the dependence of the amplification factor N on the frequency ω. Contrary to this, the improved van Ingen full e^N database method considers a great number of Tollmien-Schlichting wave frequencies in a broad frequency range. The method is presented in detail in references [17], [135] and [135]. It is based on 15 stability diagrams for Falkner-Skan boundary-layers with different shape factors H published by Arnal [9]. It is a database method, meaning that the stability information is stored in a database using splines and characteristic parameters and does not need to be calculated from the Orr–Sommerfeld solutions calculated during run time. This avoids significant additional computational effort. In the improved van Ingen method, the assumption is made that the boundary-layer stability diagrams are almost self-similar, when proper shifting and scaling is applied. This facilitates and precises interpolation between data points to calculate the amplification rate, T.

The Arnal stability diagrams, as shown in figure 4.8, give the amplification ratio $\alpha_i\theta$ in dependence of the boundary layer momentum-loss thickness Reynolds number Re_θ and non-dimensional frequency $\frac{\omega\delta^*}{u_e}$. The stability diagrams are scaled and shifted using basic Falkner-Skan boundary-layer properties. After scaling and shifting, the data is interpolated with splines to obtain the amplification rate T as a function of the boundary-layer thickness Reynolds number Re_θ and the Tollmien-Schlichting wave frequency $\frac{\omega\theta}{Re_\theta}$. The critical Reynolds number Re_{θ_o} defines the onset of the unstable region and can be taken from the Arnal stability diagrams. It depends solely on the shape factor H. The dependence is shown in fig. 4.11 for the van Ingen full e^N method and the envelope method (repeated from fig. 4.10). Although both curves should theoretically be identical, they interestingly differ slightly. Particularly at shape factors $H < 2.2$ and $H > 3$ with reasons unknown.

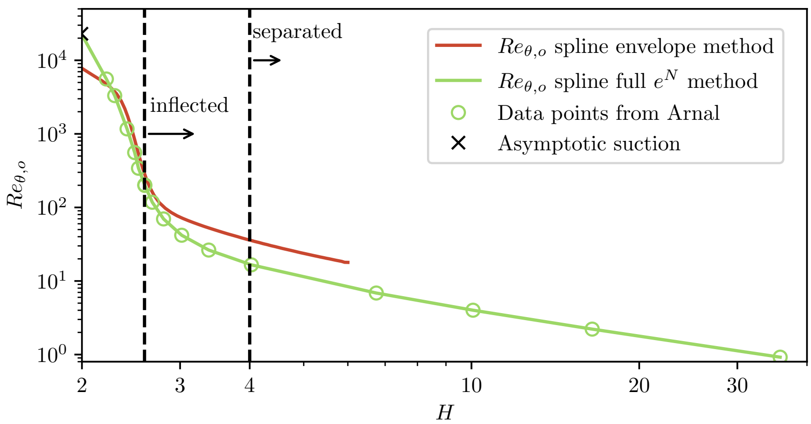

Figure 4.11: Critical Reynolds number $Re_{\theta,o}$ as splined for the improved van Ingen method, from [17]

Scaling, shifting and interpolation is performed as follows: Van Ingen [135] shows, that the interpolation of the stability diagrams can be improved, if they are properly scaled and shifted. He proposes a scaling for the Re_θ axis of the stability diagram, introducing the scaled and shifted non-dimensional value r:

$$r = \log\left(Re_\theta\right) - \log\left(Re_{\theta_o}\right). \tag{4.49}$$

The neutral curve ($T = -\alpha_i\theta = 0$) for the Blasius zero pressure gradient boundary layer case using this scaling is shown in fig. 4.12. The neutral curve touches the vertical axis, because the critical Reynolds number Re_{θ_o} is subtracted in eq. 4.49. The location of the absolute maximum amplification rate in the diagram, which is further denoted as T_{maxmax}, is indicated as *top*, characterized by r_{top}. The line connecting the local maxima $T_{\max}(r)$ of the amplification rate for each r is denoted as *axis*. These characteristic properties of stability diagrams will be used for further scaling and shifting.

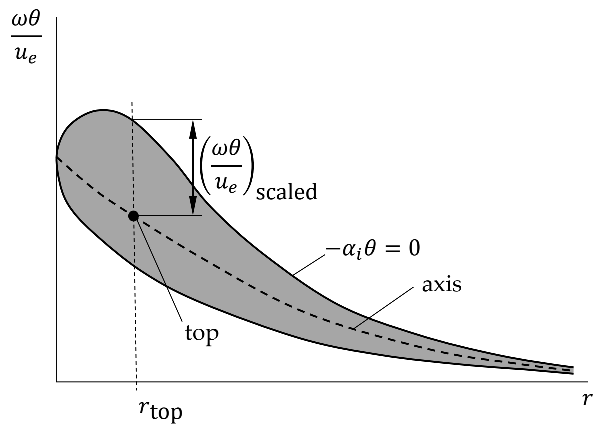

Figure 4.12: Neutral curve ($T = 0$) for the Blasius case with scaling of the Re_θ axis according to eq. 4.49. Own figure based on [17]

For the vertical axis, the following scaling is used:

$$\overline{\left(\frac{\omega\theta}{u_e}\right)} = \frac{\left(\frac{\omega\theta}{u_e}\right) - \left(\frac{\omega\theta}{u_e}\right)_{\text{top}}}{\left(\frac{\omega\theta}{u_e}\right)_{\text{scaled}}}. \tag{4.50}$$

The scaling value $\left(\frac{\omega\theta}{u_e}\right)_{\text{scaled}}$ is given for each of the 15 Arnal stability diagrams. Hence, it depends only on the shape factor H. The value for $\left(\frac{\omega\theta}{u_e}\right)_{\text{top}}$ which shifts the stability diagrams in the non-dimensionalized frequency direction, is defined as the *axis* in fig. 4.12. The axis in dependence of r for all 15 Arnal stability diagrams is shown in fig. 4.13. As can be seen, the axis can be approximated with good precision with a power law, indicated by a straight line in the double logarithmic $r - \frac{\omega\theta}{u_e^2}$ scale. However, this is only true, if no inflection point exists in the Falkner-Skan boundary-layer (green curves, Arnal cases 1 - 6). If an inflection point exists, the curve has a kink in the double logarithmic $r - \frac{\omega\theta}{u_e^2}$ scale (red curves, Arnal cases 7 - 15). The slope in the double logarithmic plot is $-\sqrt{2}$ in case of no inflection point and before the kink in case of an inflection point. After the kink, the slope is -1. Therefore, only one stored value is required for the database for cases without an inflection point and two values for the case with an inflection point. These are the offset of the curve $\frac{\omega\theta}{u_e^2}(r = 0)$ and the location of the kink if an inflection point exists.

Furthermore the stability information is shifted using:

$$\bar{T}\left(\frac{\omega\theta}{u_e}\right) = \frac{T(r, \frac{\omega\theta}{u_e}) - T_{\max}(r)}{T_{\text{maxmax}}}\ , \tag{4.51}$$

where $T_{\max}(r)$ is the maximum amplification depending on r, hence specifying the T values of the *axis*. It has been shown by van Ingen and Bongers that the maximum amplification factor along the axis can be approximated with very good precision using:

$$T_{\max} = \bar{r}e^{1-\bar{r}}, \tag{4.52}$$

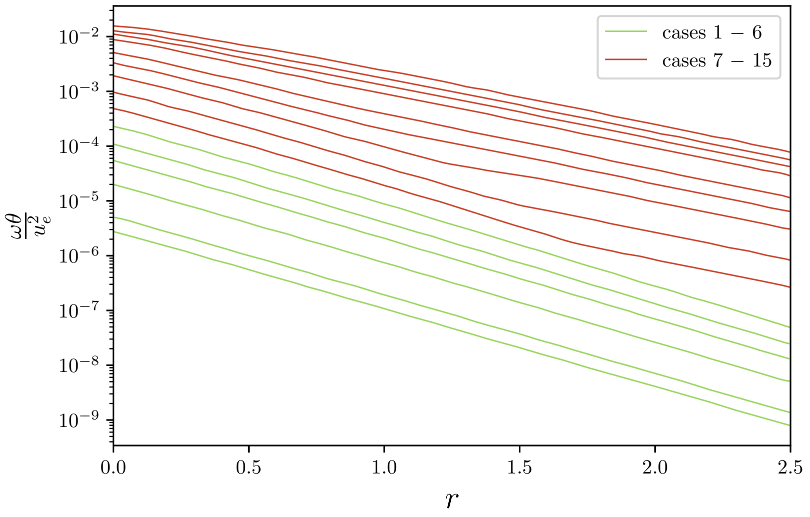

Figure 4.13: Axis of maximum amplification $T_{\max}$. Green lines: Boundary layers without inflection point ($H \leq 2.59$). Red lines: Boundary layers with inflection point ($H > 2.59$). Own figure based on [17]

where:

$$\bar{r} = \frac{r}{r_{\text{top}}}. \tag{4.53}$$

The information for r_{top} as a function of the shape factor H is stored in a spline. A graphical representation is given in [17]. With this shifting and scaling, the cross-cuts along the r axis becomes almost self-similar, as fig. 4.14 shows. Cross-cuts of the amplification $\bar{T}$ at constant r with varying $\overline{\left(\frac{\omega\theta}{u_e}\right)}$ are shown. As they are almost coincident, errors introduced by subsequent interpolation become small. $\bar{T}(H, \frac{\bar{\omega\theta}}{u_e}, r)$ is stored in a data base. Together with the data for Re_{θ_o}, the information about the *axis* location from fig. 4.13 and the information of $T_{\max}$, the amplification T is calculated using a quadratic Lagrange interpolation with the nearest data points.

The original intent for developing the *improved van Ingen e^N method* was to find a transition prediction, which allows to calculate the damping effect of boundary-layer suction on the Tollmien-Schlichting waves. For that purpose, it was investigated, if H can be used as a representative parameter for the stability diagrams of suction/blowing boundary-layers. van Ingen and Bongers found some evidence that H is a good choice for that purpose.

A very similar full e^N database method was implemented by Drela [31] in the integral boundary-layer/Euler code *MSES*. The underlying stability information was also scaled and shifted, but in a simpler way than in the work of van Ingen and Bongers. One computational advantage of Drela's method is that only one frequency is calculated for each airfoil side, which is the most amplified frequency at the transition location. This frequency is a variable in the calculation and is solved iteratively. Whereas in the *improved van Ingen e^N method*, 600 frequencies are calculated during each iteration and the most amplified at the transition location is considered. This not only increases the computational effort, but also leads to stability issues if the most amplified frequency jumps back and forth between iterations. However, *MSES* with the full e^N database method is not publicly available. Therefore, the *improved van Ingen method* is used in this work, which was made available by the *TU Delft*. Good convergence behavior is found, when the airfoil

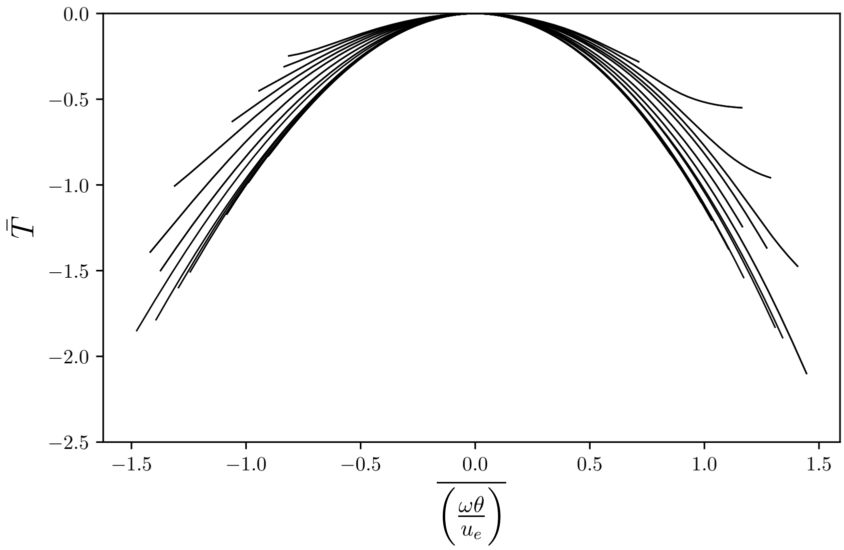

Figure 4.14: scaled and shifted cross-cuts of stability diagrams at constant r. Data from [134]

discretization is fine. In this work, 360 panels are used for the *improved van Ingen method*, whereas 260 panels are used for the *envelope method*.

4.4.2.4 *Calibration of the critical amplification factor*

The critical amplification factor is a measure for the free-stream disturbance level. The environmental disturbances are diverse. They can be distinguished between vortical (turbulence) and pressure (sound) disturbances. The disturbance frequency spectra can differ significantly between different environments. Vortical disturbances can be anisotropic in nature. Therefore it is difficult to correlate the critical amplification factor to quantities describing the free-stream disturbance level. Nevertheless, Mack [73] defined a correlation for N_{crit} based on the free-stream turbulence level $Tu = \frac{1}{U_\infty}\sqrt{\frac{1}{3}\left(|u'|^2 + |v'|^2 + |w'|^2\right)}$:

$$N_{\text{crit}} = \min\left(-8.43 - 2.4\ln(Tu), 9\right). \tag{4.54}$$

However this correlation is purely empirical, derived from flat-plate boundary layer flow transition location measurements at different turbulence levels. Saric [104] pointed out that the vortical parts of the free-stream disturbance (turbulence) dominate the three-dimensional aspects of the breakdown process and the irrotational parts of the free-stream disturbances (sound) dominate the initial amplitudes of the two-dimensional Tollmien-Schlichting waves. As the Tollmien-Schlichting wave growth predominately determines the transition location, sound disturbances seem to drive the initial disturbance level and hence the N_{crit} value. It this light, Mack's correlation is highly questionable, because it correlates N_{crit} to the wind tunnel turbulence level.

A more straightforward approach is to calibrate the N_{crit} value to experimental results. In-flight measurement results, which would allow to set the critical amplification factor to realistic operating conditions, are rather scarce. Such are done by Horstmann et al. [53] and documented by Althaus [6]. However, in the first paper, the airfoil coordinates are not published, whereas in the latter no transition locations are measured. It must be accepted, that the N_{crit} can not be correlated to in-flight free-stream conditions with available data. Therefore, one must rely on wind-tunnel experiments. Correlation of the critical amplification factor to transition locations in this work is done by comparing transition curves of wind tunnel measurements and *XFOIL-mod* and *XFOILSUC-mod* calculations. At least, this allows to correlate the computational results with the disturbance environment in one specific wind tunnel.

The *AH 93-157* is a typical laminar airfoil designed for the Reynolds number range of sailplane main wing airfoils with a laminar rooftop pressure distribution and a bubble-type transition ramp on the upper surface, which makes it well suited as a calibration reference. Wind tunnel measurements were performed in the Stuttgart laminar wind tunnel by Althaus [7]. Data of transition locations is available for $Re = 1.5 \times 10^6$.

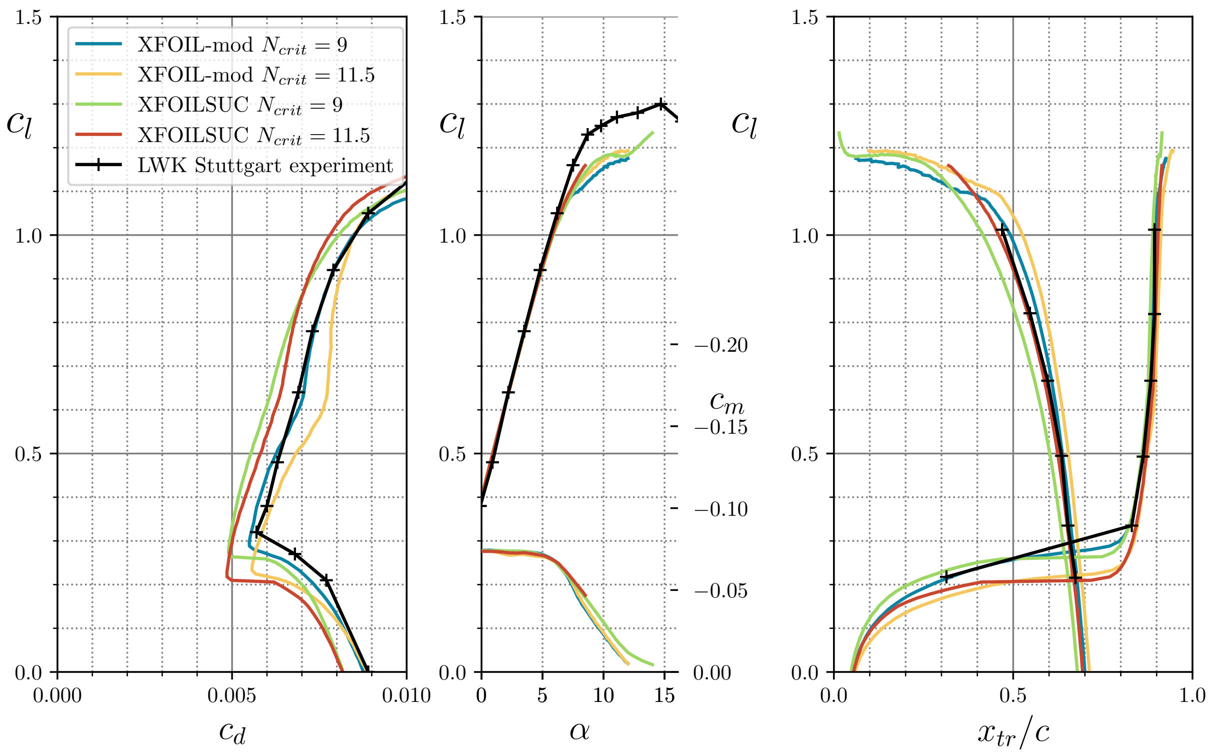

Figure 4.15: Stuttgart laminar wind tunnel measurements and calculated polars and transition curves of *AH 93-157* airfoil at $Re = 1.5 \times 10^6$

The measured lift-drag curve, lift curve and transition locations as well as simulation results obtained with *XFOIL-mod* and *XFOILSUC-mod* using different N_{crit} values are shown in fig. 4.15. The full e^N method and $N_{\text{crit}} = 11.5$ shows the best match of the transition curve for the upper and lower surface within the laminar low-drag region. The lower corner of the laminar low-drag region is predicted at too low c_l values, probably due to the appearance of a suction spike on the lower surface of the airfoil at low lift coefficients.

For the envelope method, the closest correlation was obtained with $N_{\text{crit}} = 9$, also closely corresponding to Mack's correlation [73] accounting for the turbulence level [7] of the Stuttgart laminar wind tunnel. The envelope method with $N_{\text{crit}} = 9$ shows the best agreement with the experimental results regarding the lower corner of the laminar low-drag region. Flapped airfoils are thinner than airfoils without flaps and therefore also have a smaller leading edge radius and a more pronounced suction peak when approaching the angle of attack of the lower corner of the laminar low-drag region. Therefore it is advised to calibrate the N_{crit} factor for the lower surface with measurements of a flapped laminar airfoil. Transition curves for flapped airfoils used on sailplanes are published by Althaus in the *Stuttgarter Profilkatalog II* [7]. Unfortunately, the resolution of the transition curves shown in this reference is too coarse at angles of attack near the corner of the laminar low-drag region. Modern flapped laminar airfoils used on sailplanes rely on

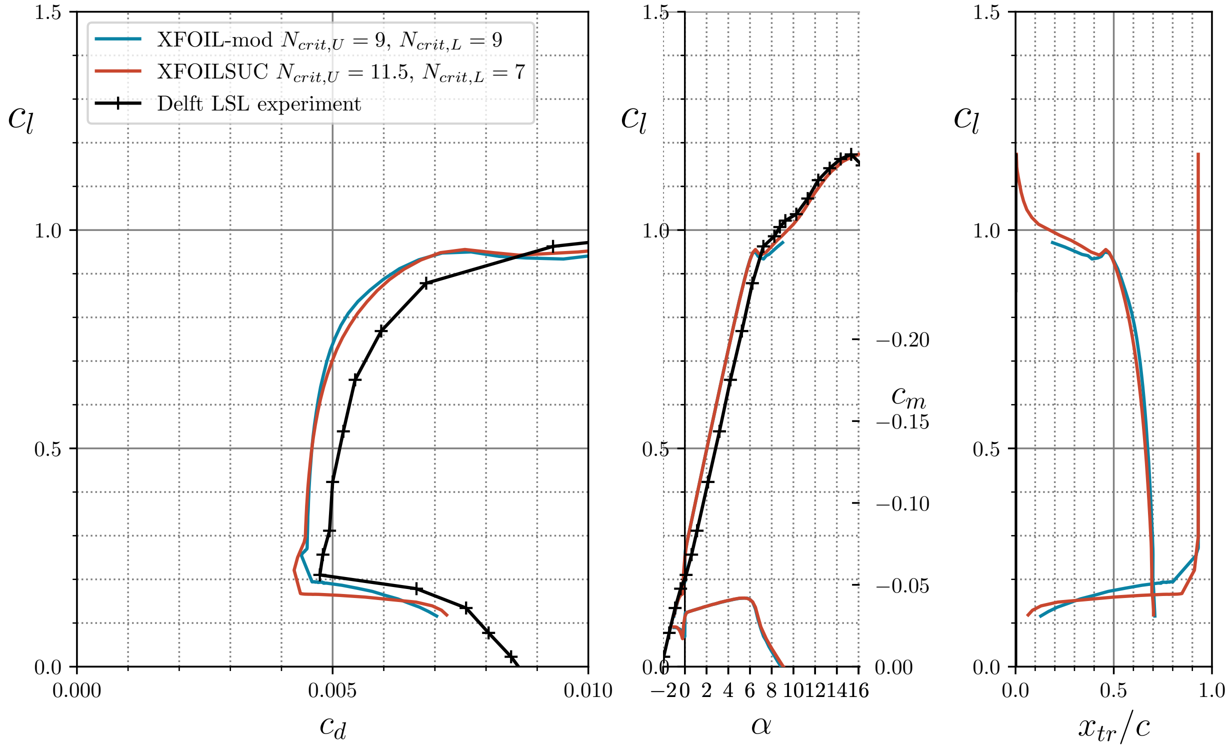

Figure 4.16: TU Delft LSL wind tunnel measurements and calculated polars of DU89-134-14 airfoil at $Re = 1.5 \times 10^6$

turbulators on the lower surface for laminar-turbulent boundary layer tripping and consequently avoiding laminar separation bubbles. The design philosophy incorporating such leads to designs with pronounced lower corners of the laminar low drag region. This indicates rapid forward movement of the transition location with decreasing angle of attack once the lower corner of the laminar low drag region is surpassed. Therefore the onset of forward movement of transition is the only point of interest. This can be clearly seen in the drag polar. For calibration of the $N_{crit,L}$ of the lower surface, the measured polars of the DU 89-134-14 airfoil [16] at $Re = 1.5 \times 10^6$ are used. The polars are shown in fig. 4.16.

The best correlations of the onset of forward movement of transition location corresponding with the lower corner of the laminar low-drag region is found for $N_{crit,L} = 7$ for *XFOILSUC-mod* with the full e^N method and for $N_{crit,L} = 9$ for *XFOIL-mod* utilizing the envelope method. Interestingly, $N_{crit,L}$ is significantly lower than $N_{crit,U}$ for the full e^N method. Drela [31], who implemented a full e^N method for the integral boundary-layer/Euler code *MSES* observed a similar behavior when analyzing the drag polar of the *Eppler 387* airfoil. Some evidence was found that this may be caused by increased receptivity at the leading edge region in case of a low pressure peak, as occurs close to the lower corner of the laminar low-drag region for the bottom side of the airfoil. Receptivity effects are stronger for smaller leading edge radii, as pointed out by Saric et al. [104], particularly when suction peaks occur. The leading edge radius is smaller for the lower surface. And on flapped laminar airfoils as used on sailplanes, a suction peak arises when the lower corner of the laminar low drag region is approached from within the laminar low drag region. This justifies the use of different N_{crit} values for the upper and the lower surface.

A second source for the differences in N_{crit} for the upper and lower surface could be an imprecision in the laminar boundary-layer calculation. Bongers [17] calculated the boundary-layer properties using *XFOILSUC* with the integral boundary-layer method and compared it to a finite difference method. He found significant differences of the amplification factor on the bottom surface of an airfoil with a flat plate (constant c_p) pressure distribution. Bongers concluded that the differences come from errors in the calculation of the laminar boundary-layer properties in *XFOILSUC*.

Both the increased receptivity effect as well as laminar boundary layer computation errors may play a role for the found differences in N_{crit} for the upper and lower surface. However, as shown in fig. 4.16, *XFOIL-mod* with the envelope method does not need different N_{crit} factors for the upper and the lower surface. It seems that it somehow counteracts the enhanced receptivity effect due to a smaller leading edge radius on the lower surface in combination with the occurrence of a low pressure spike.

As a consequence of these findings, the following procedure is used for the airfoil optimization:

- In the undeformed configuration at the lowest design lift coefficient, where a low pressure peak is suspected to occur at the bottom side, *XFOILSUC-mod* with the *full van Ingen e^N method* with $N_{crit,L} = 7$ and $N_{crit,U} = 11.5$ is used.

- For more robustness of the optimized airfoil w.r.t. suction spike occurrence, the result of *XFOIL-mod* and $N_{crit,L} = N_{crit,U} = 9$ with the envelope method is also considered.

- *XFOILSUC-mod* with the *full van Ingen e^N method* only with $N_{crit,L} = 7$ and $N_{crit,U} = 11.5$ for the upper design lift coefficient in undeformed configuration

- In the morphed configuration, it is not a priori clear, if a suction spike exists. If not, prediction of the transition location is most precise with the *full van Ingen e^N method* and $N_{crit,U} = N_{crit,L} = 11.5$. If a suction spike occurs, this setting would predict too late transition. For capturing that, the more robust envelope method with a lower weight and $N_{crit,L} = N_{crit,U} = 9$ is utilized.

4.4.2.5 *Improvements of turbulent closure relations for improved maximum lift prediction*

For wind turbines, the prediction of maximum lift of airfoils is very essential, because it directly influences their maximum achievable power output. As the Reynolds and Mach number regime is similar to that of sailplanes, Blade element momentum theory coupled with two-dimensional integral boundary-layer method airfoil analysis is very popular [28]. Therefore, numerous approaches have been undertaken to improve the prediction of maximum lift of airfoil sections [136] [96] [84] [122].

van Rooij [136] published some investigations on the turbulent closure relations for improving airfoil lift prediction. Accompanied by the consideration of rotational effects in the modeling of the turbulent flow, this results lead into the development of the integral boundary-layer code *RFOIL*, which is also based on the *XFOIL* source code. Some findings on the turbulent closure relations are reported. Van Rooij showed, that the *G*-β-locus parameters A & B have great influence on the start of turbulent separation and hence on the maximum lift value. This influence was exemplified by van Rooij by a thorough literature study and by comparing measurements of the *NLF(1)-0416* with simulations in *RFOIL* varying the parameters A and B. A similar study is done in this work using the *DU84-158* airfoil. The results are shown in fig. 4.17, which compares wind tunnel test results of the *DU84-158* with *XFOIL* results with varying *G*-β-locus parameters A & B. In the left plot, the measured polar in the Delft Low Speed Laboratory (LSL) wind tunnel is shown as a black curve. All other curves are polars calculated with *XFOIL*, with varying A and B values. The blue and the yellow curve show the polars with $B = \text{const} = 0.83$. Yellow has a high $A = 8.0$, whereas blue has a low $A = 5.5$. $c_{L,\max}$ decreases with an increasing A value. Comparing the green and the red curve, where $A = \text{const} = 6.75$, a decrease in $c_{L,\max}$ with increasing B value is obvious. The right plot shows the dependence of $c_{L,\max}$ on A and B. In the red curve, A is held constant. In the blue curve, B is constant. The measured $c_{L,\max}$ is shown as a horizontal dashed line. Increasing either A or B leads to a monotonic decrease of $c_{L,\max}$, as already indicated by the polars. For the *DU84-158*, $A = 6.75$ and $B = 1.0$ or $A = 7.6$ and $B = 0.83$ would be a good choice. Drela used $A = 6.7$ and $B = 0.75$ in *ISES* and *XFOIL*, which lead to a significant over-prediction of maximum lift in this case. Van Rooij suggested $A = 6.75$ and $B = 0.83$. These values are used in this work, because they are carefully calibrated for a wide variety of airfoils.

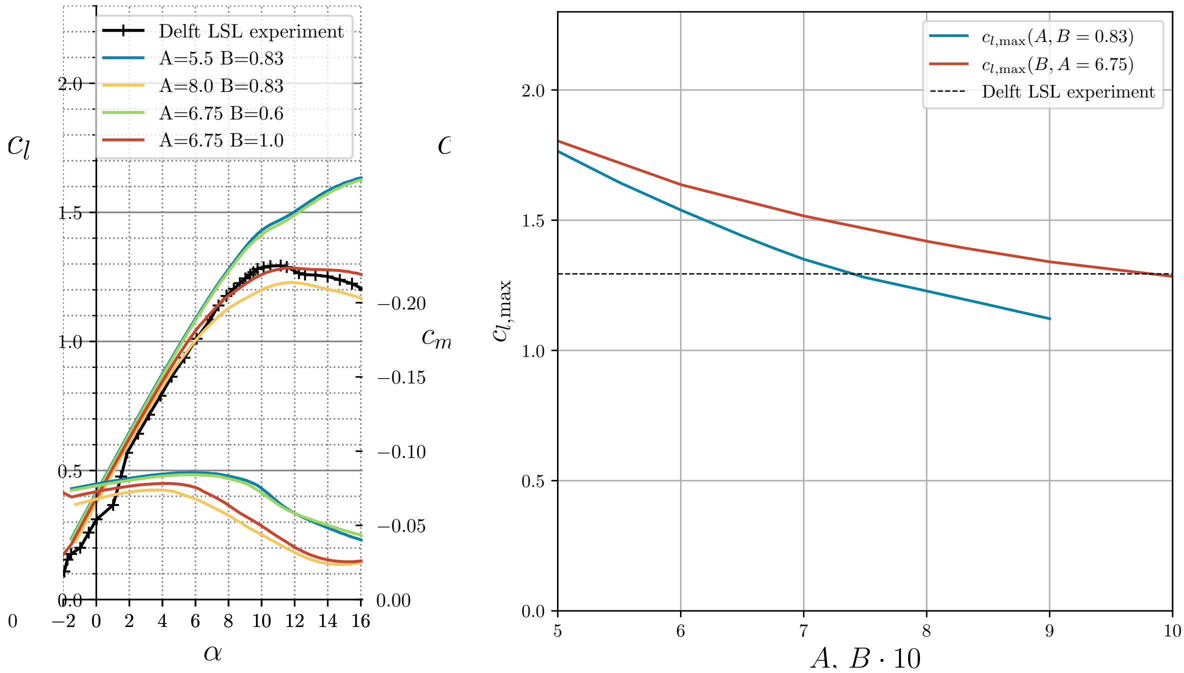

Figure 4.17: Influence of the G-β locus parameters A and B on the prediction of the maximum lift coefficients and comparisons with measurements of the *DU84-158* airfoil

Furthermore, the influence of the shear lag parameter K_c in Green's shear lag equation [44] is discussed by van Rooij [136]. The shear lag parameter K_c determines, how much the actual shear stress c_τ of the turbulent boundary layer lags behind the equilibrium value $c_{\tau_{EQ}}$. An increased K_c delays turbulent separation and hence leads to an increase of the maximum lift coefficient. Green [44] suggested a value of 5.7, which is also used by Drela. Melnik and Brooks [129] suggested a reduction of K_c by one third for separated flows ($H_k > 4$). Hence, van Rooij suggested to couple the K_c parameter to the kinematic shape parameter H_k, using a smooth $\tanh$ blend function:

$$K_c = 4.65 - 0.95 \tanh\left(0.275 H_k - 3.5\right). \tag{4.55}$$

The function is shown in fig. 4.18. It shows a smooth transition beginning with the separation shape factor $H_k = 4$ from the high value of $K_c = 5.7$ to the low value at $K_c = 3.65$ for high shape factors.

This equation makes a smooth reduction of K_c from the original value of 5.7 to the reduced value of 3.65. The coupling was implemented in the original *XFOIL 6.99* code by Hansen [49] and courtesy made available to the author, further referenced as *XFOIL-mod*. Furthermore, the coupling was also implemented in *XFOILSUC* by the author. The modified code is further referenced as *XFOILSUC-mod*. The influence of the improvements by the K_c-H_k coupling and the modified G-β-locus parameters $A = 6.75$ and $B = 0.83$ on lift prediction are shown in fig. 4.19. The *DU84-158* standard class airfoil and the *DU89-134-14* flapped sailplane airfoil at $\delta = 20°$ flap setting

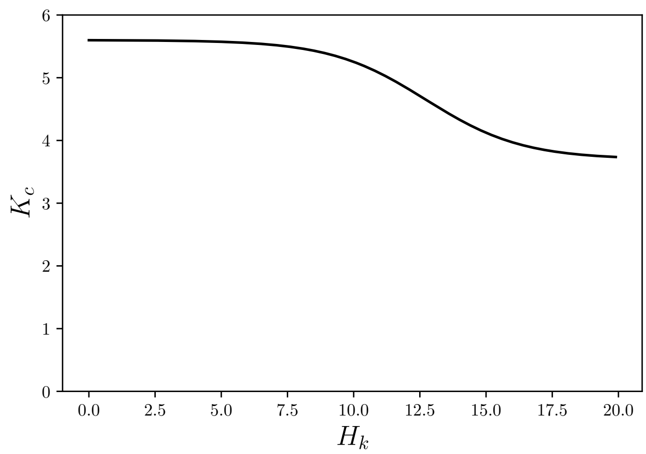

Figure 4.18: coupling of the shear lag parameter K_c to the kinematic shape factor H_k according to van Rooij [136]

are analyzed. $Re = 1 \times 10^6$ and $N_{crit} = 9$ was used. Compared to wind tunnel data measured in the Delft low turbulence tunnel (LSL), the over-prediction of maximum lift for the *DU84-158* is mitigated. For the *DU89-134-14* airfoil, a very good match of the maximum lift coefficient is achieved with the modifications.

4.4.3 *Limitations of the integral boundary-layer method*

Some effects are not captured by the coupled integral boundary-layer-panel method. The first is leading edge stall that causes an abrupt and severe loss of lift and hence detrimental handling characteristics. An estimate of the angle of attack, where leading edge stall occurs is given in section 4.4.3.1. The second effect is transition caused by steps, for example the backward-facing step as found with flap gap seals. Such a step can lead to an excessive increase in drag, discussed in section 4.4.3.2. It should also be noted that the integral boundary-layer-panel method can also not account for transition due to cross-flow instabilities and attachment line instabilities, which occur at high sweep angles. This poses no limitation for this work, since the wing analyzed in this work has small sweep angles. Also nonlinear compressibility effects (shocks and expansion fans) are not considered by the panel method. However, a Prandtl-Glauert transformation is implemented for moderate Mach numbers.

Furthermore, the drag values calculated with the introduced integral boundary-layer-panel method are too low compared to wind tunnel data, as can be seen in figures 4.19, 4.15 and 4.16. However, for airfoil optimization, this error is linear with respect to the objective function. Hence it does not influence the optimization behavior. For the wing planform optimization the situation is different. If the profile drag would remain uncorrected, the induced drag would play an overly dominant role on wing planform design. Hence it is paramount that the profile drag offset is corrected for this purpose. The correction is shown in section 5.4.2.

4.4.3.1 *Leading edge stall*

Leading-edge, deep or sometimes also called thin airfoil stall occurs due to the burst of a short laminar separation bubble at the leading edge. It causes a sharp drop of lift just above some critical angle of attack. When the angle of attack is reduced after the stall has occurred, reattachment

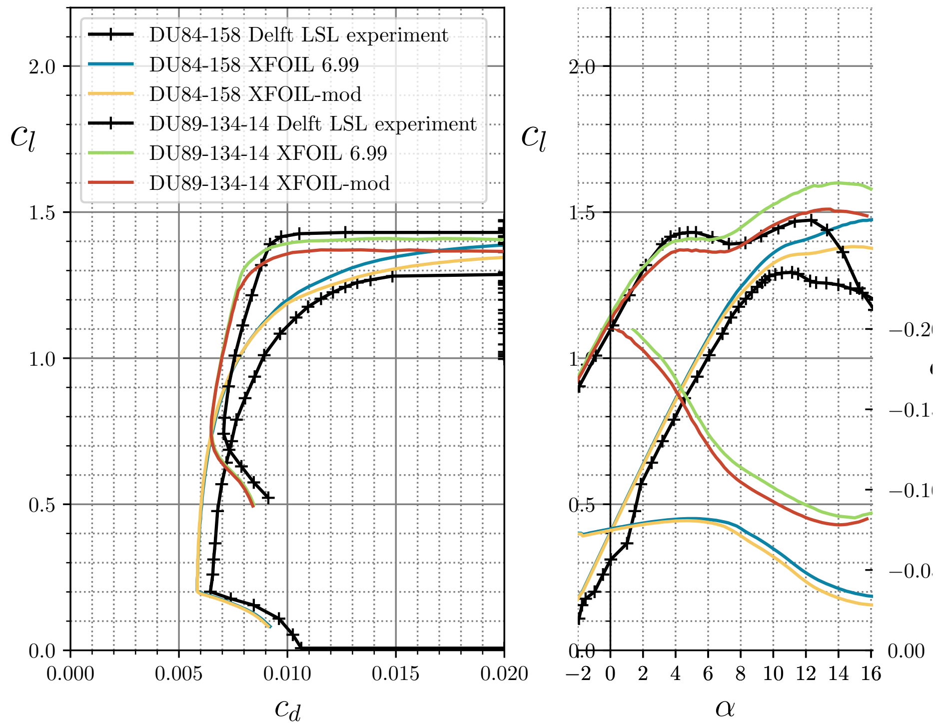

Figure 4.19: Improvements of lift prediction due to modified G-β-locus parameters A&B and coupling of the shear lag parameter K_c to the kinematic shape factor H_k

typically occurs at lower angle of attack than the stall, resulting in an c_l - α curve with a hysteresis loop. This results in very bad and unpredictable stall characteristics from pilot's view. The aircraft is prone to sudden stall/spin from which it is furthermore difficult to recover. Such a behavior may just be desired for aerobatic planes.

The bubble is caused by the steep adverse pressure gradient following the leading edge suction peak at high angles of attack. If the adverse pressure gradient is steep enough, laminar-turbulent transition occurs a short distance downstream of the separation point. The turbulent flow then reattaches to the airfoil surface and remains turbulent. Further increasing of the angle of attack moves the bubble closer to the leading edge and it becomes shorter. If the adverse pressure gradient is steep enough, the turbulent flow fails to reattach or separates directly downstream of the transition location. Prediction of bubble bursting is impossible using integral boundary-layer or RANS methods due to the strong interaction of viscous and inviscid flow phenomena and laminar-turbulent transition and because of the transient characteristic of this flow phenomenon. Further theoretical and experimental insight into leading edge bubble formation, transition and separation is given by Rist [100]. An integral boundary-layer approach based on correlation of local shear-layer parameters for determining the onset of transition and with an iterative procedure for the strong interaction effects is presented by Crimi and Reeves [19]. More recently, Large Eddy Simulation (LES)/RANS hybrid methods were developed for capturing these effects and applied for thin airfoil stall prediction [58]. Also Detached Eddy Simulation (DES) was successfully applied for predicting leading edge bubble burst [67].

These methods come with significant computational effort, making them unsuited for use within a numerical optimization approach. Without capturing the leading-edge stall properly, any optimization would favor airfoils with small leading edge radii. To compensate for this deficiency, a simple geometry correlation method is used. Gault [42] shows a coincidence between the airfoil y coordinate of the top surface at $x = 0.0125$ and the stall type. This is further elaborated by

Timmer and van Rooij [120], who show a correlation between the top surface coordinate y of the airfoil at $x = 0.0125$ and the angle of attack, where leading edge separation occurs. The correlation between the deep-stall angle and the top surface coordinate at the $x = 0.0125$ location is shown for a number of wind turbine airfoils in fig. 4.20. A linear dependence of the deep stall angle to the y coordinate at $x = 0.0125$ is found:

$$\alpha_{\text{deep-stall}} = 1114\ y_u(x = 0.0125). \tag{4.56}$$

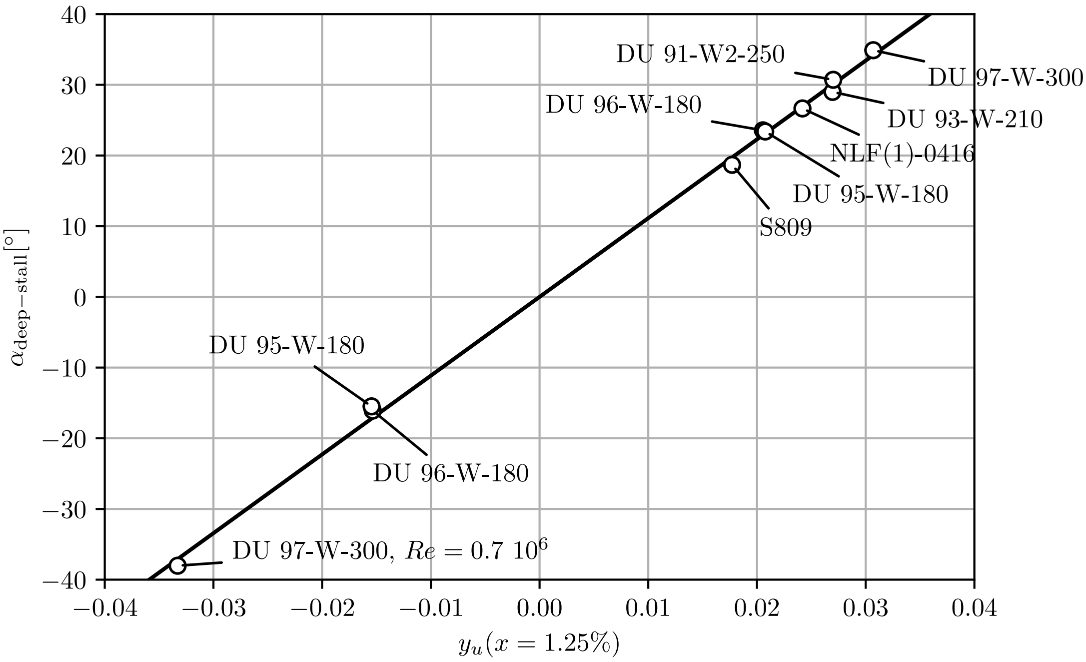

Figure 4.20: Correlation of deep-stall angle with leading edge thickness for a number of wind turbine airfoils. Own figure based on [120]

For good handling qualities, leading edge stall should occur well beyond the angle of attack for maximum lift α_{max} and hence the occurrence of trailing edge stall. For typical laminar airfoils used on sailplanes, the trailing edge stall occurs at $12° \lesssim \alpha_{\text{max}} \lesssim 16°$, depending on the flap deflection (c.f. [16], [8], [7]). More positive flap deflection gives lower α_{max}. In this work, it is decided that leading edge stall should not occur before $\alpha = 20°$. Therefore, a minimum value of:

$$y_{0.0125,\text{min}} = 0.018 \tag{4.57}$$

is used in this work to mitigate the risk of leading edge separation at angles of attack within the range of operation. This is enforced by the penalization approach as discussed in section 4.2.

4.4.3.2 *Boundary-layer transition on gap seals*

As described in section 2.2, the top morphing wing shell seamlessly connects to the primary wing structure, whereas the bottom shell has a gap to ensure that the leading edge region undergoes only a rigid body motion and the morphing wing shell experiences only bending deformation without tensile or compressive deformation. Such a gap can cause laminar-turbulent transition. However, a proven sealing technique exists, which successfully enables the flow to overcome gaps without transition to turbulence. This was first introduced by Boermans and van Garrel [16], who were the first to design a laminar airfoil with a laminar flow region on the bottom side extending on the flap up to 93% chord. The sealing technique invented for that purpose is common for all flap gap sealings on modern sailplanes.

The application of this sealing type to the morphing leading edge is shown in fig. 4.21. A thin, curved (190 μm thickness) PolyEthylene Terephthalate (PET) foil, also known under the brand name Mylar, is bonded with double-faced adhesive tape in a submerged step. The height of the recession is the thickness of the Mylar plus the bonding tape, so that the Mylar tape surface remains flush with the wing surface. The slot, between the Mylar leading edge and the morping wing shell is sealed with a thin ($\approx$ 70 μm) adhesive tape. The Mylar tape trailing edge slides on the fixed portion of the wing, which creates a backward facing step with the height of only the Mylar foil thickness. It is desired that the boundary-layer overcomes this step without laminar-turbulent transition. However, this has to be estimated beforehand, because premature transition would lead to significantly increased drag, possibly offsetting all the performance gains from the morphing concept.

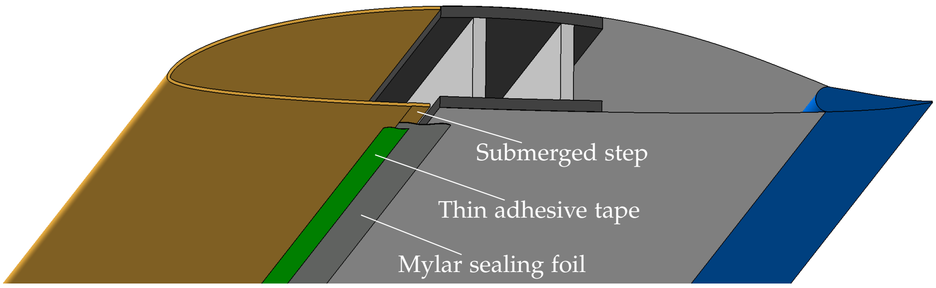

Figure 4.21: Schematic sketch of the mylar morphing leading edge gap sealing

The influence of backward facing steps on laminar-turbulent transition behavior has been investigated experimentally by Perraud et al. [88], [90], [89] and numerically by Hildebrand et al. [51]. The research indicates, that a backward facing step locally increases the amplification by some increase $\Delta\tilde{N}$. At some distance downstream of the step, the amplification curve of the disturbed case becomes almost parallel to the one of the undisturbed case. This means that increasing step height moves the transition location gradually forward. Hildebrand et al. applied the harmonic linearized Navier–Stokes equations to calculate the development of the amplification factor behind backward facing steps of various heights. They found a good correlation between simulations and experiments and suggested the following relation between the increase of the critical amplification factor ΔN and the step height h in relation to the boundary layer displacement thickness δ^*:

$$\Delta N = \begin{cases} 2.47\left(h/\delta^*\right)^2 + 0.62\left(h/\delta^*\right), & \text{if } h/\delta^* < 0.38 \\ 3.0\left(h/\delta^*\right) - 0.55, & \text{if } h/\delta^* \geq 0.38 \end{cases} \tag{4.58}$$

The increase of the critical amplification factor in the vicinity of the lower corner of the laminar low-drag region will be numerically investigated in section 4.8. In future, this needs to be verified by wind tunnel experiments. If a significant detrimental effect exists, reversal of the gap sealing could be considered, so that the Mylar tape is bonded in an submerged step on the rigid rear part of the wing and a forward facing step would result, which has a smaller effect on the boundary layer disturbance. However, if the Mylar foil lifts from the morphing wing shell due to small defects or lost pretension of the foil, the flow could cause a destabilizing effect finally leading to debonding of the whole Mylar sealing tape in flight, which of course is not desired. The intended backward facing solution as depicted in fig. 4.21 is stable in this regard and hence is the preferred solution for sealing.

4.5 SUBPLEX OPTIMIZATION ALGORITHM

The SUBPLEX optimization algorithm is used, developed by Rowan [102]. It is a subspace function comparison (sometimes called direct search) method using the gradient free Nelder–Mead-Simplex [83] method as an inner-loop optimization algorithm on subdomains. Subdomains are domains with a smaller sub-set as design variables, whereas the remaining design variables remain fixed. As the convergence behavior of the Nelder–Mead algorithm gets considerably worse when more than five to seven design variables are used [102], the SUBPLEX algorithm classifies the design variable vector into limited size subdomains, on which subsequent Nelder–Mead inner optimizations are done. The subdomains are selected, so that they are as orthogonal as possible mutually and ordered to decreasing influence to the objective function.

An advantage of the SUBPLEX method is that it is extremely robust, even if the objective function is noisy. It's convergence behavior is superior to evolutionary algorithms [130]. However, gradient based methods are superior in this respect [64]. As calculation of sensitivities via finite differences is very ineffective and implementation of analytical or adjoint sensitivity analysis methods to existing software is a tedious, time consuming task, a gradient free method as SUBPLEX is generally preferred in this work. Furthermore, the integral boundary-layer/panel method used here for calculating the aerodynamic coefficients is extremely fast. Therefore, the non-use of analytical/adjoint sensitivity information is a good choice considering overall time effort for the work in this thesis. A further disadvantage of the SUBPLEX method is that it is a minimization technique only, meaning that it is not capable of handling inequality g_j or equality h_j constraint functions explicitly. This is overcome here by adding penalty terms to the objective function in order to transfer the constrained optimization problem into an unconstrained minimization problem by the use of the SUMT by Fiacco and McCormick technique [40]. This penalization of the objective function is already introduced in section 4.2 with eq. 4.2.

4.5.1 *Inner loop algorithm: Nelder–Mead*

The Nelder–Mead simplex method [83] compares distinct objective function values f on a simplex in the design space. It has to be noted, that the objective function f is used here synonymously with the penalized objective function, depending on whether a penalization according to eq. 4.2 is used to enforce constraints or not. The Nelder–Mead simplex method uses the values of the objective function to decide, which design variable vector $\mathbf{d}$ should be investigated in the next iteration $k+1$. A simplex is the convex hull of a set of $n+1$ points in an n-dimensional space, i. e. in a two-dimensional space it can be interpreted as a triangle, in a three-dimensional space as a tetrahedron. The Nelder–Mead algorithm changes the vertices of the simplex in subsequent iterations. The initial simplex is determined by the initial guess $\mathbf{d}_0$ and the other vertices $\mathbf{d}_i$ for $i = 1 \cdots n$:

$$\mathbf{d}_i = \mathbf{d}_0 + \sigma_{NMS,i}\, \mathbf{e}_i, \tag{4.59}$$

where $\mathbf{e}_i$ is the unit vector in the i-th dimension and the initial simplex size factor $\boldsymbol{\sigma}_{\mathrm{NMS}}$ determines the size of the initial simplex.

At the start of each Nelder–Mead cycle, the objective function is evaluated at the initial guess $\mathbf{d}_0$ and each vertex $\mathbf{d}_i$. The vertices, where the highest, second highest and lowest (best) objective function values are found are denominated with index h, s and l.

Then, in the first iteration, the vertex $\mathbf{d}_h$ with the highest objective function value is *reflected* (reflection shown in fig. 4.22a) through the centroid $\mathbf{c}_{\text{NMS}}$ of the remaining vertices, determining the reflected vertex $\mathbf{d}_r$:

$$\mathbf{d}_r = \mathbf{c}_{\text{NMS}} + \alpha_{\text{NMS}} \left(\mathbf{c}_{\text{NMS}} - \mathbf{d}_h \right), \tag{4.60}$$

where the centroid $\mathbf{c}_{\text{NMS}}$ is calculated as:

$$\mathbf{c}_{\text{NMS}} = \frac{1}{n} \sum_{\substack{i=1 \\ i \neq h}}^{n} \mathbf{d}_i. \tag{4.61}$$

The objective function at the reflected vertex is evaluated. If it is the new best point ($f_r < f_l$), an *expansion* (shown in fig. 4.22b) in the direction is performed:

$$\mathbf{d}_e = \mathbf{c}_{\text{NMS}} + \gamma_{\text{NMS}} \left(\mathbf{d}_r - \mathbf{c}_{\text{NMS}} \right). \tag{4.62}$$

If the expanded point $\mathbf{d}_e$ is the new best solution, the vertex $\mathbf{d}_h$ is replaced with $\mathbf{d}_e$. Else it is replaced with d_r.

If the reflected point $\mathbf{d}_r$ is neither the best nor the worst solution ($f_l < f_r < f_s$), the vertex $\mathbf{d}_h$ is replaced with $\mathbf{d}_r$. If the reflected point $\mathbf{d}_r$ is the new worst or second worst solution, a *contraction*, shown in fig. 4.22c, is performed:

$$\mathbf{d}_c = \mathbf{c}_{\text{NMS}} + \beta_{\text{NMS}} \left(\mathbf{d}_h - \mathbf{c}_{\text{NMS}} \right) \text{ if } \left(f_h < f_r \right). \tag{4.63}$$

Or:

$$\mathbf{d}_c = \mathbf{c}_{\text{NMS}} + \beta_{\text{NMS}} \left(\mathbf{d}_r - \mathbf{c}_{\text{NMS}} \right) \text{ if } \left(f_r < f_h \right). \tag{4.64}$$

If the contraction was successful ($f_c < \min(f_r, f_h)$), the point is accepted, i.e. $\mathbf{d}_h$ is replaced with $\mathbf{d}_c$ for the next cycle. If not, a *shrinkage (massive contraction)*, shown in fig. 4.22d, of all vertices i toward the vertex with the best objective function value $\mathbf{d}_l$ is performed):

$$\mathbf{d}_i = \mathbf{d}_l + \delta_{\text{NMS}} \left(\mathbf{d}_i - \mathbf{d}_l \right) \text{ if } i \neq l. \tag{4.65}$$

Then the next Nelder–Mead cycle is started. This is done, until convergence criteria are met, which are discussed in the next section 4.5.2. The principal steps of the Nelder–Mead method described above are shown in fig. 4.22. A pseudo-code is given in reference [102].

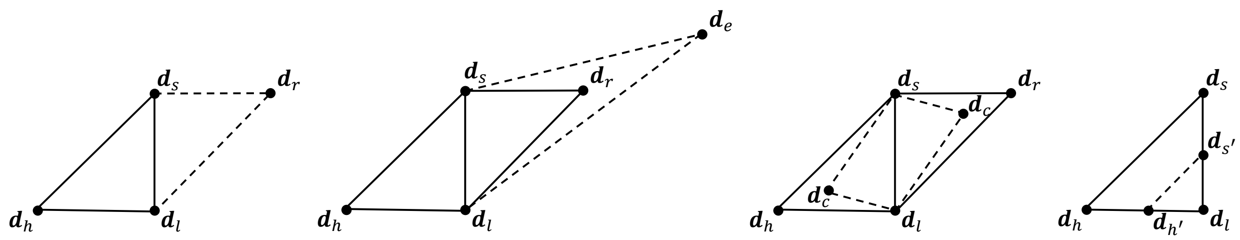

(a) Reflection (b) Expansion (c) Contraction (d) Shrinkage

Figure 4.22: Principal steps of the Nelder–Mead Simplex method. Own figure based on [102]

Summing up, five user-determined coefficients in the Nelder–Mead method exist: α_{NMS}, β_{NMS}, γ_{NMS}, δ_{NMS} and σ_{NMS}, which are referred to as a strategy. The values used in this work are:

- $\alpha_{\text{NMS}} = 1$

- $\beta_{\mathrm{NMS}} = 0.5$
- $\gamma_{\mathrm{NMS}} = 2$
- $\delta_{\mathrm{NMS}} = 0.5$
- $\sigma_{\mathrm{NMS},i} = 0.25 \quad i = 1 \dots n$

4.5.2 *Outer loop algorithm*

The SUBPLEX method classifies the design variable vector in a number of subspaces for more efficient optimization. It uses the Nelder–Mead method for optimization on these subspaces. The goal is to find subspaces, which are as mutually orthogonal as possible. The direction of progress, i.e. the set of design variables which lead to the best improvement of the objective function is intended to lie in the first subspace. As the Nelder–Mead method becomes increasingly inefficient for high dimensional problems with more than five design variables, the subspace size is restricted:

$$n_{s,\min} \leq n_{s,j} \leq n_{s,\max}, \qquad \text{for } j = 1, \dots, n_{\mathrm{SUB}}. \tag{4.66}$$

In this work, $n_{s,\min} = 3$ and $n_{s,\max} = 5$ is used. The total size of all subspaces must correspond to the number of design variables n:

$$\textstyle\sum_{j=1}^{n_{\mathrm{SUB}}} n_{s,j} = n \ . \tag{4.67}$$

The subspaces are generated by sorting the vector of progress $\Delta \mathbf{d} = [\Delta d_1, \dots, \Delta d_n]^{\mathsf{T}}$ (i.e. the change of the design variables between subsequent inner Nelder–Mead cycles) in decreasing order:

$$\widetilde{\Delta d} = \left[\Delta d_{p,1}, \dots, \Delta d_{p,n}\right]^{\mathsf{T}}, \tag{4.68}$$

where $\left|\Delta d_{p,i}\right| \geq \left|\Delta d_{p,i+1}\right|$, for $i = 1, \dots, n-1$. The first subspace size $n_{s,1}$ is calculated by the value k that maximizes the following function:

$$\begin{aligned} n_{s,1} = \operatorname{argmax}_k \quad & \begin{cases} \frac{\sum_{i=1}^{k} \Delta d_{p,i}}{k} - \frac{\sum_{i=k+1}^{n} \Delta d_{p,i}}{n-k} & \text{if } k < n \\ \frac{\sum_{i=1}^{n} \Delta d_{p,i}}{n} & \text{if } k = n \end{cases} \\ \text{subject to:} \quad & n_{s,\min} \leq k \leq n_{s,\max} \\ \text{and:} \quad & n_{s,\min} \frac{n-k}{n_{s,\max}} \leq n - k \end{aligned} \quad . \tag{4.69}$$

Eq. 4.69 thus identifies the largest gap in the mean of the progress vector $\widetilde{\Delta d}$. The largest gap is located at index k. The first constraint in eq. 4.69 ensures that the subspace size is within the desired limits. The second constraint ensures that the remaining design variable vector can be partitioned. The process is repeated, until the design variable vector is fully partitioned into subspaces of size according to eq. 4.66. The design variables belonging to the subspaces are assigned according to the variables which belong to the corresponding entries $\Delta d_{p,i}$.

The quantity $\mathbf{r}_{\mathrm{SUB}}$ is a vector, which determines the step size and orientation of the initial simplex in each inner Nelder–Mead optimization. Hence $\sigma_{NMS,i} \leftarrow r_{SUB,i}$ at the start of each inner optimization. $\mathbf{r}_{\mathrm{SUB}}$ is updated according the following rule:

$$\mathbf{r}_{\mathrm{SUB}} \leftarrow \begin{cases} \min\left(\max\left(\sum_i \Delta d_i / \ \sum_i r_{SUB,i}\right), 1/\omega_{\mathrm{SUB}}\right) \cdot \mathbf{r}_{\mathrm{SUB}} & \text{if } n_{\mathrm{SUB}} > 1, \\ \psi_{\mathrm{SUB}} \cdot \mathbf{r}_{\mathrm{SUB}} & \text{if } n_{\mathrm{SUB}} = 1 \end{cases}, \tag{4.70}$$

where ω_{SUB} is the step reduction/expansion coefficient. If ω_{SUB} is chosen to be large (i.e. close to 1), the convergence of the algorithm may be slower, but with improved design space exploration. Otherwise, if ω_{SUB} is chosen to be small, the convergence is improved, but the optimization may tend to converge to local optima. In this work, $\omega_{\text{SUB}} = 0.1$ is used. The sign of the initial simplex size factor $\sigma_{NMS,i} = r_{SUB,i}$ is chosen according to the sign of the component of the vector of progress in the previous inner Nelder–Mead optimization iteration:

$$r_{SUB,i} \leftarrow \begin{cases} \text{sign}\,(\Delta d_i) \cdot |\, r_{SUB,i} \,| & \text{if } \Delta d_i \neq 0, \\ -r_{SUB,i} & \text{if } \Delta d_i = 0 \end{cases} . \tag{4.71}$$

Termination of the inner Nelder–Mead optimization is performed, if $\|\mathbf{d}_l - \mathbf{d}_h\|_2 \leq \psi_{\text{SUB}}$. The outer loop terminates, if the design variable vectors of successive inner Nelder–Mead optimizations are close enough and if $\mathbf{r}_{\text{NMS}}$ is small enough:

$$\frac{\max\left(\|\Delta\mathbf{d}\|_\infty, \|\mathbf{r}_{\text{NMS}}\|_\infty \cdot \psi\right)}{\max\left(\|\mathbf{d}\|_\infty, 1\right)} \leq \text{ tol} . \tag{4.72}$$

In this work, $tol = 1 \times 10^{-10}$ and $\psi_{\text{SUB}} = 0.25$ is used.

Nelder–Mead and SUBPLEX are *zeroth-order optimization algorithms*, which do not use first or second order design sensitivities (i. e.the first or second derivatives of the objective and constraint functions w.r.t. design variables). *First-order optimization algorithms* like the convex linearization method (CONLIN) [41], the method of moving asymptotes (MMA) [118] and *second-order optimization algorithms* like sequential least squares programming (SLSQP) or Nonlinear Linearization Programming using a Quasi-Newton method with Lagrange Penalties (NLPQLP) show faster convergence rates compared to *zeroth-order optimization algorithms*. Consequently, the computation times are significantly faster, as long as efficient analytical sensitivity information is provided. However, implementation of *first-order optimization algorithms* is much easier, because the calculation of analytical design sensitivities requires access to the solver source code and implementation of a direct or adjoint sensitivity calculation method. Furthermore, if the design responses are noisy (i. e.oscillatory behavior w.r.t. design variable changes), a gradient based optimization algorithm may perform inferior. Because the number of design variables for both the airfoil optimization in section 4 and the three-dimensional wing planform and winglet optimization in section 5 is low and the potential flow theory solvers are fast, the use of a gradient based optimization algorithm is not required. Furthermore, in case of the airfoil optimization, it turned out that the objective function shows some noisy behavior. The SUBPLEX algorithm can handle design problems with a moderate number of design variables and a noisy objective function pretty well. The SUBPLEX algorithm was tested against serveral other *first-order optimization algorithms* in a preliminary study to this work for the airfoils as described in table 4.1, except the root airfoil. SUBPLEX was compared against:

- Nelder-Mead Simplex (NMS) (c.f. 4.5.1)
- Differential evolution (DE) [115]
- Constrained optimization by linear approximations (COBYLA) [92]
- Bound optimization by quadratic approximation (BOBYQA) [93]

In this study, SUBPLEX, COBYLA and BOBYQA showed similar convergence rates, whereas DE required almost one order of magnitude more function evaluations to converge. In contrast to

COBYLA and BOBYQA, SUBPLEX reliably achieved low objective function values. COBYLA and BOBYQA often got stuck in low quality local minima. Consequently, SUBPLEX was chosen as optimization algorithm for this work. The implementation of the SUBPLEX and Nelder–Mead simplex algorithms used in this thesis is done in the programming language *Python* by Brezillon et al. [18].

4.6 OPTIMIZATION RESULTS OF THE MAIN WING AIRFOIL

In this section, the optimization result of the main wing airfoil with the morphing droop leading edge is shown. The morphing region extends from the leading edge to $x_e = 0.25$ and has a camber changing flap with a flap hinge axis at $\mathbf{x}_r = [0.84, -0.004]^T$. The performance of the optimization result is compared with the main wing airfoil of the *ASG 29*, the *DU89-134-14*.

4.6.1 *Optimization setup*

The morphing and trailing edge flap settings, optimization weights, Reynolds numbers, N_{crit} values and the transition criterion used for all operation points i at specified lift coefficients c_l are given in table 4.3. The Reynolds number is calculated according to equations 1.8 and 1.1, based on the assumption of a flight altitude of $2000\ \mathrm{m}$ in International Civil Aviation Organization (ICAO) standard atmosphere. This results in a kinematic viscosity of $\nu = 1.715 \times 10^{-5}$ and a density of air $\rho = 1.007\ \mathrm{kg/m^3}$. Only the fully ballasted configuration at MTOM=600 kg is considered, resulting in a wing loading of $68.7 \frac{\mathrm{kg}}{\mathrm{m}^2}$. Level flight is assumed for the undeformed configuration, whereas for circling flight in morphed configuration a bank angle of $\phi_b = 45°$ is assumed, resulting in a normal acceleration of $n_{z,\mathrm{circ}} = \frac{1}{\cos\phi} = 1.41$. Deck [26] performed measurements on a high aspect ratio *Ventus-3* sailplane, where he showed, that C_L is close to the two-dimensional section lift coefficient c_L within a 3% margin. So a reasonable assumption can be made, that $C_l \approx C_l$. Nearly two-dimensional flow can be assumed for the most part of the wing as discussed in section 1.4 based on the calculations by Axten [10]. Hence, the section lift coefficient C_l closely resembles airfoil lift coefficient c_l and thus $c_l \approx C_l \approx C_L$. The spanwise station for which the main airfoil is optimized is $y = 3306\ \mathrm{mm}$, resulting in a chord length of $c = 533\ \mathrm{mm}$ (c.f. table 4.1). The Reynolds numbers are calculated from equations 1.8 and 1.1. This results in a constant $Re\ \sqrt{c_l} = 1.14 \times 10^6$ for the level flight conditions and $Re\ \sqrt{c_l} = 1.35 \times 10^6$ for circling flight.

Table 4.3: Operation points for the morphing main wing airfoil optimization

op	$c_{l,op}$	configuration	w_{op}	*Re*	$N_{crit,U}$	$N_{crit,L}$	solver
1	0.3	undeformed	0.24	2.08×10^6	11.5	7	*XFOILSUC-mod*
2	0.3	undeformed	0.0792	2.08×10^6	9.0	9.0	*XFOIL-mod*
3	0.9	undeformed	0.04531	1.2×10^6	11.5	11.5	*XFOILSUC-mod*
4	1.3	morphed	0.05139	1.19×10^6	11.5	11.5	*XFOILSUC-mod*
5	1.725	morphed	0.02385	1.03×10^6	11.5	11.5	*XFOILSUC-mod*
6	1.725	morphed	0.02385	1.03×10^6	9.0	9.0	*XFOIL-mod*

A turbulator is used at $92\ \%$ at the lower surface. For all lift coefficients and configurations, *XFOILSUC-mod* with the more precise *improved van Ingen e^N method* is used. At the lowest lift coefficient in undeformed configuration and for the highest lift coefficient low pressure spikes could occur. As shown in section 4.4.2.4, the *improved van Ingen e^N method* shows less reliable results in this case. Therefore, these operation points are additionally calculated with *XFOIL-mod* with the envelope transition criterion, but with a lower weight w_i compared to the *XFOILSUC-mod* results. This is to penalize the design in the case, if the airfoil falls out of the laminar low-drag region with the envelope transition criterion, but remains inside the laminar low-drag region with *XFOILSUC-mod*. If the design is inside the laminar low-drag region considering both transition criterions, the drag coefficients calculated with *XFOILSUC-mod* dominates due to the higher weight.

The weights for the respective operation point *op* are calculated as the product of the frequency distribution of flight time at the respective lift coefficient $f_t(c_{l,op})$ as described in section 3.1.2, the fraction of profile drag to total drag of the aircraft $\frac{D_p(c_{l,op})}{D(c_{l,op})}$ and a user defined weight factor w_{user}:

$$w_{op} = f_t(c_{l,op}) \frac{D_p(c_{l,op})}{D(c_{l,op})} w_{\text{user}}. \tag{4.73}$$

The user defined weight factor is used to give higher emphasis to the low lift operation points. It was found in preliminary studies, that this leads to better results. It has to be noted that the frequency distribution and the fraction of profile drag to total aircraft drag used in table 4.3 are coarse approximations to the values given in references [79] and [14]. However, in preliminary studies it was found that the optimization result is very insensitive to small variations of the weights, thus allowing the use of coarser approximations.

An overall minimum airfoil thickness $t_{min,tot} = 12.5\%$ was specified to ensure sufficient space for the structure and control systems. The minimum flap thickness constraint defined in table 4.2 is used, as well as the minimum thickness coordinate according to section 4.4.3.1. As airfoil and flap thickness are no hard limits and a good compromise between structure mass and aerodynamic performance should be found, a relatively soft constraint penalization is used with the values $c_{tol} = 0.1$ and $r_0 = 5 \times 10^{-6}$ for eq. 4.2.

4.6.2 *Optimization studies*

In the airfoil optimization procedure of this work, the optimal CST parameters of the airfoil base shape and for the camber line and thickness change are sought, as discussed in 4.2. However, the flap hinge location x_r and the end location of the morphing leading edge section x_{end} are no design variables and thus remain fixed. Therefore, a good choice for this parameters has to be made. Therefore, optimization studies were performed first to find the best values for these parameters. For both studies, the morphing leading edge section is set to start at $x/c = 3.75\%$ and the y-coordinate of the flap hinge is $y_r = -0.004$. First, the morph length study is conducted. As a starting guess, $x_r = 86\%$ is selected for the morph length study. x_{end} is successively reduced starting from $x_{\text{end}} = 0.4$ and the converged result of the former optimization run served as starting guess for the next.

The results are shown in fig. 4.23. The best performance is found for the longest morphing section, which is not surprising, because it enables the largest design freedom. However, a longer morphing section comes with increased loads on the compliant mechanisms and control system. Consequently, this may lead to higher susceptibility to contour deviations. Therefore, it is decided to used $x_{\text{end}} = 0.25$ as a good compromise. Between $x_{\text{end}} = 0.27$ and $x_{\text{end}} = 0.29$ the optimized objective function values are significantly higher than the adjacent values. The reason for this is unknown. It could be, that the optimization algorithm converged to local optima.

A morphing region length of $x_{\text{end}} = 0.25$ is selected for the flap hinge position study. The results of the x_r study are shown in fig. 4.24. The best position in terms of objective function is

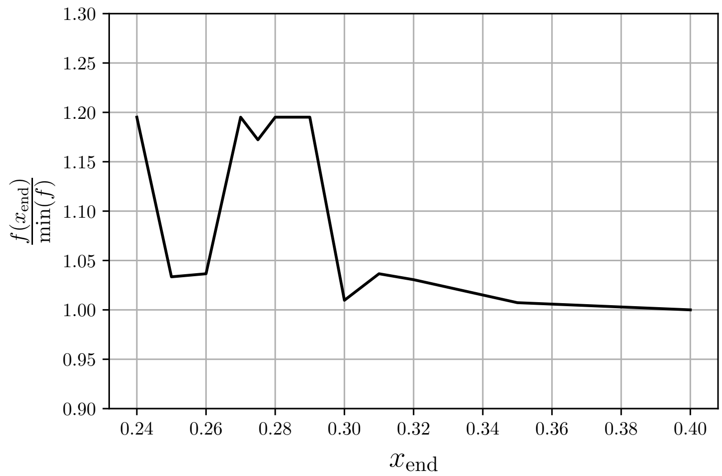

Figure 4.23: Study of end of morphing section x_{end} on objective function f

found to be $x_r = 0.8$. For the morphing aircraft, $x_r = 0.84$ is selected, which has an only slightly higher objective function value than the best location, but comes with the advantage of more available space for the control systems and with reduced torsional loads on the flap.

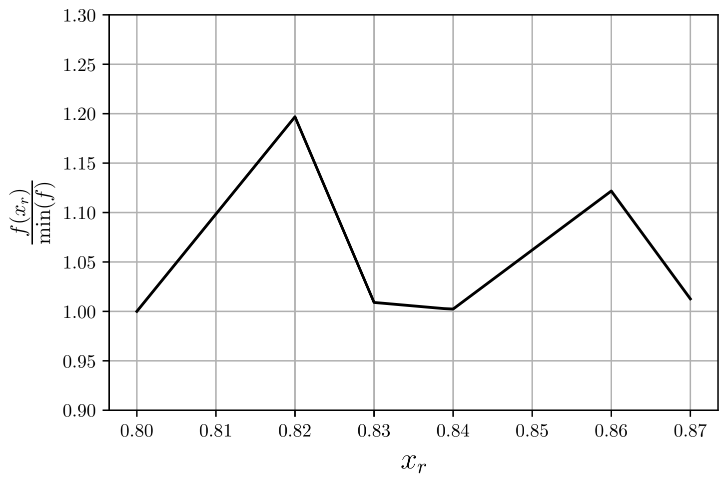

Figure 4.24: Study of impact of flap axis location x_r on objective function f

4.6.3 *Optimization results*

From the parametric study results in section 4.6.2, the end of the morphing region is set to $x_{\text{end}} = 0.25$. The flap axis is set to $x_r = 0.84$. The resulting optimized main wing airfoil is shown in fig. 4.25. In high lift configuration, the morphing section droops 2.4% down and the flap deflects $\delta = 19.1°$ down. The airfoil fulfills the minimum upper side contour limit at $x = 1.25\%$ for avoiding leading edge stall. This contour limit is indicated as a red cross in fig. 4.25. The local thickness constraint at the flap region is also fulfilled, which is indicated by a red dashed line in the thickness distribution plot. The airfoil is 12.4% thick, which means, that the thickness constraint with 12.5% is slightly violated. This is, because the constraint penalization allows slight violation. As a slightly smaller thickness has no abrupt negative consequences, this is accepted. Compared to the *DU89-134-14* airfoil, the optimized main wing airfoil is thinner, but the location of maximum thickness is shifted further aft. This relieves the problem with limited space for the control system and the airbrakes, but further minimizes the available volume for water ballast in the morphing section. Therefore, additional water tanks behind the spar are a must.

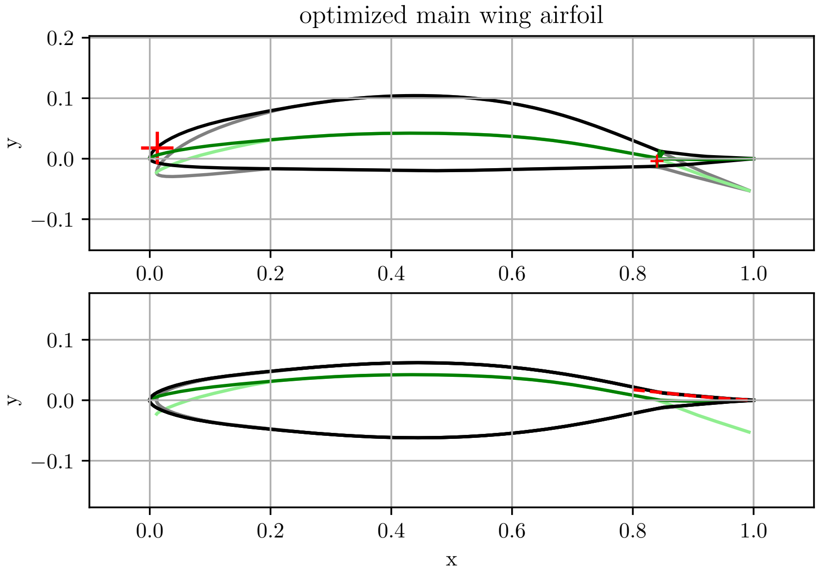

Figure 4.25: Contour (top) and thickness distribution with camber line (bottom) of the optimized main wing airfoil

The performance of the optimized morphing main wing airfoil is compared to the *DU89-134-14*. For a fair comparison, the airfoils are compared considering the chord length of the same spanwise station $y = 3306$ mm. For the morphing airfoil, this results in $c = 533$ mm, whereas for the *DU89-134-14* airfoil used on the *ASG 29* sailplane, this results in $c = 672$ mm. It is assumed that both aircraft operate at MTOM. This results in constant $Re\sqrt{c_l} = 1.14\ 10^6$ for the morphing main wing airfoil and $Re\sqrt{c_l} = 1.31\ 10^6$ for the *DU89-134-14* in level flight. For circling flight with $\phi_b = 45°$, Reynolds numbers $Re\sqrt{c_l} = 1.35\ 10^6$ for the morphing main wing airfoil and $Re\sqrt{c_l} = 1.55\ 10^6$ for the *DU89-134-14* are assumed. For analysis, *XFOILSUC-mod* with the *improved van Ingen e^N criterion* $N_{crit,U} = 11.5$ is used. For the low lift configuration of both airfoils, $N_{crit,L} = 7$ is used, because the occurrence of a leading edge low pressure spike is likely to occur, which amplifies receptivity (c.f. sec. 4.4.2.4). For the high lift configurations, no low pressure spikes are expected, hence $N_{crit,U} = N_{crit,L} = 11.5$.

The calculated polars are shown in fig. 4.26. The morphing airfoil shows higher drag coefficients than the *DU89-134-14* airfoil. However, it has to be pointed out, that the Reynolds number is lower. Furthermore, the wings profile drag depends on the product of the drag coefficient and the chord length. Therefore, a wing equipped with the morphing wing airfoil is expected to have lower profile drag than a wing with the *DU89-134-14* airfoil. The morphing main wing airfoil reaches a calculated maximum lift coefficient of $c_{l,\max} = 1.7589$ at high lift configuration, with relatively low drag. $c_{l,\max}$ also marks the upper corner of the laminar low-drag region. Hence the onset of rapid forward movement of transition coincides with the onset of trailing edge stall. This is in contrast to the behavior of the *DU89-134-14* airfoil, where the transition moves forward first, coming with a significant increase of profile drag and a plateau in the lift curve. $c_{l,\max}$ is reached at α values far higher than the upper corner of the laminar low-drag region. For thermalling, that behavior of the morphing airfoil could be beneficial for the pilot. Assume flying at an average lift coefficient/angle of attack corresponding to the upper corner of the laminar low-drag region and hence the onset of the plateau of the lift curve in a turbulent thermal. Due to the vertical gusts, the angle of attack fluctuates around the average within a certain range. If the lift curve of the airfoil has a plateau, the sailplane is not accelerated upwards in case of an upward gust, but downwards in case of a downward gust. Furthermore, the drag is increased significantly, if the laminar low-drag region is exceeded due to the upward gust. Both effects cause an increased sink rate and therefore reduce the overall climb speed in the thermal. This effect is originally discovered by Boermans [15] and described more into detail in [62]. In case of the morphing airfoil, where trailing edge stall and the forward movement of transition occur simultaneously, the pilot can recognize leaving the beneficial laminar low-drag region. This is indicated by normal stall signals like shaking of the aircraft or the stick, which are caused by shedded vortices of the separated flow hitting the horizontal stabilizer. At a flap setting of $\delta = 30°$, a $c_{l,\max} = 1.89$ is reached at $Re = 9.13\ 10^5$, corresponding to unaccelerated straight flight at MTOM. This provides ample reserve for loss of lift due to the fuselage lift drop. The moment coefficient is significantly higher for the morphing wing airfoil. A higher pitching moment causes increased trim drag for the overall aircraft. However, as with the drag coefficient, the airfoil chord due to the increased maximum lift coefficient has to be considered. As the pitching moment scales with c^2, the absolute pitching moment will be decreased, despite the higher c_m.

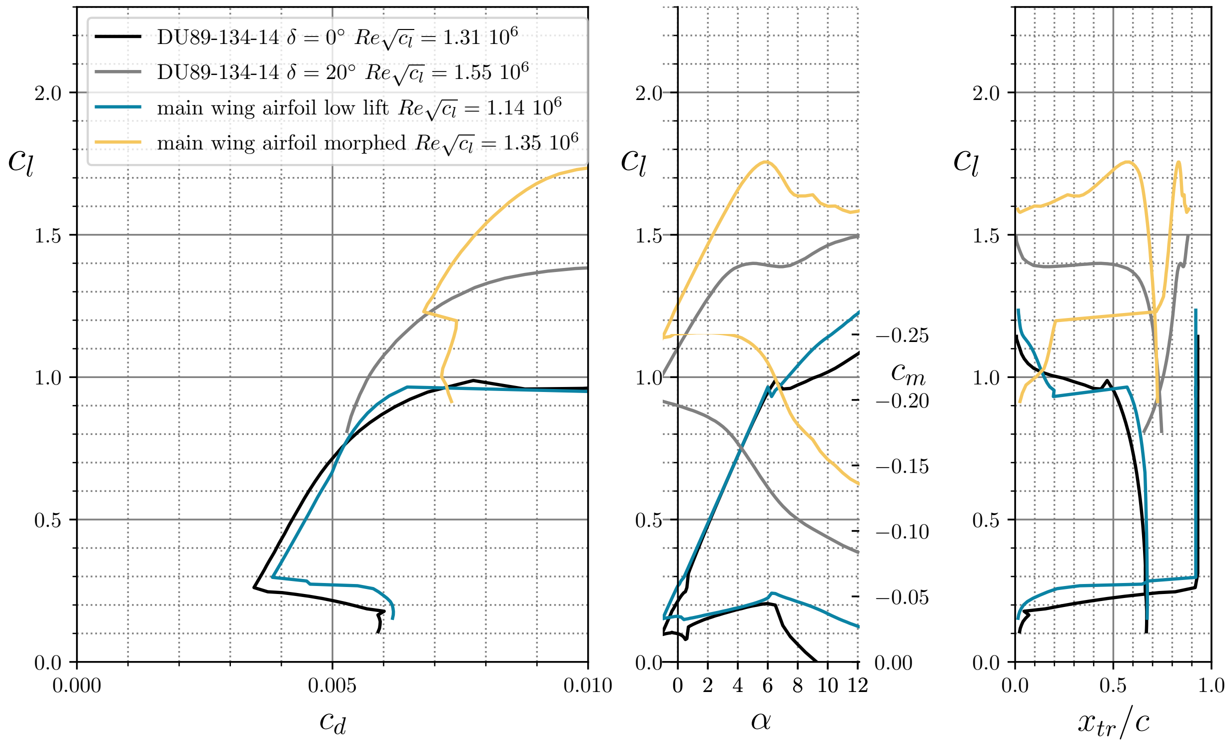

Figure 4.26: Polars of main wing morphing airfoil and *DU89-134-14* airfoil in low lift and high lift configurations

4.6.4 *Airfoil rework with the inverse method*

The airfoil rework has been done using the inverse design routine of *XFOIL-mod*. Fig. 4.27 shows the viscous pressure distribution in undeformed and morphed configuration at $\alpha = 1°$ and $\alpha = 5°$

respectively. The curves before rework are shown as solid lines, the curves after the rework are shown as dashed lines. First the pressure distributions in both configurations have been smoothed. As shown in section 4.3, the CST parameterization method is not capable of generating non-smooth geometric details. When designing an airfoil with a turbulator on the lower surface, it is desired, that the pressure immediately starts to increase behind the turbulator, so that the laminar region may be as large as possible. A sudden sharp pressure increase demands a contour with a sudden change in curvature at the location of the pressure increase, which is a small geometric detail. Therefore, manual rework of the pressure distribution and subsequently on the airfoil contour is done. Furthermore, the leading edge region in morphed configuration has been modified, so that the low pressure spike first occurs at higher angle of attack, thus leading to a more gradual forward movement of transition and subsequently gradual decrease of lift after $c_{l,\max}$. The lift decreases due to a forward movement of the separation point beginning at the trailing edge. As the transition point is moving forward, the boundary-layer thickness at the beginning of the pressure recovery section between $60\%c$ and $70\%c$ increases, as the boundary-layer thickness grows faster when the boundary-layer is turbulent and not laminar. The thicker the boundary-layer, the lower the adverse pressure gradient which can be sustained before separation.

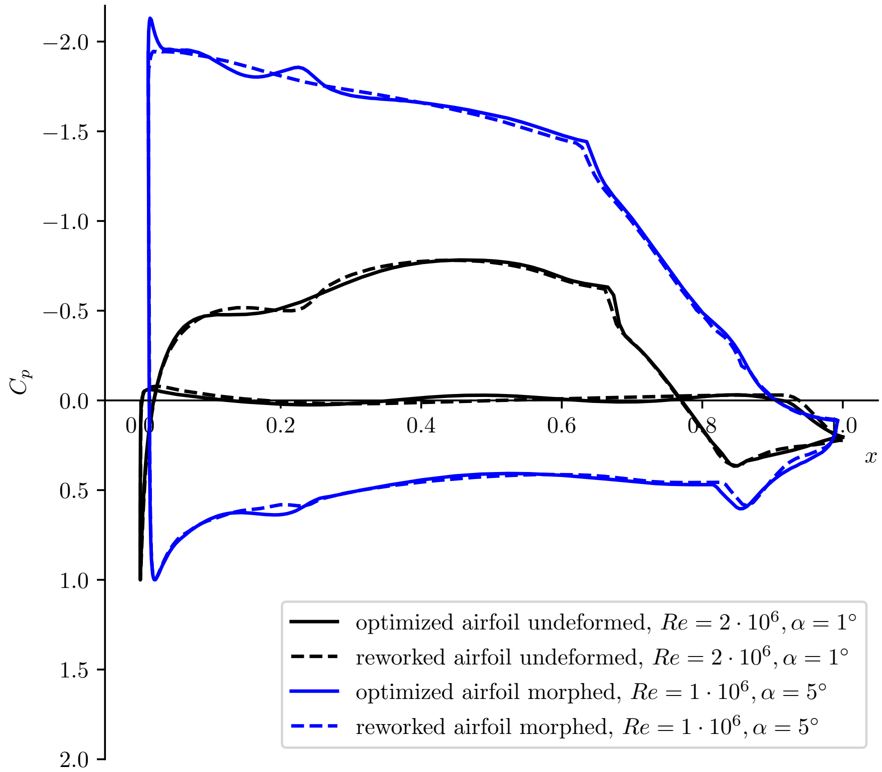

Figure 4.27: Viscous pressure distribution of the optimized (solid) and of the reworked (dashed) airfoil in undeformed (black) and morphed configuration (blue)

It has to be mentioned that the inverse redesign of a morphing airfoil is an iterative process. Changing the airfoil geometry and therefore the pressure distribution in one configuration leads also to a changed pressure distribution and geometry in the other configuration. Changing the pressure distribution in the undeformed configuration influences the behavior in the morphed configuration and vice versa. Therefore, the pressure distributions and the required geometry change for morphing have to be carefully modified and analyzed in both configurations over several iteration cycles.

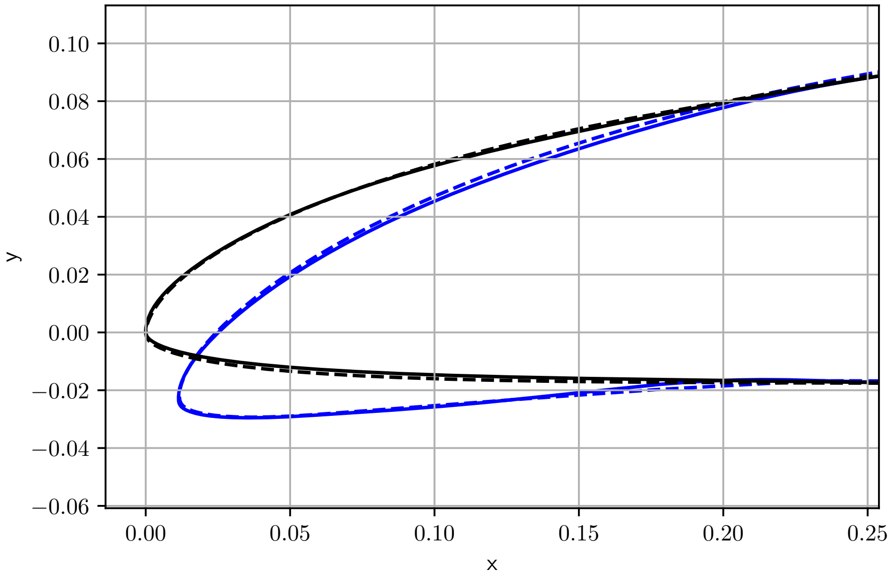

Figure 4.28: Geometry changes due to airfoil rework. Optimized airfoil (solid lines), reworked airfoil (dashed lines)

Figure 4.28 shows the airfoil geometry changes due to the inverse design rework in the forward region. Again, the optimized contours are shown as solid lines, whereas the reworked contours are shown as dashed lines. The upper side thickness is increased due to the decreased low pressure spike. On the lower side the pressure distribution is designed to be more continuous, leading to a more continuous curvature in the forward morphing region in front of $25\%c$ and a less abrupt curvature change close to the rigid part of the airfoil. This subsequently leads to an increased width of the laminar low-drag region in deformed configuration because the short region of constant pressure at $20\%c$ is almost removed, which becomes a region with adverse pressure gradient at lower angles of attack, thus leading to preliminary transition. The disadvantage of this modification is that the drag values increase, as can be seen in the polars in figure 4.29 at lift coefficients between $c_l = 1.3$ and $c_l = 1.7$. These higher drag values are caused by an increase in bubble drag due to the laminar separation bubble in the kink below the flap axis, indicated by the further aft transition location on the lower side compared to the optimized airfoil. But the increased width of the laminar low-drag region and the more continuous curvature in morphed configuration outweigh this slight performance decrease. A fix could be the use of a dual row pneumatic turbulator system, one at the designated $92\%c$ location on the flap and one in front of the flap hinge line. This though leads to increased complexity of the system. The resulting main wing airfoil is designated *ARS-20-124-16-24* (design based on contributions by Achleitner, Rhode-Brandenburger, Simon, 12.4% relative thickness, camber changing flap chord 16%, 2.4% nose droop).

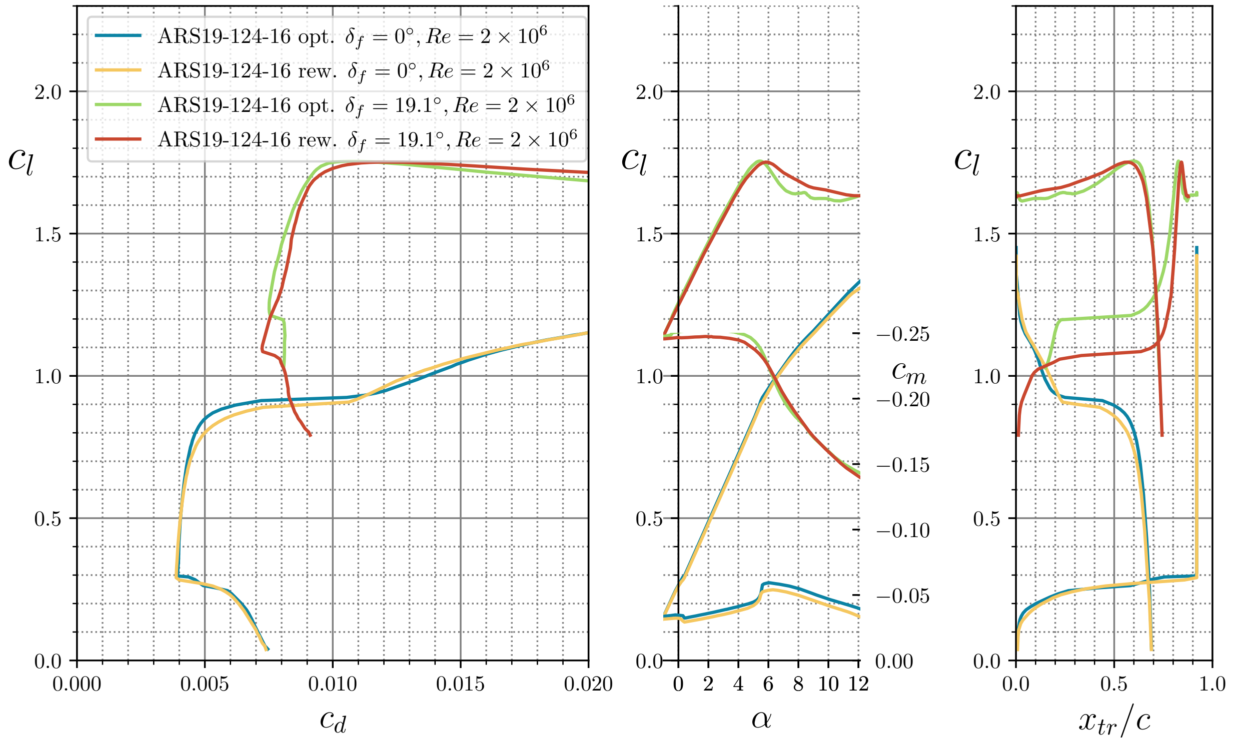

Figure 4.29: Comparison of optimized and reworked airfoil polars of the main wing airfoil *ARS19-124-16*. Drag polar (left), lift curve (middle) and transition location (right) calculated with XFOIL-mod, $n_{crit} = 9$

4.7 ROOT, INNER AND OUTER WING AIRFOILS

In this section, the root airfoil and the airfoils for the inner wing section, the outer wing section and the tip airfoil are introduced. The performance is compared to the main wing airfoil and the outer wing airfoil of the *ASG 29* sailplane, the *DU92-131-14*. Furthermore, the airfoils characteristics are evaluated with respect to the requirements defined in section 4.1.

The airfoils are designed with the numerical optimization method described in this chapter. Except the root airfoil is derived from the inner wing airfoil using the geometrical modification with the *GDES* module from *XFOIL-mod* and the inverse design method. After optimization, post processing according to section 4.6.4 was performed. All airfoils have been optimized for the respective Reynolds number range at the location of use on the wing. First, the outer wing airfoil has been optimized. The start design vector used for optimization is the main wing airfoil optimization result. However, the first camber design variable, which specifies the droop in y-direction of the leading edge was fixed to the main wing optimization result to achieve the same leading edge droop. The wing tip airfoil is consecutively based on the outer wing airfoil result. Both the two outer wing and tip airfoils are designed to have a lift reserve at angles of attack at and beyond α_{max} compared to the main and inner wing airfoils for a gentle overall aircraft stall behavior. This was done by increasing the highest lift coefficient from $c_l = 1.725$ to $c_l = 1.735$.

Furthermore, during post processing with the inverse method, care was given that the outer wing airfoils have higher c_l in post-stall ($\alpha > \alpha_{\max}$) than the main and inner wing airfoil. Also the flap length was increased by 0.741% for the outer wing airfoil and by 1% for the tip airfoil to compensate loss of lift in the morphed configuration due to viscous effects caused by the lower Reynolds numbers at the outermost airfoil. The PS-01 airfoil, designed by Scholz [108] has been used for the winglet. It is also shown in fig. 4.31.

The inner wing airfoil has an increased thickness constraint of 14.5% for structural reasons. The remaining parameters for optimization are taken from the main wing airfoil, except the Reynolds number, which was adopted to the increased wing chord length at the spanwise position where it is used.

The flow approaching the root section of the wing is already turbulent, as the transition location on the fuselage is upstream of the wing root at approximately the thickest point of the fuselage. Therefore, this has to be accounted for in the design of the wing root airfoil. The boundary-layer is thicker at the onset of the main pressure recovery section of the airfoil at the top surface and hence more prone to turbulent separation. Hence an airfoil designed for fully turbulent flow must have a less steep main pressure recovery section. First trials designing the root airfoil with the numerical optimization method described above lead to geometrically deteriorated airfoils. Consequently, the root airfoil was derived from the inner wing airfoil by shifting the location of maximum thickness and the location of maximum camber from $x/c = 0.437$ (thickness) and $x/c = 0.498$ to $x/c = 0.339$ and $x/c = 0.33$ with the *GDES* module from *XFOIL-mod*. The pressure distribution was subsequently smoothed. The viscous pressure distributions of the inner wing and root airfoil in morphed configuration ($Re = 1e6, \alpha = 5°$) and in undeformed configuration ($Re = 2e6, \alpha = 1°$) are shown in fig. 4.30. Note that free transition is assumed for the upper surface of the inner wing airfoil, whereas transition is forced at $x_{tr} = 0.05$ for the root airfoil.

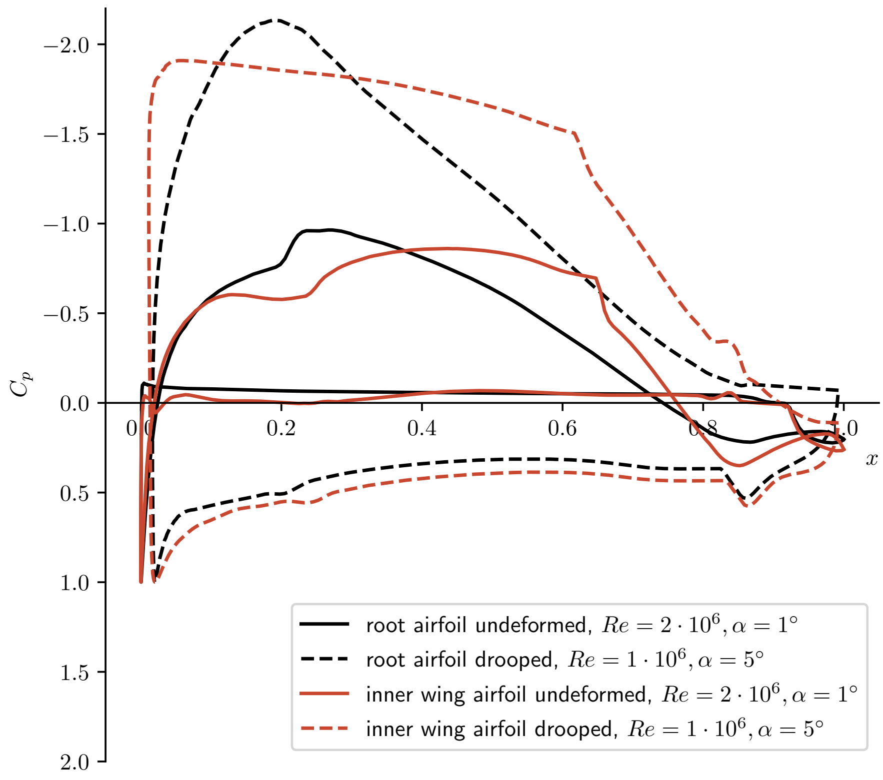

Figure 4.30: Viscous pressure distribution of the root (black) and inner wing airfoil (red) in undeformed (solid) and morphed (dashed) configuration

All final reworked airfoils used on the morphing wing are shown in fig. 4.31. The root airfoil is designated *ARS19-141-16-22*. It has a 16% deep trailing edge flap with 2.2% nose droop.

The airfoils are becoming thinner, the closer to the wingtip they are designed for. As the structural requirements demands more height for the main spar further inboard, this is as intended. Furthermore, the location of maximum thickness and maximum camber shift forward, the further outside the airfoils and hence the smaller the chord and Reynolds number. This is normal, because the laminar separation bubble gets longer for smaller chord Reynolds numbers and therefore bubble drag plays an increasing role. The forward movement of the location of maximum thickness and maximum camber implies a more gentle pressure recovery. As the bubble drag directly depends on the pressure increase between the separation and the reattachment point, a more gentle pressure recovery reduces bubble drag (c.f. [33]).

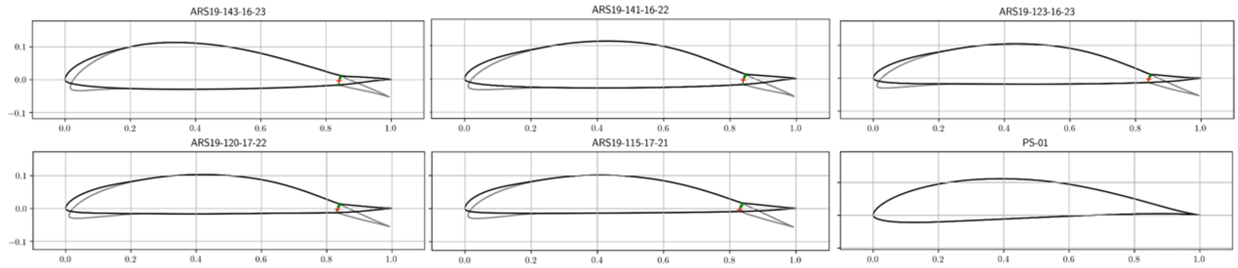

Figure 4.31: All airfoils of the morphing wing, root airfoil (top left), inner wing airfoil (top center), main wing airfoil (top right), outer wing airfoil (bottom left), tip airfoil(bottom center) to winglet airfoil (bottom right)

The polars of the post-processed main and outer wing airfoils of the morphing wing sailplane and the outer wing airfoil of the *ASG 29* sailplane, the *DU92-131-14* are shown in fig. 4.32. $Re\sqrt{c_l}$ is calculated assuming level flight at the respective MTOM for the morphing wing sailplane as well as the *ASG 29*. The spanwise locations and chords, for which the airfoils are designed for are $y = 3306$ mm and $\bar{c} = 633$ mm for the main wing airfoil, $y = 7467.5$ mm and $\bar{c} = 380.5$ mm for the outer wing airfoil and $y = 8920$ mm and $\bar{c} = 220$ mm for the tip airfoil. For comparison, the *DU92-131-14* airfoil is assumed to be designed for the same spanwise location as the outer wing airfoil, resulting in a chord length of $\bar{c} = 412.5$ mm and a $Re\sqrt{c_l} = 8.03\ 10^5$.

Comparing the low lift configurations, the outer wing morphing airfoil shows slightly lower drag coefficient values than the *DU92-131-14*. The drag coefficients become increasingly larger the further outboard the respective airfoil is designed for, which is due to the decreased chord length and Reynolds number. The outer wing and wingtip airfoil both reach a slightly higher maximum lift coefficient than the main wing airfoil, as desired for gentle stall characteristics. It is expected that the airfoils have a leading edge stall angle of attack beyond $\alpha = 20°$, which is enforced with the geometrical constraint defined in eq. 4.57. All three discussed airfoils reach a maximum lift coefficient above 1.825 with $\delta = 30°$ flap deflection, which is required for achieving the stall speed requirements specified by *CS 22.49*. The leading edge section undergoes a rigid body motion only, because the thickness change is allowed to start at $x > 0.0375\%$. The trailing edge angle is ensured due to the thickness constraint defined by constraint g_0 in the optimization problem eq. 4.1 and the $t_{\min}(x)$ values defined in table 4.2. Aileron effectiveness is ensured, because $\frac{\mathrm{d}c_l}{\mathrm{d}\delta}$ is clearly positive in morphed condition with full droop and flap deflection $\delta = 20°$. Furthermore, the maximum lift coefficient is reached at higher angles of attack and there is an ample lift reserve in post stall for the outer wing and tip airfoils compared to the main wing airfoil.

4.8 ANALYSIS OF POSSIBLE BOUNDARY-LAYER TRANSITION ON GAP SEAL

In this section, the influence of the backward facing step occurring due to the Mylar gap sealing on the bottom wing surface on the laminar boundary-layer stability is analyzed. In section 4.4.3.2, the criteria are developed. Here, these criteria are applied to the main wing airfoil and the more critical wing tip airfoil.

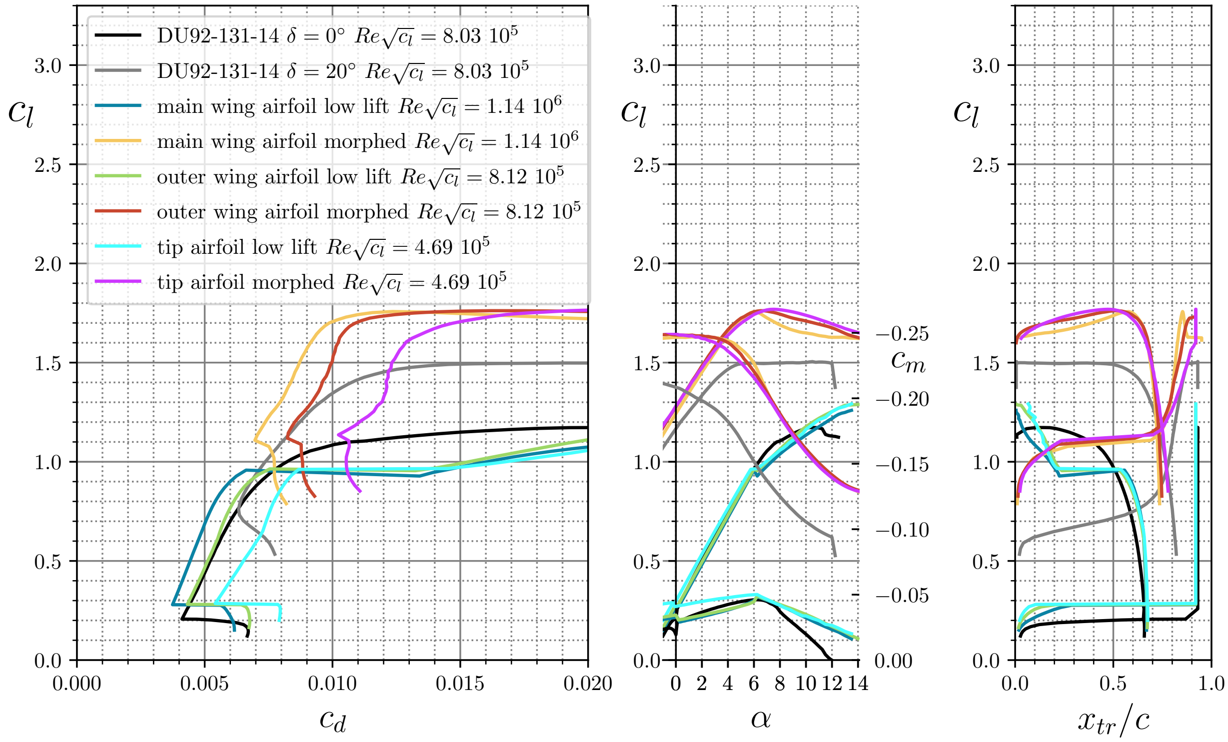

Figure 4.32: polars of postprocessed outer wing and wing tip airfoils in comparison with *ASG 29* outer wing airfoil *DU92-131-14*

The Mylar sealing foil has a thickness of $190\ \mu\mathrm{m}$. The main wing airfoil is designed for a chord length of $533\ \mathrm{mm}$. Hence $h = 3.57\ 10^{-4}$. The analysis is done at the lower corner of the laminar low-drag region ($c_l = 0.3, Re = 2.08\ 10^6$) as this marks the most critical case with the thinnest boundary-layer and the highest edge velocities. The edge velocity u_e at the end of the morphing section $x/\bar{c} = 0.25$ is evaluated. Also the displacement thickness δ^* is evaluated at this location for evaluating eq. 4.58. For the main wing airfoil, this results in the following values:

$$\delta^* = 6.75\ 10^{-4}$$
$$\frac{h}{\delta^*} = 0.529$$
$$\Delta\tilde{N} = 1.037.$$

Although the increase of the N_{crit} factor is not negligible, an analysis with *XFOIL-mod* shows, that the lower corner of the laminar low-drag region is increased only by $\Delta c_l = 0.01$. No drag increase within the laminar low drag region is found. Therefore, only insignificant influence of the sealing on airfoil performance is expected for the main wing airfoil.

The wing tip airfoil is designed for a chord length of $\bar{c} = 273\ \mathrm{mm}$. Assuming equal Mylar foil thickness everywhere, this results in $k = 6.95\ 10^{-4}$. The Reynolds number at the lower corner of the laminar low-drag region is $Re = 8.57\ 10^5$. Analyzing the boundary-layer properties at the gap location $x/\bar{c} = 0.25$, this results in the following values:

$$\delta^* = 1.034\ 10^{-3}$$
$$\frac{h}{\delta^*} = 0.529$$
$$\Delta\tilde{N} = 1.466.$$

Also for the wing tip airfoil, the Mylar gap seal decreases the critical amplification factor by a small amount. *XFOIL-mod* analysis shows an increase of the lower corner of the laminar low-drag region by $\Delta c_l = 0.015$. Again, the influence on total aircraft performance is expected to be very limited.

Concluding, no significant influence is expected due to the Mylar sealings of the gap at the end of the morphing section both for the main wing airfoil as well as the tip airfoil. Nevertheless, the sealing has to be crafted with utmost care, because every small extent reaching significantly into the boundary-layer may cause premature transition.

5 THREE-DIMENSIONAL WING AND WINGLET SHAPE DESIGN OPTIMIZATION

In this chapter, the design of the wing planform of the morphing wing sailplane is shown. As with the airfoil design method, a numerical optimization approach is used. The requirements on the wing planform and the winglet are derived from the overall aircraft requirements and discussed in section 5.1. The mathematical optimization problem formulation, aiming at a minimization of the drag, is shown in section 5.2. It is essential, that the geometry can be described precisely using a low number of design variables. A new simple and effective geometry parameterization is developed in section 5.3, that allows wide design freedom of possible wing and winglet geometries. For the wing planform optimization it is important that all wing drag components are precisely represented. These include the induced and profile drag of the wing. The induced drag calculation, using the multi lifting line method *Lifting_Line* and the profile drag calculation using lookup tables generated with *XFOILSUC-mod* are shown in section 5.4. The optimization algorithm is the same as used for the airfoil optimization, briefly discussed in section 5.5. Finally the results are shown and discussed in section 5.6.

5.1 WING PLANFORM AND WINGLET DESIGN OBJECTIVE AND REQUIREMENTS

As shown in section 3.1, the main design objective for a racing sailplane is the minimization of the average sink rate. The wing planform directly influences the induced drag and the profile drag. The drag of the fuselage and the tailplane are not considered here. It is assumed, that the influence of the wing planform on the drag of those components can be neglected for high aspect ratio sailplane wings. Then only the induced drag and the profile drag of the wing are of interest. The wing design aims to minimize the sum of induced and profile drag across various lift coefficients and flap configurations. The weighing of the different lift coefficients is derived from the overall aircraft performance objective, the minimum average sink rate, as shown in section 3.1.

Additional requirements set constraints for wing planform optimization. First, as the sailplane is intended for the *FAI* 18 meter class, the wing span is limited to $b \leq 18$ m. Second, the stall speed requirement from *CS 22.49* directly influences the minimum required maximum lift, as discussed in section 3.2.1. According to eq. 3.8, the maximum lift of a wing depends on the product of the wing area A and the maximum lift coefficient $c_{l,\max}$. The airfoils are already defined prior to the wing planform optimization. Therefore, the airfoil's $c_{l,\max}$ values are already fixed. The aircraft C_L may be slightly lower than the airfoils c_l, even with an elliptical planform wing, as shown by Deck [26]. Taking this into account, the wing area is set to $A = 8.6\ \mathrm{m}^2$, which gives a little reserve to the stall speed constraint.

The requirements on handling qualities are discussed in section 3.2.2. The certification specification requires, that the aircraft remains controllable in a wings level stall. It must also remain controllable in a stall during a coordinated $45°$ banked turn. This must be without aileron control reversal and without encountering uncontrollable rolling or spinning tendencies. On badly designed aircraft, which show such a behavior, the wing tip stalls before the wing root (c.f. [107], p.47f). Hence, it is essential that maximum lift is reached at the wing root before it is reached at the tips. The outboard and wing tip airfoils are designed such that the angle of attack at maximum lift $\alpha_{\max}$ is higher than at the root airfoils, as shown in section 4.7. It is assumed, that this measure is sufficient for benign stall/spin handling characteristics. Therefore, for the wing planform optimization, no constraint is set for handling characteristics, as long as the local lift coefficients c_L on the outboard wing stations are smaller or equal than on the inner wing stations. The optimization result is checked if it fulfills this requirement in section 5.6.

5.2 MATHEMATICAL PROBLEM FORMULATION

The objective and constraints discussed in section 5.1 are transferred to the following optimization problem:

$$\begin{array}{lll}
\min_{\mathbf{d}} & f(\mathbf{d}) = \sum_{op} w_{op}\, C_{D,\text{wing}}(C_{L,op}, \mathbf{d}) & \\
\text{subject to:} & h_0 = 1 - \frac{A}{A_{\text{target}}} = 0 & \text{where } A_{\text{target}} = 8.6\ \text{m}^2 \\
 & h_1 = 1 - \frac{b}{b_{\text{target}}} = 0 & \text{where } b_{\text{target}} = 18\ \text{m} \\
 & d_i^l \leq d_i \leq d_i^u & i = 0, \dots, n \\
\text{where:} & \mathbf{d} = [d_0, d_1, \dots, d_n]^\mathsf{T} & \mathbf{d} \in \mathbb{R}^n
\end{array} \tag{5.1}$$

The wing drag coefficient is the sum of the induced drag coefficient and the profile drag coefficient:

$$C_{D,\text{wing}} = C_{Di} + C_{Dp}. \tag{5.2}$$

The induced drag coefficient is calculated with *Lifting_Line*, discussed in section 5.4.1. The wing profile drag calculation is discussed in section 5.4.2. The constraint h_0 enforces the wing area to be $A = A_{\text{target}} = 8.6\ \text{m}^2$. The constraint h_1 ensures, that the span is equal to the maximum allowable span for the *FAI* 18 meter class. The constraints h_0 and h_1 are directly enforced via the wing planform geometry parameterization method, as will be shown in section 5.3. Therefore, the constraints do not need to be enforced by the optimization algorithm or with a penalization method as with the airfoil optimization. The optimization problem reduces to a pure minimization of the objective function.

The weights for the respective operation point *op* are based on the mean sink rate as described in section 3.1.2. The weights represent the influence of the frequency distribution, the normal acceleration and the lift coefficient on the mean sink rate eq. 3.7. Based on that equation, the weights are calculated as:

$$w_{op} = f_{t,op}(\hat{C}_{L,op})\sqrt{n_{z,op}}\frac{1}{{C_{L,op}}^{3/2}}, \tag{5.3}$$

with:

$$\frac{\hat{C}_{L,op}}{C_{L,op}} = \frac{10.5}{8.6},$$

which is the ratio of the wing areas and hence wing loadings between the *ASG 29* reference sailplane and the morphing wing sailplane.

As a good balance between calculation time and a good coverage of the operating range of the sailplane, it is decided to analyze three lift coefficients in high speed configuration and two lift coefficients in low speed configuration. Circling flight with $\phi_b = 37°$ is assumed for the low speed calculation points, resulting in $n_{z,\text{circ}} = \frac{1}{\cos\phi} = 1.252$. The selected aircraft flap configurations, the respective lift coefficients, normal accelerations and weights are given in table 5.1.

Table 5.1: operation points for the wing planform optimization

op	flap configuration	C_L	$n_{z,op}$	w_{op}
1	undeformed	0.325	1.0	26.1
2	undeformed	0.525	1.0	27.3
3	undeformed	0.8	1.0	10.4
4	morphed	1.5	1.252	15.2
5	morphed	1.65	1.252	5.7

5.3 WING PLANFORM AND WINGLET GEOMETRY PARAMETERIZATION

For efficient numerical optimization a well suited wing planform geometry parameterization method is necessary. It should efficiently parameterize a wide range of geometries (i. e., a large design space) using a low number of design variables. The fundamental geometry parameters to be described are the wing chord distribution, the dihedral distribution, the sweep and the twist distribution. Most methods found in literature (e.g. [77], [125], [60], [85], [61]) directly parameterize these properties at several distinct spanwise stations. This induces a non-orthogonality of design variables on the geometry description. If one considers the parameterization of the wing planform, a change in a subset of the design variable vector, i. e.some chord length values are held constant and others change, always leads to a non-smooth, jagged spanwise chord distribution. This in consequence leads to an increase of induced drag and an increase of the objective function value. This results in a multi-modal design space with numerous local minima, making it difficult for the optimization algorithm to identify optimal designs. Therefore, it was decided to develop a new, simple and versatile geometry parameterization method for wing planform design, which naturally decouples the design variables and is able to describe a multitude of possible wing and winglet configurations efficiently with a low number of design variables. Furthermore, the method enables to directly set a desired wing span and wing area. This removes the need for constraint enforcement for the optimization algorithm or a penalization strategy. The method is introduced in this section.

5.3.1 *Basis functions*

The geometry parameterization method presented in this work describes the combined wing and winglet geometry, i.e. the wing chord distribution $\bar{c}(s)$, the wing sweep distribution $\phi(s)$, the dihedral distribution $\kappa(s)$ and the twist distribution $\varepsilon(s)$. This distributions are obtained via a combination of three simple basis functions $a(s)$, $e(s)$ and $q(s)$ and their integrals/derivatives. The basis functions depend on a non-dimensional arc length coordinate s, with $s = 0$ being the wing root and $s = 1$ being the winglet tip, or the wing tip if no winglet exists. With a combination of these basis functions and their derivatives/integrals, the fundamental distributions $\bar{c}(s)$, $\phi(s)$, $\kappa(s)$ and $\varepsilon(s)$ are described. After parameterization, the y-coordinates are scaled, so that $\max(y) = b/2$. Also the chord distribution $\bar{c}(s)$ is parameterized in normalized form first, with the normalization with the root chord $\bar{c}_r$:

$$\tilde{\bar{c}}(s = 0) = \frac{\bar{c}}{\bar{c}_r} \tag{5.4}$$

.

5.3.1.1 *First basis function: Hyperbolic tangent*

The first basis function is the a shifted and scaled hyperbolic tangent function:

$$a_1(s;\sigma,\omega,a_r,a_t) = \frac{\tanh(\sigma\ \omega) + \tanh(\sigma(s-\omega))}{\tanh(\sigma\omega) + \tanh(\sigma(1-\omega))}(a_t - a_r) + a_r, \tag{5.5}$$

with the non-dimensional spanwise coordinate $0 \le s \le 1$ as the primary variable and with fixed parameters σ, ω, a_r and a_t. These parameters are later set as design variables to influence the shape of the basis functions and in consequence of the wing geometry. The derivative of the first basis function a_1 is designated as a_0:

$$a_0(s;\sigma,\omega,a_r,a_t) = \frac{\mathrm{d}a_1}{\mathrm{d}s} = \frac{\sigma}{\cosh^2(\sigma(s-\omega))(\tanh(\sigma\omega) + \tanh(\sigma(1-\omega)))}(a_t - a_r) \tag{5.6}$$

The integral of the first basis function a_0 is designated as a_2:

$$\begin{aligned} a_2(s;\sigma,\omega,a_r,a_t) &= \int_0^s a_1(s;\sigma,\omega,a_r,a_t)\,\mathrm{d}s = \\ &= \frac{\sigma s\sinh(\omega\sigma) + \cosh(\omega\sigma)\left(\ln(\cosh(\sigma(\omega-s))) - \ln(\cosh(\sigma\omega)\right)}{\sinh(\sigma)\sigma} \\ &\quad \cdot \cosh(\sigma - \omega\sigma)\left(\tan(a_t) - \tan(a_r)\right) + \tan(a_r)s \end{aligned} \tag{5.7}$$

The parameter ω determines the location of the inflection point of $a_1(s)$. The parameter σ determines the gradient at the inflection point. The parameter a_r is the left or root side asymptotic value and a_t is the right or tip side asymptotic value of the function. The functions a_0, a_1 and a_2 are shown in fig. 5.1 with $\omega = 0.95$ and $\sigma = 100$.

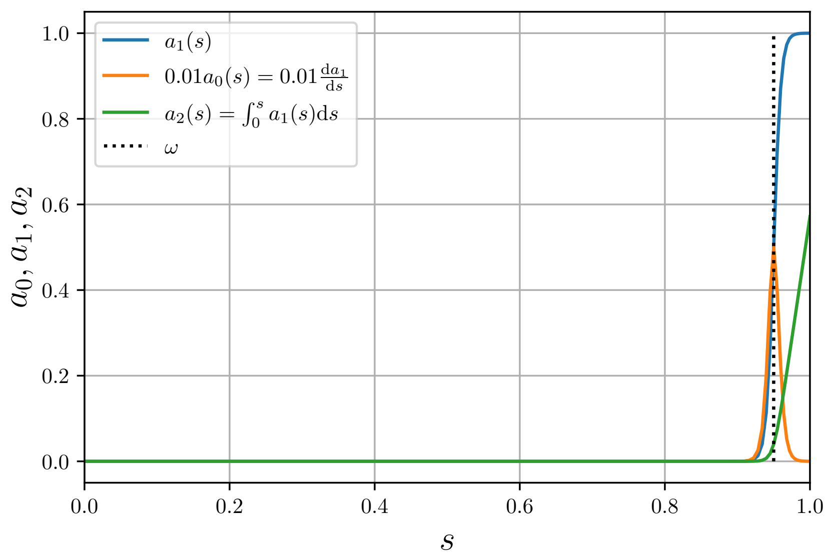

Figure 5.1: Scaled and shifted tanh basis function $a_1(s)$, it's derivative $a_0(s)$ and integral $a_2(s)$ with $\omega = 0.95, \sigma = 100$

There are two important locations which will be used for further considerations. These are the normalized spanwise coordinates s, where the tangent at the inflection point crosses the asymptotes a_r and a_t. These locations are designated s_0, that is the location closer to the root and s_1, that is the location closer to the tip. As will be shown later, s_0 is the onset location of the winglet transition and s_1 is the location, where the winglet transition is finished. These locations s_0 and s_1 are calculated as:

$$s_0 = \omega - \frac{1}{2a_0(\omega)} \qquad \text{with } a_r = 0 \text{ and } a_t = 1 \tag{5.8}$$

and:

$$s_1 = 2\omega - s_0. \tag{5.9}$$

5.3.1.2 *Second basis function: Superellipse*

The second basis function is the superellipse equation:

$$e_1(s;n) = \left(1 - |s|^n\right)^{1/n}. \tag{5.10}$$

The superellipse basis function for $n \in [1, 2, 4]$ and for $n \to \infty$ is shown in fig. 5.2. For $n = 1$, a linear decreasing function is obtained, for $n = 2$ the normal ellipse equation is obtained, whereas for $n \to \infty$ a rectangular function is obtained. The derivative of the superellipse equation reads as:

$$e_0(s;n) = \left(1 - |s|^n\right)^{1/n-1} s^{n-1}. \tag{5.11}$$

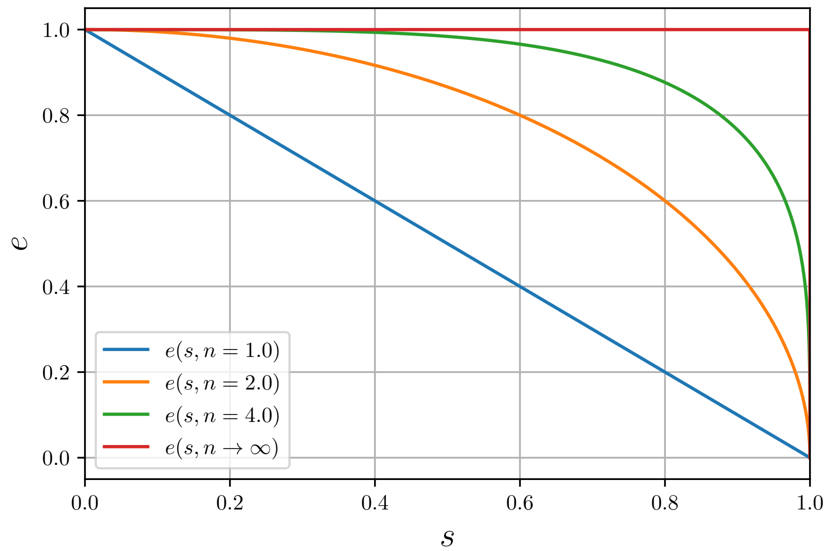

Figure 5.2: Superellipse basis function $e(s)$ with $n \in [1, 2, 4]$

5.3.1.3 *Third basis function: Parabolic function*

The third basis function required is a parabola:

$$q(s; q_0, q_1, q_2) = q_0 + q_1 s + q_2 s^2, \tag{5.12}$$

with the variable s and three fixed parameters q_0, q_1 and q_2.

5.3.2 *Parameterization of the wing geometry*

The basis functions defined in section 5.3.1 are all what's needed for describing the wing geometry. For this, the chord distribution, the wing reference axis, the twist and sweep distributions and the relative location of the reference axis on the wing chord needs to be defined. These distributions are described with a linear combination of the basis functions, as will be shown in the following sections.

5.3.2.1 *Parameterization of the chord distribution*

First the normalized wing chord distribution is defined as:

$$\tilde{\bar{c}}(s) = e_1(s; n = n_{SE}) a_1(s; \sigma = \sigma_{WL}, \omega = \omega_{WL}, a_r = 1.0, a_t = e_{WL,c}) f_A. \tag{5.13}$$

The superellipse equation is multiplied with the hyperbolic tangent basis function a_1. This is to represent the chord reduction of the winglet, with the chord reduction factor $e_{WL,c}$. The location of the winglet transition region is determined with ω_{WL}, the transition gradient with σ_{WL}, which also determines the winglet radius as will be seen later. The factor f_A is later used to scale the chord distribution, so that the actual wing area A matches the target wing area A_{target}.

For easier manufacturing, it is desired to have a wing with a chord distribution, that consists of multiple trapezoidal sections. This trapezoidal sections approximate the desired continuous chord distribution $\bar{c}(s)$. Beginning just before the winglet transition location s_0 up to the winglet tip, the chord distribution is desired to be continuous. The chord distribution of the trapezoidal approximation is designated as $\bar{c}_{tr}(s)$. For a good approximation of the continuous chord distribution, the trapezoidals are defined to be tangent to the continuous chord distribution at the following s-coordinates:

$$s_{tr,tan,i} = \cos\left(\frac{i \arccos\left(2\omega_{WL} - s_0\right)}{n_{tr}}\right) \quad \text{with} \quad i = 1 \cdots n_{tr}. \tag{5.14}$$

Using the derivative of the chord distribution

$$\begin{aligned}\tilde{\bar{c}}'(s) = \frac{\mathrm{d}\tilde{\bar{c}}}{\mathrm{d}s} &= e_1(s; n = n_{SE}) a_0(s; \sigma = \sigma_{WL}, \omega = \omega_{WL}, a_r = 1.0, a_t = e_{WL,c}) + \\ &\quad + e_0(s; n = n_{SE}) a_1(s; \sigma = \sigma_{WL}, \omega = \omega_{WL}, a_r = 1.0, a_t = e_{WL,c}),\end{aligned} \tag{5.15}$$

the s coordinates of the trapezoidal kinks can then be calculated as:

$$s_{tr,i} = \begin{cases} \frac{\tilde{\bar{c}}(s_{tr,tan,i}) - \tilde{\bar{c}}(s_{tr,tan,i+1}) + \tilde{\bar{c}}'(s_{tr,tan,i+1}) s_{tr,tan,i+1} - \tilde{\bar{c}}'(s_{tr,tan,i}) s_{tr,tan,i}}{\tilde{\bar{c}}'(s_{tr,tan,i+1}) - \tilde{\bar{c}}'(s_{tr,tan,i})} & \text{if} \quad i < n_{tr} \\ s_{tr,tan,n_{tr}} & \text{if} \quad i = n_{tr}. \end{cases} \tag{5.16}$$

And the corresponding normalized chords are:

$$\tilde{\bar{c}}_{tr}(s) = \begin{cases} \tilde{\bar{c}}'(s_{tr,tan,i}) \left(s_{tr,tan,i+1} - s_{tr,tan,i}\right) + \tilde{\bar{c}}(s_{tr,tan,i}) & \text{if} \quad 0 \le s_{tr,i} \le s < s_{tr,i+1} \le s_{tr,n_{tr}} \\ \tilde{\bar{c}}(s) & \text{if} \quad s > s_{tr,n_{tr}} \end{cases}. \tag{5.17}$$

Between those locations, the chords are evaluated using linear interpolation. Beginning from a certain distance inside of the winglet transition ($s > s_{tr,n_{tr}}$), the winglet shape is continuous, instead of trapezoidal. An exemplary continuous (light blue) and trapezoidal (dark blue) normalized chord distribution with four trapezoidal sections is shown in fig. 5.3. Finally, the normalized chord distribution has to be scaled so that the wing area matches the target wing area. This is shown in section 5.3.3.3.

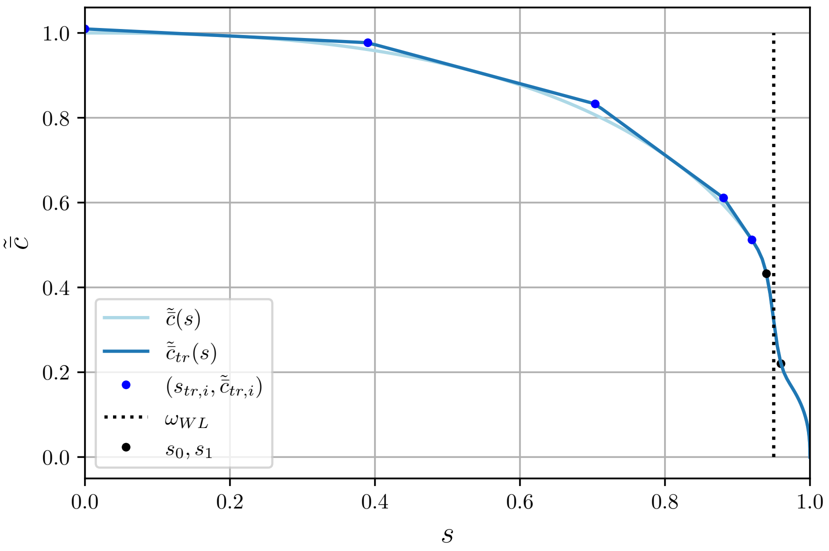

Figure 5.3: continuous (light blue) and trapezoidal (dark blue) chord distribution $\tilde{\tilde{c}}(s)$ with kinks (blue dots), using $n = 2, e_{WL,c} = 0.5, n_t r = 4$

5.3.3 *Wing reference axis*

Second, the wing reference axis is defined via it's sweep angle $\phi(s)$ and it's dihedral angle $\kappa(s)$. The sweep angle $\phi(s)$ is defined as:

$$\phi(s) = e_1(s; \sigma = \sigma_{WL}, \omega = \omega_{WL}, a_r = \phi_r, a_t = \phi_t) + e_0(s; \sigma = \sigma_{WL}, \omega = \omega_{WL}, a_r = 0.0, a_t = \Delta\phi_{WL}), \tag{5.18}$$

where s is the variable, while the parameters σ, ω, a_r and a_t are fixed to the values shown. ϕ_r is the wing sweep angle of the main wing and ϕ_t is the sweep angle at the winglet tip. The reference axis is the trailing edge flap hinge line on the main wing and the trailing edge on the winglet. This ensures, that the flap hinge axis is straight, which is essential for free flap movement. Also it is desired to have a straight trailing edge on the winglet. Therefore, the reference axis is shifted back in the transition region between wing and winglet. The back-shift value $\Delta\phi_{WL}$ is calculated as:

$$\Delta\phi_{WL} = c(s_0)(1 - x_{r,tip}), \tag{5.19}$$

where s_0 is the approximate spanwise length coordinate and $x_{r,t} = 0.83$ is the normalized x-coordinate of the flap hinge axis of the tip airfoil. The dihedral angle is defined as:

$$\kappa(s) = e_1(s; \sigma = \sigma_{WL}, \omega = \omega_{WL}, a_r = \kappa_r, a_t = \kappa_t) + \kappa_{\text{bendingline}}(s), \tag{5.20}$$

where the root dihedral angle is set to be equal to the *ASG 29* sailplane $\kappa_r = \kappa_{r,\text{ASG 29}} = 3.25°$ and κ_t is the winglet dihedral. An additional distribution $\kappa_{\text{bendingline}}(s)$ can be used to simulate wing bending. The cartesian coordinates of the reference axis are calculated by integration from the dihedral and sweep distributions:

$$\bar{\mathbf{x}}_{\text{axis}}(s) = \left\{ \begin{array}{c} \bar{x}_{\text{axis}}(s) \\ \bar{y}_{\text{axis}}(s) \\ \bar{z}_{\text{axis}}(s) \end{array} \right\} = \left\{ \begin{array}{c} \int_0^s \sin\phi(s')\,\mathrm{d}s' \\ \int_0^s \cos\phi(s')\cos\kappa(s')\,\mathrm{d}s' \\ \int_0^s \sin\kappa(s')\,\mathrm{d}s' \end{array} \right\}. \tag{5.21}$$

The angle conventions and the transformation between $\mathrm{d}s'$ and the angles κ and ϕ are shown in fig. 5.4. The integrals are evaluated numerically using the Clenshaw-Curtis quadrature method [21]. The transformation from the dimensionless axis coordinates $\bar{\mathbf{x}}_{\text{axis}}$ to the dimensional axis coor-

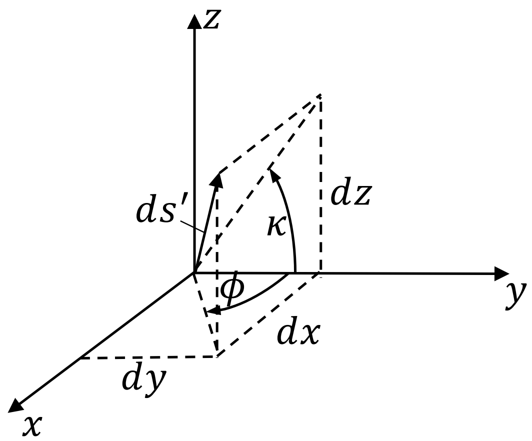

Figure 5.4: definition of the sweep angle ϕ and the dihedral angle κ in the aircraft reference axis system

dinates $\mathbf{x}_{\text{axis}}(s)$ is obtained by scaling the tip axis coordinate $\bar{y}_{\text{axis}}(s = 1)$ to the half span $b/2$:

$$\mathbf{x}_{\text{axis}}(s) = \bar{\mathbf{x}}_{\text{axis}}(s)\frac{b_{\text{target}}/2}{\bar{y}_{\text{axis}}(s=1)}. \tag{5.22}$$

With this scaling, the span of the wing is hard-wired. With this, no equality constraint needs to be enforced by the optimization algorithm, because it is already ensured with this parameterization method, that the span is always set as desired.

5.3.3.1 *Relative flap hinge axis location*

Furthermore, the position of the flap hinge axis $\bar{x}_r$ in relative airfoil coordinates is needed to describe the wing geometry. As mentioned in section 4.6.4, the main wing airfoil has a 16% deep flap, hence $\bar{x}_{r,m} = 0.84$. The tip airfoil has a 17% deep flap (c.f. section 4.7), giving $\bar{x}_{r,t} = 0.83$. The relative flap axis has a linear transition in spanwise direction starting at the begin of the blend between the main wing airfoil and the outer wing airfoil ω_{trans}. Hence, two linear segments are obtained, with a kink at the start of the blend between the main wing airfoil and the outer wing airfoil. For comparison, the airfoil distribution is shown in fig. 4.1. The winglet as well as the winglet transition region have no flap, therefore the $\bar{x}_r$ location can be arbitrarily defined. In this work, it is chosen that the $\bar{x}_r$ location moves gradually to the trailing edge $\bar{x}_r = 1$, thus giving a straight trailing edge on the winglet, if the reference axis is straight. Using the base functions 5.5 and 5.7, the relative flap axis location can be described as:

$$\begin{aligned}\bar{x}_r(s) = \bar{x}_{r,m} &+ a_2\left(s;\sigma=500,\omega=\omega_{\text{trans}},a_r=0,a_t=\frac{\bar{x}_{r,t}-\bar{x}_{r,m}}{\omega-\omega_{\text{trans}}}\right)\\ &- a_2\left(s;\sigma=500,\omega=\omega_{WL},a_r=0,a_t=\frac{\bar{x}_{r,t}-\bar{x}_{r,m}}{\omega-\omega_{\text{trans}}}\right)\\ &+ a_1\left(s;\sigma=\sigma_{WL},\omega=\omega_{WL},a_r=0,a_t=1-\bar{x}_{r,t}\right),\end{aligned} \tag{5.23}$$

where the kink at ω_{trans} is approximated by the base function a_1 with a high slope value of $\sigma = 500$.

5.3.3.2 *Twist distribution*

The airfoil twist distribution $\varepsilon(s)$ is defined using the basis functions a_1 and q:

$$\varepsilon(s) = a_1(s;\sigma=\sigma_{WL},\omega=\omega_{WL},a_r=0,a_t=1)q(s;q_0,q_1,q_2). \tag{5.24}$$

It is intended to have no twist on the main wing, because all airfoils have the same lower corner of the laminar low-drag region. Therefore $\varepsilon(s < s_0)$ must be approximately zero. This is achieved with the left, root side asymptotic value a_r of the base function a_1 being zero. On the winglet part, the twist should be a parabolic distribution. This is achieved by setting the right asymptotic value a_r to one. The parabola coefficients q_0, q_1, q_2 are calculated by solving the following linear equation system:

$$\left\{\begin{array}{l}\varepsilon(s=\omega_{WL}) = a_1(s=\omega_{WL})\left(q_0+q_1\omega_{WL}+q_2\omega_{WL}^2\right)\\ \varepsilon\left(s=\frac{\omega_{WL}+1}{2}\right) = a_1(s=\frac{\omega_{WL}+1}{2})\left(q_0+q_1\frac{\omega_{WL}+1}{2}+q_2\left(\frac{\omega_{WL}+1}{2}\right)^2\right)\\ \varepsilon(s=1) = a_1(s=1)\left(q_0+q_1+q_2\right)\end{array}\right\} = \left\{\begin{array}{c}2\varepsilon_1\\ \varepsilon_2\\ \varepsilon_3\end{array}\right\}. \tag{5.25}$$

With this approach, explicit twist angles $\varepsilon_1, \varepsilon_2$ and ε_3 are set at the winglet transition location ω_{WL}, at the midpoint between ω_{WL} and the tip, determining the overall twist distribution. q_1 is doubled, because the transition function $e_1(s;\sigma_{WL},\omega_{WL},0,1)$ is 1/2 at $s = \omega_{WL}$. An exemplary twist distribution with $\varepsilon_1 = -2.5°, \varepsilon_2 = -3°$ and $\varepsilon_3 = -2°$ is shown in fig. 5.5.

5.3.3.3 *Leading edge and trailing edge coordinates*

The wing planform is finally determined via the leading- and trailing edge coordinates. For that, first the normalized chord distribution $\bar{c}_{tr}(s)$ has to be scaled, so that the wing area matches the target wing area A in the x, y plane. Hence the root chord $\bar{c}_r$ is calculated as:

$$\bar{c}_r = \frac{A_{\text{target}}}{\int_0^1 \bar{c}_{tr}(s)\frac{\mathrm{d}y_{\text{axis}}}{\mathrm{d}s}\,\mathrm{d}s}, \tag{5.26}$$

where $\frac{\mathrm{d}y_{\text{axis}}}{\mathrm{d}s} = \cos\phi(s)\cos\kappa(s)\frac{b/2}{\bar{y}_{\text{axis}}(s=1)}$ as can be seen from equations 5.21 and 5.22. The numerator is the target wing area, whereas the denominator is the actual wing area. Furthermore, small twist angles are implicitly assumed, thus neglecting the influence of the wing twist on the wing area. As the twist is almost zero on the main part of the wing and small on the winglet, this assumption has almost zero effect and allows to directly calculate the scale factor instead of an iterative determination. Scaling the wing area instead of direct parameterization allows to avoid

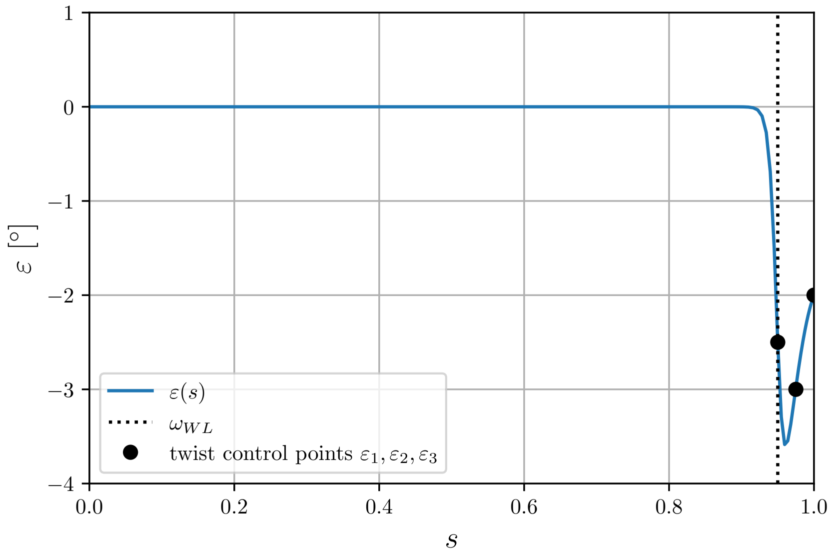

Figure 5.5: twist distribution with $q_1 = -2.5°, q_2 = -3°$ and $q_3 = -2°$

to use a constraint enforcement strategy for the wing area equality constraint in the optimization problem eq. 5.1. The wing chord distribution is finally calculated as:

$$\bar{c}_{tr}(s) = \bar{c}_r\, \tilde{\tilde{c}}_{tr}(s). \tag{5.27}$$

Subsequently, the leading edge coordinates are calculated. For that, based on the coordinates of the axis $x_{\text{axis}}(s)$, the forward part of the wing chord is added to the axis coordinates. It is rotated using the wing twist around the twist axis, which is defined by projecting $\mathbf{x}_{\text{axis}}$ to the y, z-plane. The rotation around the twist rotation vector $\mathbf{x}_{tw}$ is calculated using Rodrigues rotation formula [101]. The leading edge coordinates then can be calculated as:

$$\mathbf{x}_{LE}(s) = \mathbf{x}_{\text{axis}}(s) - \begin{Bmatrix} \cos\varepsilon(s) + x_{tw}^2(1-\cos\varepsilon(s)) \\ z_{tw}\sin\varepsilon(s) \\ z_{tw}x_{tw}(1-\cos\varepsilon(s)) \end{Bmatrix} \bar{c}_{tr}(s)\bar{x}_r(s), \tag{5.28}$$

and the trailing edge coordinates are

$$\mathbf{x}_{TE}(s) = \mathbf{x}_{\text{axis}}(s) + \begin{Bmatrix} \cos\varepsilon(s) + x_{tw}^2(1-\cos\varepsilon(s)) \\ z_{tw}\sin\varepsilon(s) \\ z_{tw}x_{tw}(1-\cos\varepsilon(s)) \end{Bmatrix} \bar{c}_{tr}(s)\left(1-\bar{x}_r(s)\right). \tag{5.29}$$

The twist axis is defined by projecting $\mathbf{x}_{\text{axis}}$ to the y, z-plane and subsequent normalization:

$$\mathbf{x}_{tw} = \begin{Bmatrix} x_{tw} \\ y_{tw} \\ z_{tw} \end{Bmatrix} = \begin{Bmatrix} x_{\text{axis}} \\ 0 \\ z_{\text{axis}} \end{Bmatrix} \frac{1}{\sqrt{x_{\text{axis}}^2 + z_{\text{axis}}^2}}. \tag{5.30}$$

A wing can now be fully parameterized by 14 parameters. These are the span b and the target wing area A_{target}. Furthermore, the twist values on the winglet root ε_1, at winglet mid-length ε_2

and at the winglet tip ε_3. Also the winglet transition location ω_{WL} and the parameter σ_{WL}, which defines the winglet radius. And the wing sweep angle at the wing root ϕ_r and at the wing tip ϕ_t as well as the dihedral angle at the root κ_r and at the winglet tip κ_t. The winglet root to wing tip chord ratio $e_{WL,c}$ is also one of these parameters as well as the planform superellipse exponent n_{SE}. Finally, the number of trapezoidal sections n_{tr} is a parameter. Any of these parameters can be used as a design variable. In this work, only some of these are used as design variables, others remain fixed as will be discussed in the next section.

5.3.3.4 *Parameterization example*

For demonstrating the capabilities of the new planform and winglet parameterization method three examples are introduced by the parameters given in table 5.2. These are a conventional winglet, a planar wing with an elliptic wing tip and a blended winglet. The three side views of the resulting wing shapes are shown in fig. 5.6. The flight shape has been modeled using the bending line calculated by Sturm et al. [117]. It can be seen, that a wide variety of wing shapes can be parameterized with few parameters. The only differences between a conventional wing tip to a winglet is only the choice of the tip chord ratio $e_{WL,c}$, which is one for the normal wingtip and $0 < e_{WL,c} \leq 1$ for a winglet and the tip dihedral κ_t, which is equal to the wing dihedral κ_r for a wing tip and $\kappa_r < \kappa_t \leq 90°$ for a winglet. The choice of ω_{WL} and σ_{WL} are arbitrary for the wing tip, since they have no effect because of $e_{WL,c} = 1$. A blended winglet differs from a conventional winglet only by $\omega_{WL} = 1$ and a chord ratio $e_{WL,c} = 1$. These parameters can be altered by an

Table 5.2: Planform examples parameters

		wing type		
Parameter	Design variable	Planar wing	Blended winglet	Winglet
b		18 m	18	18
A_{target}		8.6	8.6	8.6
ε_1	d_0	0°	0°	−2.5°
ε_2	d_1	0°	0°	−3°
ε_3	d_2	0°	0°	−2°
ω_{WL}	d_3	1	1	0.95
σ_{WL}	d_4	1	30	100
ϕ_r		−1°	−1°	−1°
ϕ_t		−1°	−1°	30°
κ_r		3.25°	3.25°	3.25°
κ_t	d_5	3.25°	80°	80°
$e_{WL,c}$	d_6	1	1	0.5
n_{SE}	d_7	2	2.25	2.5
n_{tr}		5	6	4

optimization algorithm for efficient numerical optimization. In this work, the span and the wing area is fixed to ($b = 18$ m, $A = 8.6$ m^2). The same holds for the wing dihedral $\kappa_r = 3.25°$ and the wing sweep $\phi_r = -1°$ as well as for the number of trapezoidal segments $n_{tr} = 9$. The design variables are $d_0 = \varepsilon_1$, $d_1 = \varepsilon_1$, $d_2 = \varepsilon_2$, $d_3 = \omega_{WL}$, $d_4 = \sigma_{WL}$, $d_5 = \kappa_t$, $d_6 = e_{WL,c}$ and $d_7 = n_{SE}$. It may be surprising, that the tip sweep ϕ_t is not set as a design variable. However, as mentioned by Maughmer [77], the tip sweep has a similar effect than the tip wash out angle ε_3. Therefore it is decided, that the tip sweep is fixed to $\phi_t = 30°$ in this work and the tip wash out angle ε_3 is used as a design variable.

To show the effect of winglets on performance, also a wing without winglet is optimized. All parameters are fixed as shown in table 5.2, but the superellipse exponent is altered as the only design variable ($d_0 = n_{SE}$). A blended winglet is not optimized, because it is a special case of a classical winglet in this parameterization scheme. Consequently, if a blended winglet would be optimal, the optimization algorithm would drive the design towards such one.

With only eight design variables, the shape of the wing and winglet can be described consistently and allows a wide variation of wing shapes. The design variables have a clear and distinct influence on wing shape. A particular shape can only be uniquely described with a particular set of variables. This gives a high mutual orthogonality of the design variables, which is important that no additional local optima are introduced with the design parameterization. A further advantage is that no extra constraints are needed for the wing span and the wing area. They are directly set with the parameterization method. The same holds for the twist on the main part on the wing, which should be zero. This simplifies the optimization formulation significantly. Also the fact that all transitions (chord, twist) from wing tip to winglet root start and end at the same location and all are completely smooth. A further advantage of the presented method is its easy analytical differentiability, allowing for gradient based optimization. All derivatives are continuous.

However, there are also some disadvantages to other methods. The method can only handle super-elliptical planform shapes. This however could be circumvented with a different planform shape function instead of the superellipse (eq. 5.10) or a CST approach for the chord distribution (eq. 5.13). Furthermore, consistent transformation of the geometry to Computer Aided Design (CAD) is not easy, because the underlying base functions are normally not implemented in modern CAD systems. Therefore, the geometry has to be evaluated at various locations and interpolated with standard CAD geometrical elements like B-splines.

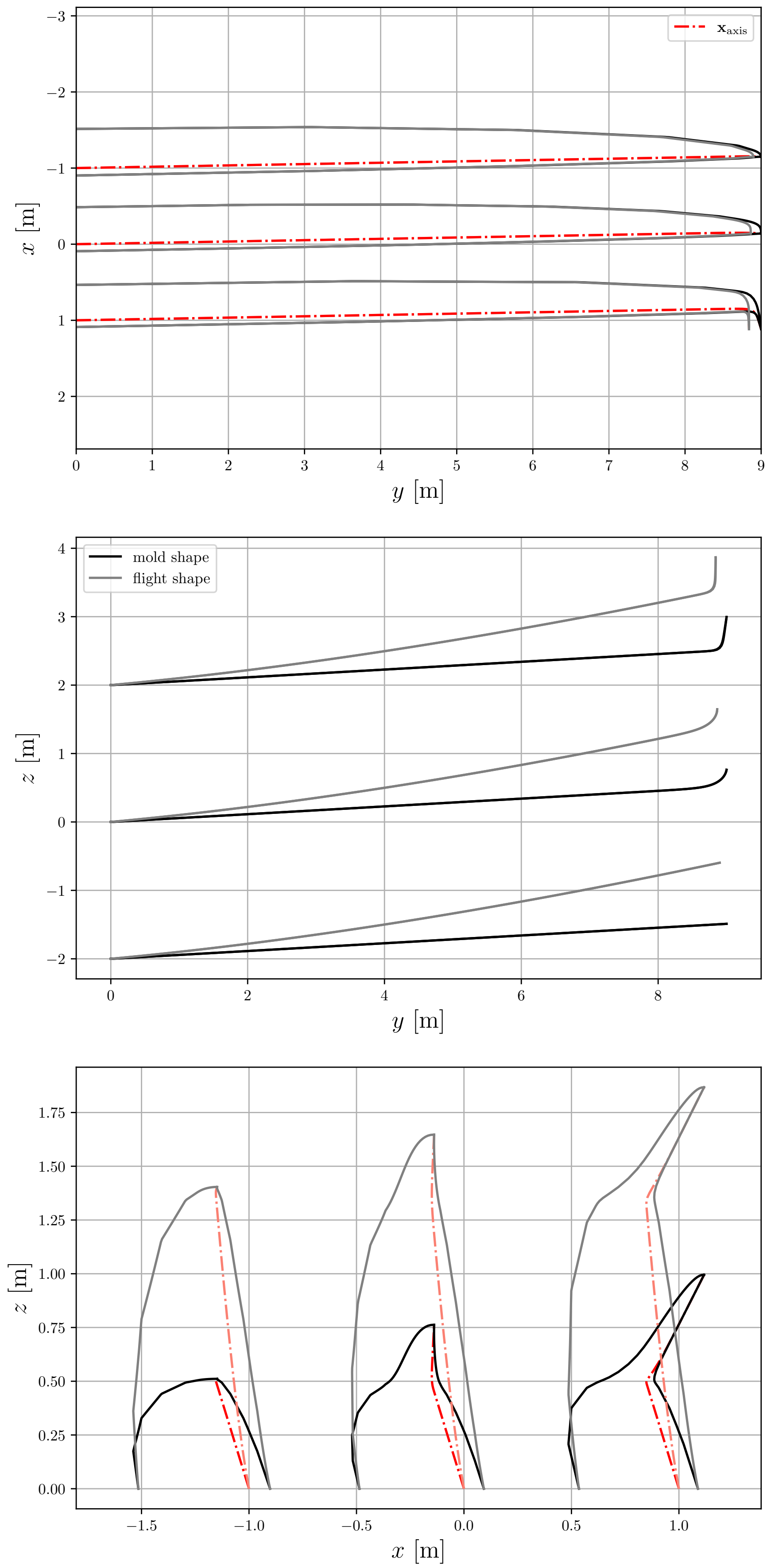

Figure 5.6: Planform parameterization examples: straight wing, blended winglet, winglet

5.4 WING DRAG CALCULATION

The wing drag calculation method used for wing planform optimization consists of the method *Lifting_Line*, version 3.0 for induced drag calculation and a profile drag calculation method based on interpolation of a pre-calculated airfoil polar database, which is calculated using *XFOILSUC-mod*.

The total drag of the wing can be calculated as:

$$C_{D,\text{wing}} = C_{Di} + C_{Dp}, \tag{5.31}$$

where C_{Di} is the induced drag calculated with *Lifting_Line* as described in section 5.4.1 and C_{Dp} is the profile drag, calculated with *XFOILSUC-mod*. Calculating profile drag with a two-dimensional integral boundary layer solver requires that the two-dimensional flow assumption is valid. Fuselage drag, interference drag, and tailplane drag are not considered in wing planform optimization. The profile drag interpolation is discussed in 5.4.2.

5.4.1 *Multi Lifting Line Method Lifting_Line*

Lifting_Line is a multi lifting line method, written in Fortran. As the viscous region of the flow field is not modeled, only the induced drag coefficient of the wing C_{Di} is calculated. The method is described in detail by it's developer Horstmann [52] and was further extended by Liersch [68]. The flow field is modeled using a vortex sheet. *Lifting_Line* uses a quadratic vorticity distribution in spanwise direction. Chordwise, the vorticity of the vortex sheet is lumped into multiple discrete vortex lines. These are bound along the spanwise direction. The vorticity arrangement of one single lifting element is shown in fig. 5.7. The displacement due to the airfoil thickness is not considered. Hence the wing middle surface, defined by the camber lines of the airfoils, is modeled. As a singularity method, only pure subsonic flows can be calculated. A Prandtl-Glauert correction is used for considering compressibility effects. The induced drag is calculated using Trefftz plane analysis.

Compared to vortex lattice methods, where the spanwise vorticity is constant along the spanwise direction of a panel, the smoothly varying vorticity distribution with the quadratic ansatz in *Lifting_Line* improves precision significantly. Drastically fewer spanwise elements are needed for equal precision, as shown by Coder [22]. This results in significantly improved induced drag prediction. In comparison to higher fidelity methods (RANS-CFD), the calculation time is considerably faster, in the order of seconds vs. hours for RANS-CFD. This allows for efficient numerical optimization.

5.4.2 *Wing profile drag calculation*

The wing profile drag is calculated via integrating the profile drag along the spanwise arc length coordinate s:

$$C_{Dp} = \frac{1}{U_\infty^2 A} \int_{-s_b}^{s_b} \left(\mathbf{u}\cdot\mathbf{u} - (\mathbf{u}\cdot\mathbf{n})^2\right) f_{d,p}\; c_d(c_l(s), Re(\mathbf{u}, s))\; \bar{c}(s)\,\mathrm{d}s, \tag{5.32}$$

where A is the wing area projected into the x, y plane and c is the local chord length. The wing sections are aligned on reference planes parallel to the x-axis, defined via the normal vector $\mathbf{n}$. These planes are obtained by a projection of the wing reference axis $\bar{\mathbf{x}}_{\text{axis}}(s)$ onto the y,z plane. Hence:

$$\mathbf{n} = \left\{0, n_y, n_z\right\}^T = \left\{0, \cos\phi(s)\cos\kappa(s), \sin\kappa(s)\right\}. \tag{5.33}$$

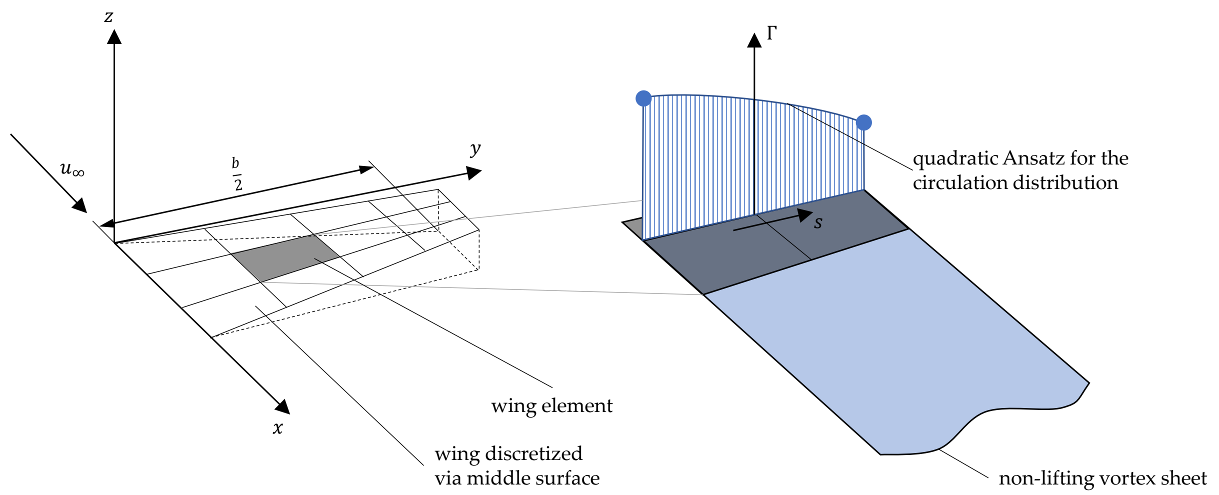

Figure 5.7: Vorticity arrangement in *Lifting_Line*

For the profile drag calculation, only the magnitude of the local velocity in this reference plane is relevant. The expression $\mathbf{u} \cdot \mathbf{u} - (\mathbf{u} \cdot \mathbf{n})^2$ is the square of the velocity magnitude projected into the reference plane. Hence the spanwise velocity component is neglected. The wing area and the local chord length in equation 5.32 are directly obtained by the geometry parameterization, as introduced in section 5.3. The local lift coefficient and the local velocity vector $\mathbf{u}$ are calculated in *Lifting_Line*. The drag coefficients $c_d(s)$ for all airfoils are pre-calculated in a range of Reynolds numbers and lift coefficients using *XFOILSUC-mod*. The profile drag coefficient is then interpolated from this database. If the bounds of this database are exceeded in an optimization iteration, the code raises a warning and the iteration is not considered. In this work, the database has been extended multiple times when warnings occurred. The final results are all calculated within the bounds of the database. However, as shown in section 4.4.2.4, the profile drag calculated with *XFOILSUC-mod* has a systematic offset towards too low drag. Consequently, the wing planform optimization would have a bias towards over-consideration of the induced drag. Hence, the offset has to be corrected. In this work, this is done using a constant correction factor $f_{d,p}$ for the profile drag. The correction factor is determined in fig. 5.8 using the polars of the *DU89-134-14* airfoil for $\delta = 0°$ and $\delta = 20°$ flap deflection at $Re = 1.5\ 10^6$. A correction factor of $f_{d,p} = 1.12$ shows a very good correlation of the corrected profile drag to the wind tunnel results. However, the drag at $\delta = 20°$ for lift coefficients close to the upper corner of the laminar low-drag region is somewhat over-predicted using the correction. At low speeds and hence high lift coefficients, the induced drag plays the dominant role at high lift coefficients, whereas the profile drag is lower, as can be seen in fig. 1.4. At high speeds and low lift coefficients, the profile drag dominates. Therefore, the emphasis was given to low lift coefficients and the $\delta = 0°$ flap setting for calibration of the correction factor $f_{d,p}$.

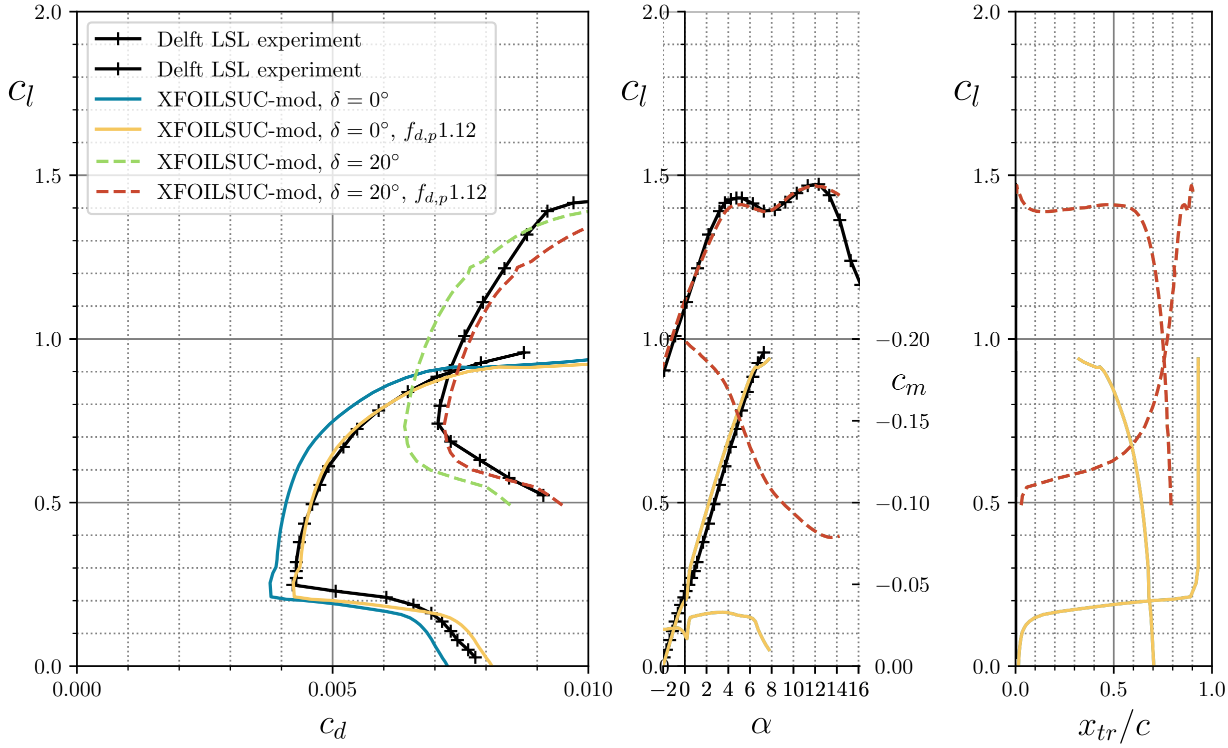

Figure 5.8: Uncorrected and corrected airfoil polars of the *DU89-134-14* airfoil at $Re = 1.5\ 10^6$, compared to wind tunnel results

5.5 OPTIMIZATION ALGORITHM

As with the airfoil optimization, the SUBPLEX optimization algorithm is used. Therefore, the reader is referred to section 4.5, where a detailed description of the algorithm is shown. The advantages of the SUBPLEX algorithm also hold in case of the wing planform optimization. As the objective function may be noisy particularly due to jagged airfoil drag polars at low Reynolds numbers, the SUBPLEX algorithm is able to demonstrate its strengths. In section 5.3 it is shown, that only eight design variables are sufficient for a precise geometry parameterization. This results in faster convergence rates compared to parameterization approaches with more design variables.

5.6 OPTIMIZATION RESULTS

In this section, the results of the wing planform and winglet optimization are shown. The results show the performance of the wing only, thus considering only induced drag and profile drag of the wing. Consequently, trim drag, fuselage drag, interference drag and parasitic drag are not considered. The optimization results of the wing with winglet are compared with the results of an optimization without a winglet.

For the optimization, the airfoils are defined at specific spanwise locations. Table 5.3 shows the distribution for the winglet configuration, and table 5.4 shows it for the wing without a winglet. The airfoil distribution is basically the same, except that all spanwise locations are scaled with the spanwise coordinate of the winglet transition begin for the optimization with winglet. Furthermore, the inner and outer winglet airfoil are used for the winglet design. the outer airfoil is defined at the winglet tip, whereas the inner airfoil is defined at 30% between winglet root and tip. The wing is discretized with 149 panels in spanwise direction, distributed in a cosine spacing in spanwise arc length s coordinates and 7 panels in chordwise direction, evenly distributed.

Table 5.3: Spanwise distribution of airfoils (c.f. fig. 4.31) for optimization with winglet

s	Airfoil
0	inner wing airfoil *ARS19-141-16-22*
$0.0686\ s_0$	inner wing airfoil *ARS19-141-16-22*
$0.0686\ s_0 - 0.27\ s_0$	*transition*
$0.27\ s_0$	main wing airfoil *ARS19-123-16-23*
$0.27\ s_0$ –$0.3722\ s_0$	main wing airfoil *ARS19-123-16-23*
$0.3722\ s_0$	main wing airfoil *ARS19-123-16-23*
$0.3722\ s_0 - 0.8744\ s_0$	*transition*
$0.8744\ s_0$	outer wing airfoil *ARS19-120-17-22*
$0.8744\ s_0 - 0.975\ s_0$	*transition*
$0.975\ s_0$	wing tip airfoil *ARS19-115-17-21*
$0.975\ s_0 - s_0$	*transition*
s_0	wing tip airfoil TE flap only *ARS19-115-17-21-mod*
$s_0 - s_0 + 0.3(s_1 - s_0)$	*transition*
$s_0 + 0.3(s_1 - s_0)$	inner winglet airfoil
$s_0 + 0.3(s_1 - s_0) - 1$	*transition*
1	outer winglet airfoil

The bending line is taken from Sturm [117] and is a spline that passes through the points given in table 5.5. The dihedral angle $\kappa_{\text{bendingline}}$ is the first derivative of that spline and added to the dihedral angle in eq. 5.20. For the morphed configuration, the bending line is multiplied by a factor of 1.17. This represents the higher wing bending due to centripetal forces in the circling flight case.

The initial values and the bounds for the design variables are chosen as:

The bounds are chosen so that the optimization is not artificially limited by them and all meaningful design variants between a planar wing design, a blended winglet and a classical winglet are possible. However, the tip dihedral is limited to $80°$. $80°$ is the sum of the root dihedral angle $\kappa_r = 3.25°$ and the tip angle of the bending line in circling flight condition. This limit ensures that the winglet dihedral angle with wing bending is bound to be $90°$ or less, because it is not favorable to have bent-in winglets , which would generate negative lift (c.f. [14]). The other variables required for the parameterization of the wing and winglet planform, which are not used as design variables are held fixed. The values are the same as given in table 5.2 for the winglet example.

The optimization of the wing with winglet converged after 200 iterations, with the best result obtained at iteration 136. The optimization took 6:59 hours on a four core Intel(R) Core(TM) i7-1065G7 CPU running at 3.90 GHz with 16 GB RAM. However, only a single core was used for the optimization, leaving some potential for speedup if the code was properly parallelized. The optimization of the planar comparison wing converged after 11 iterations due to the single design variable, with the best result obtained at iteration 8. The three side views of the optimization

Table 5.4: Spanwise distribution of airfoils (c.f. fig. 4.31) for optimization without winglet

s	Airfoil
0	inner wing airfoil *ARS19-141-16-22*
0.0686	inner wing airfoil *ARS19-141-16-22*
0.0686 – 0.27	*transition*
0.27	main wing airfoil *ARS19-123-16-23*
0.27 –0.3722	main wing airfoil *ARS19-123-16-23*
0.3722	main wing airfoil *ARS19-123-16-23*
0.3722 – 0.8744	*transition*
0.8744	outer wing airfoil *ARS19-120-17-22*
0.8744 – 0.975	*transition*
0.975	wing tip airfoil *ARS19-115-17-21*
0.975 – 1	*transition*
1	wing tip airfoil TE flap only *ARS19-115-17-21-mod*

Table 5.5: Wing bending displacement u_z vs. spanwise coordinate s

s	u_z [m]
0.0	0.0
0.6	0.0340
1.755	0.1233
3.444	0.2999
5.000	0.5114
6.36396	0.7300
7.48323	0.9349
8.3149	1.0960
8.82707	1.1933

Table 5.6: Initial values and bounds for the wing planform optimization design variables

design variable d_i	lower bound d_i^l	initial value	upper bound d_i^u
$d_0 = \varepsilon_1$	$-5°$	$-1°$	$2°$
$d_1 = \varepsilon_2$	$-5°$	$-2°$	$2°$
$d_2 = \varepsilon_3$	$-5°$	$-2°$	$2°$
$d_3 = \omega_{WL}$	0.9	0.94	1
$d_4 = \sigma_{WL}$	50	100	150
$d_5 = \kappa_t$	$0°$	$77.5°$	$80°$
$d_6 = e_{WL,c}$	0.1	5.714	1
$d_7 = n_{SE}$	1.5	2	2.5

results with and without winglets are shown in fig. 5.9. The resulting winglet height is ≈ 600 mm, which is comparable to current 18 meter class sailplanes, whereas the winglet chord is smaller.

The twist for the optimized design without winglets is zero everywhere. The twist distribution of the wing with winglet is shown in fig. 5.10. The twist distribution shows a toe washout at the winglet root, followed by a significant wash-in at winglet half-span and a tip washout.

Fig. 5.11 shows the chord distribution of the wing with winglet and the circulation distributions $\Gamma(s)$, the local section lift coefficients $C_l(s)$ and the Reynolds number $Re(s)$ in dependence of the spanwise arc length s. All distributions are shown in undeformed configuration at global lift coefficient $C_L = 0.325$ and in morphed configuration at $C_L = 1.65$. For comparison, elliptical circulation distributions Γ_{ell} with equal total lift are shown as dashed green lines. In morphed configuration, the circulation distribution is under-elliptic. The local lift coefficients are close to the maximum winglet airfoil lift coefficients, hence the winglet airfoil is highly loaded. In undeformed configuration in high speed flight, the circulation distribution is very close to an elliptic distribution with low induced drag. In combination with the small chord length at the winglet region, this results in local lift coefficients being higher than at the main wing. The reduced chord leads to an reduction in profile drag, compared to a wing with a blended winglet.

Fig. 5.12 shows the chord, circulation and local section lift coefficients over the spanwise arc length s of the wing without a winglet. The circulation distribution in both configurations is very close to elliptic. This leads to almost constant section lift coefficients. The slight deviation from the elliptic distribution stems from the multi-trapezoidal wing planform and the dihedral angle of $\kappa_r = 3.25°$.

In table 5.7, the k (c.f. eq. 1.4) factors of the optimization results with and without winglet are shown. The k factor is the ratio of the induced drag of the actual wing compared to the theoretical induced drag of a planar elliptic wing with the same wing area and span. The design with winglets saves almost 5% induced drag at high lift coefficients in morphed configuration and $\approx 8\%$ at low lift coefficients in undeformed configuration. Surprisingly, also the wing without winglet achieves k factors below 1. This is, because the wing is non planar due to the dihedral angle $\kappa_r = 3.25°$ and the wing bending.

Table 5.7: induced drag coefficient factors k for optimized wings with winglet and without winglet at different lift coefficients

configuration	undeformed	undeformed	undeformed	morphed	morphed
c_L	0.325	0.525	0.8	1.5	1.65
winglet k	0.913	0.921	0.935	0.951	0.951
no winglet k	1.002	1.000	0.998	0.995	0.994

In fig. 5.13, the glide ratio polar of the optimized wing designs with and without a winglet are shown. Here, only the profile drag and the induced drag of the wing is considered, neglecting fuselage, tailplane, interference and parasitic drag components. The wing with winglet achieves an improvement of almost one glide ratio point in morphed configuration and improves the best glide ratio by about 1.5 points at intermediate speeds. The cross-over point, where the wing without winglets becomes better than the wing with winglets is very close to the lower corner of the laminar low-drag region. Therefore, improvements over the whole useful speed range are achieved with winglets. Consequently, only the wing with winglets is considered in the overall aircraft performance analysis in chapter 6.

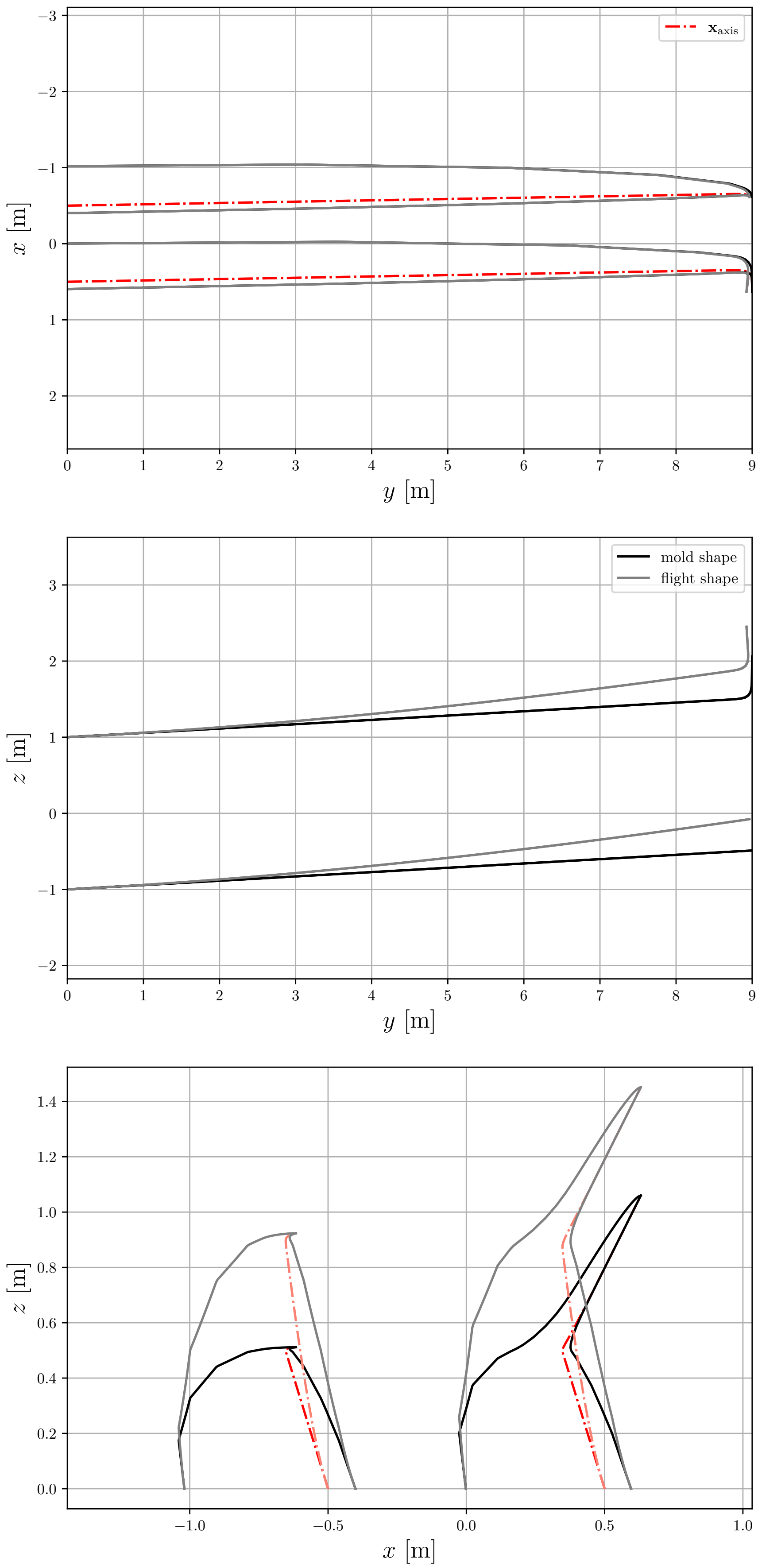

Figure 5.9: Three side view of optimization result without winglet (left) and with winglet (right)

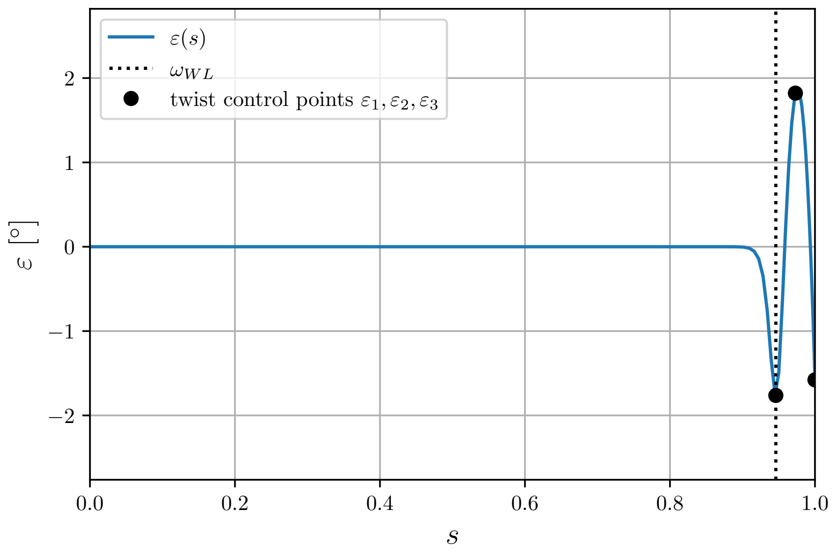

Figure 5.10: Twist distribution of optimized design with winglet

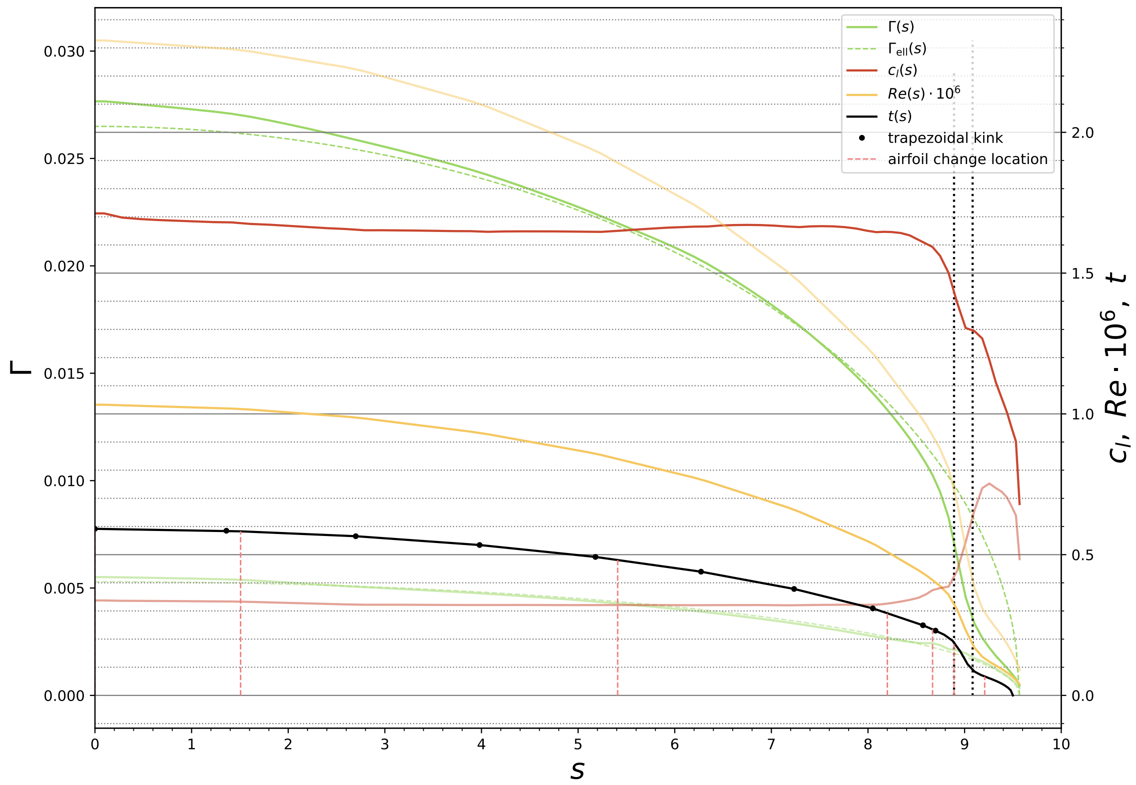

Figure 5.11: Circulation distribution Γ (green), local lift coefficients c_l (red), Reynolds numbers Re (yellow), chord distribution c (black) and elliptic circulation distribution for comparison (green, dashed) of optimization with winglet vs. spanwise curve length coordinate s for wing lift coefficient $c_L = 1.65$ (non-transparent lines) and $c_L = 0.325$ (transparent lines)

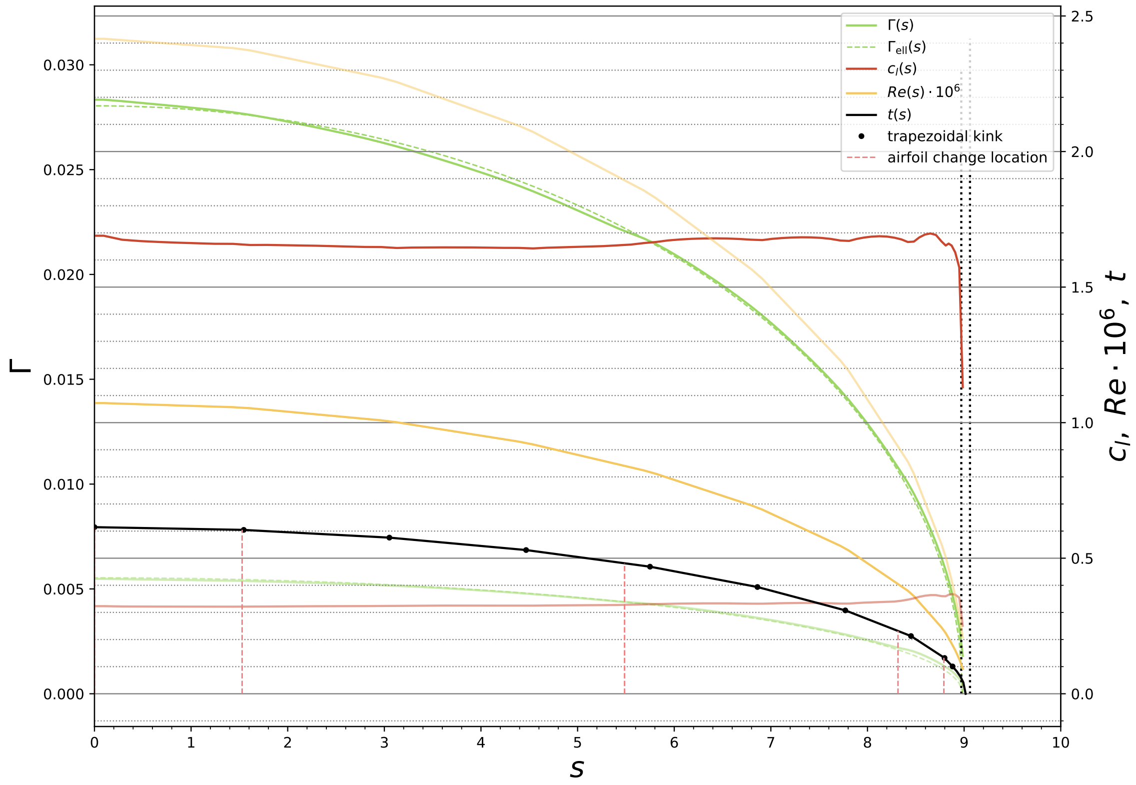

Figure 5.12: Circulation distribution Γ (green), local lift coefficients c_l (red), Reynolds numbers Re (yellow), chord distribution c (black) and elliptic circulation distribution for comparison (green, dashed) of optimization without winglet vs. spanwise curve length coordinate s for wing lift coefficient $c_L = 1.65$ (non-transparent lines) and $c_L = 0.325$ (transparent lines)

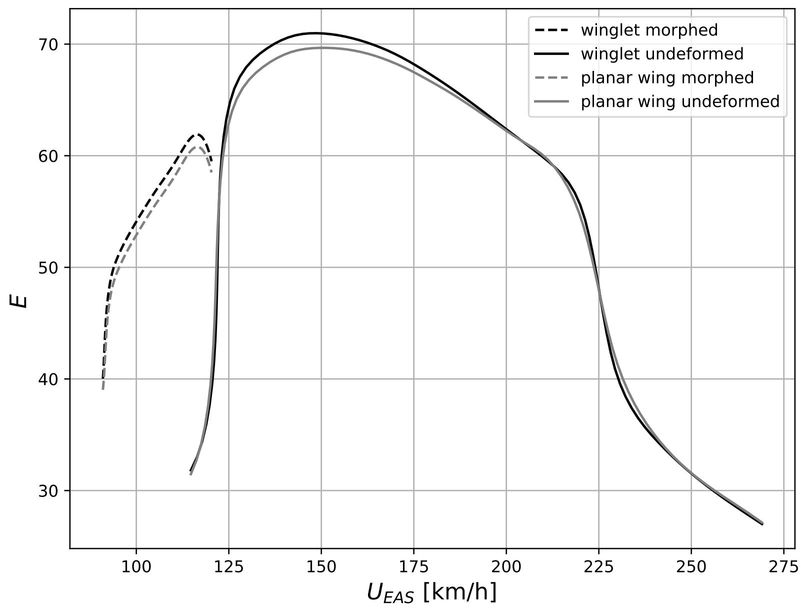

Figure 5.13: Glide ratio (induced and profile drag of the wing only) polars of optimized designs with and without winglet

6 OVERALL AIRCRAFT PERFORMANCE ESTIMATION

In this chapter, the performance estimation of the morphing wing sailplane is conducted and the results are compared to the *ASG 29* sailplane. For the performance estimation of the morphing wing sailplane, the performance data of the *ASG 29* is required. In section 6.1, the in-flight measurement method for the determination of an aircraft performance polar is discussed. Also, the measurement results for the *ASG 29* sailplane are shown. In section 6.2, the performance estimation method for a new sailplane based on the measurements and on calculations is introduced and it's limitations are discussed. Based on this, the residual drag polar of the *ASG 29* is evaluated. The residual drag polar is then used for the performance estimation of the proposed morphing wing sailplane and the *ASG 29* at MTOM for comparison. Finally, the mean sink rates of both sailplanes are evaluated.

6.1 SIDE-BY-SIDE FLIGHT PERFORMANCE MEASUREMENTS OF SAILPLANES

The performance estimation assumes that the fuselage and parasitic drag of the morphing wing sailplane remain the same as those of the *ASG 29*, with which it shares the fuselage and tailplane. The performance estimation method requires precise overall sailplane performance data. The gold standard for obtaining such data for sailplanes is the side-by-side flight performance measurement method, as described by Thomas [119]. Most of these measurements are performed annually in Germany by the Interessensgemeinschaft Deutscher Akademischer FLIEGergruppen, umbrella organization of German academic flying groups (Idaflieg) and the DLR. In that method, the sink rate differences of a precisely calibrated reference sailplane and the comparison sailplane, of which the performance should be evaluated, are measured. Both sailplanes fly side by side at constant airspeed in a not too close formation to mitigate interference effects for gathering the data of one measurement segment. The flights are performed early in the morning at altitudes above the inversion layer to minimize atmospheric influence.

The reference sailplane must have a precisely calibrated airspeed system and a well-determined center of gravity. The sink polar of the reference sailplane is measured by a large amount of timed descend flights. Great care is taken to ensure that the aerodynamic quality of the reference sailplane remains consistent over its lifetime. Currently, the *Discus 2c DLR* serves as the reference sailplane for all Idaflieg - DLR flight performance measurement campaigns. The *Discus 2c DLR* has a nose boom for precise static and total pressure, angle of attack and sideslip angle measurements and is equipped with a high quality GPS receiver, an Inertial Measurement Unit (IMU) and a flight data acquisition unit for data processing and recording. It has recently been retrofitted with a control surface position measurement system and an autopilot system, so that pilot induced effects to the measurements are minimized. Raab and Rohde-Brandenburger [94] provide a thorough description of the *Discus 2c DLR* and its equipment. Until 2015, the predecessor of the *Discus 2c DLR*, a *DG-300*, also equipped with a nose boom, an IMU and a flight data acquisition system was used. The comparison sailplane is also equipped with an IMU, a high quality GPS receiver and a flight data acquisition unit. It's flight center of gravity and take off mass m_{TOM} is accurately measured by weighing the load on the front- and tail wheel in reference position.

Until the turn of the century, the sink rate differences between the reference sailplane and the comparison sailplane have been measured using a photogrammetric method. In that, photos of the formation have been taken from a powered chase plane at the beginning and the end of a measurement segment. This method has been replaced with a more accurate differential GPS method, proposed by Lipp [69] and developed by Wende [127]. Recent improvements in data evaluation by considering the point-mass equations of motion of the aircraft have been introduced by Pätzold [86]. Fig. 6.1 shows the flight performance measurement of the *Mü31* comparison sailplane with the *Discus 2c DLR* reference sailplane in background.

Figure 6.1: Photograph of side-by-side flight performance measurement of the *Mü31* comparison sailplane. Reference sailplane *Discus 2c DLR* in background

The measured performance polar of the *ASG 29* sailplane for flap settings one to six is shown in fig. 6.2. The measurements took place on August 17, 2008 at the Aalen-Elchingen airfield. The take off mass was determined to be $M_{TOM} = 384\ kg$, the center of gravity location was $x_{cg} = 295$ mm behind reference plane. The reference sailplane used was the *DG-300*. According to the measurement, the *ASG 29* reaches a best glide ratio of 49.9 at $U_\infty = 97.6$ km/h. The minimum sink rate is $w_s = 0.508$ m/s at $U_\infty = 78.4$ km/h.

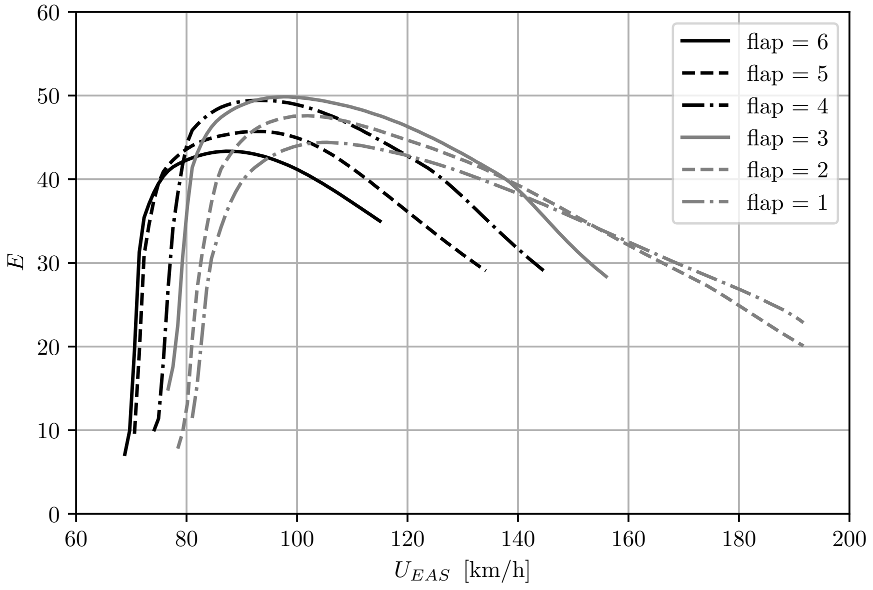

Figure 6.2: Measured polars of the *ASG 29* sailplane for flap setting one to six

6.2 PERFORMANCE ESTIMATION METHOD AND LIMITATIONS

In this work, it is assumed, that the fuselage and tailplane of the *ASG 29* sailplane are used for the morphing wing aircraft. The overall performance estimation assumes that the fuselage, interference, and parasitic drag remain the same as for the *ASG 29*. Only the profile drag and the induced drag of the wing and tailplane change. These drag components are subtracted analytically from the *ASG 29* drag polar and the residual drag polar is obtained. Then the profile and induced drag of the wing-tailplane combination of the morphing wing sailplane is added onto the residual drag polar. This gives an estimate for the overall aircraft performance polar of the new sailplane. In this section, the *ASG 29* is referenced as the comparison sailplane. The symbols referencing to the *ASG 29* are designated with index $\square_{\text{comp}}$. The quantities of the new morphing wing sailplane are designated with the index $\square_{\text{new}}$.

The total drag of the *ASG 29* is determined with the side-by-side flight performance measurement method as discussed in section 6.1. The primary available data is the sink speed as a function of the airspeed $w_s(U_\infty)$. The aircraft drag force D can be calculated from eq. 1.1, when the flight mass m_{TOM} and the wing area A are known, level flight ($n_z = 1$) and a small glide angle γ is assumed:

$$D = \frac{w_s m_{TOM} g}{U_\infty} \tag{6.1}$$

The drag force can be split up into the components created by the wing D_{wing}, by the horizontal tail D_H, the vertical tail D_V and the fuselage D_F. Furthermore, the interference drag D_{inter} and the parasitic drag D_{Pa}:

$$D = D_{wing} + D_H + D_V + D_F + D_{\text{inter}} + D_{Pa}. \tag{6.2}$$

The sum of the fuselage drag D_F, the interference drag D_{inter} and the parasitic drag D_{Pa} is denominated as the residual drag D_{res}:

$$D_{res} = D_F + D_{\text{inter}} + D_{Pa}. \tag{6.3}$$

The sum of the induced drag of the wing-tailplane combination and the profile drag of the wing and the vertical and horizontal tailplane is designated as the wing-tailplane drag:

$$D_{W,H,V} = D_i + D_{W,p} + D_{H,p} + D_{V,p}. \tag{6.4}$$

As the geometry (planform and airfoils) of the lifting surfaces of the comparison sailplane *ASG 29* are known, the drag of the wing-tailplane combination $D_{W,H,V}$ can be calculated using the methods introduced in section 5.4. Different to the drag calculation of that chapter, not only the wing drag is considered, but also the stabilizer drag. A trim calculation for the elevator deflection is done for each operation lift coefficient C_L. In that, the actual flight mass and center of gravity location as documented in the performance polars must be considered. With the drag of the wing-tailplane combination $D_{W,H,V}$ known, the residual drag can be calculated by subtracting the wing-tailplane drag from the total drag:

$$D_{res}(\alpha) = D(\alpha) - D_{W,H,V}(\alpha). \tag{6.5}$$

The angle of attack, the primary variable, is taken from *Lifting_Line* results and matched with the measured and calculated airspeed U_∞, as the former is not provided in the flight data. Furthermore, it is assumed, that the fuselage lift and pitching moment is negligible.

The residual drag area is calculated as:

$$C_{D,res}A_{\text{comp}} = \frac{2D_{res}}{\rho U_\infty^2} = \frac{2w_s m_{TOM} g}{\rho U_\infty^3} - C_{D,W,H,V}A_{\text{comp}}, \tag{6.6}$$

where the reference area A_{comp} is the wing area of the measured comparison sailplane *ASG 29*. For performance estimation of a new sailplane, denoted with index $()_{new}$, it is assumed, that the residual drag depends solely on the angle of attack α and the flap deflection angle δ_F. However, the fuselage Reynolds number also influences the residual drag considerably. A higher Reynolds number leads to earlier transition, but smaller laminar and turbulent friction coefficients and lower pressure drag. Due to the large Reynolds numbers of the fuselage, it may be assumed, that the friction and pressure drag reduction outweigh the further upstream transition. Consequently, it is assumed that the parasitic drag decreases with increasing Reynolds number. Therefore, a Reynolds correction for the residual drag is proposed here. The correction is adopted from Schiffleithner [106]. It is assumed, that the residual drag scales with the Reynolds numbers with:

$$C_{D,res}(Re_F) = \left(c_1 + \frac{c_2}{Re_F}\right) C_{D,res}(Re_{F,norm}), \tag{6.7}$$

where Re_F is the fuselage Reynolds number:

$$Re_F = \frac{U_\infty l_F}{\nu}, \tag{6.8}$$

with l_F being the fuselage length. $C_{D,res}(Re_{F,norm})$ is the fuselage drag at a chosen reference Reynolds number $Re_{F,norm}$. For evaluation of the correction constants c_1 and c_2, wind tunnel measurement data of the *Mü31* from *Akaflieg München* by Schiffleithner [106] is evaluated with respect to the Reynolds number influence. Here, only the measurements with neutral flap configuration $\delta_F = 0°$ are considered. Data for three different wing Reynolds numbers were measured, $Re_W = 0.7\ 10^6$, $Re_W = 9.78\ 10^6$ and $Re_W = 1.23\ 10^6$. However, the Reynolds number in Schiffleithner's work is referenced to the model wing chord. For a clean comparison, the Reynolds number must be referenced to the fuselage length. As the wind tunnel model wing chord is $c = 0.26$ m and the model's fuselage length is $l_F = 2.067$ m, the fuselage Reynolds numbers are obtained as

$Re_F = Re_W \frac{l_f}{c}$. Hence $Re_F = 5.57\ 10^6$, $Re_F = 9.78\ 10^6$ and $Re_F = 11.93\ 10^6$. The measurement data is given in appendix A.3. For evaluation of the correction constants c_1 and c_2, the reference fuselage Reynolds number $Re_{F,norm} = 9.78\ 10^6 \equiv Re_W = 1.23\ 10^6$ is used. The residual drag is calculated by subtracting the wing drag from a separate measurement of a sole wing from the total drag of the wing-fuselage combination. Finally, the values for $\frac{C_{D,res}(Re_F)}{C_{D,res,norm}}$ as a function of Re_F are evaluated for all investigated lift coefficients and plotted in fig. 6.3. Each distinct lift coefficient corresponds to a data point in the plot, indicated by an "x" symbol. At $Re = Re_{F,norm} = 9.78\ 10^6$, all $\frac{C_{D,res}(Re_F)}{C_{D,res,norm}}$ values are unity because this is the chosen reference. The mean value for all lift coefficients for each $Re_F = 5.57\ 10^6$ and $Re_F = 11.93\ 10^6$ are shown as large blue "+" symbols. Particularly between $Re_F = 5.57\ 10^6$ and $Re_F = 9.78\ 10^6$, a clear increase of drag can be seen. The data for $Re_F = 11.93\ 10^6$ has more scatter. The constants c_1 and c_2 are evaluated, so that a best fit through the data is achieved. The best fit is obtained with correction coefficients $c_1 = 0.89$ and $c_2 = 1.075\ 10^6$. These coefficients are used for correcting the Re influence on residual drag due to different airspeeds caused by different wing loadings.

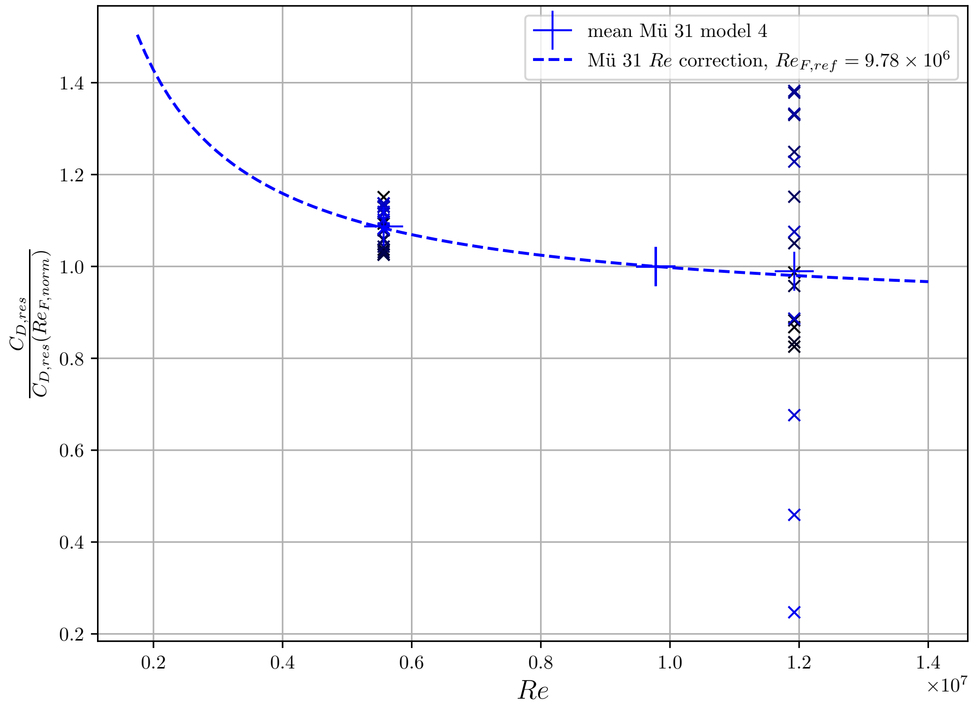

Figure 6.3: Residual drag vs. Re evaluation for *Mü31* wind tunnel test campaign, $\delta_F = 0°$

The residual drag area $C_{D,res,norm}(\alpha)A_{\text{comp}}$ of the in-flight performance measurement data of the comparison sailplane has to be normalized to the reference fuselage Reynolds number $Re_{F,norm} = 9.78\ 10^6$ first:

$$C_{D,res,norm}(\alpha)A_{\text{comp}} = C_{D,res}A_{\text{comp}}\frac{1}{\left(c_1 + \frac{c_2}{Re_F}\right)} \tag{6.9}$$

The residual drag coefficients for the *ASG 29* sailplane in dependence of the angle of attack for six different flap settings are shown in fig. 6.4. The actual residual drag values $C_{D,res}$ are shown as solid lines. The drag values normalized to the reference fuselage Reynolds number

$Re_F = 9.7810^6$ are shown as dotted lines. With these results, an envelope residual drag polar can be approximated, that is independent from the flap deflection. This envelope residual drag polar is used for calculation of the performance of the new morphing wing sailplane as well as the *ASG 29* sailplane at MTOM in all wing flap configurations.

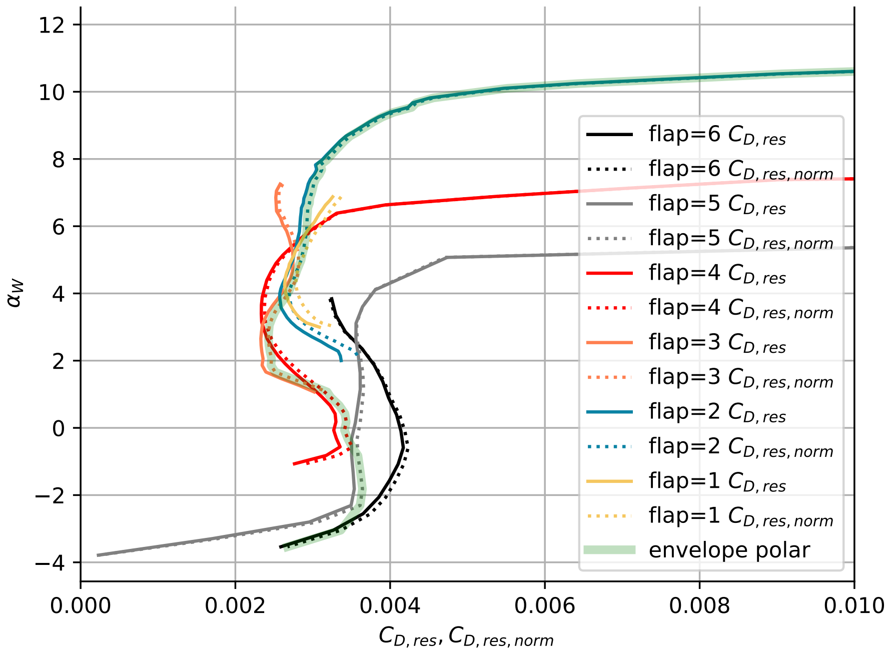

Figure 6.4: Residual drag $C_{D,res}$ and normalized residual drag $C_{D,res,norm}$ vs. Re of the *ASG 29* sailplane for flap settings 1 to 6

For estimating the polar of the morphing wing sailplane with the same fuselage as the comparison sailplane *ASG 29*, the induced drag and profile drag of the wing-tailplane combination of the morphing wing sailplane is calculated again with the method shown in section 5.4. The drag of the morphing wing sailplane can then be estimated by adding the new wing-tailplane drag to the corrected residual drag:

$$D_{new} = \frac{1}{2}\rho U_\infty^2 C_{D,res,norm} A_{\text{comp}} \left(c_1 + \frac{c_2}{Re_F}\right) + D_{W,H,V,new}, \tag{6.10}$$

or the drag coefficient as:

$$C_{D,new} = \frac{1}{A_{new}} C_{D,res,norm}(\alpha) A_{\text{comp}} \left(c_1 + \frac{c_2}{Re_F}\right) + C_{D,i,new} + C_{W,H,V,new}. \tag{6.11}$$

6.3 RESULTS AND PERFORMANCE COMPARISON

In this section, the performance analysis results of the morphing wing sailplane at $m_{TOM} = 600$ kg, which are obtained with the method described in section 6.2 and using the performance data from the Idaflieg measurement of the *ASG 29* sailplane at a take off mass of $m = 384$ kg are shown. The results must be compared to the *ASG 29* performance data at $m_{MTOM} = 600$ kg, of which no measurements are available. Hence, the same performance extrapolation method as for the morphing wing sailplane is used to extrapolate the performance of the *ASG 29* from the flight mass of $m = 384$ kg to $m_{MTOM} = 600$ kg.

According to the pilot flight manual [45] of the *ASG 29*, a center of gravity range between 290 mm and 310 mm is beneficial. For the calculations of the *ASG 29*, a center of gravity of $x_{cg} = 295$ mm is used. For the morphing sailplane, the center of gravity with the same stability margin is chosen. This gives a center of gravity of $x_{cg} = 270$ mm.

The calculated glide ratio polars of the morphing wing sailplane and the *ASG 29*, both at MTOM, are shown in fig. 6.5. The fuselage angle of incidence of the morphing wing sailplane is increased by $1°$, because this gives better performance both at low and high speed with slight disadvantages in the mid-speed range. According to the frequency distributions of lift coefficients from Maughmer [79] (see fig. 3.4), the best glide speed range is the least used in sailplane competition flying, which justifies this decision. The performance polars are evaluated for the drooped configuration with $\delta_F = 19.1°$ trailing edge flap deflection and full leading edge morphing and the undeformed configuration with zero flap deflection, as well as two configurations in between. These are the $\delta_F = 4.8°$ and the $\delta_F = 9.6°$ configurations. The morphing leading edge deflection for these trailing edge flap settings is a linear interpolation between the fully morphed configuration and the undeformed configuration, using the trailing edge flap deflection as the interpolating value.

The glide ratio polars of the morphing wing sailplane in comparison to the *ASG 29* are shown in figure 6.5. The morphing wing sailplane has a clear performance advantage over the whole speed range. Even at the low speed range used for thermalling, the morphing wing sailplane shows better performance. This would give better climb rates in thermals despite the significantly higher wing loading ($70\ ^{kg}/_{m^2}$ vs. $57\ ^{kg}/_{m^2}$). The stall speed of the morphing wing sailplane in the morphed configuration is just below 90 km/h, comparable to the *ASG 29* with flap setting 6. A landing configuration with the same nose droop as in morphed configuration, but with an increased trailing edge flap deflection should give ample lift reserve for safe fulfillment of the 90 km/h stall speed requirement as discussed in section 3.2.1. Specifically at high speeds beyond the best glide speed, the morphing wing sailplane offers a significant performance advantage. It is able to glide $10 - 20$ km/h faster than the *ASG 29* at the same glide ratio. Also the best glide speed is increased significantly.

Finally the performance figure of merit, the average sink speed over an average competition flight profile as introduced in section 3.1.2 is evaluated for the morphing wing sailplane in comparison to the *ASG 29*. For that, the envelope polar of all flap settings, which gives the minimum drag for each lift coefficient is evaluated for both sailplanes.

The evaluation results of the climb index and the frequency distribution according to Maughmer [79], as well as the weighted climb index polars are shown in fig. 6.6. As already indicated by the glide ratio polar in fig. 6.5, the morphing wing sailplane gains it's advantage mainly in the high speed and low speed regions. The performance advantage is most significant in the lift coefficient range with the highest contribution to the frequency distribution, between $C_{L,\mathrm{R}} = 0.2$ and $C_{L,\mathrm{R}} = 0.6$, as can be seen in fig. 6.6 left. By integrating the weighted frequency distributions from fig. 6.6 left according to eq. 3.7, the mean sink speed $\overline{w}_s$ over a typical competition flight profile can be evaluated. For the *ASG 29*, this gives an average sink speed $\overline{w}_s = 1.019$ m/s. For the morphing wing sailplane, an average sink speed of $\overline{w}_s = 0.985$ m/s is calculated. All in all, this is a performance advantage of 3.4%. The reduced sink speed allows pilots to achieve higher inter-thermal and average speeds. As sailplane competitions are often won by less than one percent difference between the first and the second place, this is a beckoning perspective.

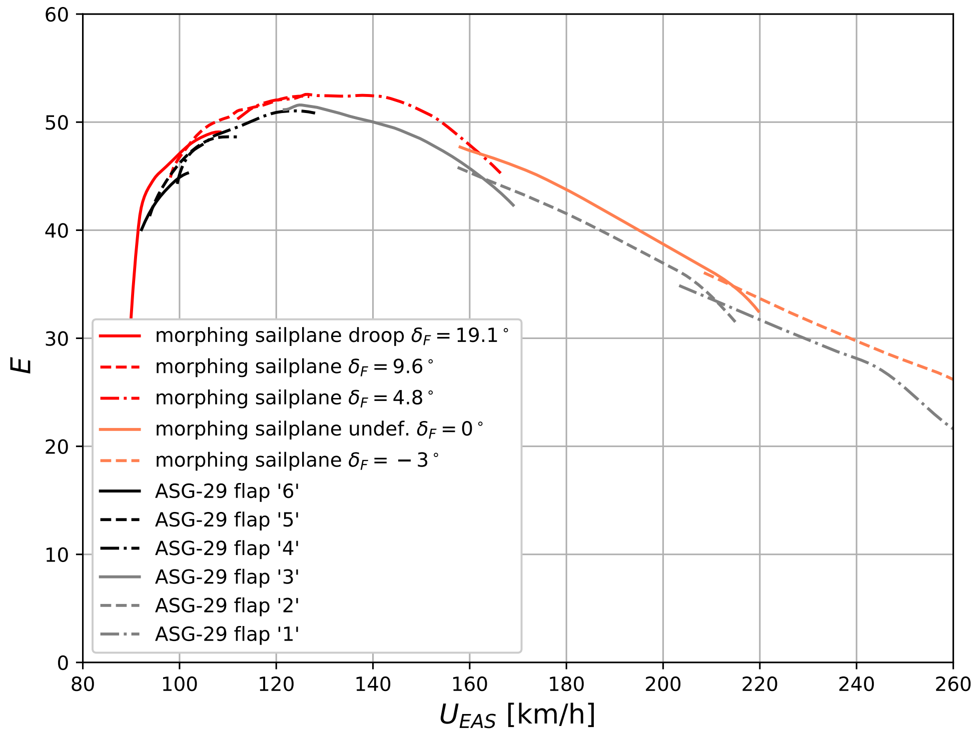

Figure 6.5: Calculated polars of the morphing wing sailplane and the *ASG 29* sailplane at MTOM

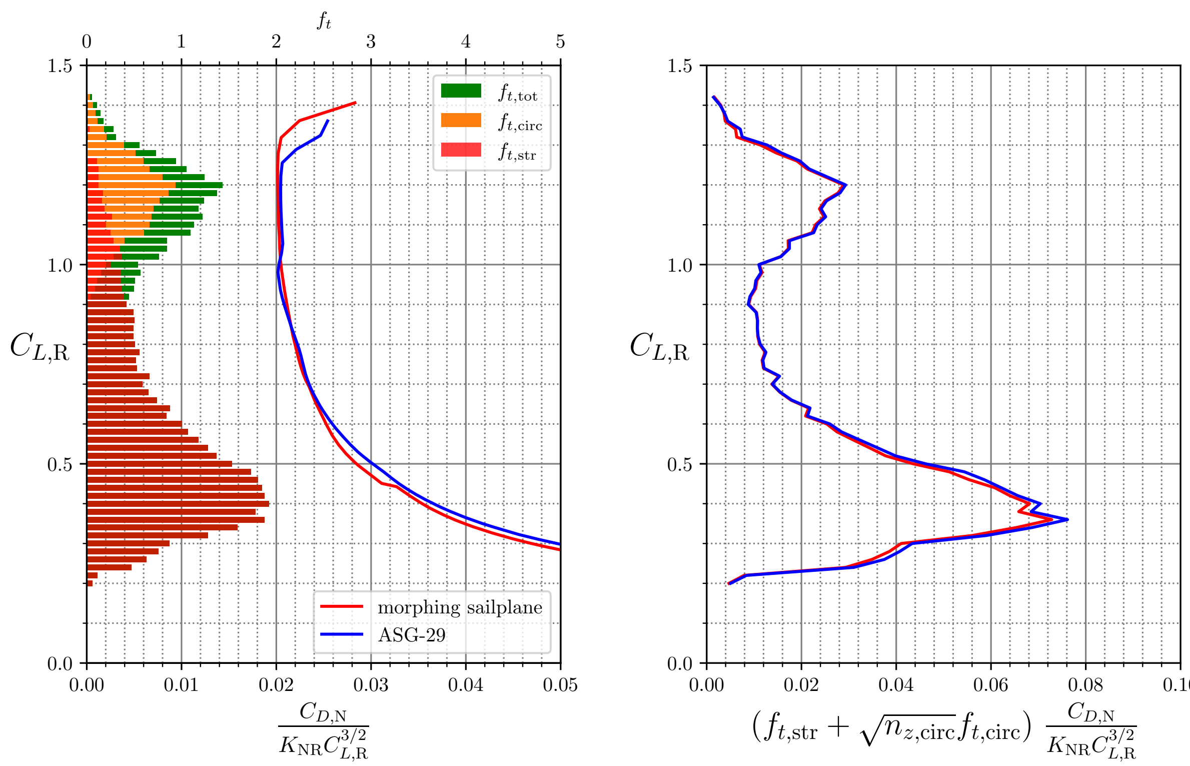

Figure 6.6: climb index polar with lift coefficient frequency distribution (left) and the weighted climb index polar (right) of the morphing wing sailplane and the *ASG 29*

7 CONCLUSION

7.1 SUMMARY

In this dissertation, a new concept and a new design methodology for a morphing wing sailplane is introduced that promises to increase sailplane performance significantly compared to current sailplanes. The main scope is the aerodynamic design of this kind of sailplane. The concept for the wing consists of a morphing forward section and a conventional trailing edge flap.

To optimize aerodynamic design, it is crucial to understand the structural concept of the morphing wing and its implications. Therefore, the structural concept is thoroughly discussed. Compliant mechanisms are designed to deform a flexible wing shell, which covers the morphing forward section of the wing. Different concepts for this morphing wing shell are introduced and the selection of the preferred variant, a thin monolithic fiber reinforced composite structure is discussed. Aeroelastic twist can reduce sailplane performance by changing the spanwise lift distribution from optimal. With the morphing wing concept, the primary load carrying structure part of the wing is reduced to the area between the morphing forward section and the trailing edge flap. This decreases the cross sectional area of the torque box and shifts the center of shear rearward. Using aeroelastic tailoring methods, the adverse wing twist can be reduced to acceptable values.

It is shown that the objective of performance improvement can be condensed in one scalar value, the average sink speed. This metric is developed in this thesis. It is based on an already existing extensive evaluation of the lift coefficients flown at actual competition flights, resulting in a lift coefficient frequency distribution. It is shown, that from this measurement data, the average sink rate for an average competition flight can be evaluated. It is a simple scalar metric well suited for performance comparison of different sailplanes. With this metric, the performance of the morphing wing sailplane is later compared to the *ASG 29* sailplane, a current 18 meter class sailplane.

Analytic considerations show, that a performance advantage can be achieved by decreasing the wing area. It is shown, that this leaves the induced drag almost unchanged but decreases the profile drag. However, regulatory requirements demand a minimum stall speed of the sailplane. This in turn imposes a lower limit on the maximum lift of the wing. Hence it is shown, that wing area can only be decreased, if the maximum lift coefficient of the wing and subsequently of the airfoils is increased.

The aerodynamic design is performed with a decomposed design philosophy. In this, the isolated two-dimensional airfoils are designed separately from the wing and wing planform shape. This allows to use very fast potential flow methods for analysis and optimization. Prerequisite for the decomposed design philosophy is, that the two-dimensional flow assumption holds for the bulk of the wing. It is shown, that this is the case for sailplane wings. Both the isolated two-dimensional airfoil design and the wing planform design are done with newly developed aerodynamic shape optimization approaches. Due to the fast solution speed of the potential flow solvers, gradient based optimization is not required, that would require laborious implementation of analytical gradient solvers.

For the airfoil design, a new geometry parameterization method is introduced. It is based on the CST method. The new extended method allows an efficient geometry description of airfoils with an intentional concave kink on the transition between the main wing and the trailing edge flap (*kinked flapped airfoil*) and a morphing forward section. Precise numerical optimization requires precise flow solvers. The integral boundary layer solver *XFOIL* is used as a basis. However, *XFOIL* is known to have deficiencies in the prediction of the transition location and to over-predict maximum lift. The prediction of the transition location is improved by using *XFOILSUC* in addition to *XFOIL*. Instead of the simple envelope e^N transition prediction method, *XFOILSUC* uses the more sophisticated *improved van Ingen full* e^N *database method*. Over-prediction of maximum lift, if not considered, leads to a design with the wing area being too small. To improve the prediction of the maximum lift, enhancements in the turbulent closure relations are implemented in *XFOIL* and *XFOILSUC*, then designated as *XFOIL-mod* and *XFOILSUC-mod*. With the new parameterization method in combination with the fast potential flow solvers and the efficient optimization algorithm *SUBPLEX*, good airfoil designs for the inner wing section, the main wing section and the wing tip are obtained. These show an increase of the upper usable lift coefficient of $\approx 20\%$ compared to conventional airfoils with camber changing trailing edge flaps in combination with comparable drag coefficients. This allows to decrease the wing area from $10.5\ \mathrm{m}^2$ of the *ASG 29* sailplane to $8.6\ \mathrm{m}^2$ with significant advantages in terms of overall wing profile drag. The structural concept of the morphing wing consists of a sliding joint on the lower wing surface, which needs to be properly sealed with a thin plastic foil. This could potentially lead to laminar-turbulent transition, vastly offsetting the potential performance advantage of the morphing wing concept. The influence of this seal is analyzed. It is shown, that this influence is small.

After the airfoils are defined, the wing planform shape including winglets is designed. For this, also a numerical optimization approach is developed. Geometry parameterization is done with a new method, that is based on three simple analytical basis functions and their derivatives. The method allows to generate a wide range of possible wing geometries with only 14 parameters. It is shown, that planar wings and wings with blended winglets are just special cases of the general formulation with a dedicated choice of parameters. The calculation of the wing drag is done by a summation of the induced drag and the profile drag. The induced drag is calculated with the multi lifting line solver *Lifting_Line*, which shows higher precision than VLM at the same level of discretization. The profile drag is interpolated from a database, that is pre-generated from *XFOILSUC-mod* airfoil polars. *SUBPLEX* is again used as optimization algorithm. Two designs are optimized. One without winglets and one with winglets. The design with winglets achieves a 1.5 points higher best glide ratio than the design without winglets.

A method for overall aircraft performance estimation is shown. This is based on the fact, that the morphing wing sailplane shares the fuselage and the stabilizer with the *ASG 29* aircraft. This makes it possible to subtract the calculated wing-stabilizer drag from the measured total aircraft drag and obtain a residual drag polar, which covers the fuselage drag, interference drag and parasitic drag. The drag of the morphing wing sailplane can then be estimated as the sum of the calculated wing-stabilizer drag of the new wing plus the existing *ASG 29* tailplane and the previously calculated residual drag of the *ASG 29* sailplane. With this method, estimates predict a significant performance advantage of the morphing wing sailplane. The average sink rate is reduced by 3.4% compared to the *ASG 29*.

7.2 OUTLOOK

Although the morphing wing sailplane concept offers a good performance advantage over the current state of the art, improvements both of the concept and of the design and analysis method are conceivable.

On the conceptual side, one possible improvement would be the use of a specifically designed smaller horizontal stabilizer instead of the *ASG 29* stabilizer. The morphing wing has a smaller wing chord, which reduces the aerodynamic moments. This would allow a smaller tailplane, that subsequently would lead to decreased overall aircraft drag. Furthermore, new fuselage concepts with shoulder wing arrangements and a minimum cross section tailboom like the *Mü-31* from the *Akaflieg Munich* or the *JS-3* from *Jonker Sailplanes* could further offer a performance advantage. In this work, no detailed design of the wing-fuselage intersection is done. However, interference effect could cause large losses in performance due to premature laminar-turbulent transition or flow separation. Hence, the wing-fuselage intersection should be revisited.

On the design and analysis method side, both the airfoil design and the wing planform design can be improved in various ways. Further improvements of the integral panel method regarding maximum lift prediction could possibly be achieved by implementing improved turbulent closure relations, as proposed by de Oliveira Andrade [84]. Furthermore, a gradient based optimization algorithm could offer a significant speed-up of the optimization. This requires the implementation of analytical sensitivity analysis, an adjoint solver or algorithmic differentiation into *XFOILSUC-mod*. Furthermore, the geometry parameterization method must be differentiated.

The wing planform optimization relies on the linear solver *Lifting_Line*. However, particularly the outer wing and wing tip airfoils show significant viscous decambering effects, which influences the spanwise lift distribution and hence induced drag. This could be considered by using a non-linear solver instead of *Lifting_Line* or by upgrading *Lifting_Line* to handle non-linear effects. Furthermore, a sailplane circles during climbing in thermals. The wing planform optimization method introduced in this work does not fully consider this. Only the increased load factor due to circling flight is considered. Besides that, level flight conditions are assumed. *Lifting_Line* offers the possibility to prescribe roll, nick and yaw rates, which can be used to simulate circling flight. However, the aileron deflection must be calculated with a trim iteration to obtain correct spanwise circulation distributions and hence correct induced drag values.

An alternative approach would be to optimize the airfoil and wing planform shapes simultaneously, rather than using the decomposed design philosophy. This would require a completely different geometry parameterization method, like Free-Form Deformation. A flow solver capable of capturing dominant aerodynamic effects in sailplane aerodynamics, such as laminar-turbulent transition and laminar separation bubbles, is necessary. In the last years, RANS CFD codes with the γ-Re_θ transition criterion have been developed. Also the AFT model, developed by Coder [25] has been implemented in the RANS CFD code *ADFLOW* by Halila et al. [48]. However, only two-dimensional airfoil optimization examples are documented with this method to date. Furthermore, this approach requires large computational resources. Alternatively, a three-dimensional integral boundary layer solver, such as introduced by Drela [32] or by Zhang et al. [132] could be used, which are more computationally efficient.

Finally, the morphing wing sailplane concept should undergo experimental testing. A full-scale mechanical demonstrator has been constructed and tested, demonstrating the structural and mechanical feasibility of the concept. Fig. 7.1 left shows the demonstrator in the bottom side mold before bonding the top shell. The stacked compliant mechanism ribs and the primary structure are visible. Fig. 7.1 right shows the assembled demonstrator in the test rig with wing bending load applied during photogrammetric deformation measurement. Alongside structural testing, wind tunnel tests of an representative airfoil model could further prove the possible performance advantage of the morphing wing concept, paving the way for a future use on a full scale sailplane.

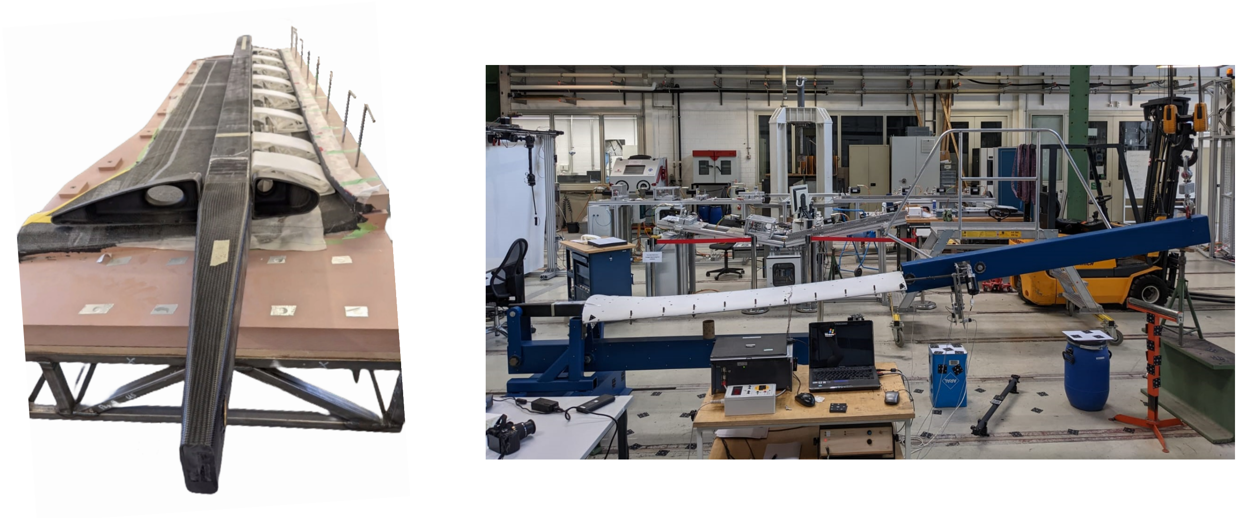

Figure 7.1: Morphing wing demonstrator in bottom side mold with stacked compliant mechanism ribs and primary structure (left). Demonstrator during wing bending test (right)

BIBLIOGRAPHY

[1] Niels Aage, Erik Andreassen, Boyan Stefanov Lazarov, and Ole Sigmund. "Giga-voxel computational morphogenesis for structural design." In: *Nature* 550.7674 (2017), pp. 84–86. ISSN: 0028-0836. DOI: 10.1038/nature23911.

[2] Ira H. Abbott and Albert E. von Doenhoff. *Theory of wing sections*. 2nd ed., revised. New York: Dover Publications Inc., 1959.

[3] Johannes Achleitner, Kai Rohde-Brandenburger, Paul Rogalla von Bieberstein, Fabian Sturm, and Mirko Hornung. "Aerodynamic Design of a Morphing Wing Sailplane." In: *AIAA Aviation 2019 Forum*. Reston, Virginia: American Institute of Aeronautics and Astronautics, 2019. ISBN: 978-1-62410-589-0. DOI: 10.2514/6.2019-2816.

[4] Johannes Achleitner and Erich Wehrle. "On material selection for topology optimized compliant mechanisms." In: *Mechanism and Machine Theory* 167 (2022), p. 104474. ISSN: 0094114X. DOI: 10.1016/j.mechmachtheory.2021.104474.

[5] Akademische Fliegergruppe Braunschweig. *SB 5 - SB 15, Segelflugzeug Braunschweig: Segelflugzeug-Entwicklungen 1951-2012*. 2. Aufl. Braunschweig: Appelhans, 2013. ISBN: 978-3-941737-73-0.

[6] Dieter Althaus. *Windkanalmessungen am Profil HQ17/14.38 und Vergleich mit Messungen der University of Technology Delft sowie der DFVLR*. Ed. by University of Stuttgart. 1984.

[7] Dieter Althaus. *Niedriggeschwindigkeitsprofile*. Braunschweig/Wiesbaden: Vieweg Verlag, 1996. ISBN: 3-528-03820-9.

[8] Dieter Althaus and Franz Xaver Wortmann. *Stuttgarter Profilkatalog I: Messergebnisse aus dem Laminarwindkanal des Instituts für Aerodynamik ind Gasdynamik der Universität Stutgart*. Braunschweig: F. Vieweg, 1981. ISBN: 3-528-08464-2.

[9] Daniel Arnal. "Diagrammes de stabilite´ des profils de couche limite auto-semblables, en ecoulement bidimensionnel incompressible, sans et avec courant de retour." Rapport Technique OA Nr 34/5018. ONERA, 1986.

[10] Christopher J. Axten and Mark D. Maughmer. "Demonstrating the Potential of CFD Transition Modeling for Racing Sailplane Design." In: *AIAA AVIATION 2020 FORUM*. Reston, Virginia: American Institute of Aeronautics and Astronautics, 2020, p. 20. ISBN: 978-1-62410-598-2. DOI: 10.2514/6.2020-2710.

[11] Horst Baier, Christoph Seeßelberg, and Bernhard Specht. *Optimierung in der Strukturmechanik*. Softcover reprint of the hardcover 1st ed. 1994. Braunschweig [u.a.]: Vieweg, 2012. ISBN: 978-3322907011.

[12] M. P. Bendsøe. "Optimal shape design as a material distribution problem." In: *Structural and Multidisciplinary Optimization* 1.4 (1989), pp. 193–202. ISSN: 1615-1488. DOI: 10.1007/BF01650949.

[13] Martin Philipp Bendsøe and Ole Sigmund. *Topology Optimization: Theory, Methods and Applications*. Berlin Heidelberg: Springer Verlag, 2004.

[14] Loek M.M. Boermans. "Research on Sailplane Aerodynamics at Delft University of Technology." In: *Technical Soaring* 30.1 (2006).

[15] Loek M.M. Boermans. "On the way to glide ratio 100:1." In: *XXXIV OSTIV Congress*. 2018, pp. 107–110. ISBN: 978-3-947623-07-5.

[16] Loek M.M. Boermans and A. van Garrel. "Design and Windtunnel Test Results of a Flapped Laminar Flow Airfoil for High-Performance Sailplane Applications." In: *ICAS 19 - Proceedings of the 19th Conference of the International Council of Aeronautical Sciences* (1994), pp. 1241–1247.

[17] Jeroen Bongers. "Implementation of a new transition prediction method in xfoil." Masters thesis. Delft, Netherlands: TU Delft, 2008.

[18] Joel Brezillon, Olaf Brodersen, R. Dwight, A. Ronzheimer, and Jochen Wild. "Development and application of a flexible and efficient environment for aerodynamic shape optimisation." In: *Proceedings of the ONERA-DLR Aerospace Symposium (ODAS), Toulouse* (2006). URL: `https://citeseerx.ist.psu.edu/viewdoc/download?doi=10.1.1.711.1496&rep=rep1&type=pdf`.

[19] P. CRIMI and B. L. Reeves. "Analysis of leading-edge separation bubbles on airfoils." In: *AIAA Journal* 14.11 (1976), pp. 1548–1555. DOI: `10.2514/3.7250`.

[20] Marco Ceze, Marcelo Hayashi, and Ernani Volpe. "A Study of the CST Parameterization Characteristics." In: *27th AIAA Applied Aerodynamics Conference*. Reston, Virigina: American Institute of Aeronautics and Astronautics, 2009. ISBN: 978-1-62410-130-4. DOI: `10.2514/6.2009-3767`.

[21] C. W. Clenshaw and A. R. Curtis. "A method for numerical integration on an automatic computer." In: *Numerische Mathematik* 2 (1960), pp. 197–205.

[22] J. G. Coder. "Accuracy of high-order, discrete approximations to the lifting-line equation." In: *The Aeronautical Journal* 127.1315 (2023), pp. 1536–1553. ISSN: 0001-9240. DOI: `10.1017/aer.2023.16`.

[23] James G. Coder. "Further Development of the Amplification Factor Transport Transition Model for Aerodynamic Flows." In: *AIAA Scitech 2019 Forum*. Reston, Virginia: American Institute of Aeronautics and Astronautics, 2019, p. 58. ISBN: 978-1-62410-578-4. DOI: `10.2514/6.2019-0039`.

[24] James G. Coder and Mark D. Maughmer. "Comparisons of Theoretical Methods for Predicting Airfoil Aerodynamic Characteristics." In: *Journal of Aircraft* 51.1 (2014), pp. 183–191. ISSN: 0021-8669. DOI: `10.2514/1.C032232`.

[25] James G. Coder and Mark D. Maughmer. "Computational Fluid Dynamics Compatible Transition Modeling Using an Amplification Factor Transport Equation." In: *AIAA Journal* 52.11 (2014), pp. 2506–2512. DOI: `10.2514/1.J052905`. URL: `https://www.easa.europa.eu/sites/default/files/dfu/TCDS_A_220_ASW_27_issue04.pdf`.

[26] Ulrich Deck and Werner Würz. "In-flight measurements on the Influence of Freestream Turbulence on a NLF Airfoil." In: *AIAA AVIATION 2023 Forum*. Reston, Virginia: American Institute of Aeronautics and Astronautics, 2023. ISBN: 978-1-62410-704-7. DOI: `10.2514/6.2023-3675`.

[27] Paolo Dini, Michael S. Selig, and Mark D. Maughmer. "Simplified linear stability transition prediction method for separated boundary layers." In: *AIAA Journal* 30.8 (1992), pp. 1953–1961. DOI: `10.2514/3.11165`.

[28] S. L. Dixon and C. A. Hall. "Wind Turbines." In: *Fluid Mechanics and Thermodynamics of Turbomachinery*. Elsevier, 2014, pp. 419–485. ISBN: 9780124159549. DOI: 10.1016/B978-0-12-415954-9.00010-3.

[29] Mark Drela. "Integral Boundary Layer Formulation for Blunt Trailing edges." In: *AIAA Paper 89–2166* (1989).

[30] Mark Drela. "XFOIL: An Analysis and Design System for Low Reynolds Number Airfoils." In: *Low Reynolds Number Aerodynamics Conf. Proc.* (1989).

[31] Mark Drela. "Implicit Implementation of the Full e^n Transition Criterion." In: *21st AIAA Applied Aerodynamics Conference*. Reston, Virigina: American Institute of Aeronautics and Astronautics, 2003, p. 10. ISBN: 978-1-62410-092-5. DOI: 10.2514/6.2003-4066.

[32] Mark Drela. "Three-Dimensional Integral Boundary Layer Formulation for General Configurations." In: *21st AIAA Computational Fluid Dynamics Conference*. Reston, Virginia: American Institute of Aeronautics and Astronautics, 2013. DOI: 10.2514/6.2013-2437.

[33] Mark Drela. *Flight vehicle aerodynamics*. Cambrdge, Massachusetts: MIT Press, 2014. ISBN: 9780262526449.

[34] Mark Drela and Michael B. Giles. "ISES - A two-dimensional viscous aerodynamic design and analysis code." In: *25th AIAA Aerospace Sciences Meeting*. Reston, Virigina: American Institute of Aeronautics and Astronautics, 1987, p. 117. DOI: 10.2514/6.1987-424.

[35] Mark Drela and Michael B. Giles. "Viscous-inviscid analysis of transonic and low Reynolds number airfoils." In: *AIAA Journal* 25.10 (1987), pp. 1347–1355. DOI: 10.2514/3.9789.

[36] Richard Eppler. *Airfoil Program System 'PROFIL07' User's Guide,* Stuttgart, Germany, 2007.

[37] European Union Aviation Safety Agency. *Certification Specifications for Sailplanes and Powered Sailplanes CS-22: Amendmend 2*. 5 March 2009.

[38] Fédération Aéronautique Internationale. *Sporting Code Section 3 – Gliding: CLASS D (gliders) including Class DM (motorgliders)*. 1.10.2019. URL: https://www.fai.org/sites/default/files/documents/sc3_-_2019b-2.pdf.

[39] Fédération Aéronautique Internationale. *Annex A to Sporting Code Section 3 – Gliding: Rules for world and continental championsships*. 7.10.2019. URL: https://www.fai.org/sites/default/files/sc3a_2019.pdf.

[40] Anthony Fiacco and Garth P. McCormick. "The Sequential Unconstrained Minimization Technique for Nonlinear Programing, a Primal-Dual Method." In: *Management Science* 10.2 (1964), pp. 360–366. ISSN: 0025-1909. DOI: 10.1287/mnsc.10.2.360.

[41] Claude Fleury and Vincent Braibant. "Structural optimization: A new dual method using mixed variables." In: *International Journal for Numerical Methods in Engineering* 23.3 (1986), pp. 409–428. ISSN: 0029-5981. DOI: 10.1002/nme.1620230307.

[42] Donald E. Gault. "A correlation of low-speed, airfoil-section stalling characteristics with Reynolds number and airfoil geometry." In: *NACA-TN-3963* (1957).

[43] C. Gleyzes, J. R. Cousteix, and J. L. Bonnet. "Theoretical and Experimental Study of Low Reynolds Number Transitional Separation Bubbles." In: *Presented at the Conference on Low Reynolds Number Airfoil Aerodynamics, University of Notre Dame, Notre Dame, IN* (1985).

[44] J. E. Green, D. J. Weeks, and J. W. F. Brooman. "Prediction of Turbulent Boundary Layers and Wakes in Compressible Flow by a Lag-Entrainment Method." In: *Aeronautical Research Council Reports & Memoranda* R&M No. 3791 (1977).

[45] Michael Greiner, Gerhard Waibel, and Lutz Werner Jumtow. *Flight manual for the self-sustaining powered sailplane ASW 27-18E "ASG 29 Es"*. 1.12.2007. Poppenhausen/Rhön: Alexander Schleicher GmbH & Co., 2007.

[46] Nico Grosse. "Nonlinear Topology Optimization with Compressible Hyperelastic Material Models." Master Thesis. München: TU München, 2019.

[47] Hannah Hajdik, Bernardo Pacini, Anil Yildirim, Benjamin J. Brelje, and Joaquim R. Martins. "Combined systems packaging and aerodynamic shape optimization of a full aircraft configuration." In: *AIAA AVIATION 2023 Forum*. Reston, Virginia: American Institute of Aeronautics and Astronautics, 2023. ISBN: 978-1-62410-704-7. DOI: 10.2514/6.2023-3589.

[48] Gustavo Luiz Olichevis Halila, Anil Yildirim, Charles A. Mader, Krzysztof J. Fidkowski, and Joaquim R. R. A. Martins. "Linear Stability-Based Smooth Reynolds-Averaged Navier–Stokes Transition Model for Aerodynamic Flows." In: *AIAA Journal* 60.2 (2022), pp. 1077–1090. DOI: 10.2514/1.J060481.

[49] Thomas H. Hansen. "Aerodynamic Optimisation of Airfoils and Winglets for Wind Turbine Application." Dissertation. Norway: NTNU, 2017.

[50] Martin Heide. *ASH 25 Technische Mitteilung Nr.18*. Ed. by Alexander Schleicher GmbH & Co. URL: https://www.alexander-schleicher.de/wp-content/uploads/2015/02/250_TM18_D.pdf.

[51] Nathaniel Hildebrand, Meelan M. Choudhari, and Pedro Paredes. "Predicting Boundary-Layer Transition over Backward-Facing Steps via Linear Stability Analysis." In: *AIAA Journal* 58.9 (2020), pp. 3728–3734. DOI: 10.2514/1.J059713.

[52] Karl-Heinz Horstmann. "Ein Mehrfach-Traglinienverfahren und seine Verwendung für Entwurf und Nachrechnung nichtplanarer Flügelanordnungen." In: *DFVLR-FB–87-51* (1987).

[53] Karl-Heinz Horstmann, A. Quast, and G. Redeker. "Flight and wind-tunnel investigations on boundary-layer transition." In: *Journal of Aircraft* 27.2 (1990), pp. 146–150. ISSN: 0021-8669. DOI: 10.2514/3.45910.

[54] Gerrit Illenberger. "Numerical Investigations on the Static Aeroelasticity of a Sailplane with a Morphing Forward Wing Section." term thesis. Technical University of Munich, 2019.

[55] Katharina Jocham. "Untersuchung und Bewertung formvariabler Flügelschalenkonzepte anhand mechanischer Versuche." master thesis. Technical University of Munich, 2019.

[56] A. S. Jonker, J. J. Bosman, E. H. Mathews, and L. Liebenberg. "Flow over a glider canopy." In: *The Aeronautical Journal* 118.1204 (2014), pp. 669–682. ISSN: 0001-9240. DOI: 10.1017/S0001924000009428.

[57] Melissa Karman, Michelle McNamara, and James G. Coder. "Airfoil Optimization via the Class-Shape Transformation and Orthogonal Deformation Modes." In: *AIAA Aviation 2019 Forum*. Reston, Virginia: American Institute of Aeronautics and Astronautics, 2019, p. 460. ISBN: 978-1-62410-589-0. DOI: 10.2514/6.2019-3173.

[58] Soshi Kawai and Kozo Fujii. "Analysis and Prediction of Thin-Airfoil Stall Phenomena with Hybrid Turbulence Methodology." In: *AIAA Journal* 43.5 (2005), pp. 953–961. DOI: 10.2514/1.11672.

[59] Markus Kintscher, Hans Peter Monner, Timo Kühn, Jochen Wild, and Martin Wiedemann. “Low speed wind tunnel test of a morphing leading edge.” In: *AIDAA - Italian Association of Aeronautics and Astronautics XXII Conference*. 2013.

[60] Frank Kody, Götz Bramesfeld, and Sven Schmitz. “An Efficient Methodology for Using a Multi-Objective Evolutionary Algorithm for Winglet Design.” In: *Technical Soaring* 37.3 (2013).

[61] Travis Krebs and Götz Bramesfeld. “Using an optimisation process for sailplane winglet design.” In: *The Aeronautical Journal* 120.1233 (2016), pp. 1726–1745. ISSN: 0001-9240. DOI: 10.1017/aer.2016.83.

[62] Krzysztof Kubrynski. “Design of a Flapped Laminar Airfoil for High Performance Sailplane.” In: *30th AIAA Applied Aerodynamics Conference*. 2012, pp. 94–115. DOI: 10.2514/6.2012-2662.

[63] Brenda Kulfan and John Bussoletti. “"Fundamental" Parametric Geometry Representations for Aircraft Component Shapes.” In: *11th AIAA/ISSMO Multidisciplinary Analysis and Optimization Conference*. Multidisciplinary Analysis Optimization Conferences. American Institute of Aeronautics and Astronautics, 2006. DOI: 10.2514/6.2006-6948.

[64] Udit Kumar, Sumit Soman, and Jayadeva. “Benchmarking NLopt and state-of-the-art algorithms for continuous global optimization via IACOR.” In: *Swarm and Evolutionary Computation* 27.3 (2016), pp. 116–131. ISSN: 22106502. DOI: 10.1016/j.swevo.2015.10.005.

[65] Boyan Stefanov Lazarov and Ole Sigmund. “Filters in topology optimization based on Helmholtz type differential equations.” In: *International journal for numerical methods in engineering* 86.6 (2011), pp. 765–781. DOI: 10.1002/nme.3072.

[66] Daniel M. de Leon, Joe Alexandersen, Jun S. O. Fonseca, and Ole Sigmund. “Stress-constrained topology optimization for compliant mechanism design.” In: *Structural and Multidisciplinary Optimization* 52.5 (2015), pp. 929–943. ISSN: 1615-1488. DOI: 10.1007/s00158-015-1279-z.

[67] Dong Li. “Numerical simulation of thin airfoil stall by using a modified DES approach.” In: *International Journal for Numerical Methods in Fluids* 54.3 (2007), pp. 325–332. ISSN: 02712091. DOI: 10.1002/fld.1403.

[68] Carsten Liersch, Thomas Engelbrecht, and Karl-Heinz Horstmann. *User Handbook Lifting_Line Version 3.1 Revision 0*. Ed. by DLR, Institute AS. 2020.

[69] A. Lipp. “Use of Satellite Navigation for Sailplane Performance Measurement: Presented at the XXV OSTIV Congress, St. Auban, France, 1997.” In: *Technical Soaring* 22.1 (1998), pp. 17–23.

[70] Thorsten Lutz. “airfoil design (Profilentwurf).” lecture notes. University of Stuttgart, 2008.

[71] M&D Flugzeugbau GmbH. *JS-MD 3 Aircraft Flight Manual: Doc. Nr.: MD10-AFM-00-001*. 0th ed. M&D Flugzeugbau GmbH, 2017.

[72] Paul MacCready. “Die Beste Streckenfluggeschwindigkeit für Segelflugzeuge.” In: *Schweizer Aero Revue, Zurich* 24 (1949), pp. 441–443.

[73] L. M. Mack. “Transition and laminar instability.” In: *NASA-CR-153203, JPL-PUBL-77-15* (1977).

[74] Charles A. Mader, Gaetan K. W. Kenway, Anil Yildirim, and Joaquim R. R. A. Martins. “ADflow: An Open-Source Computational Fluid Dynamics Solver for Aerodynamic and Multidisciplinary Optimization.” In: *Journal of Aerospace Information Systems* 17.9 (2020), pp. 508–527. DOI: 10.2514/1.I010796.

[75] Gerhard Marzinzik. "Binder EB29R und EB29DR: R für Racing." In: *Aerokurier* 7 (2017), pp. 86–91.

[76] D. A. Masters, N. J. Taylor, T. C. S. Rendall, C. B. Allen, and D. J. Poole. "Geometric Comparison of Aerofoil Shape Parameterization Methods." In: *AIAA Journal* 55.5 (2017), pp. 1575–1589. DOI: 10.2514/1.J054943.

[77] Mark D. Maughmer. "Design of Winglets for High-Performance Sailplanes." In: *Journal of Aircraft* 40.6 (2003), pp. 1099–1106. ISSN: 0021-8669. DOI: 10.2514/2.7220.

[78] Mark D. Maughmer and James G. Coder. *Comparisons of Theoretical Methods for Predicting Airfoil Aerodynamic Characteristics*. Ed. by Airfoils. Incorporated. Port Matilda, PA, USA, 2010.

[79] Mark D. Maughmer, James G. Coder, Christoph Wannenmacher, and Werner Würz. "The Design of a New Racing Sailplanes: A New Thermal Mix Model and the Role of Transitional CFD." In: *17th AIAA Aviation Technology, Integration, and Operations Conference*. Reston, Virginia: American Institute of Aeronautics and Astronautics, 2017, p. 87. ISBN: 978-1-62410-508-1. DOI: 10.2514/6.2017-4091.

[80] F. R. Menter, R. Langtry, and S. Völker. "Transition Modelling for General Purpose CFD Codes." In: *Flow, Turbulence and Combustion* 77.1-4 (2006), pp. 277–303. ISSN: 1386-6184. DOI: 10.1007/s10494-006-9047-1.

[81] J. Morgado, R. Vizinho, M.A.R. Silvestre, and J. C. Páscoa. "XFOIL vs CFD performance predictions for high lift low Reynolds number airfoils." In: *Aerospace Science and Technology* 52 (2016), pp. 207–214. ISSN: 12709638. DOI: 10.1016/j.ast.2016.02.031.

[82] Mark V. Morkovin, E. Reshotko, and T. Herbert. "Transition in open flow systems – a reassessment." In: *Bulletin of the American Physical Society* 39.9 (1994), p. 1882.

[83] J. A. Nelder and R. Mead. "A Simplex Method for Function Minimization." In: *The Computer Journal* 7.4 (1965), pp. 308–313. ISSN: 0010-4620. DOI: 10.1093/comjnl/7.4.308.

[84] Gael de Oliveira, Ricardo Pereira, Nando Timmer, and Ruud van Rooij. "Improved airfoil polar predictions with data-driven boundary-layer closure relations." In: *Journal of Physics: Conference Series* 1037 (2018), p. 022009. ISSN: 1742-6588. DOI: 10.1088/1742-6596/1037/2/022009.

[85] P. Panagiotou, P. Kaparos, and K. Yakinthos. "Winglet design and optimization for a MALE UAV using CFD." In: *Aerospace Science and Technology* 39 (2014), pp. 190–205. ISSN: 12709638. DOI: 10.1016/j.ast.2014.09.006.

[86] Falk Pätzold. "Windmessung mittels Segelflugzeug." Dissertation. Technische Universität Braunschweig, 2018. DOI: 10.24355/dbbs.084-201805221102-1.

[87] Claus B. W. Pedersen, T. Buhl, and O. Sigmund. "Topology synthesis of large-displacement compliant mechanisms." In: *International journal for numerical methods in engineering* 50.12 (2001), pp. 2683–2705.

[88] Jean Perraud. "Linear Stability of the Incompressible Boundary Layer over 2D Steps and Gaps." In: *EUROMECH 380, Laminar- turbulent transition mechanisms and prediction, Göttingen, Germany* (1998).

[89] Jean Perraud, Daniel Arnal, and Winfried Kuehn. "Laminar-turbulent transition prediction in the presence of surface imperfections." In: *International Journal of Engineering Systems Modelling and Simulation* 6.3/4 (2014), p. 162. ISSN: 1755-9758. DOI: 10.1504/IJESMS.2014.063129.

[90] Jean Perraud, Daniel Arnal, A Seraudie, and D Tran. *Laminar-turbulent transition on aerodynamic surfaces with imperfections*. 2004. DOI: 10.13140/RG.2.1.3532.1364.

[91] M. J. D. Powell. "A hybrid method for nonlinear equations." In: *Numerical methods for nonlinear algebraic equations*. Ed. by Philip Rabinowitz. New York: Gordon and Breach Science Publishers, 1970, pp. 87–114.

[92] M. J. D. Powell. "A Direct Search Optimization Method That Models the Objective and Constraint Functions by Linear Interpolation." In: *Advances in Optimization and Numerical Analysis*. Ed. by Susana Gomez and Jean-Pierre Hennart. Dordrecht: Springer Netherlands, 1994, pp. 51–67. ISBN: 978-90-481-4358-0. DOI: 10.1007/978-94-015-8330-5{\textunderscore}4.

[93] M. J. D. Powell. *The BOBYQA algorithm for bound constrained optimization without derivatives*. Ed. by University of Cambridge. 2009.

[94] Christian Raab and Kai Rohde-Brandenburger. "Dynamic flight load measurements with MEMS pressure sensors." In: *CEAS Aeronautical Journal* (2021). ISSN: 1869-5590. DOI: 10.1007/s13272-021-00529-3.

[95] Martin Radestock, Johannes Riemenschneider, Hans-Peter Monner, and Rose Michael. "Structural optimization of an UAV leading edge with topology optimization." In: *DeMEASS Design, Modelling and Experiments of Advanced Structures and Systems Conference* (2014).

[96] Giridhar Ramanujam and Hüseyin Özdemir. "Improving Airfoil Lift Prediction." In: *35th Wind Energy Symposium 2017*. Red Hook, NY: Curran Associates Inc, 2017, p. 1. ISBN: 978-1-62410-456-5. DOI: 10.2514/6.2017-1999.

[97] Joseph Reinisch. "Topologieoptimierung von Compliant Mechanisms mit nichtlinearer FEM und Spannungsrestriktionen." Term Thesis. Technical University of Munich, 2017.

[98] Joseph Reinisch. "Synthesis of Compliant Mechanisms for Morphing Wings with Nonlinear Topology Optimization." Master Thesis. München: Technical University of Munich, 2018.

[99] Joseph Reinisch, Erich Wehrle, and Johannes Achleitner. "Multiresolution Topology Optimization of Large-Deformation Path-Generation Compliant Mechanisms with Stress Constraints." In: *Applied Sciences* 11.6 (2021), p. 2479. DOI: 10.3390/app11062479.

[100] Ulrich Rist. "Zur Instabilitat und Transition in laminaren Abloseblasen." Habilitationsschrift. Stuttgart, Germany: University of Stuttgart, 1998.

[101] Olinde Rodrigues. "Des lois géométriques qui régissent les déplacements d'un système solide dans l'espace, et de la variation des coordonnées provenant de ces déplacements considérés indépendants des causes qui peuvent les produire." In: *Journal de Mathématiques Pures et Appliquées* 5 (1840), pp. 380–440.

[102] T. H. Rowan. "Functional Stability Analysis of Numerical Algorithms." Dissertation. Austin: University of Texas, 1990.

[103] Luka Salehar. "Preliminary Design of a Compliant Mechanism for a Morphing Wing Leading Edge." Term Thesis. Technical University of Munich, 2015.

[104] William S. Saric, Helen L. Reed, and Edward J. Kerschen. "Boundary layer receptivity to freestream disturbances." In: *Annual Review of Fluid Mechanics* 34.1 (2002), pp. 291–319. ISSN: 0066-4189. DOI: 10.1146/annurev.fluid.34.082701.161921.

[105] M. Schevenels, Boyan Stefanov Lazarov, and O. Sigmund. "Robust topology optimization accounting for spatially varying manufacturing errors." In: *Computer Methods in Applied Mechanics and Engineering* 200.49-52 (2011), pp. 3613–3627. DOI: 10.1016/j.cma.2011.08.006.

[106] Georg Schiffleithner. "Wind tunnel tests of current sailplane wing-fuselage configurations." Diploma thesis. TU München, 2007.

[107] Hermann Schlichting and Erich Truckenbrodt. *Aerodynamik des Flugzeuges*. Berlin, Heidelberg: Springer Berlin Heidelberg, 2001. ISBN: 978-3-642-63148-1. DOI: 10.1007/978-3-642-56911-1.

[108] Peter Scholz. "Entwurf und Analyse eines Winglets für Segelflugzeuge am Beispiel des Segelflugzeuges SB 14." Studienarbeit. Braunschweig: Technische Universität Braunschweig, 2000.

[109] Peter F. Selinger. *Rhön-Adler: Drei Generationen Alexander Schleicher Segelflugzeugbau*. 3. berichtigte und ergänzte Auflage. Poppenhausen/Rhön: Alexander Schleicher GmbH & Co.KG, 2015. ISBN: 978-3-00-048851-1.

[110] Ole Sigmund. "Design of material structures using topology optimization." PhD thesis. Lyngby: Technical University of Denmark, 1994.

[111] Martin Simons. *Sailplanes*. Königwinter: EQUP Werbung & Verlag, 2004. ISBN: 978-3980883818.

[112] Michael Sinapius, Hans-Peter Monner, Markus Kintscher, and Johannes Riemenschneider. "DLR's Morphing Wing Activities within the European Network." In: *23rd International Congress of Theoretical and Applied Mechanics, ICTAM2012* (2014), pp. 416–426. DOI: 10.1016/j.piutam.2014.01.036.

[113] A. M. O. Smith and N. Gamberoni. "Transition, Pressure Gradient and Stability Theory." Report ES-26388. Douglas Aircraft, 1956.

[114] Jason D. Stanko, James G. Coder, and Sven Schmitz. "Shape optimization of rotorcraft airfoils using a genetic algorithm." In: *Annual Forum Proceedings - AHS International* 2018-May (2018). ISSN: 1552-2938.

[115] Rainer Storn and Kenneth Price. "Differential Evolution – A Simple and Efficient Heuristic for global Optimization over Continuous Spaces." In: *Journal of global optimization* 11.4 (1995), pp. 341–359. ISSN: 1573-2916. DOI: 10.1023/A:1008202821328.

[116] Fabian Sturm, Johannes Achleitner, Katharina Jocham, and Mirko Hornung. "Studies of Anisotropic Wing Shell Concepts for a Sailplane with a Morphing Forward Wing Section." In: *AIAA Aviation 2019 Forum*. Reston, Virginia: American Institute of Aeronautics and Astronautics, 2019, p. 4. ISBN: 978-1-62410-589-0. DOI: 10.2514/6.2019-2817.

[117] Fabian Sturm, Gerrit Illenberger, David Techmer, and Mirko Hornung. "Static aeroelastic tailoring of a high-aspect-ratio wing with a forward morphing wing section." In: *ICAS 13 - Proceedings of the 32nd Conference of the International Council of Aeronautical Sciences* (2021).

[118] Krister Svanberg. "The method of moving asymptotes—a new method for structural optimization." In: *International Journal for Numerical Methods in Engineering* 24.2 (1987), pp. 359–373. ISSN: 0029-5981. DOI: 10.1002/nme.1620240207.

[119] Fred Thomas. *Fundamentals of sailplane design: Grundlagen für den Entwurf von Segelflugzeugen*. 3. Aufl. College Park Md.: College Park Pr, 2001. ISBN: 0-9669553-0-7.

[120] W. A. Timmer and Ruud P. J. O. M. van Rooij. “Summary of the Delft University Wind Turbine Dedicated Airfoils.” In: *Journal of Solar Energy Engineering* 125.4 (2003), p. 488. ISSN: 01996231. DOI: 10.1115/1.1626129.

[121] David J. J. Toal, Neil W. Bressloff, Andy J. Keane, and Carren M. E. Holden. “Geometric Filtration Using Proper Orthogonal Decomposition for Aerodynamic Design Optimization.” In: *AIAA Journal* 48.5 (2010), pp. 916–928. DOI: 10.2514/1.41420.

[122] Rajesh Vaithiyanathasamy, Huseyin Ozdemir, Gabriele Bedon, and Arne van Garrel. “A double wake model for interacting boundary layer methods.” In: *2018 Wind Energy Symposium*. Reston, Virginia: American Institute of Aeronautics and Astronautics, 2018, p. 1. ISBN: 978-1-62410-522-7. DOI: 10.2514/6.2018-0516.

[123] Srinivas Vasista, Alessandro de Gaspari, Bram van de Kamp, Johannes Riemenschneider, Hans-Peter Monner, and Sergio Ricci. “Compliant structures-based wing and wingtip morphing devices.” In: *Aircraft Engineering and Aerospace Technology* 88.2 (2016), pp. 311–330. ISSN: 0002-2667. DOI: 10.1108/AEAT-02-2015-0067.

[124] Fengwen Wang, Boyan Stefanov Lazarov, and Ole Sigmund. “On projection methods, convergence and robust formulations in topology optimization.” In: *Structural and Multidisciplinary Optimization* 43.6 (2011), pp. 767–784. ISSN: 1615-1488. DOI: 10.1007/s00158-010-0602-y.

[125] Jacob Weierman and Jamey Jacob. “Winglet Design and Optimization for UAVs.” In: *28th AIAA Applied Aerodynamics Conference*. Reston, Virigina: American Institute of Aeronautics and Astronautics, 2010. ISBN: 978-1-62410-141-0. DOI: 10.2514/6.2010-4224.

[126] Matthias Weinzierl, Johannes Achleitner, and Horst Baier. “Highly Extensible Skin of a Variable Geometry Wing Leading Edge of a High-Performance Sailplane.” In: *Technical Soaring* 39.1 (2015), pp. 4–9.

[127] Gerko Wende. “Ermittlung der Flugleistung von Segelflugzeugen.” Dissertation. TU Braunschweig, 2003.

[128] Michael Wiessmeier. “Konzept einer formvariablen Tragflügelvorderkante bei einem Segelflugzeug mit innenliegender Ansteuerung über ein Rotary Drive System (RDS).” Semester thesis. TU Munich, 2011.

[129] David C. Wilcox. *Turbulence modeling for CFD*. Third edition. [Place of publication not identified]: DCW Industries, 2010. ISBN: 978-1928729082.

[130] Thomas Wortmann, Christoph Waibel, Giacomo Nannicini, Ralph Evins, Thomas Schröpfer, and Jan Carmeliet. “Are Genetic Algorithms Really the Best Choice in Building Energy Optimization?” In: *Proceedings of the 2017 Symposium on Simulation for Architecture and Urban Design (SimAUD 2017)*. Society for Modeling and Simulation International (SCS), 2017. ISBN: 9781510870185. DOI: 10.22360/simaud.2017.simaud.006.

[131] Shengli Xu, Yuanwu Cai, and Gengdong Cheng. “Volume preserving nonlinear density filter based on heaviside functions.” In: *Structural and Multidisciplinary Optimization* 41.4 (2010), pp. 495–505. ISSN: 1615-1488. DOI: 10.1007/s00158-009-0452-7.

[132] Shun Zhang, Mark Drela, Marshall C. Galbraith, Steven R. Allmaras, and David Darmofal. “An Integral Boundary Layer Method using Discontinuous Galerkin Discretization and Captured Transition Modeling.” In: *AIAA AVIATION 2020 FORUM*. Reston, Virginia: American Institute of Aeronautics and Astronautics, 2020. ISBN: 978-1-62410-598-2. DOI: 10.2514/6.2020-2973.

[133] Jan L. van Ingen. "A suggested semi-empirical method for the calculation of the boundary layer transition region." Rapport VTH-74. TU Delft, 1956.

[134] Jan L. van Ingen. *A new e^N database method for transition prediction*. Ed. by TU Delft. 2006.

[135] Jan L. van Ingen. "The eN Method for Transition Prediction. Historical Review of Work at TU Delft." In: *38th Fluid Dynamics Conference and Exhibit*. Reston, Virigina: American Institute of Aeronautics and Astronautics, 2008, p. 110. ISBN: 978-1-60086-989-1. DOI: 10.2514/6.2008-3830.

[136] Ruud P. J. O. M. van Rooij. "Modification of the boundary layer calculation in RFOIL for improved airfoil stall prediction." Tech Report IW-96087R. TU Delft, 1996.

Part I

APPENDIX

A

APPENDIX A: DEFINITIONS AND REFERENCE DATA

A.1 SAILPLANE COMPETITION CLASSES

In international gliding competitions, currently seven sailplane classes exist, as defined in the FAI sporting code section 3 [38]:

- Open class
- 20 meter multi-seat class
- 18 meter class
- 15 meter class
- 13.5 meter class
- Standard class
- Club class

The open class has no limitations according to the FAI sporting code section 3 [38]. The 20 meter multi-seat class, the 18 meter class, the 15 meter class and the 13.5 meter class are limited in span as the class names suggest. The 20 meter multi-seat class shall have a crew of two persons on board. The standard class is limited to a wing span of 15 m and the wing must not be able to change its wing profile except normal usage of ailerons. And lift increasing devices are prohibited. Hence, a morphing wing sailplane cannot be specified for the standard class. The club class is defined for older sailplanes in order to allow club pilots with limited financial resources to participate in national and international gliding competitions. The approved sailplane types for the club class have to be specified on a list of handicaps, issued by the IGC. On this list, only older sailplanes are approved, where serial production has ceased. Therefore, a morphing wing sailplane can also not be considered for the club class.

One example for the state of the art for a modern open class sailplane design is the *Butler Concordia*, which is a 28 m span prototype with an ultra slender wing with an aspect ratio of 57, shown in the left part of fig. A.1. The *Binder EB29R* (fig. A.1 right) has similar design features as the *Concordia*. The wing span is 28 m, the aspect ratio is slightly lower than the *Concordia's* with 52.6. Both the *Concordia* and the *EB29R* show the trends of sailplane design. The wing area is reduced to a minimum and consequently the wing loading is increased to the maximum. The limiting design specification for wing area and wing loading is shown in section 3.2. Both aircraft feature a multitude of last generation airfoils with camber changing flaps for the wing, accounting for their specific Reynolds number range due to the chord length, for structural requirements which limit the airfoil thickness and for handling and stall requirements on the outer section of the wing, which implies an ample lift reserve compared to the inner wing airfoils. The wing planform features multi-trapezoidal sections resulting in a close to optimum circulation distribution in combination with the blended winglets. These are increased in height compared to older designs and also feature multiple airfoils for the winglet blade and the root. The wing-fuselage intersection is designed for minimum interference drag by accounting for the loss of lift due to the fuselage with increased chord length of the airfoils and an increase of the angle of incidence close to the fuselage. Also the turbulent inflow due to the fuselage in the root section is considered with a turbulent root airfoil. The horizontal tailplane is reduced in area compared to older designs. All that measures result in best glide ratios of above 70 and very low sink rates at high speeds [109] [75].

Figure A.1: Open class sailplanes *Butler Concordia* (left, Photo: Paul Remde/flickr.com) and *Binder EB29R* (right, Photo: Jens Trabolt/NORDICGLIDING.COM) in flight

Many sailplane types are designed with exchangeable wingtip for both the 18 meter and the 15 meter class, because the difference in span allows nearly optimal planforms to be designed for both span widths. Modern examples are the *Jonkers JS-3*, the *Schempp-Hirth Ventus-3*, the *Schleicher AS 33*, shown in fig. A.2. In this latest designs, modern RANS CFD methods found their way into sailplane design and optimization ([56], [79], [10]), because of the rise of efficient and fairly accurate laminar-turbulent transition prediction methods ([80], [24], [23]). The 18 meter class is one of the most popular classes, because of both very good handling qualities and performance of those sailplanes. The morphing wing sailplane introduced in this thesis is designed for the 18 meter class. Besides the popularity and hence market potential of this class, there are some other reasons that give preference for the 18 meter class over other classes. First, the bending and torsional loads for an 18 m wing are moderate compared to an open class design, thus allowing for very thin wing airfoils and for limiting the torsional box to the aft spar segment of the wing due to the morphing forward section. Second, the wing can be designed as a two-piece wing and be accommodated in a standard trailer without the need for separate outer and inner wing panels and wing interconnection. This makes design easier and an optional wing cut can be introduced in a future design iteration. The morphing wing sailplane in this thesis is based on the *Schleicher ASG 29* (fig. A.2 bottom right), the predecessor of the *AS 33*, because the airfoils and wing and tailplane geometry are known and available, as well as wind tunnel measurement data for the main wing and tailplane airfoils. Furthermore, comprehensive overall aircraft performance measurement data exists for realistic performance extrapolation for the morphing wing aircraft.

A further limitation affecting the design is specified in the Annex A to the FAI sporting code section 3 [39], where further rules for international and continental championships are defined. The MTOM of an 18 meter class sailplane is limited to $m_{MTOM} = 600$ kg, which is an important value for determining the wing area, as pointed out in the next subsection.

Figure A.2: 18 meter class sailplanes:
Jonkers JS3 (top left, Photo: Jonker Sailplanes/`jonkersailplanes.co.za`)
Schempp-Hirth Ventus-3 (top right, Photo: Schempp-Hirth/`schempp-hirth.com`)
Schleicher AS 33 (bottom left, Photo: Manfred Münch/`alexander-schleicher.de`)
Schleicher ASG 29 (bottom right, Photo: Manfred Münch/`alexander-schleicher.de`)

A.2 AERODYNAMIC DATA OF THE ASG 29 SAILPLANE

The aerodynamic data of the *ASG 29* sailplane, which is required for calculating the aerodynamic performance of the sailplane as performed in this thesis is given in this section. A three side view is shown in fig. 1.3. The reference axis is the axis of the rear (conical) part of the fuselage. The wing is mounted with an incidence angle of $\varepsilon_W = -0.65°$ to the reference axis. The horizontal stabilizer has an angle of incidence of $\varepsilon_H = -1.9°$ to the reference axis. According to the pilot flight manual [45], a center of gravity range between 290 mm and 310 mm is beneficial. For all calculation, a center of gravity of $x_{cg} = 295$ mm is used.

A.2.1 *Wing data*

In this subsection, the wing planform, twist distribution and the airfoils of the *ASG 29* wing is given. However, the wing root airfoils are not required, because wing-fuselage interference effects are not considered in this thesis. The wing area is $A = 10.5\ \mathrm{m}^2$. The dihedral angle is constant $\kappa = 3.25°$ up to the winglet root. The wing planform data is given in table A.1. Up to the winglet root location, the wing sections are trapezoidals. From the winglet begin location on to the winglet root, a cubic spline transition is used for the leading and trailing edges. The winglet itself is trapezoidal again, with an elliptic tip at the outermost 60 mm in spanwise curve length coordinates s.

The wing airfoils *DU89-134-14* and *DU92-131-14* are 13.4% and 13.1% thick and have a camber changing flap of 14% of the chord. The design and wind tunnel measurements of the *DU89-134-14* is shown in reference [16].

Table A.1: ASG 29 wing planform data

y mm	x_{LE} mm	z_{LE} mm	$\bar{c}$ mm
0	0	0	780
4612.5	37.5	261.9	630
6644	109	377.3	500
8291	226.8	470.8	325
8888	301.9	504.7	224
8950.25	435.9	508.2	180
9000	636.4	955.3	90

The camber changing flap starts close to the wing root at $y = 350$ mm and extends to $y = 4000$ mm. The aileron begins adjacent to the flap end and ranges up to $y = 8888$ mm. For all seven flap settings, the flap and aileron deflections are given in table A.2.

Table A.2: ASG 29 flap and aileron deflections (aileron neutral)

Flap setting	δ_{flap} °	δ_{ail} °
L	47	12
6	24	22
5	20	19
4	12	11
3	5	5
2	0	0
1	-2.5	-2.5

A.2.2 *Horizontal stabilizer*

The horizontal stabilizer of the *ASG 29* sailplane is also used for the morphing wing sailplane design. It has a span of $b_H = 2.3$ m and an area of $A_H = 0.7232$ m^2. Its origin is located at $x = 3969$ mm and $z = 965$ mm behind and above the wing origin. It's angle of incidence is $\varepsilon_H = -1.9°$ relative to the aircraft reference axis, giving $-1.25°$ relative to the wing. The planform data is shown in table A.3. The outermost 125 mm are shaped as an elliptic tip with zero tip chord. The elevator hinge axis is a straight line, located at 75% relative chord length. The airfoil is the *DU92-131-25*. However, as the mean aerodynamic chord of the morphing wing is smaller than the mean aerodynamic chord of the *ASG 29*, a smaller horizontal tailplane could be used maintaining an equal tail volume coefficient and presumably similar elevator handling characteristics.

Table A.3: ASG 29 horizontal stabilizer planform data

y mm	x_{LE} mm	z_{LE} mm	$\bar{c}$ mm	Airfoil
0	3969	965	420	*DU92-131-25*
4612.5	4119	969	220	*DU92-131-25*

In the multi lifting line method it is discretized with 89 panels in spanwise direction, distributed in a cosine spacing and 6 panels in chordwise direction, evenly distributed.

A.2.3 *Vertical stabilizer*

As with the horizontal stabilizer, also the vertical stabilizer is taken unchanged from the *ASG 29* sailplane. The vertical tailplane origin is located at $x = 3649$ mm and $z = -235$ mm behind and below the wing origin. The planform data is shown in table A.4. It has a span of $b_V = 1200$ mm and an area of $A_V = 0.95\ \mathrm{m}^2$. The airfoil is the symmetric *DU86-131-30*. The rudder has 30% relative chord.

Table A.4: ASG 29 vertical stabilizer planform data

y mm	x_{LE} mm	z_{LE} mm	$\bar{c}$ mm	twist ε °	Airfoil
0	3649	−235	945	0	*DU86-131-30*
0	4119	969	220	0	*DU86-131-30*

In the multi lifting line method it is discretized with 20 panels in spanwise direction, distributed in a cosine spacing and 6 panels in chordwise direction, evenly distributed.

A.3 MÜ31 WIND TUNNEL DATA

Here, the wing and wing + fuselage wind tunnel polars of the Mü31 sailplane for flap setting $\delta_F = 0°$, $Re_W = 0.7\ 10^6$, $Re_W = 1.23\ 10^6$ and $Re_W = 1.5\ 10^6$, as measured by Schiffleithner [106] are presented. It has to be noted, that the Reynolds number is referenced to the model wing chord. In this work, the fuselage length is the reference for the fuselage Reynolds number Re_F. As the wind tunnel model wing chord is $c = 0.26$ m and the fuselage length is $l_F = 2.067$ m, the fuselage Reynolds numbers are obtained as $Re_F = Re_W \frac{l_f}{c}$. Hence $Re_F = 5.57\ 10^6, Re_F = 9.78\ 10^6, Re_F = 11.93\ 10^6$.

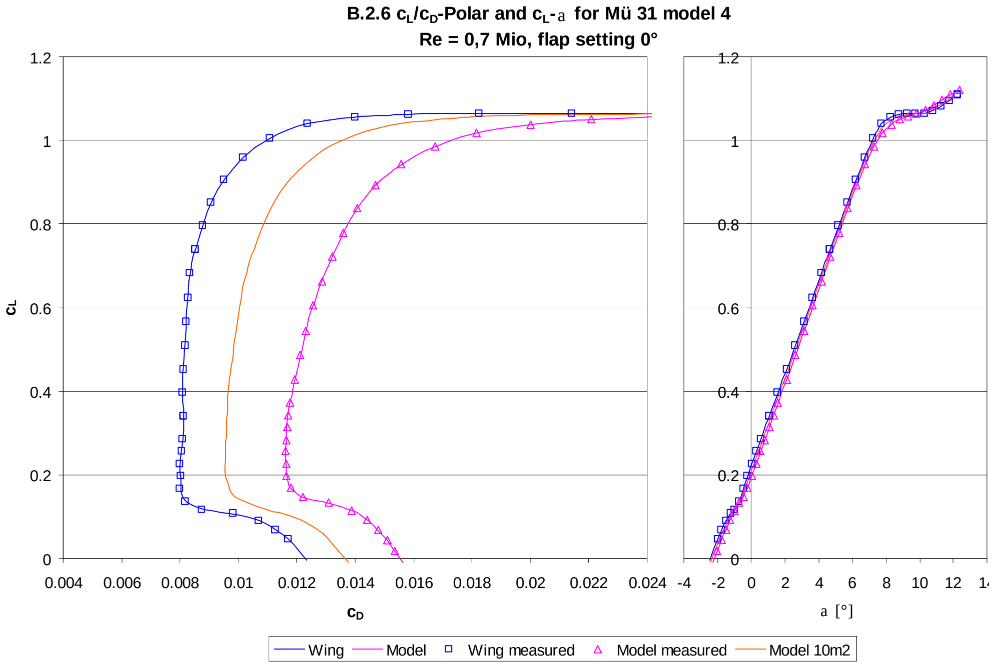

Figure A.3: Wing and Wing-Fuselage drag polar of the *Mü31* wind tunnel models for $\delta_F = 0°$, $Re_W = 0.7\ 10^6 = Re_F = 5.57\ 10^6$, as measured by Schiffleithner [106]

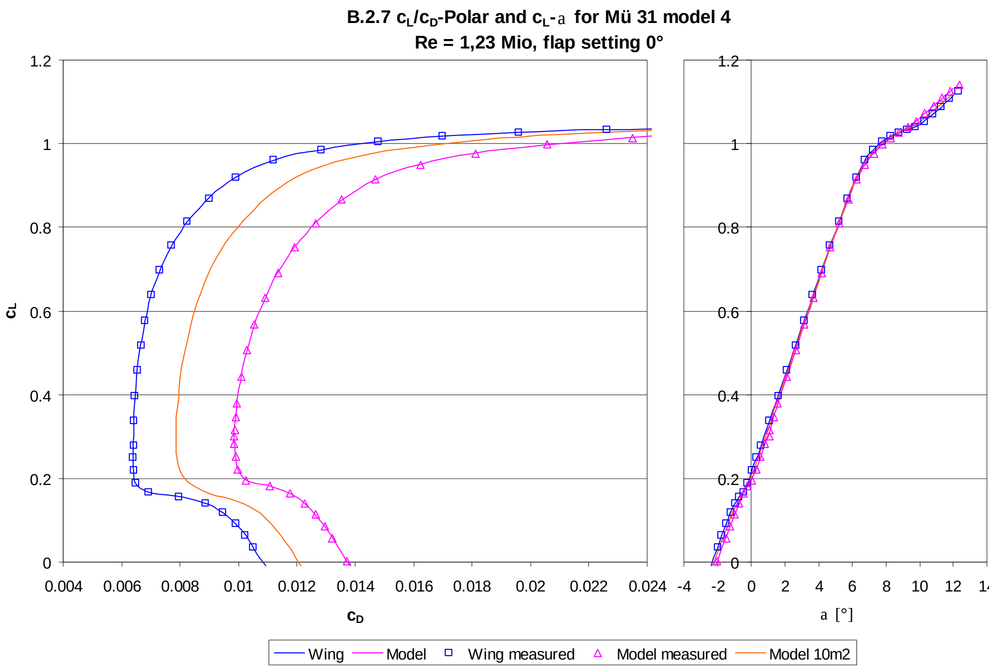

Figure A.4: Wing and Wing-Fuselage drag polar of the *Mü31* wind tunnel models for $\delta_F = 0°$, $Re_W = 1.23\ 10^6 = Re_F = 9.78\ 10^6$, as measured by Schiffleithner [106]

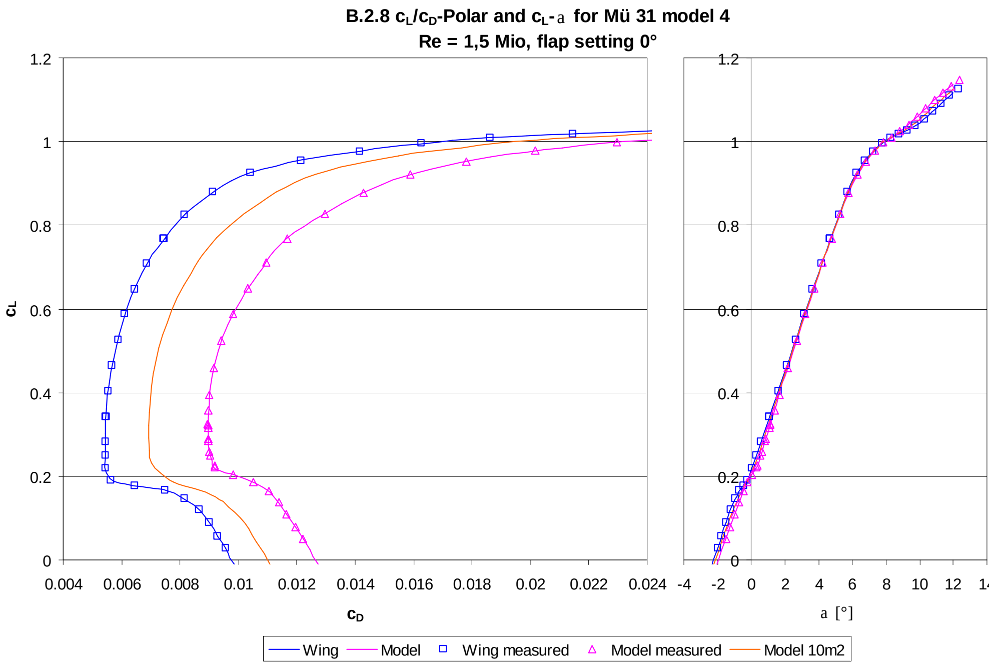

Figure A.5: Wing and Wing-Fuselage drag polar of the *Mü31* wind tunnel models for $\delta_F = 0°$, $Re_W = 1.5\ 10^6 = Re_F = 11.93\ 10^6$, as measured by Schiffleithner [106]

APPENDIX B: INVERSE CALCULATION OF CAMBER LINE AND THICKNESS DISTRIBUTION

For the decomposition of the airfoil, the thickness distribution $t(x)$ and the camber line $c(x)$ must be calculated. Both are represented by a cubic spline with n points, where $t_i(x_i), 1 \leq i \leq n$ are the points for the thickness distribution and $c_i(x_i)$ are the points of the camber line. The problem is written as a root search problem, where the root of a residual vector being the deviation in y-direction between the decomposed airfoil defined by its thickness distribution and camber line and the original airfoil contours $y_u(x)$ and $y_l(x)$ defined by its CST parameterization is sought. We write the problem as:

$$R_i = \begin{cases} c_i + \cos\left(\tan^{-1}\left(\frac{dc}{dx}(x_i)\right)\right)\frac{t_i}{2} - y_u\left(x_{u,i}\left(x_i, c_i, t_i\right)\right) = 0 \text{ if } 1 \leq i \leq n, x_{u,i} \leq x_c \\ c_i + \cos\left(\tan^{-1}\left(\frac{dc}{dx}(x_i)\right)\right)\frac{t_i}{2} - y_u\left(x_{u,i}\left(x_{s,i}\right)\right) = 0 \text{ if } 1 \leq i \leq n, x_{u,i} > x_c \end{cases} \tag{B.1}$$

$$R_{n+i} = c_i - \cos\left(\tan^{-1}\left(\frac{dc}{dx}(x_i)\right)\right)\frac{t_i}{2} - y_l\left(x_{l,i}\left(x_i, c_i, t_i\right)\right) = 0 \text{ if } 1 < i \leq n \tag{B.2}$$

$$R_{2n+j} = x_{s,j} - x_r - \cos\left(\delta_d\right)\left(x_{u,i} - x_r\right) - \sin\left(\delta_d\right)\left(y_{u,i} - y_r\right) = 0 \text{ if } 1 \leq j \leq n_{flap}, i = n - n_{flap} + j \tag{B.3}$$

The airfoil y-coordinates of the upper surface y_u and the lower surface y_l for eq. B.1 are calculated from eq. 4.17, for which the x-coordinates $x_{l,i}$ and $x_{u,i}$ are required. They are calculated from equations 4.22 and 4.24. However, if the design flap methodology is utilized, de-rotation according to equations 4.12 – 4.16 has to be applied. Hence, the x-coordinates after rotation are not directly determinable. They also have to be calculated iterative by the root search algorithm. The residual entries R_{2n+j} being the difference between the x-coordinate calculated from the camber line and thickness distribution according to eq. 4.22 and from de-rotation from a search coordinate $x_{s,i}$. The slope $\frac{dc}{dx}(x_i)$ is the first derivative of the cubic spline. The vector of unknowns for the root finding problem is defined as follows:

$$u_i = c_i \quad \text{if} \quad 1 < i \leq n \tag{B.4}$$

$$u_{n+i} = t_i \quad \text{if} \quad 1 < i \leq n \tag{B.5}$$

$$u_{2n+j} = x_{s,j} \quad \text{if} \quad 1 < j \leq n_{flap} \tag{B.6}$$

(B.7)

For the root search, the efficient hybrid method by Powell [91] is used. For that, the Jacobian matrix is required. We assume that $\frac{dc}{dx}$ is small, which is valid for conventional airfoils with moderate camber. Hence the term $\cos\left(\tan^{-1}\left(\frac{dc}{dx}(x_i)\right)\right)$ is close to unity. Therefore the Jacobian simplifies becoming the following constant:

$$J_{i,j} = \begin{cases} 1 & \text{if} \quad 1 \leq i \leq 2n, 1 \leq j \leq n, i = j \\ 1 & \text{if} \quad n < i \leq 2n, 1 \leq j \leq n, i = j - n \\ \frac{1}{2} & \text{if} \quad 1 \leq i \leq n, n < j \leq 2n, i = n + j \\ -\frac{1}{2} & \text{if} \quad n < i \leq 2n, n < j \leq 2n, i = j \\ 1 & \text{if} \quad 2n < i < 2n + n_{flap}, 2n < i < 2n + n_{flap} \\ 0 & \text{otherwise} \end{cases} \tag{B.8}$$

The camber line and thickness distribution x-coordinates x_i in our case are calculated using a cosine distribution:

$$x_i = \frac{1}{2}\left(1 - \cos\left(\frac{i-1}{n-1}\pi\right)\right) \tag{B.9}$$

The residuals and the variables used are visualized in fig. B.1. The thickness distribution is normal to the camber line. The residuals R_i are the difference between the upper side y-coordinate calculated from camber line and thickness distribution guess and the actual y-coordinate calculated by the CST parameterization. The residuals R_{n+i} are accordingly calculated for the lower side. On the flap, not only the camber line and the thickness distribution are unknown, also the x-coordinate before de-rotation $x_{s,i}$ is not a-priori known, hence it is also calculated iterative by the root-finding algorithm. The corresponding residual entry is the difference between the coordinate x_u calculated via thickness distribution normal to the camber line and via de-rotation of the point calculated by the CST parameterization as a function of $x_{s,i}$. As an initial guess both the camber line and thickness distribution can be set to zero everywhere. Alternatively the initial guess can be calculated via the "classical" approach, which is:

$$t_i = y_{u,i} - y_{l,i} c_i = \frac{1}{2}\left(y_{u,i} + y_{l,i}\right) \tag{B.10}$$

Note that the camber line calculated with the inverse approach does not need to end at $(0, 0)$ (see fig. B.1b. The problem may be ill-posed during intermediate iterations. This is the case, when the first x-coordinate $x_{u,1}$ calculated from thickness distribution normal to the camber line becomes negative. Therefore a special treatment is necessary. In this case $x = 0$ is set artificially.

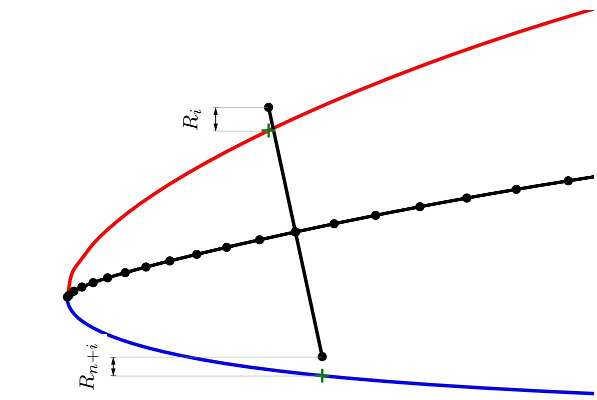

(a) Leading edge region at iteration 1

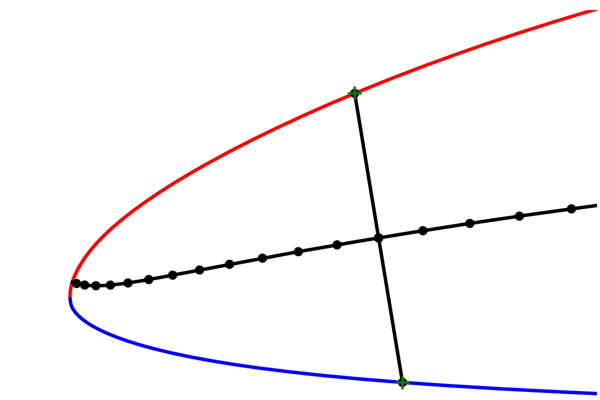

(b) Leading edge region after convergence

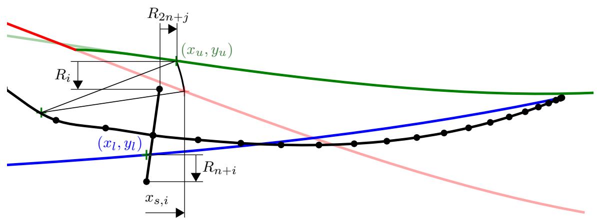

(c) Flap region at iteration 1

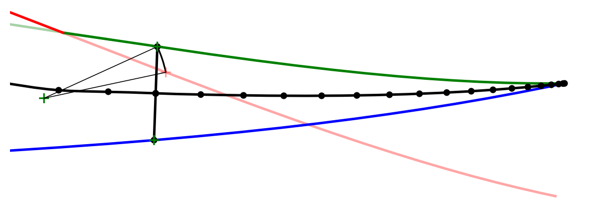

(d) Flap region after convergence

Figure B.1: Visualization of residuals for camber line and thickness distribution search